1. E.

PURDUE UNIVERSITY
APR 2 1961
LIBRARY

JOURNAL OF THE

AEROSPACE SCIENCES

VOLUME 28 APRIL 1961 NUMBER 4

CONTENTS

Possibilities of Aeronautical and Space Research in the Federal Republic of Germany (Twenty-Fourth Wright Brothers Lecture) ..... A. W. QUICK 257

Closing Remarks ..... HUGH L. DRYDEN 283

Missile Structural Loads by Nonstationary Statistical Methods ..... R. E. BIEBER 284

Vibration of Stepped Beams ..... N. J. TALEB AND E. W. SUPPIGER 295

Radiative Heat Transfer in Free-Molecule Flow ..... SAUL ABARBANEL 299

Buckling of a Column With Random Initial Displacements ..... WILLIAM E. BOYCE 308

Supersonic Boom of Wing-Body Configurations ..... I. L. RYHMING AND Y. A. YOLER 313

On the Aerodynamic Noise of a Turbulent Jet ..... SIN-I CHENG 321

Readers' Forum 332

MECHANICAL ENGINEERING
APR 10 1961
LIBRARY

Published by
INSTITUTE OF THE AEROSPACE SCIENCES, INC.

JOURNAL OF THE AEROSPACE SCIENCES

Editor: W. R. SEARS
Director, Graduate School of Aeronautical Engineering, Cornell University

Associate Editor: ROBERT R. DEXTER *Managing Editor:* RITA J. TURINO

Editorial Assistant: CHARLOTTE C. ROBB

IAS Aerospace Technology Panels

Paul J. Burr, Technical Services Director, Coordinator

The members of the IAS Aerospace Technology Panels shown here are to be available, collectively or as individuals, to assist and advise IAS committees, Sections, and staff members as to currently interesting and important technical topics related to their specialties and as to people most qualified to speak or write on such topics. The panels will also stimulate thought and scientific papers of potential value for the future, and they should be sensitive to technical activity of other professional groups, seeking through joint action the enlightenment of all having professional aerospace interests. Panel chairmen are indicated with an asterisk (*).

Aerodynamics and Fluid Mechanics

Lester Lees*
Dean R. Chapman
Antonio Ferri
Paul Germain
Wayland C. Griffith
Hans W. Liepmann
C. C. Lin
W. R. Sears
John R. Sellars
R. T. Whitcomb
Hideo Yoshihara

Aeroelasticity

R. L. Bisplinghoff*
Y. C. Fung
I. E. Garrick
Martin Goland
Kurt H. Hohenemser
J. C. Houbolt
W. P. Jones
W. J. Mykytow
Robert F. Speaker

Biomedical Sciences

Brig. Gen. D. Flickinger, USAF*
W. Ross Adey
Capt. Wm. Augerson, USA
Hilding Bjurstedt
Stuart Bondurant
A. Scott Crossfield
Cdr. J. H. Ebersole, USN
W. R. Lovelace, II
Capt. Bruce Pinc, USAF
Stanley Roscoe

Communication

P. C. Sandretto*
James M. Bridges
Leonard Jaffe
David S. Little
Cdr. D. O. Mann, USN
William Sen
Arnold Shostack
Teck A. Wilson

Control, Guidance, and Navigation

C. S. Draper*
R. C. Berendsen
B. Paul Blasingame
Robert N. Brown
S. F. Eyestone
Percy Halpert
B. J. O'Connor
Robert L. Roderick
S. F. Schmidt
O. Hugo Schuck
H. Philip Whitaker

Energy Conversion

David Altman*
Robert Bromberg
M. U. Clauser
J. Preston Layton
Frank Marble
G. H. Markstein
A. M. Rothrock
Milton M. Slawsky
Martin Summerfield
T. Y. Toong

Flight Mechanics

H. J. Kelley*
Malcolm J. Abzug
H. Julian Allen
A. E. Bryson, Jr.

Flight Mechanics (Cont.)

T. N. Edelbaum
William C. House
Angelo Miele
John D. Nicolaides
Charles B. Westbrook

Instrumentation

R. H. Tripp*
Paul F. Bechberger
J. M. Hungerford
Mac Lowy
Walter McKay
M. David Prince
Charles P. Sonett
George I. Toumanoff
William A. Wildhack

Meteorology

Thomas F. Malone*
Robert D. Fletcher
Henry T. Harrison
Joseph Kaplan
Donald T. Perkins
Herbert Riehl
Morris Tepper
Harry Wexler

Nuclear Applications

J. Donald Rauth*
Jack L. Armstrong
Robert W. Bussard
H. M. Dieckamp
Capt. R. L. Duncan, USN
Harold B. Finger
Donald J. Keirn
Frank E. Rom
Raymer E. Schreiber
D. Roy Shoults
T. B. Taylor

Operations

Benjamin S. Kelsey*
Maj. Gen. Otis Benson, USAF (MC)
Ernest A. Cutrell
Capt. E. E. Fawkes, USN
Melvin N. Gough
Franklin W. Kolk
Col. J. L. Marinelli, USA
Richard V. Rhode
W. E. Rhodes
M. B. Spaulding, Jr.
Maj. Gen. D. Yates, USAF

Propulsion Systems

Bruce T. Lundin*
Robert H. Boden
George W. Brady
David Cochran
Elliot Mitchell
Perry W. Pratt
C. C. Ross
John G. Wilder, Jr.
Maurice J. Zucrow

Space Physics

H. G. Stever*
John C. Evvard
Herbert Friedmann
Leo Goldberg
C. F. Hansen
Arthur Kantrowitz
Bruno Rossi
S. F. Singer
Leo Steg
Fred L. Whipple

Structures and Materials

Nicholas J. Hoff*
Samuel B. Batdorf
Bruno A. Boley
Pol Duwez
R. R. Heldenfels
Samuel Levy
George N. Mangurian
S. S. Manson
Nathan E. Promisel
Ernest E. Sechler

Support

Ernest G. Stout*
Albert D. Brown
Edward I. Brown
Col. Paul T. Cooper, USAF
Cdr. P. J. Daniel, USN
Paul Hartline
Donald R. Hill
Capt. H. D. Hodson, USN
Lt. Col. George L. Lovett
R. R. Malik
John McKenna
Gilbert Rolan
Richard A. Schmidt
William R. Owens

Vehicle Design

C. E. Pappas*
Ralph Alex
Adolph Burstein
C. H. Christenson
A. J. Eggers, Jr.
E. V. Marshall
Rene H. Miller
John R. Ragazzini
George S. Schairer
George S. Trimble, Jr.

SUBSCRIPTION RATES

JOURNAL OF THE AEROSPACE SCIENCES, Published Monthly. United States and Possessions: 1 Year, $15.00; Single Copies, $1.50. Foreign Countries Including Canada (American Currency Rates): 1 Year, $16.00; Single Copies, $1.50.

AEROSPACE ENGINEERING, Published Monthly. United States and Possessions: 1 Year, $5.00; Single Copies, $0.50. Foreign Countries Including Canada (American Currency Rates): 1 Year, $6.00; Single Copies, $0.50.

Notices of change of address, which should be sent at least 30 days prior to actual change of address, and correspondence regarding subscriptions should be sent to the Circulation Department, JOURNAL OF THE AEROSPACE SCIENCES, 2 East 64th Street, New York 21, N.Y.

Manuscripts for publication, proofs, and all correspondence should be addressed to the Editorial Office of the JOURNAL.

© *Copyright, 1961, by the Institute of the Aerospace Sciences, Inc.*

Publication Office, 20th and Northampton Sts., Easton, Pa. Second-Class Mail Privileges Authorized at Easton, Pa. Acceptance for mailing at a special rate of postage provided for in Section 1103, Act of October 3, 1917, authorized April 29, 1937.

JOURNAL OF THE AEROSPACE SCIENCES

VOLUME 28 APRIL 1961 NUMBER 4

Possibilities of Aeronautical and Space Research in the Federal Republic of Germany

The Twenty-Fourth Wright Brothers Lecture

A. W. QUICK*

Technical University of Aachen

(1) Introduction

The first six decades of our century have greatly changed the life of mankind. Incidental to the technical age, with its inventions and discoveries, was a stormy development which has increased progressively up to the present, leading us into an uncertain future. Never quieted is our concern that man use for a good cause the admirable accomplishments of scientific research, development, and production, we must always seek to prevent a misuse of the power thus gained.

The true inventor, however, will always think only of beneficial utilization; this was true 57 years ago, when the great sons of your country, the brothers Wilbur and Orville Wright, performed the first powered flight ever to be accomplished by man. They started a development in aeronautical techniques which today is continuing quite naturally into space flight.

It is only natural for you to celebrate this event with an annual memorial lecture. Please accept the expression of my appreciation for the honor of being asked to commemorate the historic event this year before this distinguished audience.

Permit me to relate an event from the life of the Wright brothers which is connected with Germany. When the great success of their flights became known in France, and thus in Europe, the Wright brothers were granted by the Technical University of Munich the highest honor they have to give: the title of Doctor honoris causa of Technical Sciences. The honorary documents (Fig. 1) read as follows:

"In acknowledgment of your unswerving, bold, and consequential solution of the problem of flying, the Senate of the Technical University of Munich confers on 5 March 1909 the title of Doctor honoris causa of Technical Sciences on Wilbur, and Orville Wright" (respectively).

This event may serve to indicate that the great achievements of the Wright brothers were widely recognized in Germany as well, where Lilienthal had lived ten years previously. His ventures in the field of gliding inspired the Wright brothers to continue their efforts with improved methods and scientific thoroughness.

In compliance with a suggestion made by your President, I will now try to give you a review of the potentialities of German aeronautical and space research.

It is now about five years since international agreements were reached permitting Germany to resume aeronautical research. However, it was by no means easy to make a new start because large parts of the population, the parliaments, and Federal as well as State governments showed little inclination to reestablish aeronautical research and an aircraft industry. There was first the aversion to rehabilitating an industry which is needed largely for military purposes, and second, a large number of people thought that the foreign countries had meanwhile won so great an advantage that it would be very difficult for Germany to catch up. The same people therefore advocated the purchase of products of aircraft industry from abroad, and our favorable foreign exchange situation favored this view.

It was some time, therefore, before it was realized that a highly industrialized country cannot do without an aircraft industry, since such an industry acts as a

Presented before the Institute of the Aerospace Sciences in the Natural History Building Auditorium, Smithsonian Institution, Washington, D.C., December 17, 1960.

* Professor of Aeronautical Engineering.

stimulus to the industrial life of the country as a whole. If one disregards the minor, although important, preliminary work, it can be said that effective promotion of aeronautical research began about three years ago.

(2) Capacity of Aerospace Research in Germany*

I shall now briefly outline the present and probable future capacity of German aerospace research, and then give a number of typical examples of results of research activities which will demonstrate that Germany is rendering some worthwhile contributions in certain fields, and may also be expected to do so in the future.

Aerospace research activities in Germany are conducted at the universities, the technical universities, some of the Max Planck Institutes, several governmental establishments, and at special research institutes of the Deutsche Gesellschaft für Flugwissenschaften (DGF); (German Association for Flight Sciences). While at the universities and technical universities research is closely connected with the instruction of students, all other institutes serve the sole purpose of research.

Fig. 2 shows the number of personnel working in aerospace research, including all employees and auxiliary help. The first two columns refer to the present status, i.e., to the year 1960. The first column includes the total number of personnel, and the second those working in space research. Hence we have at present a total of 2,200 persons employed in aerospace research, of which about 480 are engaged in space research.

The third and fourth columns indicate the number of personnel we expect to have in 1961. We plan to increase the total to 2,700, with approximately 1,030 employees for space research. The percentage of personnel working in space research will probably increase in years to come.

Fig. 3 represents available funds in million Deutschmarks. The first two columns are the funds we have at our disposal in 1960. The total is about 78 million DM, with 7.2 million DM for space research. The third and fourth columns indicate the funds for aeronautical research for 1961 and those to be expected in subsequent years. They will probably comprise similar amounts.

On the other hand, an increase is contemplated in the field of space research. A respective plan is being prepared at present. On the basis of the present situation, it is planned to allocate investment funds of about 84 million DM for the next four years, with annual operating expenses amounting to 18.8 million DM.

We expect that, within a few years, the annual expenses for aerospace research will total about 125 million DM.

(3) Some Results of Research Activities

Having reviewed the German aerospace research capacity, I would now like to give some examples of

* This section is based partially on a 1960 survey of the Deutsche Forschungsgemeinschaft (DFG); (German Research Association) in Bonn-Godesberg.

UNTER DER REGIERUNG
SEINER MAJESTÄT DES KÖNIGS
OTTO
VON BAYERN
UND
UNTER DER REGENTSCHAFT
SEINER KÖNIGLICHEN HOHEIT
LUITPOLD
VON GOTTES GNADEN KÖNIGLICHEN PRINZEN VON BAYERN
VERLEIHT MIT DIESER URKUNDE
DIE KÖNIGLICHE TECHNISCHE HOCHSCHULE ZU MÜNCHEN
UNTER IHREM DERZEITIGEN REKTOR
PROFESSOR DR. MORITZ SCHRÖTER
AUF EINSTIMMIGEN ANTRAG DER ALLGEMEINEN ABTEILUNG
UNTER IHREM DERZEITIGEN VORSTANDE PROFESSOR Dr SEBASTIAN FINSTERWALDER
DURCH EINSTIMMIGEN BESCHLUSS VON REKTOR UND SENAT
KRAFT DES ALLERHÖCHST VERLIEHENEN RECHTES
HERRN
ORVILLE WRIGHT
IN DAYTON OHIO
IN ANERKENNUNG SEINER ZIELSICHEREN KÜHNEN UND FOLGENREICHEN LÖSUNG DES FLUGPROBLEMS
DIE WÜRDE EINES
DOKTORS DER TECHNISCHEN WISSENSCHAFTEN
EHRENHALBER.
MÜNCHEN DEN 5. MÄRZ 1909.
REKTOR UND SENAT
DER KÖNIGLICHEN TECHNISCHEN HOCHSCHULE.
Dr. M. SCHRÖTER.

UNTER DER REGIERUNG
SEINER MAJESTÄT DES KÖNIGS
OTTO
VON BAYERN
UND
UNTER DER REGENTSCHAFT
SEINER KÖNIGLICHEN HOHEIT
LUITPOLD
VON GOTTES GNADEN KÖNIGLICHEN PRINZEN VON BAYERN
VERLEIHT MIT DIESER URKUNDE
DIE KÖNIGLICHE TECHNISCHE HOCHSCHULE ZU MÜNCHEN
UNTER IHREM DERZEITIGEN REKTOR
PROFESSOR DR. MORITZ SCHRÖTER
AUF EINSTIMMIGEN ANTRAG DER ALLGEMEINEN ABTEILUNG
UNTER IHREM DERZEITIGEN VORSTANDE PROFESSOR Dr SEBASTIAN FINSTERWALDER
DURCH EINSTIMMIGEN BESCHLUSS VON REKTOR UND SENAT
KRAFT DES ALLERHÖCHST VERLIEHENEN RECHTES
HERRN
WILBUR WRIGHT
IN DAYTON OHIO
IN ANERKENNUNG SEINER ZIELSICHEREN KÜHNEN UND FOLGENREICHEN LÖSUNG DES FLUGPROBLEMS
DIE WÜRDE EINES
DOKTORS DER TECHNISCHEN WISSENSCHAFTEN
EHRENHALBER.
MÜNCHEN DEN 5. MÄRZ 1909.
REKTOR UND SENAT
DER KÖNIGLICHEN TECHNISCHEN HOCHSCHULE.
Dr. M. SCHRÖTER.

FIG. 1. Honorary doctor's degrees.

	1960		1961	
	Total	Space	Total	Space
Universities Techn. Universities Max Planck Institutes Government Institutes	900	280	1100	430
DGF	1300	200	1600	600
Total	2200	480	2700	1030

FIG. 2. Research personnel.

	Amounts in Million DM					
	Status 1960		Aeronautical Research		Space Research Planned for next 4 years x)	
	Total	Space Research	1961	later x)	Invest	Operatexpens per year
Universities Techn.Universities Max Planck Inst. Governm. Inst.	36	3,2	35	35	18	7,5
DGF	42,2	4,0	40	50	66	11,3
Total	78,2	7,2	75	85	84	18,8

x) estimated

FIG. 3. Funds for aerospace research.

research activities in this field. Although I have chosen these examples at random, I hope that they will serve the purpose of giving you an idea of how this research is carried on, and what contributions might be expected from Germany.

(3.1) *Structure*

The first example pertains to research on the fatigue life of construction parts. An important problem in the construction of airplanes and space vehicles is the fatigue life of construction parts which are subject to loads fluctuating with respect to time. Examples of such loads are gusts, stalled flow, sonic pressure, shock waves, turbulence of boundary layers, etc.

The Institute for Structures of the DVL* is engaged primarily in research on this problem, and has studied the question of how, for instance, sonic or gust loads on construction parts might be examined by tests.[1] Above all it had to be decided whether loads that actually are complicated and randomly alternating could be simulated by simplified tests.

Fig. 4 shows a typical case, representing the result of a simple bending load imposed on a cantilever beam of aluminum alloy. Plotted on the vertical scale is a nominal stress which is unimportant here because only the changes are of interest. The horizontal scale plots the fatigue life, with each test point indicating that 50% of the 15 beams used for each of the test points attained this value. Curve *a* expresses the fatigue life for the actual load under a typical spectrum, which may serve as an example for gust loads as well as for sonic loads. Curve *b* expresses the results obtained when the spectrum of curve *a* was arranged in such a way that all loads of equal size were put together, thus creating a step-by-step loading. Breakage resulted after only about five periods of these loadings. It is to be recognized that the lifetime decreases to about one half. Thus the order of succession of loads is of importance. In practice this means that tests of this kind, which are of course much simpler, yield results which deviate but, however, on the safer side. Curve *c* shows the results of test with an alternating constant load of amplitude corresponding to the root mean square value of the loads from the tests *a* and *b*. This result is recognized to be far from realistic, with the fatigue life curtailed by the factor 200. Hence tests of this kind result in a completely wrong picture.

The tests pertaining to curve *a* were performed in such a way that the spectra of actual loads were transmitted via an amplifier to an exciter.

We believe that continuing this research will contribute to assisting the design engineer in making a relatively safe evaluation of the fatigue life of his constructions.

(3.2) *Propulsion*

Now for some examples from the field of propulsion.

Considerable importance is attached in Western Germany to the development of VTOL airplanes; the industry concerned is busily seeking a suitable solution for airplanes with jet engines which may be turned during flight. To obtain an optimal weight of the jet engines, engines with relatively low thrust are used; this brings about the problem of cluster engines.

The research department of the firm of Heinkel in

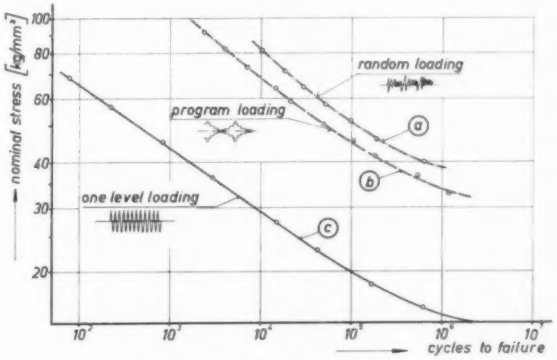

FIG. 4. Fatigue tests.

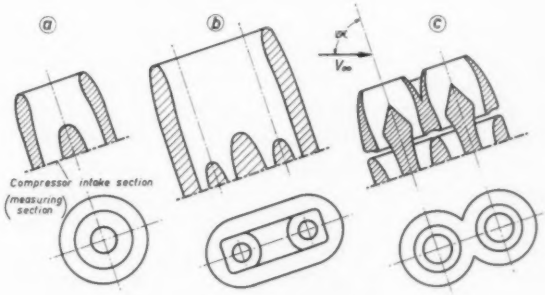

FIG. 5. Models of engine intakes.

* DVL: Deutsche Versuchsanstalt für Luftfahrt e.V.

Munich examined the behavior of the intakes of two engines being turned simultaneously, both of which had large lateral airflow angles.[2] Fig. 5 shows the models tested. Example *a* is the intake of a single engine, which had been measured for comparison purposes. The front edge of the intake was adapted to subsonic conditions, so that relatively favorable results are to be expected. Example *b*, shown in the middle, combines both intakes into one, and it has an equally well-rounded front edge. On the right-hand side, *c*, is shown as a double intake with the front edge adapted to supersonic flight. The front part of the intake, however, is axially adjustable and releases a small annular slot which is opened for take-off and landing.

Measurements of the maximal velocity V_{max} at the compressor intake have been performed in comparison with the mean velocity $\bar{V}$ in this plane. In Fig. 6 is plotted, as an example, for an angle of attack of $\alpha = 90°$, $V_{max}/\bar{V}$ as a function of $V_\infty/\bar{V}$, with V_∞ designating the flight velocity. Curve *a* for the single engine reveals excessive hyperspeeds which are inadmissible for the compressor. Intake *b* of the double engine is considerably better, but it yields quite different values for each of the engines. The front engine has a greater hyperspeed than the rear one. Intake *c*, also provided for a double engine, and constructed to release a slot by axial adjustment, yields quite favorable values for the front engine as well as for the rear one. Thus a satisfactory solution has been found to this somewhat complicated question.

At the Aerodynamic Testing Establishment (AVA) in Göttingen, the problem of calculating cascades has received great attention for many years. Lately the strongly curved and thick cascade profiles have been investigated which heretofore, in spite of many efforts, had been calculated only imperfectly.[4]

These efforts have now resulted in a satisfactory solution to the second problem of the wing theory in its application to cascades, namely, the calculation of the pressure distribution in given profiles.[3] The method provides only a continuity of vortices on the profile contour, as shown in Fig. 7. Isay[5] had already used this method, but he was only partially successful because the numerical treatment of his integral equation was quite tedious owing to the singularity of the nucleus of this equation, and to limitations imposed on the allowed thickness ratio.

By the new method the velocity is brought to disappear within the profile at each place so that the vortex continuity on the profile contour corresponds directly to the velocity distribution. The mathematical treatment of this concept, which is known for single wings, was successfully extended to cascade profiles. The resulting integral equation is satisfied at N points of the contour, so that a system of linear equations develops; its solution is three basic flows which yield the desired velocity distribution at the contour by superposition. Fig. 8 shows the three basic flows. Flow *a* results from the flow attacking vertically to the cascade axis; this flow is free from circulation. Flow *b* is the corresponding flow, also free from circulation, for the flow attacking parallel to the cascade axis. Flow *c*, finally, represents the circulation flow around the cascade profiles.

The integral equation thus yielded three systems of linear equations, with the right sides of the equations differing from one another. The linear equations were easily solved with the use of an electronic computer. The solution showed that the selection of $N = 36$ points for the integral equation to be satisfied on the profile contour almost always yields satisfactory results. A computer of the IBM 704 type calculates the entire velocity distribution within a few minutes.

An example of a turbine cascade, the result of a great number of calculations, is given in Fig. 9 and compared with measurements[4]; the cascade, the attacking flow conditions, and geometrical data are illustrated on the right-hand side. Agreement between theory and measurements is considered to be very satisfactory. The same holds true for the case represented in Fig. 10, which is a deceleration cascade with strong deflection. Here, too, theory and measurements agree quite satisfactorily.[6]

These results having been achieved, it is now possible to calculate with relatively little work the frictionless flow through a two-dimensional cascade; and this applies to practically all possible cascades. Moreover, these results may now serve as a basis for calculating boundary layers and thus determining the loss coefficient. In this field, too, many an effort has been exerted in this institute, and results have been quite satisfactory.[7]

At the Institute for Turbomachines of the Technical University in Aachen, the problem of stress on rotating turbine blades caused by nonuniform temperature distribution during the acceleration phase has been investigated.[8] The rotor of a test turbine, shown in Fig. 11, with a diameter of 12.7 in. and a speed of 8,000 rpm, was fitted with 31 thermocouples, 23 measuring points of which were situated in the rotor blades. There are 48 blades in the rotor.

Fig. 12 shows the distribution of the points measured in three sections, namely, the hub section, the mean section, and the top section. The local temperatures were measured by means of a reversible system of slip-rings which allowed the simultaneous measurement of temperatures in eight spots. The highest rate of difference in temperatures during acceleration was measured between the trailing edge and the profile center. The blades used in this test were solid ones.

Fig. 13 shows an example of an extensive program. The turbine was accelerated from ignition to operating speed within about 1/2 min. In the diagram the temperature T of gas in front of the nozzles is plotted against time. The gas temperature was only about 480°C. In addition, the temperature difference ΔT between trailing edge and profile center is shown for the hub section; the maximum difference was 120°C., i.e., 25 per cent of the gas temperature. Such a gradient results in considerable thermostresses in the blade

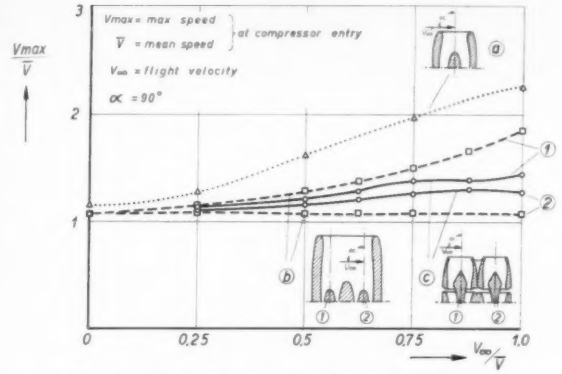

FIG. 6. Maximum hyperspeed at engine intake.

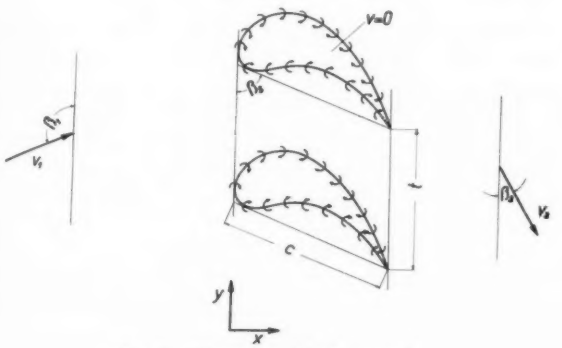

FIG. 7. Vortex model of a cascade.

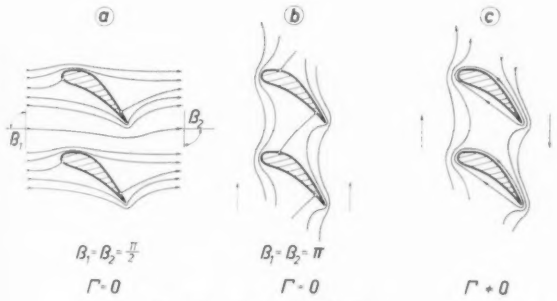

FIG. 8. Basic cascade flows.

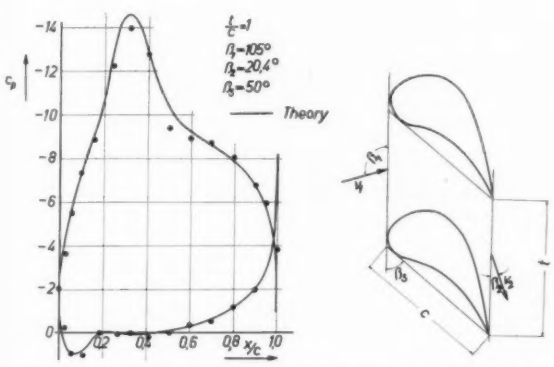

FIG. 9. Pressure distribution theory and measurements.

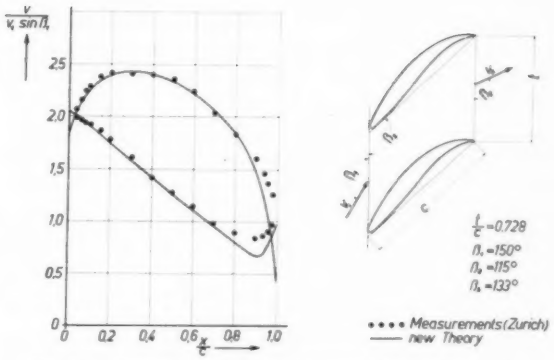

FIG. 10. Pressure distribution theory and measurements.

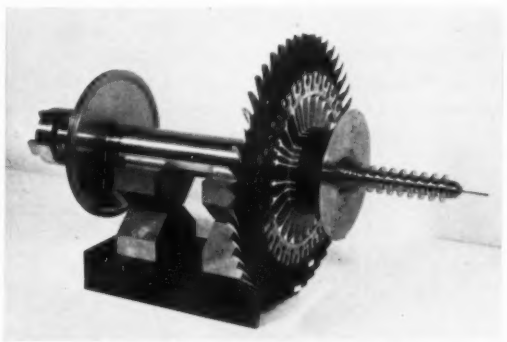

FIG. 11. Test rotor (48 blades).

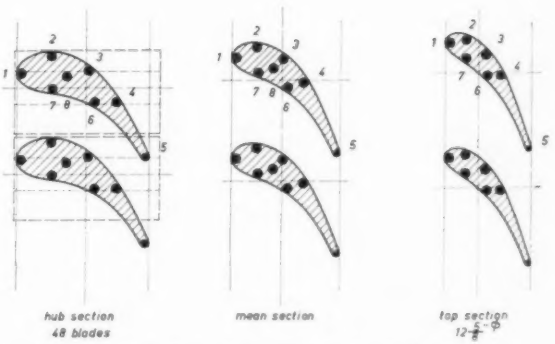

FIG. 12. Location of temperature measuring points.

material; these were roughly calculated to amount to 31,000 lb./sq. in. in this case.

With this complex measuring system working satisfactorily, it can be used for investigating turbine blades with desirably small temperature gradients.

The same institute devotes some of its resources to the problem of measuring high temperatures varying with respect to time. A measuring device was developed to serve this purpose.[9] The principle of this instrument, shown on the left-hand side of Fig. 14 is based on a pneumatic effect. The hot gas at temperature T is absorbed by the randomly shaped intake shown on the lower left; then the gas flows through a capillary with a diameter of $d = 0.04$ in. and a length l of 2–3 in., and then arrives at the vacuum pump. The capillary is cooled in order to maintain a constant wall temperature, and the suction pressure is always kept sufficiently low that sonic speed—i.e., Mach 1—is maintained at the exit. The pressures P_0 and P_1 are measured at the entry of the capillaries, and the pressures P_2 and P_3 in the back part. Only the two pressure differences ΔP_1 and ΔP_2 are required for determining the temperatures, since the quotient $\Delta P_1/\Delta P_2$ depends with good approximation only on the gas temperature T. ΔP_1 and ΔP_2 are measured by very small electric transducers and fed to an indicator.

On the right-hand side of Fig. 14 is a typical gage characteristic. It should be added that each of the pressures ΔP_1 and ΔP_2 depends solely on the temperature and P_0. By additional measurement of P_0, the gauge characteristic is considerably improved, which is quite practical in case of high temperatures.

Fig. 15 is a photograph of the measuring instrument, showing the outer dimensions and the connections for vacuum pump, water, and electric energy. The pressure device, which is of very small dimensions, is also included in the instrument.

Fig. 16 illustrates the results when two measuring instruments are repeatedly brought from room temperature into a hot flame of approximately 1,100°C. Curve a shows temperature measured by the pneumatic instrument, and curve b that measured by a chromel–alumel element with a wire diameter of 0.002 in. and a junction diameter of 0.01 in. It is to be recognized that the new instrument responds quite rapidly to the unstationary variations of the flame. The thermocouple, on the other hand, is comparatively slow in reaching its final values, and does not follow the rapid variations.

The pneumatic instrument has been tested up to temperatures of 1,600°C., and it is expected that it will work at even considerably higher temperatures.

(3.3) *Navigation, Guidance, and Control*

Two of the DVL Institutes are working in the field of navigation, guidance, and control. At the Institute for

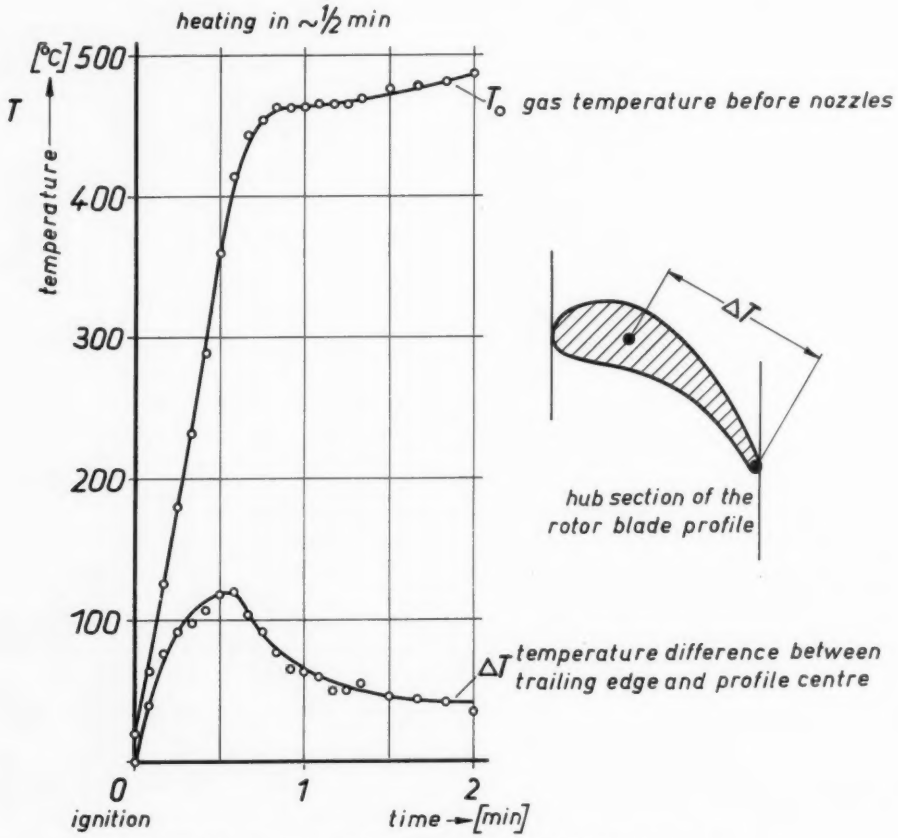

FIG. 13. Increase of temperature difference during acceleration.

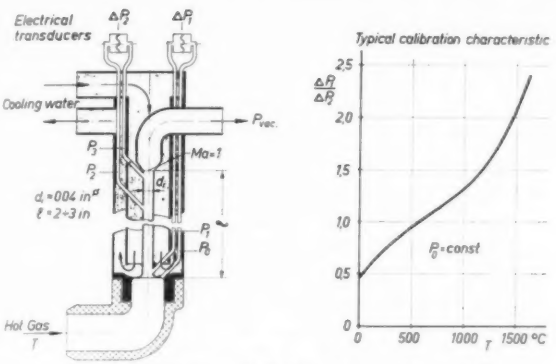

FIG. 14. Pneumatic high gas temperature probe.

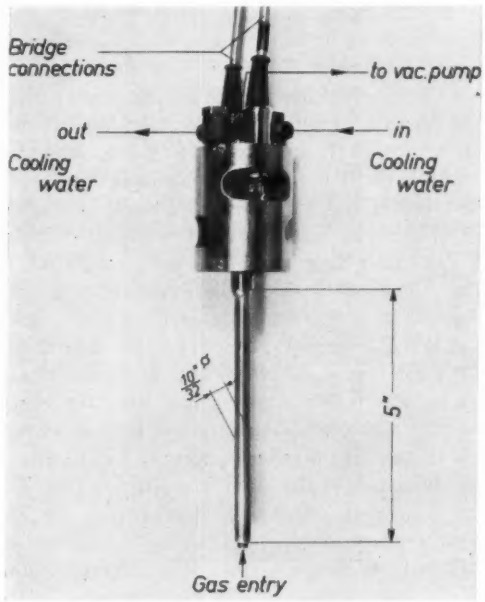

FIG. 15. High gas temperature probe.

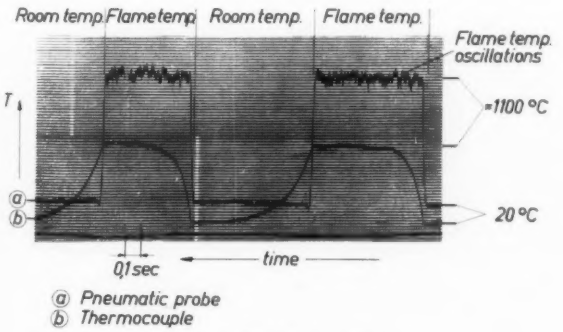

FIG. 16. Sample recording.

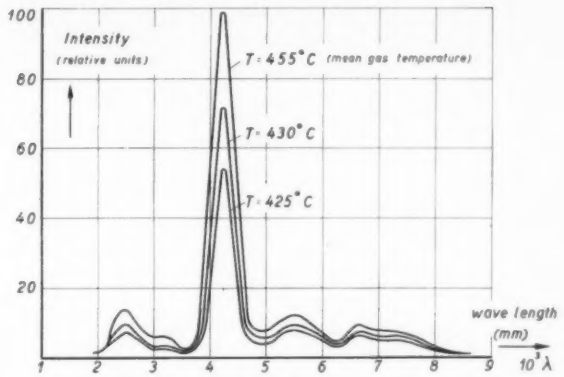

FIG. 17. Emission spectrum of gas jets.

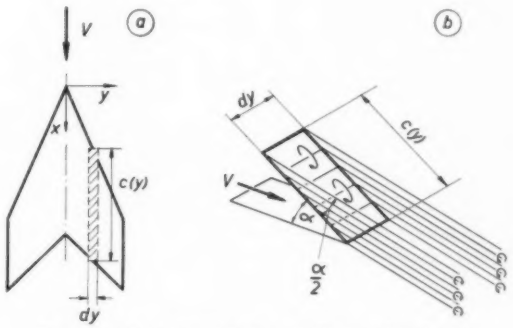

FIG. 18. Vortex models for nonlinear wing theory.

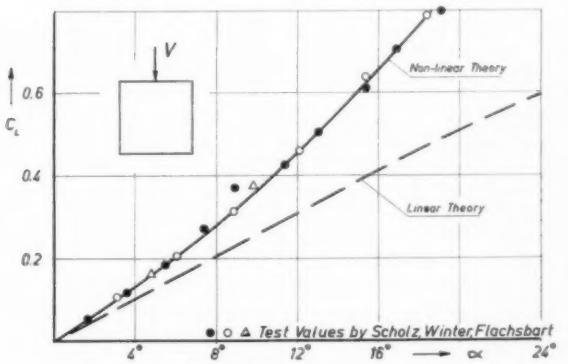

FIG. 19. Lift coefficient vs. angle of attack.

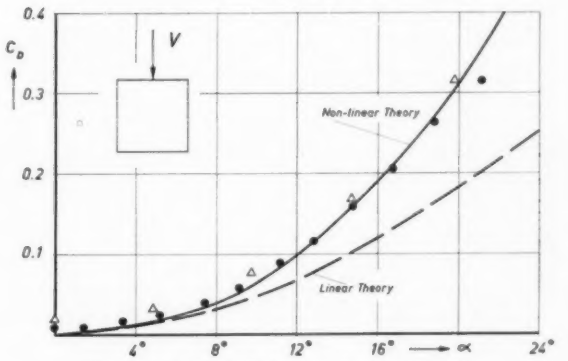

FIG. 20. Drag coefficient vs. angle of attack.

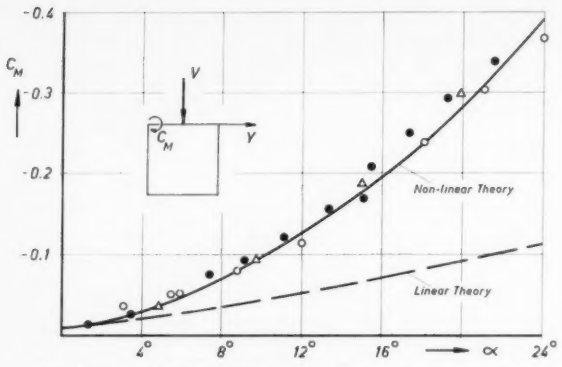

FIG. 21. Pitching moment coefficient vs. angle of attack.

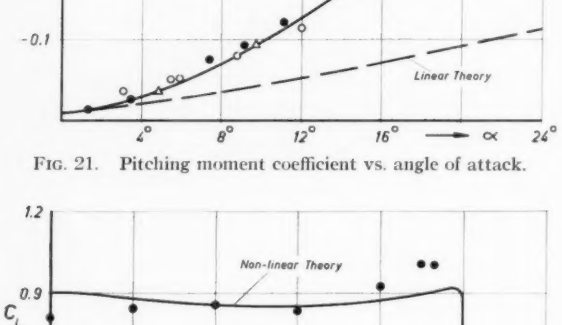

FIG. 22. Lift distribution vs. semispan.

Aeronautical Radio and Microwaves, extensive theoretical calculations on the exactness of position-finding by radio methods have been performed. Their detailed explanation would take up too much space here, and they will shortly be published as agardographs of the AGARD Panel.[10]

The DVL Institute for Guidance and Control Techniques deals with, among other things, the research of ultrared radiation of jet engines and their exhausts in order to collect the basic data needed for the development of ultrared direction-finding devices. The literature at our disposal relates only very few experimental data. Therefore, the spectral distribution of emitted radiation was determined at this institute in a jet engine of the type SNECMA Atar 101 B.[11]

It is to be noted first that the radiation emanates from the hot parts of the engine as well as from the exhaust jet. The intensity of radiation from the hot engine parts has spatial directionality, with high values resulting, along those directions in which hot metal parts of the inner engine may radiate. Naturally these zones are located behind the engine; the remaining radiation area corresponds approximately to the spectral distribution with temperature of a black body.

The hot jet, however, must be considered a selective radiator, emitting favorably in the zones of water, steam, and carbon dioxide bands. Fig. 17 shows results at three different temperatures of the exhaust gas. The intensity of the emitted radiation has been plotted in relative units against the wavelength λ. One can see clearly that the maximum emission is in the CO_2 band at a wavelength of $4.26\,\mu$ ($1\mu = 0.001$ mm.).

In the spectral regions in which emission takes place absorption occurs also. However, as the absorption range is very narrow, the total absorption over the entire spectral region of the jet remains quite small. Hence, in measuring the total intensity in jet engines, background radiation that may be present must be deducted practically in full from the measured result. In consequence of these experiments it was imperative to improve the sensitivity of the devices used for measuring the ultrared radiation of the jet by developing selective receivers. The maximum spectroscopic sensitivity of these receivers must coincide with that of the CO_2 band.

This important characteristic of jets, while not treated in the literature at our disposal, is probably well known already in other countries which are intensely active in developing ultrared target-seeking devices. But, just as in many other instances, we are here in the awkward position of having to work on problems well known to others without receiving the benefit of information on their results. On the other hand, however, we cannot forego their study and research, as these form the basis for constructive development in this field.

The staff of this same institute engages also in detailed theoretical research on the so-called sampling data systems which, combined with respective tests, lead to a generalization of the sampling data systems theory.[12]

(3.4) *Aerodynamics*

Let us now review some of the fluid mechanics research. A remarkable success has been achieved recently in the field of wing theory at the Institute for Fluid Mechanics of the Technical University in Brunswick. Heretofore there existed no theory to describe in a satisfactory manner the nonlinear behavior of arbitrarily shaped wings. This applies above all to wings with small aspect ratios which, however, have lately become of special interest. This problem was satisfactorily solved first for the incompressible case,[13] and thus the theory could be extended to include the case of compressible subsonic flow.

The method is developed from a vortex model which is only slightly different from that of the linear theory. It is based on the linear wing theory of E. Truckenbrodt,[14] who used for the calculation a model in which the wing is substituted by numerous elementary wings of infinitesimal span. The left-hand side of Fig. 18 shows a wing into which an elementary wing of a depth $c(y)$ and a span dy has been sketched.

Each elementary wing has a circulation distribution, variable over the depth in which the free vortices flow off at the rear at an angle of $\alpha/2$. This has been illustrated under b in Fig. 18. A model of this kind was first used by W. Bollay,[15] but for the entire wing instead of for elementary wings. This way, free vortices flow off at the rear at an angle of $\alpha/2$ in any place on the wing

where vortex intensity is changing. In the case of small angles of attack ($\alpha \to 0$), the vortex model becomes the usual model of the linear theory.

The problem is now to determine the induced velocities at the wing area in the model thus defined. The resulting integral equation can be solved in two steps, the first step being identical with the linear solution of the simple calculation method of Truckenbrodt. From the solution of the first step, we obtain for the nonlinear part a modified equation whose structure is analogous and which may be solved by the same calculation method. Numerous examples for rectangular, swept, and delta wings were calculated according to this method; furthermore, the aerodynamic coefficients as well as the lift distribution were determined and compared with measured results. Theory and measurements agree quite satisfactorily. The following figures refer to a rectangular wing with an aspect ratio of one. In Fig. 19, the lift coefficient c_L is plotted against the angle of attack α, with curves for the results of both the linear and the nonlinear theory. The dots represent test values from various measurements, and they agree satisfactorily. Fig. 20 illustrates the calculated results for the induced drag c_D, which also show good agreement with test results. The same applies to the moment coefficients shown in Fig. 21. The lift distribution over the span—an important criterion for the quality of the calculation—also agrees satisfactorily with the measurement results. This is demonstrated in Fig. 22 in which is given an example for an angle of attack of $\alpha = 19.4°$.

These results prove that a satisfactory solution has been found to the problem of calculating wings of different shapes—a problem with which experts have dealt for many years.

Recently, the possibility of further improving laminar profiles has been studied at the Aerodynamic and Gasdynamic Institute of the Technical University in Stuttgart. A certain success was added to the numerous efforts, which originated years ago at the NACA and subsequently were pursued by numerous scientists,[16] to obtain a further reduction of the minimum drag and an increase in maximum lift with otherwise identical characteristics.

The basic plan of this research[17] was to investigate more closely the velocity distribution at the profile not only in the laminar part of the boundary layer, but also in the turbulent zone, and to look for a drag optimum from the study of the entire boundary layer of the profile. Theoretical deliberations about the boundary layer showed that a "concave" velocity decrease in the turbulent zone would favor a delay of the turbulent separation.* Fig. 23, exemplifying this, shows in its upper part the profile coordinates of two symmetrical profiles; the dashed contour is a profile of the NACA series 64-018 with a thickness of 18%, and the drawn curve is a modified profile with a 19.1% thickness. The velocity distributions of these two profiles are plotted in the lower part of Fig. 23, with u made dimensionless by the main flow velocity. It is clear that the new profile has

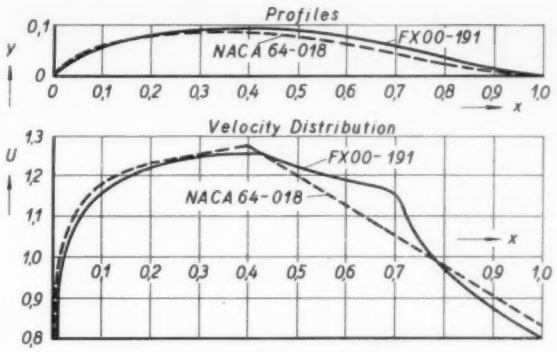

FIG. 23. Laminar airfoils.

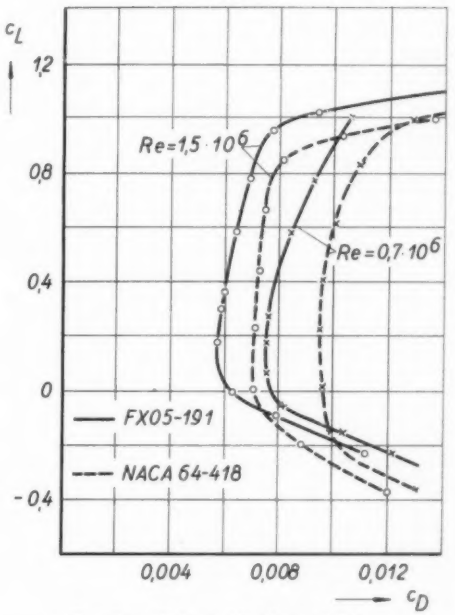

FIG. 24. Polars of laminar airfoils.

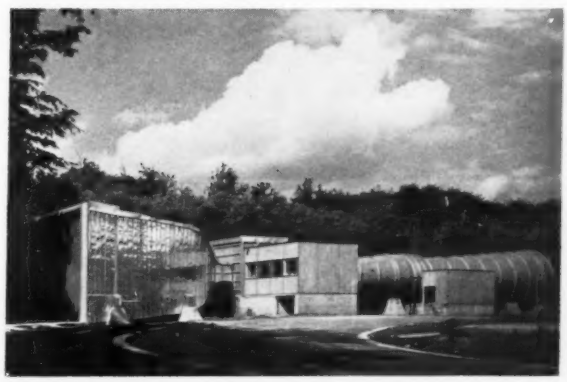

FIG. 25. Laminar wind tunnel. Test section, 0.75 × 2.75 m; contraction, 1:20; maximum speed, 90 m/sec; power, 180 kw.

two zones with "concave" velocity decrease behind its speed maximum.

Both profiles were tested in the wind tunnel at two Reynolds numbers. The results have been plotted in Fig. 24. In addition to the profiles represented in Fig. 23, these have a superimposed camber, as evidenced by the profile numbers. The tests revealed a considerably reduced drag for the new profile in spite of its greater thickness.

Special attention is also given to the spot in which the velocity gradient reverses its sign and behind which, in general, there occurs either a laminar separation with subsequent smoothing of the flow and transition to turbulent boundary layer, or an immediate passage from laminar to turbulent boundary layer. The former is quite disadvantageous with respect to the drag and thus must be avoided. Appropriate patterns of velocity distribution have been developed and are at present applied in profiles to be tested. This question is also of importance with regard to obtaining optimal $c_{L_{max}}$ values.

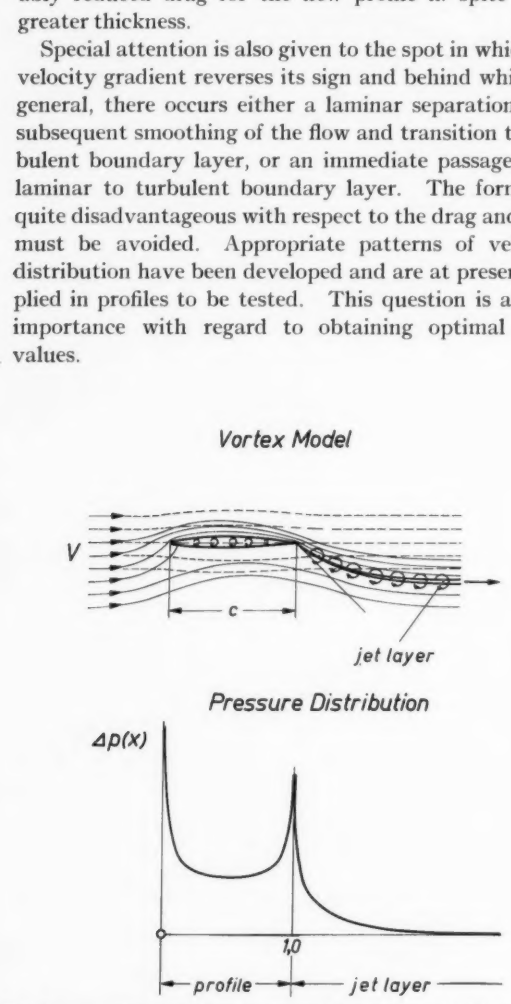

FIG. 26. Vortex model and pressure distribution at jet flap.

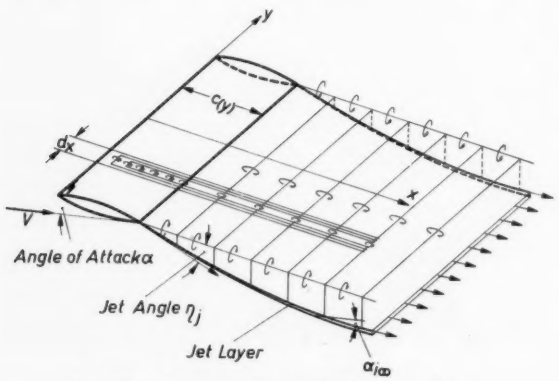

FIG. 27. Vortex model for tridimensional wing.

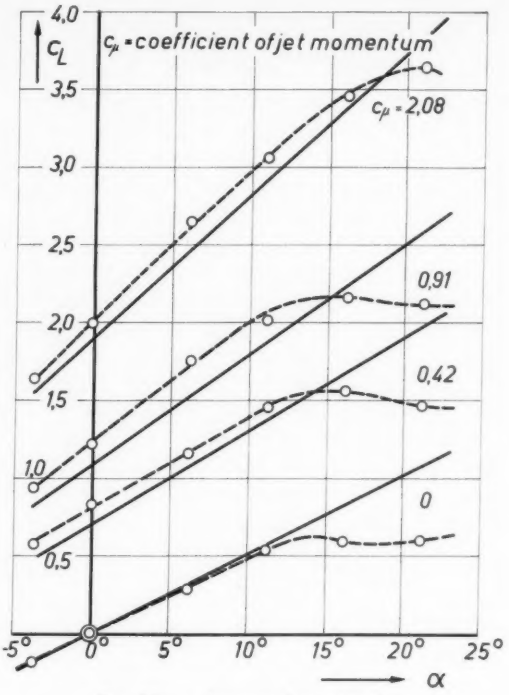

FIG. 28. c_L increase due to jet flap.

In order to facilitate a detailed study of these problems, a wind tunnel was constructed which is to be seen in Fig. 25. Its contraction ratio is 20, and it has a measuring section of 2.43 by 8.86 ft. at a velocity of 300 ft./sec., and a power of 180 kw.

The Research Department of the firm Bölkow-Entwicklungen in Munich also devoted much attention to the development of wing profiles with optimum characteristics. The theories of Lighthill and Truckenbrodt were advanced in order to develop a method permitting a relatively economic calculation of profiles and boundary layers with a given course of the pressure distribution.[18]

The DVL Institute for Applied Mathematics and Mechanics in Freiburg is especially active in research concerning the boundary-layer theory. Primarily, the stability of the laminar boundary layer and the problem of transition to turbulence, are being studied. Also, the stability theory of finite perturbations has been essentially promoted.[19] A summary on the work of this institute, which is cooperating closely with all scientists working in this field, is contained in DVL Report No. 123.[20]

Interesting results[21] in the field of theoretical boundary-layer calculations have been achieved also at the Institute for Applied Mathematics of the Technical University in Karlsruhe. By stating the limits of exact solutions, it is now possible to judge the quality of approximation methods applied in the calculation of boundary layers.

In Brunswick, at the Institute for Aerodynamics of the DFL (German Research Establishment for Aviation), research was continued toward determining the

lift distribution on wings with jet flaps, for improvement of the lift. This problem is known to be of importance in the development of STOL airplanes, which are of special interest for West Germany. Spence[22] and Maskell and Spence[23] had already treated the two-dimensional problem as well as the elliptic wing with elliptic distribution of the jet momentum. Fig. 26 shows the vortex model they used, and the resulting pressure distribution on wing and jet layer. The increase in lift is known to have two causes: first, there is the direct reaction force of the jet, and second there is an additional circulation, the so-called supercirculation. A method has now been found which permits calculation of the lift distribution for any random wing profile—and hence also rectangular, swept and delta wings—and for any random distribution of the jet momentum.[24] A theory pertaining to this was developed, combining the two-dimensional jet-flap theory of Spence[22] and the wing theory of Truckenbrodt.[25] The resulting vortex model is shown in Fig. 27, an amplification of the vortex model shown in Fig. 26. The wing is here broken up into infinitesimal wing elements with span dy and local depth $c(y)$.

This method is based on the fact that, in compliance with the results of the two-dimensional theory, the kinematic flow conditions are being met in each section in just two points of the wing and in one point far behind the wing. This result in a system of linear instead of integral equations, with $3/2(N + 1)$ equations for an identical number of unknown quantities, N designating the number of wing sections along the span. This discloses the distribution of vortex intensities on the wing, and thus all aerodynamic coefficients.

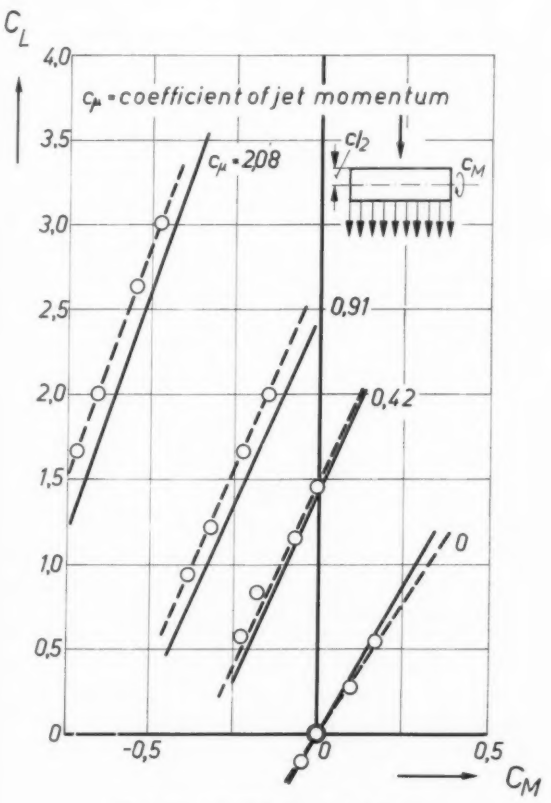

FIG. 29. c_M variation at jet flap.

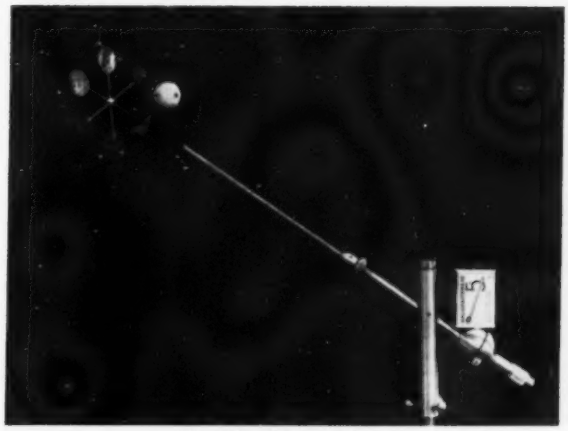

FIG. 30. Anemometer.

Fig. 28 shows the calculated results and a comparison with measurements performed by Williams.[26] We have plotted here the lift coefficient c_L as a function of the angle of attack α for the different values $c\mu$ of the jet momentum ($c\mu$ is here defined as the momentum per second divided by the product of dynamic pressure multiplied by wing area). Measurements yield results somewhat higher than the calculated ones; this is essentially due to certain approximations applied in deducing the theory.

Fig. 29 compares theory and measurements regarding the wing moments. The lift coefficient c_L has been plotted as a function of the longitudinal moment coefficient c_M for different values $c\mu$ of the jet momentum. Here, too, conformance is pretty good, considering that the moment is much more sensitive to differences in lift distribution than to the total lift.

The result of this research is a method which enables the project engineer of STOL airplanes to determine the flight performance for different wing shapes and different distributions of the jet momentum.

(3.5) *Turbulence*

At the DVL Institute for Turbulence Research, an interesting anemometer has been developed which permits one to trace the course of nonstationary flow in the atmosphere.[27] Information on the turbulence in the atmosphere near the ground is of great importance, as it influences the spreading of dust, moisture, radioactive carriers, etc., as well as the balance of temperature and humidity, i.e., fog formation.

An instrument has been developed which is to be seen in Fig. 30. It has fan-wheels with stationary axes, and the revolutions per minute are proportional to the velocity components along the revolution axis. The transducers have been installed in a sphere of 0.8 in. diameter; the wheel diameter is 4 in.

Figure 31 shows the measurements of two ane-

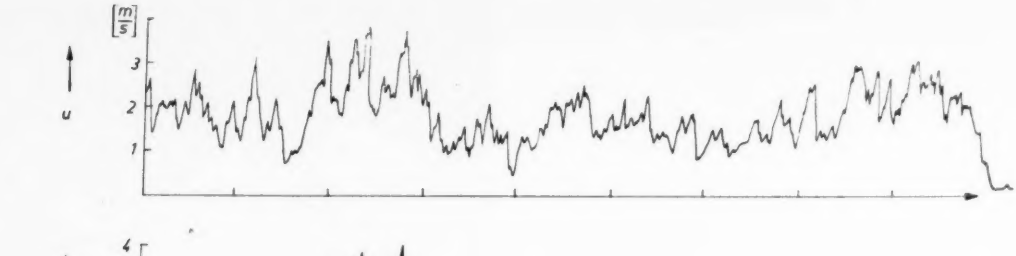

FIG. 31. Graph of two anemometers.

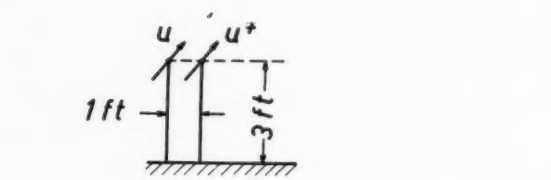
Aspect Ratio : 20
Gross Weight : 7300 lbs
Instrument Weight : 450 lbs
Crew : 2
Max. Altitude : 60000 ft
Max Range : 1800 miles / 7 hours
Engine : JT12-A6
55 ft
100 ft

FIG. 32. High altitude glider.

FIG. 34. Drag modified by shock.

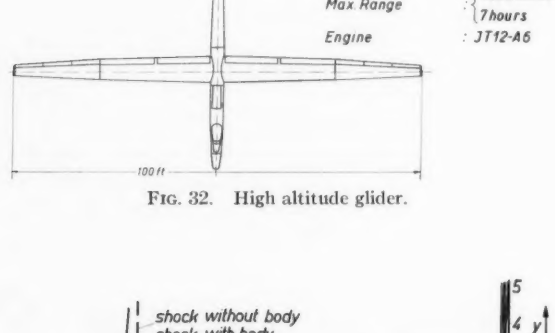

FIG. 33. Shock deformation (symmetric case).

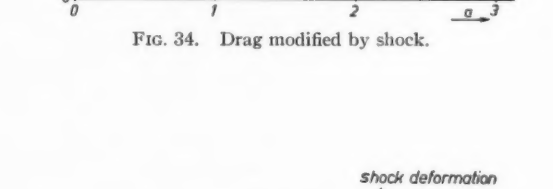

FIG. 35. Shock deformation (asymmetric case).

mometers mounted only about 3 ft. above the ground and spaced approximately 1 ft. apart. Due to their proximity, both instruments have almost the same spectrum of low velocities, which was to be expected on account of the close correlation. It is of importance that—in contrast to hot wires, for instance—negative speeds are also recorded. The instrument is used for determination of correlation functions.

In line with its tradition, the Institute for Aeronautics in Munich engages in atmospheric research. At present a high-altitude glider is being built, which will permit one to stay aloft at altitudes up to 60,000 ft. for some time.[28] Fig. 32 shows this glider along with some basic data. With its span of about 100 ft., aspect ratio of 20, and maximal weight of 7,300 lbs., its rate of descent is 6.5 ft./sec. at 46,000 ft., and 8.2 ft./sec. at 60,000 feet. It has a pressurized cockpit and its own propulsion by a Pratt & Whitney JT 12-A6 jet turbine. Flight time is up to 7 hr., 4 hr. of which are at the altitudes mentioned, and its range is up to 1,800 miles. The cockpit accommodates two persons. The payload for scientific instruments is about 450 lbs. The glider is expected to be used as follows:

(1) For investigation of the structure and turbulence of jet streams. On account of the expected extraordinary stress, the glider has been designed for an ultimate load of 12 times the normal load. In addition, an automatic flight control has been installed, which will keep the angles of the three axes of the glider constant in space, so that only translational movement of the glider will occur. The latter permits determination of the structure and intensity of gusts.

(2) For measurements of different kinds of radiation in the stratosphere, for instance, radioactive clouds, cosmic radiation, insolated and emitted radiation of the earth, or clouds, etc.

(3) For photographing the earth's surface, cloud formations, seas and sky, etc.

(4) For meteorological missions to study condensation phenomena in the atmosphere, etc.

(5) To act as carrier for some other tests, e.g., of radar techniques.

The first glider will be completed and tested late in 1961. Preparations for the construction of additional gliders are under way.

(3.6) *Gas Dynamics*

Now for some examples from gas dynamics.

The influence of a body on a shock wave upstream of the body was investigated at the Institute for Theoretical Gas Dynamics of the DVL in Aachen.[29] The deformation of the shock wave and the changes in the aerodynamic forces due to the influence of the body were calculated for a normal shock wave which is in the flow for one reason or another. It is assumed that the shock may be of arbitrary intensity, whereas the perturbations of the shock must be small. After linearization of the potential and shock equations, the deformation of the shock and the changes in the aerodynamic forces can be calculated according to the singularity theory.

The left side of Fig. 33 illustrates the influence on the shock of a two-dimensional airfoil without lift. The airfoil chord is 1 and the thickness ratio τ, and a is the distance between the leading edge on the unperturbed shock. In the following example the Mach number M upstream of the shock is 1.58 and the thickness ratio τ is 0.1. In this example, the airfoil shape is formed by two parabolic biconvex arcs. The right-hand side of Fig. 33 represents the shock deformations for different a's. The perturbed shock wave lies upstream of the unperturbed shock and is considerably disfigured. The streamlines near the x axis pass an oblique shock, and therefore the entropy increase differs in this place. The entropy change modifies the aerodynamic forces and reduces, in our case, the drag by Δc_D. Fig. 34 shows the result for the same example, with Δc_D plotted as a function of the distance a between the airfoil and the unperturbed shock wave. The influence of the shock is considerable. For the special case when $a = 0$ and τ

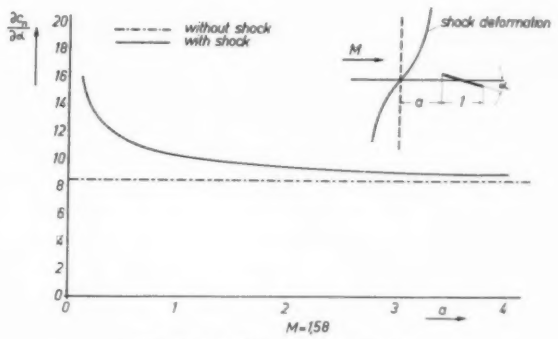

FIG. 36. Lift modified by shock.

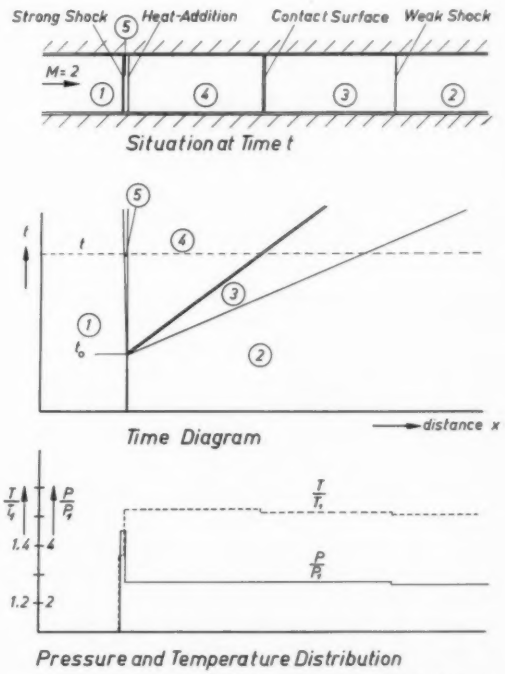

FIG. 37. Heat addition in the overcritical state.

$= 0.1$, the reduced drag approaches that of the friction. The change of the drag Δc_D is proportional to the square of the thickness ratio τ. Fig. 35 shows the influence of a flat plate at an angle of incidence on the shock wave. The angle of attack is α and the distance between the flat plate and the unperturbed shock wave is a. The deformation of the shock is asymmetrical in this case, and the results for different values of a are shown on the right-hand side. The angle of attack is 10° and the Mach number of the velocity upstream of the shock is $M = 1.58$. The deformation changes linearly with α, and it is thus possible to calculate directly other deformation values.

The influence of the perturbed shock on the airfoil is shown in Fig. 36. There results a change in the lift which may be considerable. The lift increase $\partial c_n/\partial\alpha$ is plotted as a function of the distance a. It is to be recognized that the change in the lift increase attains the same order of magnitude as the lift increase itself.

This shows that the deformation of a shock wave by a body not only is of theoretical interest but it assumes practical importance in those cases where a body approaches a shock wave not caused by it. This effect might be of special importance if a measuring instrument, for instance a Pitot tube, were to get close to the shock wave; the recording would then be erroneous. In the meantime, the calculations have been performed for axially symmetric bodies also and will be published shortly.

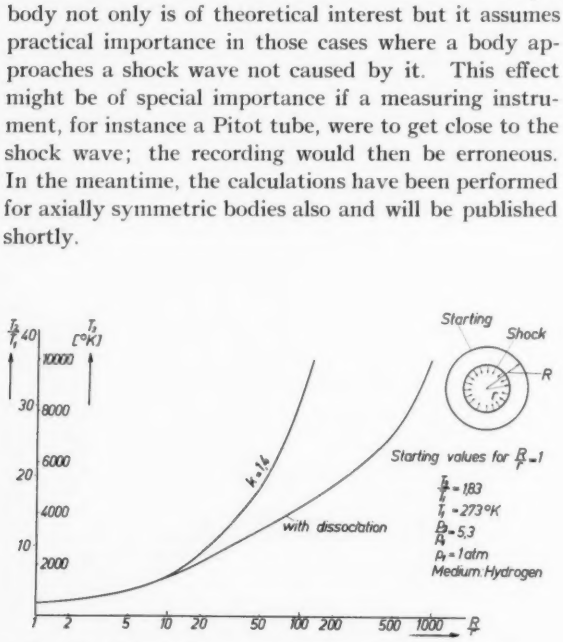

FIG. 38. Spherically symmetric shock-wave temperature.

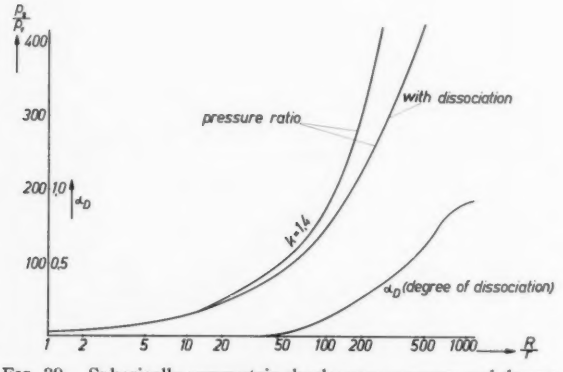

FIG. 39. Spherically symmetric shock-wave pressure and degree of dissociation.

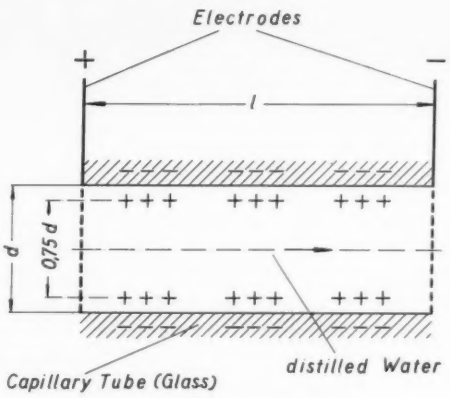

FIG. 40. Electrokinetic effect.

In the same institute of the DVL, the problem of heat addition to a gas flow in a pipe at supersonic speed was treated.[30] It is well known that the steady flow conditions in a pipe of constant cross-sectional area are modified both downstream and upstream at the region of heat addition. This happens by means of an unsteady process.

For sake of simplicity, choking was admitted as the initial state. In this case, the stream velocity behind the region of heat addition is equal to the local speed of sound. The effect of modifying the state and flow conditions by increasing the heat from the value q by Δq has been calculated, for Δq is small compared with the enthalpy of the gas. Some more idealizing assumptions have been made, such as constant specific heats, no friction, homogeneous medium downstream and upstream of the region of heat addition, and so on. The assumption of constant specific heat is not necessary and was made only for the purpose of simplifying the calculation.

Fig. 37 shows an example of the result of heat addition at supersonic speed ($M = 2$). In the stationary case, a standing normal shock is set up immediately upstream of the zone of heat addition, reducing the stream velocity from supersonic to subsonic.

If we consider a further heat addition Δq, this normal shock will be traveling slowly upstream, as shown in the time–distance diagram. At the same moment, a weak shock wave is traveling downstream. Furthermore, a contact surface, dividing the medium with the heat q from that with heat $q + \Delta q$, is also traveling downstream at a velocity identical with that of the flow. The upper half of Fig. 37 shows the positions of the shocks and the contact surface at the time t, deduced from the x–t diagram beneath it. Five regions with different state and flow parameters are to be distinguished. In regions 1 and 2 the stationary combustion equations for the case of choking are valid. The regions 2 and 3, as well as 1 and 5, are related by the shock equations; in the regions 3 and 4 the conditions for equal pressure and equal velocity at the contact surface must be applied. Finally, in regions 4 and 5 the general combustion equations are applicable.

The special conditions at the shock waves and the changes of state at the contact surface permitted linear-

ization of the defining equations. Thus analytical results could be obtained for the calculation of the changes of state at the discontinuity surfaces.

The method of calculation developed for the problem of heat addition to a choked gas flow is also applicable with other initial conditions.

The same institute investigated the contractions of spherically symmetric shock waves with a view to producing high energy densities.[31] Fig. 38 shows in the upper right-hand corner a schematic illustration of the process studied. Temperature and pressure conditions were calculated for a convergent spherical shock wave with certain basic values at the starting radius R. This example assumes that the initial value for the temperature ratio T_2/T_1 is 1.83, and the initial temperature T_1 is 273°. The pressure ratio p_2/p_1 is 5.3, with the initial pressure p_1 of 1 atm. Hydrogen was used as a medium. Temperatures and pressures increase strongly with decreasing radius r, as shown in the plot of Fig. 38. On the horizontal scale the ratio R/r is expressed logarithmically in order better to illustrate the results in the vicinity of the center of the sphere. The value of $R/r = 10^3$ thus means that the shock wave has approached the center by a thousandth part of the starting radius.

Two results are represented in Fig. 38. The first one is the course of the temperature provided that the gas is not dissociated, i.e., that the ratio of the specific heats k is constant and equal to 1.4. The second one assumes that the gas has dissociated in conformance with the equilibria pertaining to the different temperatures and

$$\eta_{max} = 1 - 2\cdot\lambda\left[\sqrt{1+1/\lambda} - 1\right]$$

$$\lambda = \frac{1}{32}\cdot\left(\frac{d}{\varepsilon\,\vartheta}\right)^2\cdot\frac{\mu}{\varrho}$$

η_{max} = maximum attainable Efficiency
d = Diameter of the Capillary Tube
ε = Dielectric constant
ϑ = Potential of the Double-layer
μ = Viscosity of the Liquid
ϱ = specific electric Resistance

FIG. 41. Efficiency of the electrokinetic effect.

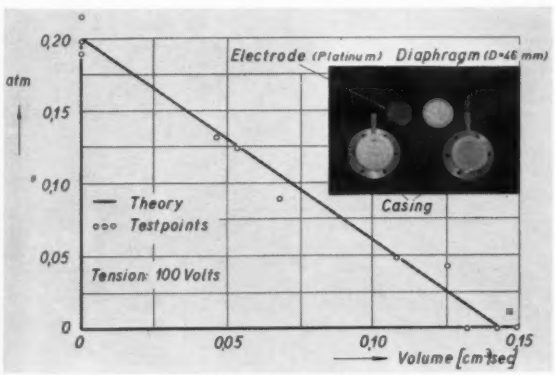

FIG. 42. Electrokinetic pump.

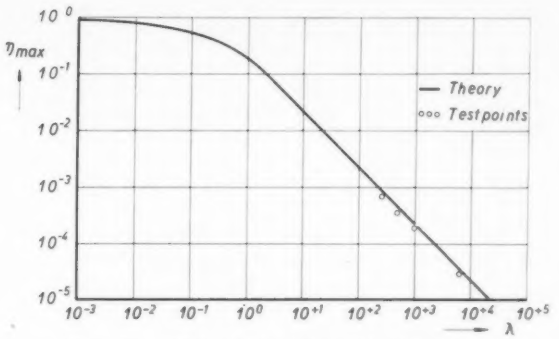

FIG. 43. Efficiency of an electrokinetic pump.

pressures. This curve shows the expected influence, which is considerable. The actual course will lie somewhere between both curves, depending on the delay of the dissociation. The values have been calculated up to a temperature of $T_2 = 10{,}000$°K., so that no noticeable ionization was yet to be registered.

Fig. 39 shows the respective pressure ratios in cases with and without dissociation. The pressure differences are less pronounced than the temperature differences which is quite understandable. Furthermore, the diagram shows the development of the degree of dissociation α_D; notice that at $R/r = 10^3$ the gas dissociation is almost complete. Parallel experiments are being conducted at the Institute for Applied Gas Dynamics of the DVL. They are aimed at producing high energy density with spherically symmetric shock waves.

(3.7) *Plasmadynamics*

Now for some examples on electromagnetically influenced fluids.

The aim of the following section is to show that a long-known physical effect may be utilized for different purpose. I am referring to an electrokinetic energy transducer which transforms the kinetic energy of fluids directly into electrical energy, and vice versa.

Since about 1880, the so-called electrokinetic phenomena in capillary tubes and diaphragms, which are to be considered as numerous parallel capillary tubes, have been known.

As shown in Fig. 40, an electric double-layer exists in capillary tubes; one layer is attached to the interior tube wall, and the other one is located in the fluid and can be moved with it. This latter layer is located at approximately three quarters of the radius. Attaching electrodes to both sides of the capillary and moving the fluid will generate electric energy. If, on the other hand, an electric tension is applied to the electrodes, there results a movement of the fluid with a pumping effect, which is also known as electroosmosis.

In the DVL,[32] the conditions were examined under which the energy generation is efficient. It was shown that the maximum attainable efficiency η_{max} is a simple function of the coefficient λ. This relationship and the equation for the coefficient λ are presented in Fig. 41.

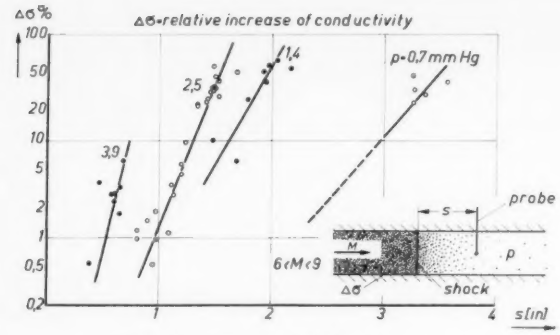

FIG. 44. Electron diffusion in argon.

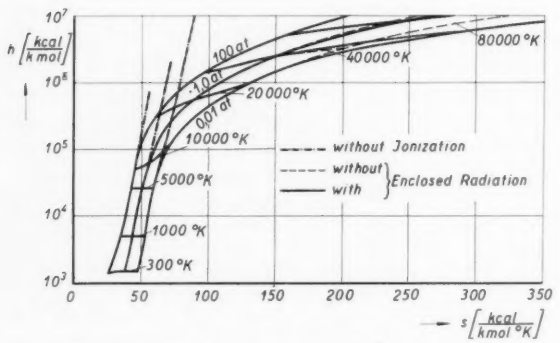

FIG. 45. Enthalpy vs. entropy for argon plasma.

λ depends on the diameter of the capillary, on the dielectric constant ϵ, on the so-called ζ-potential of the double-layer (which, in turn, depends on the selected combination of materials, i.e., liquid and wall of tube), on the viscosity μ of the liquid, and on the specific electric resistance ρ. The smaller the value of λ, the larger becomes the efficiency η_{max}. The equations show that, for instance, the combination of glass for the capillary tube and distilled water may result in a maximum efficiency of over 0.5, provided the diameter of the capillary tube is about 10^{-4} to 10^{-5} mm. Diaphragms from sintered glass or other synthetics with capillaries of radius within these limits seem possible.

Experiments were run with a diaphragm of sintered glass with capillaries of 0.002–0.006 mm. diameter, d, and 5.7 mm. length. The diaphragm was 46 mm. in diameter, D, and contained approximately 5×10^7 capillaries. Fig. 42 illustrates the results of the pumping effect under 100 v. tension. The vertical scale represents the pressure in atmospheres and the horizontal scale the output in cm.^{3}/sec. The solid line, expressing the theoretical values, and the dots, representing test values, agree satisfactorily. Fig. 43 shows the theoretical maximum efficiency as a function of the coefficient λ. The experimental efficiency is somewhat low, but in good agreement with the theory.

Further tests with capillaries of smaller diameter are under way, now that these can be manufactured.

Utilization of this effect will be beneficial in, for example, the control of missiles, when relatively small voltages are required to produce high pressures, for instance of 50 atmospheres, and to move parts of the control mechanism. Weight and retarding times will be small.

The Institute for Mechanics at the Technical University in Aachen is investigating the behavior of shock waves which can be studied in a shock tube with a 3.5×3.5 in. test section. It is well known that the electrical conductivity, i.e., the degree of ionization of a gas increases when the gas is compressed by a shock wave. It is, however, less well known that ionization of the gas starts already in front of the shock wave as a result of electron diffusion.

The conductivity of the gas in front of the shock wave was investigated at this Institute,[33] as shown in Fig. 44. These measurements were carried out in argon by installing a glow-discharge probe in the test section. The probe started to respond at an electron density of about 10^6 to 10^7 electrons/cm.^{3} The distance s in front of the shock was determined experimentally at the place of first response of the probe, i.e., where the above-mentioned value of electron density was attained. The experiments were performed at different Mach numbers M, and initial pressures p in front of the shock. The results are shown in the diagram in which the distance s is plotted on the horizontal scale and the increase in gas conductivity behind the shock on the vertical scale. There is a functional connection between the Mach number and the conductivity behind the shock wave such that the conductivity increases with increasing Mach number. The increase in conductivity is plotted in relative values for demonstration purposes. In the experiments M was varied between 6 and 9. The relation $\Delta\sigma = f(s)$ has been determined for four initial pressures. It is to be recognized that the numerical values of s are of considerable magnitude. The test results agree, in principle, with theoretical calculations. The significant result of these investigations is that, owing to electron diffusion, the conductivity keeps increasing behind the shock also, because the shock runs into already preionized gas. Furthermore, the result is of importance

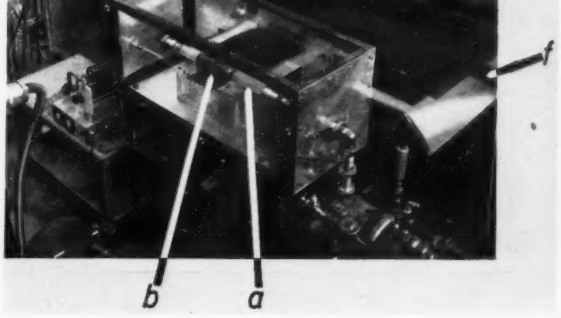

FIG. 46. Plasma generator.

in cases where the flow is influenced by magnetic fields and thus, in turn, it affects the shock itself.

One of the assignments of the Thermodynamic Institute of the Technical University in Brunswick is to investigate plasma. The behavior of argon and hydrogen at temperatures up to 100,000°K. was investigated theoretically,[34a] and Fig. 45 shows the enthalpy–entropy diagram with lines for constant pressures and temperatures calculated for argon. In the calculations the gas is assumed to be in thermodynamic equilibrium.

As can be seen in Fig. 45, ionization sets in above 8,000°K. and effects a strong shift in the curves. This is to be recognized from curves calculated without any ionization, for purposes of comparison. At temperatures exceeding 20,000°K., the influence of enclosed radiation must be considered also, since a gas is subject to this when completely enclosed by a gas of identical state. This influence gains importance with increasing temperature, as can be recognized by a comparison of the two curves with and without enclosed radiation. However, enclosed radiation need not always be taken into account. In thin plasma layers, for instance, it has no effect, and thus the curves change considerably in this case.

It should be mentioned also that ionization is not yet complete at 100,000°K., since only 7 of the 18 electrons have been separated from the atom.

Now I should like to mention studies on heat transfer between plasma and cooled bodies.[34b] The calorimeter in this test is a thin-walled copper tube with water passing through it, which is inserted in a steadily operating electric arc. Heat transfer is calculated by measuring the temperature increase in the water and the quantity of water that has passed through. In one instance, the electric arc was operating in air and in the other it was water-stabilized up to an intensity of about 100 amp. for higher temperatures.

The experiments revealed that up to 7,000°K. the heat transfer may be determined by the usual calculation methods, taking into account dissociation and ionization of the substances in question. At higher temperatures, up to 14,000°K., studies have been made but a comparison with calculations is not yet possible, because the physical properties of water plasma at these temperatures are as yet insufficiently known. Values of the thermal flow up to 6.10^7 kcal./m.^{2}hr. or 5,500 kw/ft.^{2} have been measured thus far.

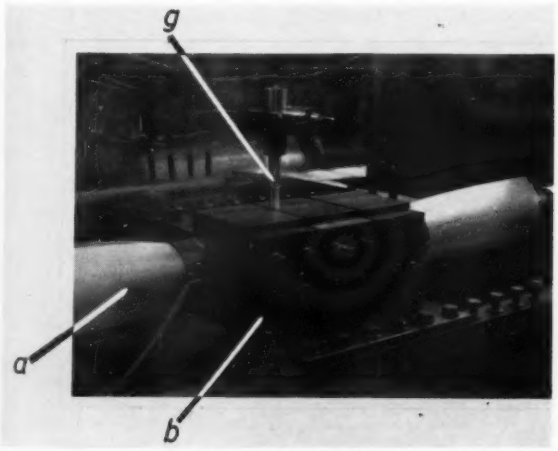

FIG. 47. Coil and probe.

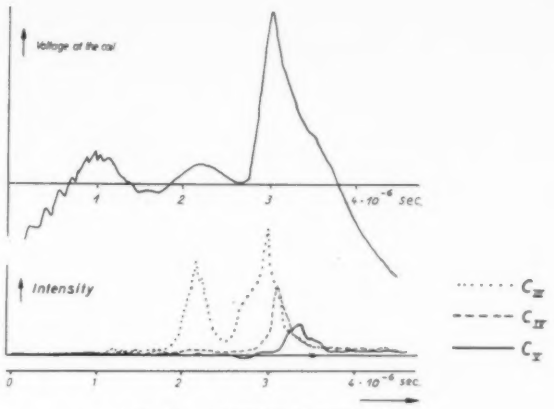

FIG. 48. Intensity of spectral lines.

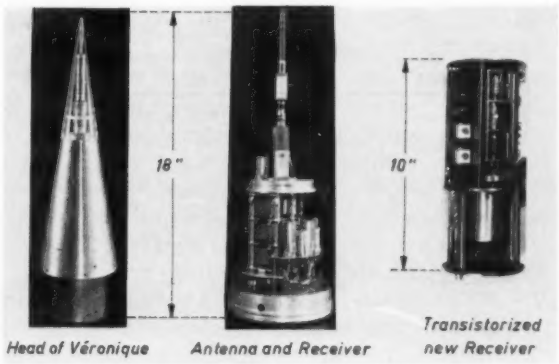

FIG. 49. Instruments for Véronique tests.

At the Institute for Plasma Physics of the Jülich Atomic Research Center,[35] experimental and theoretical research is being conducted with a view to obtaining plasma of high temperature and high values of the product of particle density and confinement time. In contrast to other experiments (for instance, stellarator) which are aimed at large confinement times at relatively low particle densities, the experiments in Jülich, with fast magnetic compression of the plasma,[36] are aimed toward high particle densities with relatively low confinement times. After preheating and preionization, the plasma is compressed by a rapidly growing magnetic field and heated. In this process, the main discharge first produces radial shock waves, followed by an adiabatic compression with a still growing magnetic field.

In the front of Fig. 46 is seen a discharge tube *a* and a coil *b* with only one turn, and the collector plates *c* which feed the current to the coil from a condensor bank *d* in the background. Preheating is effected from the connection *e* to the collector plates to be seen on the

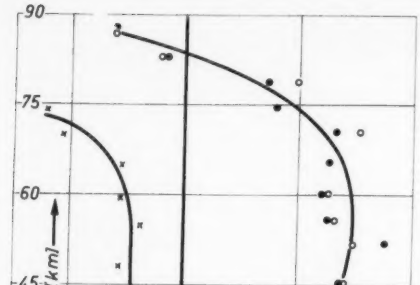

FIG. 50. Measurements of field intensity.

FIG. 51. Density at 660 km.

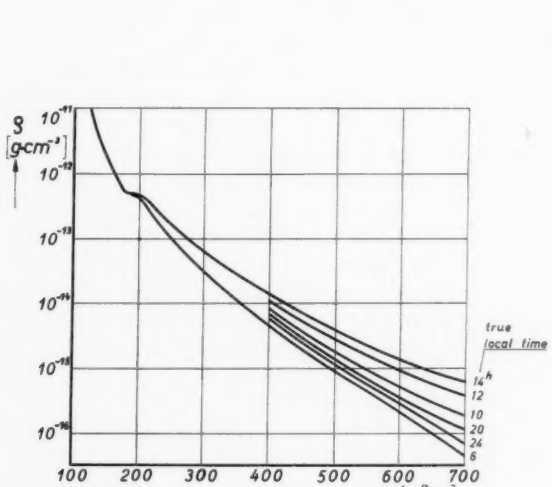

FIG. 52. Density vs. altitude at true local time.

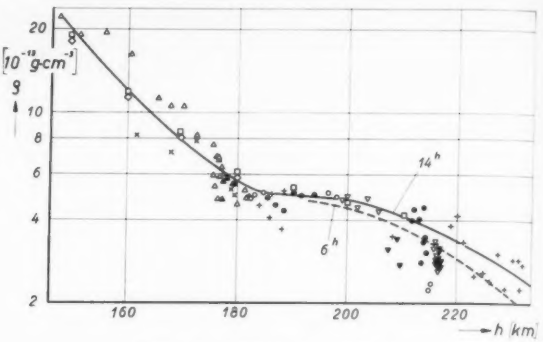

FIG. 53. Density vs. altitude.

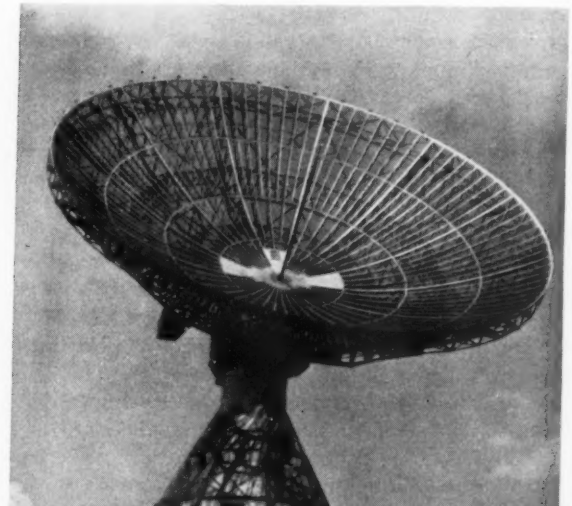

FIG. 54. Radiotelescope.

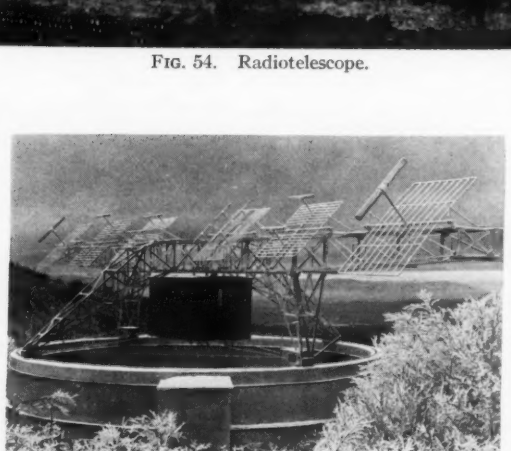

FIG. 55. Radiospectrograph Freiburg. Antenna system with box for measurements (4,100 ft altitude).

left. Prior to the firing of the main bank, a quasi-stationary axial magnetic field can be switched on the discharge through the connection f to be seen on the right side of the figure. This quasi-stationary field remains trapped in the plasma during parts of the main discharge. It can lead to an additional heating mechanism when interdiffusing with the magnetic field of the main discharge.

Fig. 47 is a sectional enlargement of Fig. 46, showing clearly the discharge tube a, which has a 1.6-in. diameter, and the coil b. The magnetic field measurements were performed by very small probes g, the diameters of which are only 1 mm., supplying the data on field distributions as functions of space and time during the periods of preheating and main discharge. The main discharge shows a remarkable separation of magnetic field and plasma.

Fig. 48 shows results[37] on the discharge as a function of time. On the horizontal scale is plotted a period of about 4 μsec. The tube had been filled with D_2 gas with a 5% addition of carbon. The upper curve gives the voltage during the preheating and the main discharge.

The lower diagram of Fig. 48 shows the intensity of a few spectral lines of the carbon in a time resolved form. The degree of ionization goes up from two to four. These lines appear successively, with double-ionized carbon present already in the preheating period. These measurements show an electron temperature between 0.5 and 1 $\times$ 10^6°K. The ion temperature, measured by the Doppler broadening of lines of the C_v spectrum, amounted to 1–1.7 kev. Neutron bursts of approximately 10^5 per pulse were observed at relatively low pressures, when the trapped magnetic field and the outer magnetic field were of opposite polarity.

Corresponding experiments are being made independently at Los Alamos, Washington, and Aldermaston. There is a continuous exchange of experiences between these groups, especially between Alan Kolb's group in Washington and the Jülich group. This, is an excellent example of the international cooperation evident in many rapidly progressing spheres of scientific-technical research.

Other experiments in the Jülich Institute are being made with a plasma gun in which the plasma is produced and accelerated by a magnetic driver. The main purpose of these experiments is to investigate the physics of high-temperature plasma, and further to prepare the way for experiments in which plasma is shot into magnetic configurations with properties especially promising for stable confinement.

(3.8) *Space Research*

Let us now turn to some examples of research on the upper atmosphere and space.

One of the missions of the Ionosphere Institute of the Federal Postal Authorities is to perform measurements of the field intensity at the lower ionospheric layer.[32] Passive frequency spectrometers have been developed for installation in rockets. In cooperation with French

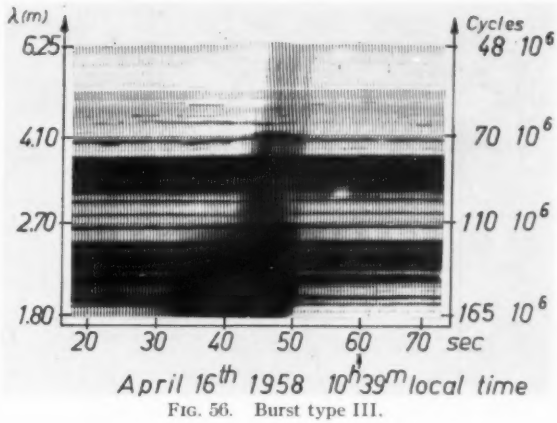

FIG. 56. Burst type III.

institutions, these are installed in Véronique rockets which are being launched in the Sahara.

Fig. 49, left, shows the nose of the Véronique into which measuring instruments such as the antenna, receiver, etc., are installed, as illustrated in the center part of the figure. Measurements with these instruments were performed as early as 1954. On the right-hand side is a new transistorized instrument which will be utilized during the next tests, scheduled for January 1961.

Fig. 50 shows the results of previous tests. The field intensity resulting from three radio stations of 200, 610, and 701 kc. is plotted against the altitude up to approximately 90 km. or 58 miles. While the results in the stratosphere disclose important information on the expansion of waves due to diffraction, the absorption of these waves in the lower layers of the ionosphere is clearly demonstrated by the reduction in the field intensity of electrons in this altitude range.

Future tests with the Véronique will also utilize a mass spectrometer which had been developed at the joint German-French Research Institute at Saint-Louis.[39] This instrument permits measurements of the concentration of nitrogen molecules N_2, oxygen molecules O_2, as well as nitrogen atoms N and oxygen atoms O, and transmits the results to the earth.

The observatory of Bonn University devotes some of its resources to the study of the characteristics of the upper atmosphere by means of satellite measurements in order to obtain reliable data on the distribution of density of the earth's atmosphere at high altitudes.[40]

Measurement results, carefully differentiated as to time of day and season, were evaluated according to a special method involving an iteration process,[41] and thus the density values were obtained. This evaluation was based on the diurnal and seasonal measurements by Sputnik III, Vanguard I, and Vanguard II, which had been supplied by the Heinrich Hertz Institute in East Berlin, the Space Track Center, and the Smithsonian Astrophysical Observatory, respectively.

Fig. 51 shows an example of the density distribution as a function of true local time at an altitude of 660 km. or 410 miles. The solid curve applies to $\Delta\delta$ smaller than 20°, the dashed curve to $\Delta\delta$ values between 20 and

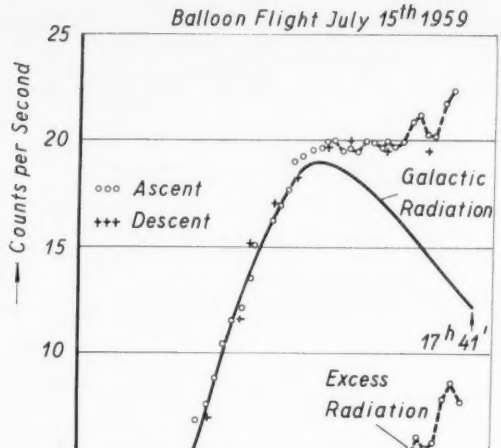

FIG. 57. Counting rates vs. altitude.

56°. $\Delta\delta$ expresses the difference between the declinations of perigee and sun. Above all, the essential influence of the true local time on the density is to be recognized, the maximum being at approximately 1400 hours. The influence of $\Delta\vartheta$, on the other hand, is less pronounced.

Results of measurement at several altitudes have thus been evaluated, so that now the density can be determined in relation to altitude and true local time. Fig. 52 shows the distribution up to an altitude of 700 km. or 435 miles. At around 200 km. (125 miles) the density starts to vary according to the true local time, and at an altitude of 700 km. it reaches values which already differ from one another by a power of ten.

At an altitude of 180 km. or 112 miles the density pattern shows an irregularity which has been closely examined.[42] Fig. 53 shows the pattern in the zone between 150 and 230 km. The solid line expresses the density at 1400 hours true local time, and the dashed line that at 0600 hours. The influence of the local time is quite minimal here. The measurements are from Sputnik III and Discoverer VI and some rocket launches; they were corrected, by use of a special method, for the fact that the density in these altitudes depends considerably on the intensity of solar radiation. A good, proportional measure was found to be the 20-cm radiation, and therefore the measured values were corrected commensurate with the variations of this radiation. Thus the stated values were obtained, and they showed relatively small scattering. It is probably the result of absorption of ultraviolet radiation that the density decreases more slowly between the altitudes of 180 and 200 km. This region, in which radiation is especially pronounced, is known as the F_1 layer of the ionosphere.

The Observatory owns a radiotelescope which is to be seen in Fig. 54. The mirror has a diameter of 82 ft., and an electromechanical computer and a drive control enable it automatically to follow the movements of a celestial body. Based on the 21-cm. radiation of the hydrogen atom, the radiotelescope is at present specifically used for research on the structure and kinematics of the galactic system, and also it provides valuable information on the density and structure of interstellar matter.

An important contribution to interplanetary research is furnished by the Fraunhofer Institute in Freiburg, which maintains two observatories: one on the Schauinsland near Freiburg, and the other in Anacapri near Naples, Italy. The studies of this Institute are directed towards time-varying solar phenomena; these are registered and published in daily charts which are probably the most complete in existence, and which are consulted by all those studying solar influences on interplanetary space or on the earth. It is well known that the state of interplanetary space is greatly affected by solar phenomena.

A radiospectograph, working in the frequency range of 48 to 165 mc./sec., registers the intensity and frequency of the so-called radiobursts. Fig. 55 shows this spectograph[43]—the only one of its kind in Europe—of which the six dipole systems mounted on a steel structure 100 ft. long automatically follow the course of the sun. From these radiobursts one can draw conclusions on the very intensive solar bursts. The burst velocities are between 100 km./sec. and values approaching the velocity of light.

Observation of these solar waves makes it possible to

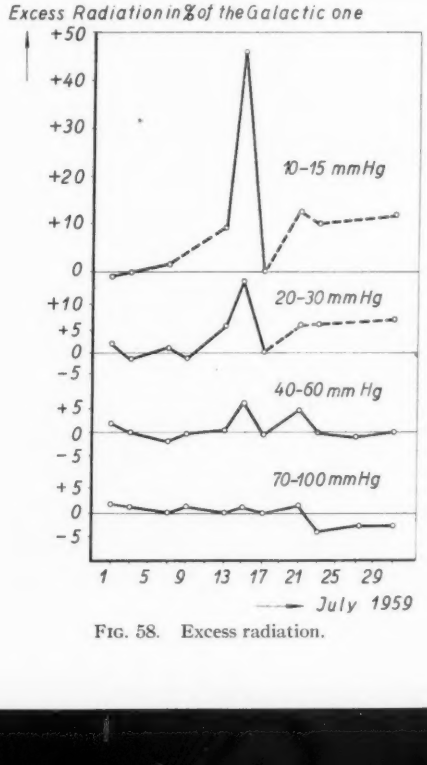

FIG. 58. Excess radiation.

trace corpuscular bursts far into space. The particle streams act simultaneously as carriers of magnetic fields, and are thus responsible for the density distribution and for the distribution of magnetic fields in interplanetary space. It is to be assumed that the particle clouds are identical with the corpuscles which cause disturbances in the earth's magnetic field.

Fig. 56 shows a burst measurement;[44] the horizontal scale defines the time and the vertical scales the frequency and wavelength, respectively. The almost vertical shadow-lines represent a burst, and it becomes evident that the radiation frequencies decrease more or less rapidly with time. The horizontal lines are interference from earth transmitters.

The results of this research are a contribution to the understanding of processes in interplanetary space as well as in the outer atmosphere of the earth.

The Max Planck Institute for Stratosphere Physics in Lindau (near Göttingen) conducts extensive studies on cosmic radiation. In addition to ground observations, measurements are taken from balloons, with special attention to fluctuations of radiation intensity.[45a]

Let me select an example from balloon flights performed in July 1959. Fig. 57 shows the remarkable measurement of 15 July. The counts per second of a single Geiger counter have been plotted as function of altitude given in mm. Hg as pressure, as well as in feet. The plotted points are the unusual values of this day, whereas the solid line gives the galactic radiation measured in days without special solar activity. Thus the course evidently deviated strongly from normal at high altitudes; this deviation is the excess radiation, which has been plotted separately in the lower part of the figure.

Fig. 58 shows the excess radiation for all flights performed in July 1959. The ordinate is the excess radiation in per cent of the galactic radiation. The four curves apply to four different altitudes given on the right side in mm. Hg. It is to be seen that on some days, and especially on 15 July, there existed considerable excess radiation which appeared, however, only at altitudes above 70–100 mm. Hg or about 50,000 ft. A radiation excess of nearly 50 per cent was measured on 15 July between 10–15 mm. Hg or about 90,000–100,000 ft.

The cause of this excess radiation is certainly to be seen in solar activity; however, investigations on the more exact interrelation of these phenomena and on the nature of this radiation have not yet progressed to a point permitting clearly defined statements.

Lately, another subject has gained importance among the numerous topics discussed by scientists attending the COSPAR meetings: a close correlation between the cosmic radiation intensity fluctuations and their effects has been determined in measurements at stations all over the world, and it has been concluded that the observed fluctuations, which are due primarily to magnetic storms and solar activity, are all modulated by one additional phenomenon. It has been found that all primary rays reaching the earth lose a certain fixed

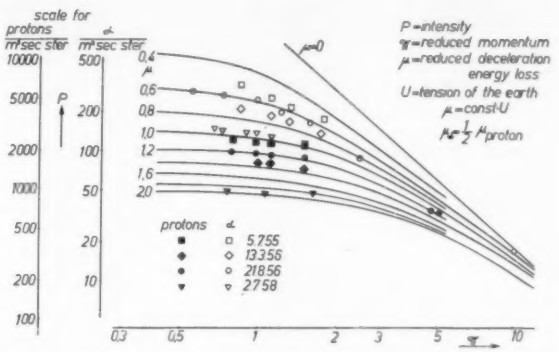

FIG. 59. Calculated and measured spectrums for different values U at different days.

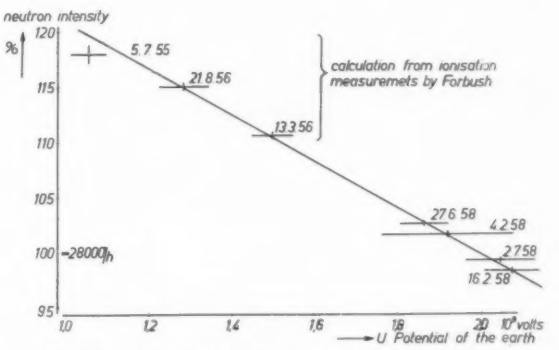

FIG. 60. Neutron intensity and retarding tension U.

amount of energy, regardless of their initial energies, and that this loss varies with time. This deceleration effect could be explained by assuming a potential difference U between earth and space, with a variance in time due to the solar activity.

The Max Planck Institute for Stratosphere Physics[45b] was able to contribute to the clarification of these relationships by calculations based on their own measurements and also on those of McDonald and Webber[46] and McDonald.[47,48] These measurements yielded integral as well as differential spectra of the radiation intensity. Fig. 59 illustrates the integral spectra, with the vertical scale expressing the intensity P, the horizontal scale the momentum π in reduced form, and the energy loss μ caused by the potential difference U as parameter. The scale of the ordinate P differs for protons and α-rays only by a constant. The solid curves are the result of calculations based on the reasoning just explained, and they evidence the important influence of U, and hence μ, on the intensity P. The curve $\mu = 0$ follows an equation in which the spectrum is proportional to $E_{\text{kin}}^{-2.5}$; E_{kin} designating the kinetic energy of the particles. It can be seen that this curve is considerably modified by different values of μ and thus U.

The results of proton and α-radiation measurements follow quite closely the course of the curve established for constant μ, and thus permitted determination of the value of U on the different days when measurements

Date of Fall of Meteorite: 11 August 1956

Radioactive Period of Na 22: 2,6 years

Intensity of Cosmic Radiation: 0,68 particles/cm² sec ster

Ratio of Intensity J of particles with Energie E

$$\frac{J(100\,MeV < E < 1BeV)}{J(E > 1BeV)} = 2,1$$

FIG. 61. Meteorite Breitscheid.

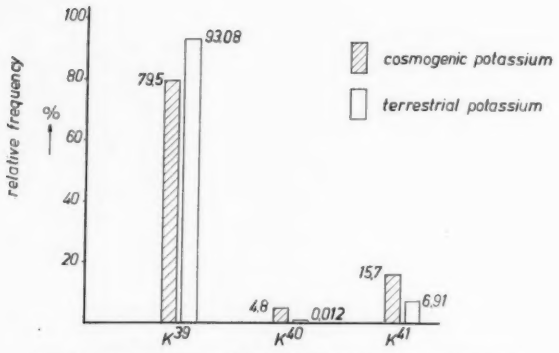

FIG. 62. Frequency of potassium isotopes in meteorites.

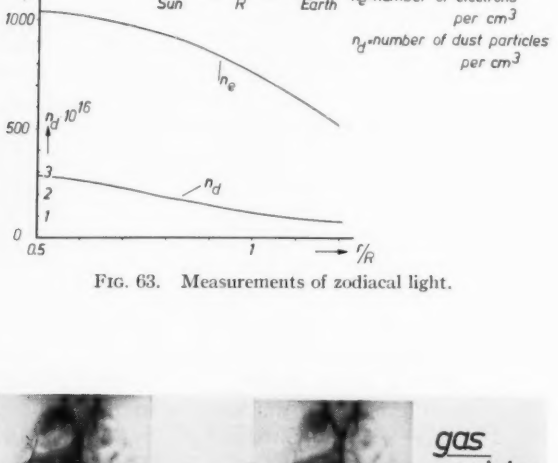

FIG. 63. Measurements of zodiacal light.

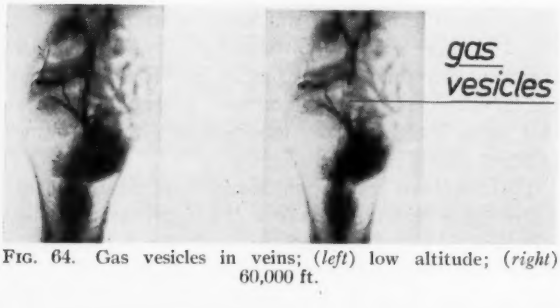

FIG. 64. Gas vesicles in veins; (*left*) low altitude; (*right*) 60,000 ft.

were made. It is to be noted that by definition there must be, for identical U,

$$\mu_\alpha = 1/2\ \mu_{\text{proton}}$$

This, too, has been very well satisfied.

Furthermore, it is now possible, for example, to express the neutron intensity measured in a certain place as a function of U, since U was found for different days according to Fig. 59 and, in general, the neutron intensity of these days is also known. This is represented in Fig. 60; the vertical scale expresses the percentage of neutron intensity in Weissenau, Germany, with the 100 per cent value taken to be a rounded-off value (28,000/hr.). From the measured values on the different days we can now see the amount and the fluctuations of the earth potential, which fluctuates between a minimum of 10^9 v. and values exceeding 2×10^9 v. Other measurements taken on 15 July, 1959 even yielded a value of about 2.7×10^9 v., the highest thus far. The minimum coincides with the sun spot minimum, and the maximum with the strongest magnetic storms. During these storms the potential may increase within several hours by approximately 1×10^9 v.

Although an insight has been gained into the amount and fluctuations of this earth potential, it now remains to study the location of the effective field. Apparently, larger potential differences develop only at greater distances from the earth (>100,000 km.); however, only with far-range rockets could information on this be gained. It is not yet known whether the field is of a geocentric or heliocentric nature. On the other hand, it seems clear that it is a dynamic electric field.

The Max Planck Institute for Chemistry in Mainz engages in the examination of meteorites which have been found on the earth. In addition to determining the age of these meteorities, they study primarily the extent to which the meteorites have been affected by cosmic radiation.

The spallation products in the meteorites, which appear as a result of cosmic radiation and which are minutely examined, permit conclusions as to radiation ages and exposure ages; they also allow one to establish data on the energy spectrum and the total intensity of the cosmic radiation and its fluctuation with respect to time. In comparison with ground measurements of the cosmic radiation, or satellite measurements, this has the advantage that it yields information on the cosmic radiation outside the magnetic field of the earth because the time required to pass through this field and the atmosphere is relatively short compared with the age of the meteorite.

While high-energy radiation (particles with energies of over 1 Bev) is quite well known because it penetrates close to the earth, low-energy radiation is less well known. It is on this subject that the meteorite examinations yield important information.

The reaction products argon-39,[49] chlorine-36,[50] and sodium-22,[51] were recently tested in detail. By studying the fissions per unit time and mass of sodium-22 in the Breitscheid meteorite of 1956, as shown in Fig. 61,

it was determined that the mean intensity of the cosmic radiation during the period 1954–1956 was about 0.68 particles/cm.²-sec.-sterad, including particles with energies down to about 100 Mev. It could furthermore be determined that the ratio of the radiation intensity for particle energies below 1 Bev to the intensity for particle energies over 1 Bev is about 2.1. This demonstrates that the largest part of the intensity is not accessible to measurements made close to the earth. These are important indications regarding the state of interplanetary matter.

By virtue of its relatively short radioactive period of 2.6 years, potassium is especially suitable for studies of the cosmic radiation intensity fluctuations caused by solar influences. Research was aimed at determining the composition of potassium isotopes in iron meteorites.[52] It was shown that the relative frequency of K^{39}, K^{40}, and K^{41} in the meteorites varies considerably from the relative frequency of these isotopes in terrestrial potassium. Fig. 62 demonstrates this difference. It must be noted that the relative frequency of the isotopes in terrestrial potassium always has identical values in all samples and shows no scattering, so that the differences between cosmogenic and terrestrial potassium permit determination of the age of the meteorite and also the cosmic radiation intensity. The calculations indicated that the mean cosmic radiation had remained constant over a long period of time.

At the Astronomic Institute of the Tübingen University, research is carried on in the field of optics and mechanics of interplanetary matter. Our knowledge of this subject, gained from studies performed on the earth or in its vicinity, is based primarily on the photometry of sunlight scattered by the interplanetary particles.

The zodiacal light plays an important part in this research. This light originates from the sunlight scattered by the relatively high-density matter in the earth's orbital plane, which can be observed. However, this must be separated from other luminous effects participating in the glow of the night sky, to which the glow of the star background and the airglow of the ionosphere contribute. Absorption and scattering of light within the atmosphere present further difficulties. Hence the determination of the light-scattering functions of electrons and dust particles are very important. They are the special subject of theoretical and experimental research carried out in the Institute at Tübingen.[53]

Another important characteristic of the zodiacal light is the polarization of a considerable part of the scattered light. This polarization has received special attention,[54] and measurements have established the preferred direction of oscillation as almost vertical to the earth's orbital plane.

It was further shown that the scattered, polarized light originates primarily from sunlight scattered by free electrons, and that interplanetary dust takes a minute part, or no part at all, in this phenomenon.

FIG. 65. Gas vesicles.

By measuring the total scattered light and the polarized part of it, the number n_e of electrons per cm.³ and the number n_d of dust particles per cm.³ can be calculated, and thus the density of the matter can be found. Fig. 63 shows the results of a series of measurements. R is the distance between sun and earth, and r the distance of the observed point P from the sun. The point P is to be seen at an elongation φ, and the light at P is scattered at an angle ϑ.

The calculated number of electrons per cm.,³ n_e, has been plotted against r/R; the number of electrons decreases from about 1,000 to 500 with increasing r between r/R of 0.5 and 1.2. A considerably smaller quantity results for the number of dust particles; however; it must be taken into consideration that for certain reasons an average radius of 10^{-3} cm. was assumed for spherical particles which reflect totally. Also, the zodiacal light can be measured only for values of $\varphi > 30°$ (i.e., $r/R > 0.5$) because the coronary glow of the sun dominates when the values are smaller than that.

From these tests the density of interplanetary matter in the earth's orbital plane can thus be found. Assuming that in addition to the electrons there is an identical number of protons, we get a density of approximately 1.2×10^{-21} gm./cm.³ in the vicinity of the earth

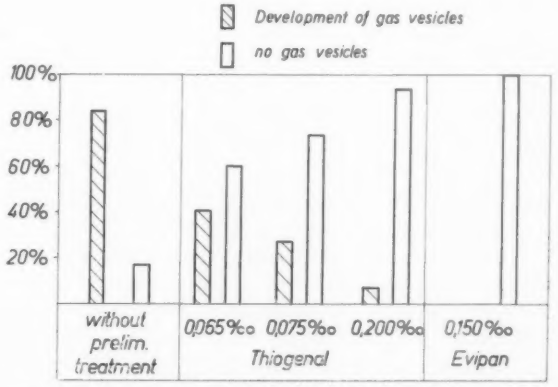

FIG. 66. Development of gas vesicles with preliminary treatment.

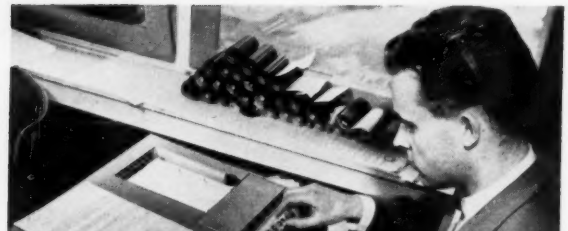

FIG. 67. Pellet recorder.

It is to be noted that these values diminish considerably outside the earth's orbital plane. For instance, at a vertical distance of $r/R = 0.5$ of the earth's orbital plane, the dust density is only 10 per cent of the values just mentioned.

(3.9) *Flight Medicine*

Finally, permit me to talk about two examples from the field of flight medicine.

The staff of the DVL Institute for Flight Medicine in Bonn is engaged in the study of the causes, prophylaxis, and therapy of the rapid decompression sickness to which high-altitude pilots are subject. The formation of intravascular gas bubbles, as might happen for instance in defective altitude chambers, etc., is known to be a great danger in connection with rapid decompression.

It was shown[55,56] that the formation of these gas vesicles not only follows the simple physical laws of gas absorption, but also depends on different influences. Fig. 64 shows the formation of such bubbles. On the left-hand side we see the blood circulation in the vein of a cat at low altitude, made visible on an X-ray screen by a radio-opaque material. The right-hand side shows the same circulation at 60,000 ft. altitude. In the middle of this image we recognize clearly an interruption in the flow, which is filled with gas vesicles. Fig. 65 shows the gas bubbles, having formed in great number, interrupting the blood circulation.

It was found that the formation of gas bubbles can be influenced considerably by premedication with ferments, injection and inhalation of narcotics, and tranquilizers. Fig. 66 presents the results of extensive tests on rats which had been treated with Thiogenal and Evipan prior to a pressure drop from 60,000 ft. On the left are the results on rats without premedication, the black column indicating the number of animals with gas bubble formation and the white indicating those without any. In 83 per cent of the rats gas vesicles developed. The succeeding three test series show the results after premedication with Thiogenal, with the dosage increasing from 0.065/thousand of the body weight to 0.200/thousand. Gas vesicle formation has decreased considerably. The last test series, on the right, shows the result after premedication with 0.150/thousand Evipan, which completely prevents gas bubble formation.

These results indicate that rapid decompression sickness can be influenced by drugs, and that the possibilities offered may be of importance.

Another department of this institute deals with suitable methods for selecting pilots who will have to withstand extreme stresses of different kinds. Heretofore, the stress resistance of pilots to acceleration, heat, cold, oxygen deficiency, etc., were tested with appropriate devices such as centrifuges, heat and cold chambers, and altitude chambers. Tests by these methods are troublesome, time-consuming, and strenuous for the person being tested. Moreover, the results are valid only for the condition of the subject at the time of the test, and this might change owing to circumstances at the time of flight.

The staff of this institute developed a method[57] which, in addition to being simple, also has definite advantages over previous methods. It is based on the idea that the limits of every organic-functional performance are determined by the oxygen supply of the tissue. The vegetatively regulated processes of the organism, on which resistance to stress depends, should therefore respond largely to the unspecific stressor, the oxygen-deficient breathing air. These processes can be utilized for testing purposes. An important conclusion is that the result of the oxygen-deficiency test should be indicative of other stresses also.

Tests were performed in a normal altitude chamber. An altitude of approximately 25,000 ft. was simulated and the test person was subjected to oxygen deficiency by removing the oxygen mask when the test was started at this simulated altitude. In order to register the decline in performance objectively, a device was developed (Fig. 67) in which the psychomotoric performance efficiency is used as a criterion. In this test, the coordination power—that is the ability to move muscles quickly and purposefully—is of primary importance. From a stock of pellets the test persons were to insert into holes of different sizes in a rotating cylinder pellets of respective diameter. These holes appeared one at a time for approximately 2 sec. each.

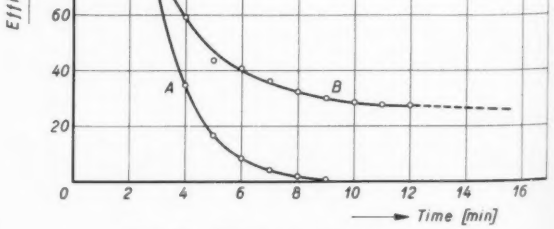

FIG. 68. Pellet recorder test.

Each correctly inserted pellet was registered, and 30 correctly placed pellets per minute constituted the index of 100 per cent efficiency. This test is so simple that practically every test person was 100 per cent efficient at sea-level conditions after having practiced for about 10–12 min.

The several thousand persons tested this way could be divided into two types. In Fig. 68 is plotted the efficiency of the test persons versus time. While efficiency was always 100 per cent with normal oxygen supply, it declines rapidly with the length of the test in type A persons, and more slowly in type B persons. In type A subjects there was an earlier failure in coordination, as compared with type B subjects who had better resistance. Moreover, it was shown that the results of the test depended also on the age of the test person and on vegetative nervous functional disturbances.

Fig. 69 shows the results of two tests taken by one person. Curve 1 is the normal result, while curve 2 represents the result immediately after a febrile disease. This strong deviation in performance occurred in spite of the fact that this person was considered healthy within the standards applied in normal examination. Only after six weeks' recuperation did he regain his former efficiency, and only then was he again permitted to fly.

Further comparative tests performed with numerous subjects for other stresses such as heat, cold, acceleration, and oxygen deficiency, as well as combinations thereof, showed results comparable to those recorded by the simple pellet test. A much simpler method of testing has thus been found. Another great advantage is that the test may be repeated a day prior to flight duty, to make certain that no acute decline in performance is imminent.

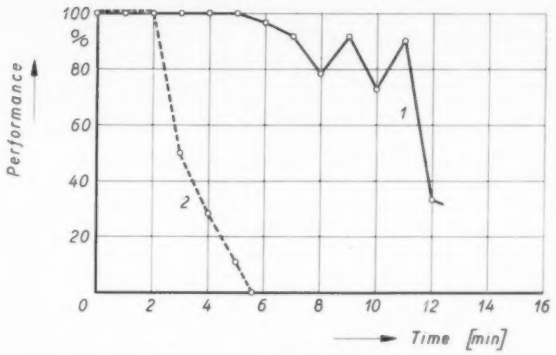

FIG. 69. Performance decline after febrile diseases.

(4) International Cooperation

This concludes my review of research results illustrated by randomly chosen examples. Permit me to close with a few words on the great importance of international cooperation.

I hope that my lecture has made it clear that West Germany has begun to contribute to aerospace research, and that it will attempt to increase its efforts in this direction.

As I mentioned at first, it was not easy for West Germany to start anew. However, international cooperation during the past years has helped greatly. After the ten-year interruption in aerospace research, it was above all AGARD (the Advisory Group for Aeronautical Research and Development) with its scientific exchange which rendered West Germany a service that can never be overestimated. Contact with scientists of the Western world was established through AGARD, and valuable information on the progress of research was passed on to us at its meetings. AGARD also promoted the exchange of extensive scientific experience by supplying valuable documentation as well as by sending a great number of experts to visit German research institutions, where they presented their specialized knowledge and initiated fruitful discussions.

Another important organization is COSPAR (the Committee on Space Research), which has been in operation for some years now; its meetings have also promoted a productive exchange of experiences. Of special value is the international exchange of data from space flight experiments. This organization, too, has already proved to be of great importance and benefit to German space research.

Other organizations, such as the International Union of Geodesy and Geophysics (I.U.G.G.), the Committee on Space Radio Research, and the International Astronautical Federation, are important as well for their world-wide exchange of experiences.

Probably the most significant result of international cooperation was the International Geophysical Year, which at the same time marked the beginning of the new age of space flight, which is the direct continuation of the development to which the great sons of your nation, Wilbur and Orville Wright, opened the way 57 years ago.

References

[1] Kowalewski, J., *On the Relation Between Fatigue Lives and Random Loading and Under Corresponding Programme Loading*, Symposium on Full-Scale Fatigue Testing of Aircraft Structures, Amsterdam, 1959.

[2] Hafer, X., *Windkanaluntersuchungen zur Entwicklung eines Triebwerkeinlaufs für starke Schräganströmung*, Hausmitteilung E. Heinkel, Flugzeugbau, München, 1960.

[3] Martensen, E., *Die Berechnung der Druckverteilung bei dicken Gitterprofil n mit Hilfe von Fredholmschen Integralgleichungen zweiter Art*, Mitteilung der Aerodyn. Versuchsanstalt Göttingen, N. 23.

[4] Riegels, F. W., *Fortschritte in der Berechnung der Strömung durch Schaufelgitter*, ZFW, H. 1, 1961.

[5] Isay, W. H., *Zur Berechnung der Strömung durch axiale Schaufelgitter*, ZAMM, No. 37, 1957.

[6] Meyer, L., *Singularitätentheorie der Flügelgitter*, Mitteilungen des Instituts für Aerodynamik, ETH, Zürich, No. 26, 1959.

[7] Schlichting, H., *Application of Boundary-Layer Theory in Turbomachinery*, J. Basic Engineering, ASME, pp. 543–551, 1959.

[8] (*a*) Leist, K., *Messungen instationärer Temperaturgradienten in Turbinenschaufeln*, Motortechnische Zeitschrift, H. 6, u.7,

1959; (*b*) Scheele, H., Dissertation, Technischen Hochschule Aachen (to be published in 1961).

[9] Förster, S., *Pneumatisches Verfahren zur Messung hoher und zeitlich schnell veränderlicher Gastemperaturen*, Dissertation, Technischen Hochschule Aachen (to be published in 1961).

[10] Ulbricht, G., *Radio Navigation Systems for Aviation and Maritime USC—A Comparative Study* (to be published soon as an Agardograph).

[11] Knausenberger, G., *Ultrarotstrahlungsmessungen an Strahltriebwerken* (to be published soon as a DVL Report).

[12] Tschauner, J., *Die Berechnung von Impulssystemen bei verschiedenen Einwirkungen*, Nachrichtentechn. Zeitschrift, H. 6, 1960.

[13] Gersten, K., *Nichtlineare Tragflächentheorie, insbesondere für Tragflügel mit kleinem Seitenverhaltnis* (to be published shortly in Ingenieur-Archiv).

[14] Truckenbrodt, E., *Tragflächentheorie bei inkompressibler Strömung*, Jahrbuch der Wissenschaftlichen Gesellschaft für Luftfahrt, 1953.

[15] Bollay, W., *A Nonlinear Wing Theory and Its Application to Rectangular Wings of Small Aspect Ratio*, ZAMM, No. 19, 1939, and Journal of the Aeronautical Sciences, Vol. 4, No. 7, pp. 294–296, May, 1937.

[16] (*a*) Thwaites, B., *A New Family of Low-Drag Wings with Improved c_L Ranges*, Rept. and Mem. No. 2292; (*b*) M. J. Lighthill, A New Method of Two-Dimensional Aerodynamic Design, Rept. and Memo No. 2112; (*c*) W. Pfenninger, *Untersuchungen über Reibungsverminderungen an Tragflügeln, insbesondere mit Hilfe von Grenzschichtabsaugung*, Mitteilung d. Instituts für Aerodynamik, ETH, Zürich, No. 13; (*d*) W. Pfenninger, *Experiments on a Laminar Suction Airfoil of 17 Per Cent Thickness*, Journal of the Aeronautical Sciences, Vol. 16, no. 4, pp. 227–236, April, 1949.

[17] (*a*) Wortmann, F. X., *Ein Beitrag zum Entwurf von Laminarprofilen für Segelflugzeuge und Hubschrauber*, Z. Flugwissenschaften, No. 73, 1955; (*b*) F. X. Wortmann, *Experimentelle Untersuchungen an neuen Laminarprofilen für Segelflugzeuge und Hubschrauber*, Z. Flugwissenschaften, No. 5, 1957; (*c*) F. X. Wortmann, *Fortschritte beim Entwurf von Laminarprofilen*, Mitteilungen d. Instituts für Aerodynamik und Gasdynamik der Technischen Hochschule Stuttgart, 1959.

[18] Eppler, R., *Ergebnisse gemeinsamer Anwendung von Grenzschicht- und Profiltheorie*, Z. Flugwissenschaften, H. 9, 1960.

[19] Kirchgässner, K., *Beiträge zu einer nichtlinearen Theorie von Schichtenströmungen längs zylindrisch gekrümmter Wände gegenüber dreidimensionalen Strömungen*, Arch. Rat. Mech. Anal. H. 6, 1960.

[20] Görtler, H., *Einige neuere Ergebnisse zur hydrodynamischen Stabilitätstheorie*, DVL, Bericht, No. 123.

[21] Nickel, K., *Einige neuere Ergebnisse aus der Grenzschichttheorie*, Mitteilungen des Instituts für Angewandte Mathematik der Technischen Hochschule Karlsruhe, 1960.

[22] Spence, D. A., *The Lift of a Blowing Wing in Parallel Stream*, Journal of the Aeronautical Sciences, Vol. 23, No. 1, pp. 92–94. January, 1956.

[23] Maskell, E. C., and Spence, D. A., *A Theory of the Jet Flap in Three Dimensions*, RAE Report No. Aero 2612, 1958.

[24] Das, A., *Tragflächentheorie für Tragflügel mit Strahlklappen*, Jahrbuch der Wissenschaftlichen Gesellschaft für Luftfahrt, 1960 (to be published shortly).

[25] Truckenbrodt, E., *Tragflächentheorie bei inkompressibler Strömung*, Jahrbuch der Wissenschaftlichen Gesellschaft für Luftfahrt, 1953.

[26] Williams, J., *British Research on the Jet-Flap Scheme*, Z. Flugwissenschaften, No. 16, 1958.

[27] Huhnt, D., *Windkomponentenmessung in der freien Atmosphäre* (not yet published).

[28] Neuber, H., *Ein Flugzeug für die Erforschung der hohen Atmosphäre*, Congresso scientifico internazionale sulle correnti a Getto (jet stream) e ondulatorie, Torino (Italy), 1959.

[29] Rues, D., *Der Einfluss ebener Körper auf stromaufwärts, liegende senkrechte Stösse*, Z. Flugwissenschaften, H. 3, 1960.

[30] Bartlmä, F., *Wärmezufuhr bei Überschallgeschwindigkeit und thermischer Verstopfung* (choking), Mitteilungen des Instituts für Theoretische Gasdynamik der DVL (will be published shortly).

[31] Teipel, J., *Starke kugelsymmetrische Verdichtungsstösse unter Berücksichtigung von Dissoziations- und Ionisationsvorgängen*, Z. Flugwissenschaften, H. 7, 1960.

[32] (*a*) Walz, A., *Betrachtungen über einen elektrokinetischen Generator*, DVL, Bericht, No. 82, 1958; (*b*) W. W. Westphal, *Das Betriebsverhalten einer elektrokinetischen Anlage*, Dissertation, Technische Hochschule Karlsruhe (to be published shortly).

[33] Grönig, H., *Mitteilungen aus dem Institut für Mechanik der Technischen Hochschule Aachen* Dissertation (not yet published).

[34] (*a*) Bosnyakovic, F., Springe, W., and Knoche, K. F., *Mollier-Diagramme für Plasmen mit und ohne Hohlraumstrahlung*, Proc. Fourth International Conference on Ionization Phenomena in Gases, Upsala, 1959; (*b*) W. Springe, *Wärmeübergang an ein gebreckühltes Rohr im Lichtbogenplasma*, Dissertation, Technische Hochschule Braunschweig (to be published early in 1961).

[35] Mitteilung aus dem Institut für Plasmaphysik der Kernforschungsanlage Jülich.

[36] Fay, H., Hintz, E., and Jordan, H. L., *Experiments on Shock Compression of Plasmas*, Proc. of Fourth International Conference on Ionization Phenomena in Gases, I.V.C. 1046, Upsala, 1959.

[37] Bogen, P., and El Khalafawi, T., Mitteilung aus dem Institut für Plasmaphysik der Kernforschungsanlage Jülich.

[38] Rawer, K., Mitteilung des Ionosphäreninstitutes Breisach,

[39] Geerk, J. and Schardin, H., Mitteilung des Deutsch-Französischen Forschungsinstitutes Saint-Louis.

[40] Priester, W., Martin, H. A., and Kramp, K., Mitteilungen der Universitätssternwarte Bonn, No. 34b.

[41] Priester, W., and Martin, H. A., Nature, 1960.

[42] Priester, W., and Martin, H. A., Mitteilungen der Universitätssternwarte Bonn, No. 34a.

[43] Kiepenheuer, K. O., and Rabben, H. H., *Der Freiburger Radiospektograph*. Z. Astrophysik, H. 1, 1960.

[44] Rabben, H. H., *Solare Burste der Type III und ihre Beziehungen zu den Eruptionen*, Z. Astrophysik, H. 2, 1960.

[45] (*a*) Ehmert, A., Erbe, H., and Pfotzer, G., *Stratospheric, Cosmic Ray Excess at 52° N Geomagnetic Latitude in July 1959*, Mitteilungen des Max-Planck-Institutes für Stratosphärenphysik, Lindau (Harz), Germany; (*b*) A. Ehmert, *Electric Field Modulation*, Proc. COSPAR Space Symposium, 1960.

[46] McDonald, B., and Webber, W. R., *The Proton Component of the Primary Cosmic Radiation*, Department of Physics, State University of Iowa, 1959.

[47] McDonald, F. B., *Phys. Rev.*, Vol. 109, 1958.

[48] McDonald, F. B., Department of Physics, State University of Iowa, 1959.

[49] Wänke, H., and Vilcsek, E., *Argon 39 als Reaktionsprodukt der Höhenstrahlung in Eisenmeteoriten*, Z. Naturforschung, H. 11, 1959.

[50] (Experiments not yet reported).

[51] Vilcsek, E., and Wänke, E., *Natrium 22 im Meteorit Breitscheid* (to be published shortly).

[52] Voshage, H., and Hintenberger, H. *Kalium als Reaktionsprodukt der kosmischen Strahlung in Eisenmeteoriten*, Z. Naturforschung, H. 9, 1959.

[53] Giese, R. H., *Zur Streuung elektromagnetischer Wellen*, Z. Astrophysik (to be published late in 1960).

[54] (*a*) Behr, A., and Siedentopf, H., Z. Astrophysik, 1953; (*b*) H. Elsässer, *Interplanetare Materie*, Mitteilung No. 35 des Astronomischen Instituts der Universität Tübingen, (*c*) H. Siedentopf, *Sterne, 1958* (in press).

[55] Wünsche, O., *Der Einfluss narkotischer und sedativer Mittel*

auf die intravasale Gasblasenbildung im Drucksturzversuch, Int. Z. angew. Physiol. einschl. Arbeitsphysiol., Bd. 17, 1958.

[56] Wünsche, O., and Hartmann, H., *Hyperelectrolytaemia and Intravascular Formation of Gas Bubbles in Rapid Decompression*, European Congress of Aviation Medicine, London, September 1960.

[57] Ruff, S., *Zur Frage der Auswahlmethoden für Besatzungen unkonventioneller Flugkörper*, ICAS, Congress, Zürich, September 1960.

[58] Brüner, H., *Belastungsuntersuchungen mit dem Kugeltestgerät in der Unterdruckkammer (zur Praxis der Fliegertauglichkeitsuntersuchung)*, DVL Bericht No. 59.

[59] Brüner, H., Dietmann, K., and Klein, K. E., *Der Sauerstoffmangeltest. Über Grundlagen und Beziehungen zu regulativen Vorgängen im Organismus*, Int. Z. angew. Physiol. einschl Arbeitsphysiol , Bd. 18, H. 1,1959.

[60] Brüner, H., Klein, K. E., and Jovy, D., *Modification of Individual Stress-Sensitivity by Adaptation to Oxygen-Want in the Low-Pressure Chamber*, Fifth European Congress of Aviation Medicine, London, August 1960.

CLOSING REMARKS

Hugh L. Dryden

Because of my personal association with Professor Quick in the work of AGARD and in other professional activities, it is a great honor and pleasure to be asked to propose a vote of thanks to him, following the custom of our British cousins, for his comprehensive picture of current aeronautical and space activities in the Federal Republic of Germany.

The indebtedness of aeronautics to German scientists and engineers of the past is well known and appreciated throughout the world. As the Wright Brothers were the pioneers in the practical art of flight, guided by their own laboratory measurements in wind tunnels, Prandtl was the pioneer in devising theoretical concepts and methods of analysis of air flow and air forces that are useful in the engineering design of aircraft. The Deutsche Versuchsanstalt für Luftfahrt (DVL), in which the lecturer is one of the leading scientists and research administrators, was for many years a major factor in advancing aeronautical technology along with its sister agencies, the National Advisory Committee for Aeronautics (NACA) in the United States; the Advisory Committee for Aeronautics, later called the Aeronautical Research Committee (ARC) in Great Britain; and the Central Aero-Hydrodynamic Institute (TSAGI) in the USSR.

We of the aerospace fraternity of the United States are happy to see our German colleagues engaged in rebuilding science and technology to restore their nation again to a position among the leaders of the world. Prof. Quick's lecture is indeed a revelation of how far this rebuilding has progressed. The statistics of the rapidly growing resources in personnel and funds devoted to aerospace research are impressive. But still more impressive are the quality and scope of the examples of current research activities. They include not only topics in the traditional areas of aero- and gasdynamics, propulsion and structures, but also those which we directly relate to the most exciting areas associated with space exploration, such as plasma dynamics, physics of the upper atmosphere and ionosphere, solar flares, cosmic rays, meteorites, and interplanetary matter. Balloons, high-altitude gliders, and sounding rockets are being or will be employed in these researches as well as satellites launched by the U.S. and U.S.S.R. whose observations yield important scientific results. The detailed surveys of aerospace research in Germany will be read and reread by interested scientists and engineers throughout the world. The lecture is an important and convincing demonstration that space research is the business of the whole world, and that every nation can make substantial contributions to it.

It is a privilege for me on your behalf to express our gratitude to Prof. Quick for the time and effort which he and his colleagues have devoted to the preparation of this highly significant lecture, and especially to thank him for coming to Washington to do honor to Wilbur and Orville Wright on this anniversary day of the first flight.

INTERNATIONAL AEROSPACE ABSTRACTS

New IAS Periodical—First Issue, January 1961

This new monthly combines, in improved format, the abstracts and books sections formerly printed in *Aerospace Engineering*. For information and subscription rates write to:

John J. Glennon, Manager, Technical Information Service
Institute of the Aerospace Sciences, 2 E. 64 St., N.Y. 21, N.Y.

Missile Structural Loads by Nonstationary Statistical Methods†

R. E. BIEBER*

Lockheed Aircraft Corporation

Summary

Nonstationary statistical methods are applied in obtaining the rigid-body structural load response of a vertical-rising ballistic missile to a flight environment of atmospheric disturbances. Results are obtained for a missile of the IRBM class. The input consists of the average and the covariance of the wind velocity at Patrick AFB during the winter months. A method which involves taking the square root of the input covariance matrix was employed in computing the covariance matrix of the response. The average and the standard deviation of the structural bending moment are shown at the critical flight altitude of 33,000 ft. The 99% extreme-value design loads obtained with a design criterion proposed in this paper are compared with design loads obtained with other criteria.

Symbols

t	= time
h, H	= altitude
Δh, ΔH	= increments of h and H
$\mathbf{e}_{X_I}$, $\mathbf{e}_{Y_I}$, $\mathbf{e}_{Z_I}$	= unit vectors in inertial reference frame
$\mathbf{e}_r$, $\mathbf{e}_E$, $\mathbf{e}_N$	= unit vectors in wind reference frame
$\mathbf{e}_{X_B}$, $\mathbf{e}_{Y_B}$, $\mathbf{e}_{Z_B}$	= unit vectors in body frame
Ω_{EI}	= earth's rotational velocity
Γ_I	= longitude
Λ_I	= latitude
r	= radius vector
g	= acceleration due to gravity
ϵ	= direction cosine
p, q, r	= angular velocity in body axes
$\ddot{X}_I$, $\ddot{Y}_I$, $\ddot{Z}_I$	= acceleration of c.g. in inertia axes
A_{X_B}, A_{Y_B}, A_{Z_B}	= acceleration of c.g. (not including that due to gravity) in body axes
I_{XX}, I_{YY}, I_{ZZ}	= moments of inertia with reference to body axes
I_{XY}, I_{XZ}, I_{YZ}	= products of inertia with reference to body axes
F	= aerodynamic forces
T	= thrust forces
M^F	= moment about c.g. due to aerodynamic forces
M^T	= moment about c.g. due to thrust forces
Δ_Y, Δ_Z	= displacement of c.g. from longitudinal geometric axis
δ_i	= angular deflection of ith control element
K_i	= control system gains
ϕ, θ, ψ	= Euler angles
$\mathbf{V}_{c.g.}$	= velocity of c.g.
u, v, w	= components of $\mathbf{V}_{c.g.}$ in body axes
$\mathbf{V}'_{c.g.}$	= velocity of c.g. with reference to surrounding air mass
u', v', w'	= components of $\mathbf{V}'_{c.g.}$ in body axes
$\mathbf{U}$	= absolute wind velocity
U_N	= north-south component of wind velocity relative to the earth's surface
U_E	= east-west component of wind velocity relative to the earth's surface
$m(\bar{x})$	= distributed mass
m	= total mass
l	= missile length
$\bar{x}/l$	= percent of missile length
α	= angle of attack
β	= sideslip angle
$\bar{q}$	= dynamic pressure
S	= reference area
b	= reference length
C_N	= normal force coefficient
C_D	= drag coefficient
C_{M_q}	= damping moment coefficient in pitch
C_{M_r}	= damping moment coefficient in yaw
$M(\bar{x}, t)$	= bending moment response
$M_I(\bar{x}, t)$	= unit bending moment
$\bar{M}(\bar{x}, t)$	= extreme value bending moment
$G(H, h)$	= unit impulse response
$\mathfrak{M}$ or $E[\ ]$	= average or expected value
R	= covariance
σ^2	= variance
σ	= standard deviation
ρ	= correlation coefficient
$P(M < \bar{M})$	= probability that $M < \bar{M}$
$p(\ )$	= probability density function
$p_G(\ )$	= Gaussian probability density function
n_P	= extreme value probability coefficient
$[\ ]$	— square matrix
$\boxed{\searrow}$	— diagonal matrix
$\{\ \}$	— column matrix
$[I]$	= unit matrix
Ξ	= eigenvectors
d	= eigenvalues
i, j, r, s	= numerical subscripts

Received August 17, 1959. Revised and received April 29, 1960.

† This report summarizes the results of a study undertaken by R. E. Bieber for LMSD Research, Lockheed Aircraft Corporation. This work was performed under Air Force Contract No. AF-04(647)-97. The author is grateful to C. Striebel and T. J. Harvey for many helpful suggestions concerning this problem, and to R. Reid and G. L. Bergst for their assistance.

* Aeronautical Engineer, Missiles and Space Division.

(1) Introduction

IN DESIGNING THE PRIMARY STRUCTURE of a ballistic missile it is necessary to investigate various loading conditions. Among these are the shock, vibration, and sustained loads imposed on the structure during ground handling, launch, maneuvers, and staging. Of particular concern here is the rigid-body response of the missile to a flight environment of atmospheric disturbances. More specifically, these disturbances are the horizontal jetstream-type winds.

Upon examination of several wind soundings, it becomes evident that the wind environment is a random process. Furthermore, this random process is nonstationary with altitude. Consequently it is necessary

TABLE 1

Average and Standard Deviation of N-S and E-W Wind Components (Patrick AFB, Feb. 1950–1955)

Alt. (km)	N-S Ave. (Knots)	N-S S.D. (Knots)	E-W Ave. (Knots)	E-W S.D. (Knots)
0	1.4	8.03	- 0.3	7.10
2	-1.9	12.99	-10.2	13.89
4	-1.6	15.30	-23.1	16.60
6	-1.2	19.98	-35.8	21.02
8	-0.6	24.68	-49.1	26.22
10	-0.1	30.14	-63.1	32.04
12	0.2	32.42	-74.5	34.91
14	0.2	27.04	-72.5	32.91
16	0.0	21.11	-55.2	26.73
18	0.0	14.71	-33.6	25.63
20	0.1	9.77	-12.0	21.18
22	0.4	7.43	- 7.3	21.68
24	0.7	9.36	-10.1	23.32
26	0.8	10.15	-15.3	24.70

to employ nonstationary methods in solving for the structural response, rather than the more popular stationary or power spectral methods.

For an airplane in horizontal flight, the horizontal component of a wind disturbance can have a pronounced effect on performance (headwind or tailwind). In the case of a vertical-rising missile the same disturbance results in a departure from the programmed trajectory. This trajectory departure is sensed by the guidance and control system which then signals for corrective control forces. During this process of dispersion and correction, significant structural bending moments can be produced in the vehicle. Furthermore, the vehicle must be designed to withstand the combination of this bending and the axial compression due to forward acceleration. Consequently the condition just described has received much attention in recent years owing to the necessity of designing highly reliable vertical-rising missiles, satellites, and space vehicles.

The method of analysis that has been widely used in solving this problem is to solve for the response due to a discrete wind profile or series of profiles. Furthermore, since the extreme-value structural loads are desired for design, an extreme wind profile must be selected. This profile is the subject of considerable controversy because of the difficulty of selecting or deriving a "critical profile."

By the use of nonstationary statistical methods, the extreme-value load response can be obtained in a straightforward manner. The assumptions involved in the solution are (1) linear equations of motion, and (2) normal probability distribution of wind input. For purposes of calculating the extreme-value design loads, these assumptions appear valid.

The usual procedure in structural design is to assure that the estimated allowable load is not exceeded by some rare-occurrence design load. As evidenced by the small number of structural failures in the aircraft and missile industry, this procedure produces a safe design. However, as the requirements of the missile become more and more exacting, the question of "how safe" becomes more and more pressing. Although the goal of designing a missile structure to a prescribed safety or probability of success is beyond reach at present, the solution of extreme-value design loads by nonstationary statistical methods is a step in that direction.

(2) Vehicle Response

For purposes of the present analysis, only the rigid-body response will be considered. The omission of the elastic modes is justified somewhat by the predominance of the rigid-body modes in determining the structural load response to wind disturbances for large and relatively stiff missiles of the IRBM or ICBM class. Another reason is that at present it would be difficult to apply the results including elasticity to an actual missile loads problem, since dynamic computer programs for solving for the statistical response of a variable-coefficient elastic system over long time spans are

TABLE 2

Correlation Coefficients of N-S Wind Components at Indicated Altitudes (Patrick AFB, Feb. 1950–1955)

Altitude (km)	0	2	4	6	8	10	12	14	16	18	20	22	24	26
0	1.000	0.511	0.370	0.291	0.231	0.183	0.101	0.103	0.120	0.074	0.048	0.025	0.022	-0.093
2		1.000	0.685	0.554	0.465	0.359	0.271	0.223	0.251	0.252	0.127	0.076	0.063	0.025
4			1.000	0.785	0.677	0.578	0.493	0.437	0.461	0.437	0.288	0.140	0.017	0.155
6				1.000	0.803	0.693	0.629	0.570	0.561	0.551	0.285	0.152	-0.037	0.154
8					1.000	0.843	0.717	0.657	0.631	0.547	0.316	0.074	-0.068	0.209
10						1.000	0.788	0.703	0.611	0.540	0.307	0.187	-0.103	0.211
12							1.000	0.780	0.682	0.558	0.274	0.116	0.000	0.113
14								1.000	0.769	0.648	0.283	0.121	0.000	0.137
16									1.000	0.688	0.368	0.188	-0.025	-0.010
18										1.000	0.372	0.239	0.000	0.052
20											1.000	0.289	0.017	0.150
22												1.000	0.193	0.068
24													1.000	0.285
26														1.000

TABLE 3

Correlation Coefficients of E-W Wind Components at Indicated Altitudes (Patrick AFB, Feb. 1950–1955)

Altitude (km)	0	2	4	6	8	10	12	14	16	18	20	22	24	26
0	1.000	0.565	0.511	0.431	0.373	0.350	0.258	0.238	0.218	0.010	0.032	0.000	-0.028	0.076
2		1.000	0.768	0.669	0.615	0.544	0.448	0.425	0.410	0.215	0.068	0.017	0.185	0.203
4			1.000	0.826	0.760	0.669	0.524	0.529	0.489	0.314	0.160	0.095	0.201	0.234
6				1.000	0.845	0.749	0.594	0.560	0.515	0.331	0.163	0.127	0.176	0.237
8					1.000	0.835	0.694	0.626	0.594	0.432	0.205	0.092	0.189	0.224
10						1.000	0.772	0.674	0.585	0.424	0.187	0.191	0.228	0.206
12							1.000	0.740	0.646	0.460	0.191	0.163	0.145	0.199
14								1.000	0.706	0.495	0.214	0.098	0.145	0.118
16									1.000	0.601	0.400	0.260	0.224	0.224
18										1.000	0.459	0.210	0.279	0.281
20											1.000	0.448	0.439	0.430
22												1.000	0.620	0.585
24													1.000	0.721
26														1.000

not available. In situations where the structural elasticity is deemed significant, estimates of the contribution to the design loads can be made by stationary methods. However, this involves making the assumptions of local stationariness of atmospheric disturbances with altitude and time-invariant linear systems.

During exit through an environment of atmospheric disturbances the structural bending moment is of primary concern in appraising the airframe compression-buckling problem. Consequently it is considered as the significant response in this study. However, the shear forces as well as other dependent variables can be evaluated by the same methods.

(3) Input Data

Atmospheric disturbances are usually divided into two distinct categories: (1) winds and (2) turbulence. The reason for this division lies primarily in the techniques used for measuring these quantities. Winds are usually obtained by balloon soundings, and consequently only the gross motions of the atmosphere are detected. Most turbulence data are obtained by direct flight measurements using directional vane techniques[1] or by reducing airplane c.g. acceleration data.[2] Also, a simple expression for the covariance or correlation function of wind-tunnel turbulence is presented in reference 3 and has been widely used in aircraft dynamic studies. Since the characteristics of stationary turbulence have already been discussed in the literature, no discussion will be presented here.

Daily wind soundings taken over a number of stations in the Northern Hemisphere are available from the U.S. Weather Bureau.[4] Many of these data, for the 5-year period of March 1951 through February 1956, have been reduced to a more convenient statistical form under a joint effort of the Office of Climatology, U.S. Weather Bureau, and the Sandia Corporation.[5]

An earlier investigation by A. Court[6] of the average and the correlation of wind velocities over Patrick AFB will be used as the input for the present study. The sample soundings were taken during the winter months of 1950–1955. The tabulation of these results is given in Appendix A. Table 1 shows the average and standard deviation of the N-S and E-W winds. Tables 2 and 3 show the correlation coefficients of the N-S and E-W components, respectively.

The data of reference 6 include the cross-correlation coefficients between N-S and E-W winds at the same but not at different altitudes. This is unfortunate, since the missing data would have completed the input for the two-dimensional response problem. However, at Patrick AFB the wind velocity exhibits strong E-W directional characteristics; consequently, a pseudo-one-dimensional wind with the following average and covariance was assumed:

$$\mathfrak{M}_U(h) = \sqrt{\mathfrak{M}_{U_E}^2(h) + \mathfrak{M}_{U_N}^2(h)} \quad (1)$$

$$R_{UU}(h_r, h_s) = R_{U_EU_E}(h_r, h_s) + R_{U_NU_N}(h_r, h_s) \quad (2)$$

The E-W average was used as the resultant average, since the N-S average is small. The resultant covariance is tabulated at 2-km. intervals in Table 4. Appendix A also illustrates the averaging techniques employed in reducing the wind data to the form of average, standard deviation, and correlation coefficients.

(4) Equations of Motion and Bending Moment Equation

An existing high-speed computer program with six degrees of freedom was utilized in obtaining the results of Section 6. A detailed description of the equations of motion is given in reference 8. A summary of the equations is presented below. Some of the auxiliary equations, as well as certain special effects such as the acceleration of the c.g. with respect to the air frame, fuel slosh, and "jet damping," have been omitted in the summary; however, they are included in reference 8.

(a) *Axes Systems*

(1) The inertial reference frame is located at the earth's center (Fig. 1). The positive Z_I axis intercepts

the earth's surface at the North Pole. The earth rotates about Z_I with angular velocity Ω_{EI}.

(2) The wind reference frame is located at the instantaneous center of mass of the missile (Fig. 1). The unit vector $\mathbf{e}_N$ is positive in the direction of north. The unit vector $\mathbf{e}_E$ is positive in the direction of east.

(3) The geometric axes are fixed in the body. They are used to locate the c.g. of the vehicle and the aerodynamic and control system forces.

(4) The missile body frame is located at the instantaneous center of mass (Fig. 2). The positive X_B axis intercepts the nose of the vehicle. The body frame is aligned with the longitudinal geometric axis; however, allowance is made for a c.g. displacement from the longitudinal geometric axis, $\Delta_y \mathbf{e}_{Y_B} + \Delta_z \mathbf{e}_{Z_B}$.

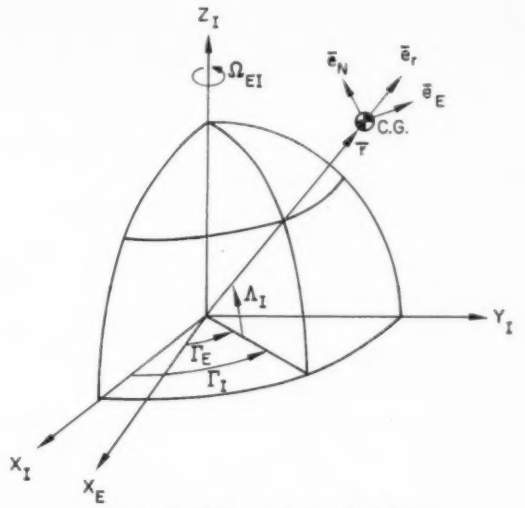

FIG. 1. Inertial, earth, and wind axes.

(b) *Vector Transformations*

From a computer programming standpoint, it is advantageous to use direction cosines in relating the body reference frame to the inertial reference frame, rather than the usual Euler angles. That is,

$$\begin{Bmatrix} \mathbf{e}_{X_B} \\ \mathbf{e}_{Y_B} \\ \mathbf{e}_{Z_B} \end{Bmatrix} = \begin{bmatrix} \epsilon_{XX} & \epsilon_{XY} & \epsilon_{XZ} \\ \epsilon_{YX} & \epsilon_{YY} & \epsilon_{YZ} \\ \epsilon_{ZX} & \epsilon_{ZY} & \epsilon_{ZZ} \end{bmatrix} \begin{Bmatrix} \mathbf{e}_{X_I} \\ \mathbf{e}_{Y_I} \\ \mathbf{e}_{Z_I} \end{Bmatrix} \tag{3}$$

The transformation from the wind reference frame to the inertial reference frame is a function of the longitude Γ_I and the latitude Λ_I,

$$\begin{Bmatrix} \mathbf{e}_{X_I} \\ \mathbf{e}_{Y_I} \\ \mathbf{e}_{Z_I} \end{Bmatrix} = \begin{bmatrix} \cos\Gamma_I \cos\Lambda_I & -\sin\Gamma_I & -\cos\Gamma_I \sin\Lambda_I \\ \sin\Gamma_I \cos\Lambda_I & \cos\Gamma_I & -\sin\Gamma_I \sin\Lambda_I \\ \sin\Lambda & 0 & \cos\Lambda_I \end{bmatrix} \begin{Bmatrix} \mathbf{e}_r \\ \mathbf{e}_E \\ \mathbf{e}_N \end{Bmatrix} \tag{4}$$

As a result of orthogonality, the inverse transformation matrix is the transpose in both transformations.

(c) *Force Equations*

Letting F denote the aerodynamic forces and T the thrust forces,

$$\begin{Bmatrix} \ddot{X}_I - g_{X_I} \\ \ddot{Y}_I - g_{Y_I} \\ Z_I - g_{Z_I} \end{Bmatrix} = \frac{1}{m} \begin{bmatrix} \epsilon_{XX} & \epsilon_{YX} & \epsilon_{ZX} \\ \epsilon_{XY} & \epsilon_{YY} & \epsilon_{ZY} \\ \epsilon_{XZ} & \epsilon_{YZ} & \epsilon_{ZZ} \end{bmatrix} \begin{Bmatrix} F_{X_B} + T_{X_B} \\ F_{Y_B} + T_{Y_B} \\ F_{Z_B} + T_{Z_B} \end{Bmatrix} \tag{5}$$

(d) *Moment Equations*

In scalar form the moment equations are:

$$I_{XX}\dot{p} - I_{XY}\dot{q} - I_{XZ}\dot{r} - (I_{YY} - I_{ZZ})qr - I_{XZ}pq + I_{XY}pr - I_{YZ}(q^2 - r^2) - \dot{I}_{XX}p + I_{XY}q + I_{XZ}r = M^F{}_{X_B} + M^T{}_{X_B} \tag{6}$$

$$I_{YY}\dot{q} - I_{YZ}\dot{r} - I_{XY}\dot{p} + (I_{XX} - I_{ZZ})pr + I_{YZ}pq - I_{XY}qr + I_{XZ}(p^2 - r^2) + \dot{I}_{YY}q - \dot{I}_{YZ}r - \dot{I}_{XY}p = M^F{}_{Y_B} + M^T{}_{Y_B} \tag{7}$$

$$I_{ZZ}\dot{r} - I_{XZ}\dot{p} - I_{YZ}\dot{q} + (I_{YY} - I_{XX})pq - I_{YZ}pr + I_{XZ}qr + I_{XY}(q^2 - p^2) + \dot{I}_{ZZ}r - I_{XZ}p - \dot{I}_{YZ}q = M^F{}_{Z_B} + M^T{}_{Z_B} \tag{8}$$

where M^F is the moment due to the aerodynamic forces and M^T is the moment due to the thrust forces.

(e) *Control-System Equations*

Vehicle control is maintained by means of a linear closed-loop autopilot and gimballed engines. The error-sensing devices are position and rate gyros (no angle-of-attack or accelerometer feedback).

Denoting the angular deflection of the ith control element by δ_i,

$$\delta_{ip} = K_{i\phi}(\phi - \phi_c) + K_{ip}p \qquad \delta_{iq} = K_{i\theta}(\theta - \theta_c) + K_{iq}q \qquad \delta_{ir} = K_{i\psi}(\psi - \psi_c) + K_{ir}r \tag{9), (10), (11}$$

where the Euler angles ϕ, θ, and ψ are obtained from

$$\phi = \tan^{-1}(\epsilon_{YZ}/\epsilon_{ZZ}) \qquad \theta = \sin^{-1}(-\epsilon_{XZ}) \qquad \psi = \tan^{-1}(\epsilon_{XY}/\epsilon_{XX}) \tag{12), (13), (14}$$

and ϕ_c, θ_c, and ψ_c are programmed commands.

The solution of the thrust forces and moments is a function of the location and orientation of the various control elements. In reference 8 the force and moment equations are derived for an array of five control elements. Since these expressions are quite lengthy, the special case of the thrust vectors initially aligned in the longitudinal direction and small deflection angles ($\cos \delta_i \approx 1$, $\sin \delta_i \approx \delta_i$) is shown below.

$$T_{X_B} = \sum_i T_i \qquad T_{Y_B} = \sum_i T_i \delta_{ir} \qquad T_{Z_B} = \sum_i T_i \delta_{iq} \tag{15), (16), (17}$$

Let $\bar{X}_i$, $\bar{Y}_i$, and $\bar{Z}_i$ represent the location of the gimbal point of the ith control element as measured from the geometric axes; then

$$M^T_{X_B} = \sum_i T_i[(\bar{Z}_i + \Delta_Z)\delta_{ir} + (\bar{Y}_i + \Delta_Y)\delta_{iq}] \tag{18}$$

$$M^T_{Y_B} = \sum_i T_i\,[(\bar{X}_{c.g.} - \bar{X}_i)\delta_{iq} + (\bar{Z}_i + \Delta_Z)] \tag{19}$$

$$M^T_{Z_B} = \sum_i T_i[(\bar{X}_{c.g.} - \bar{X}_i)\delta_{ir} + (\bar{Y}_i + \Delta_Y)] \tag{20}$$

(f) *Velocity and Angle-of-Attack Equations*

The velocity of the missile c.g. in the body coordinates is

$$\mathbf{V}_{c.g.} = u\mathbf{e}_{X_B} + v\mathbf{e}_{Y_B} + w\mathbf{e}_{Z_B} \tag{21}$$

The relative velocity of the c.g. with respect to the surrounding air mass is

$$\mathbf{V}'_{c.g.} = \mathbf{V}_{c.g.} - \mathbf{U} = u'\mathbf{e}_{X_B} + v'\mathbf{e}_{Y_B} + w'\mathbf{e}_{Z_B} \tag{22}$$

The absolute wind velocity is

$$\mathbf{U} = U_E\mathbf{e}_E + |\Omega_{EI} \times r|\mathbf{e}_E + U_N\mathbf{e}_N = U_{X_B}\mathbf{e}_{X_B} + U_{Y_B}\mathbf{e}_{Y_B} + U_{Z_B}\mathbf{e}_{Z_B} \tag{23}$$

where

$$\begin{Bmatrix} U_{X_B} \\ U_{Y_B} \\ U_{Z_B} \end{Bmatrix} = \begin{bmatrix} \epsilon_{XX} & \epsilon_{XY} & \epsilon_{XZ} \\ \epsilon_{YX} & \epsilon_{YY} & \epsilon_{YZ} \\ \epsilon_{ZX} & \epsilon_{ZY} & \epsilon_{ZZ} \end{bmatrix} \begin{bmatrix} \cos\Gamma_I \cos\Lambda_I & -\sin\Gamma_I & -\cos\Gamma_I \sin\Lambda_I \\ \sin\Gamma_I \cos\Lambda_I & \cos\Gamma_I & -\sin\Gamma_I \sin\Lambda_I \\ \sin\Lambda_I & 0 & \cos\Lambda_I \end{bmatrix} \begin{Bmatrix} 0 \\ U_E + |\Omega_{EI} \times r| \\ U_N \end{Bmatrix} \tag{24}$$

Thus,

$$\begin{Bmatrix} u' \\ v' \\ w' \end{Bmatrix} = \begin{Bmatrix} u - U_{X_B} \\ v - U_{Y_B} \\ w - U_{Z_B} \end{Bmatrix} \tag{25}$$

The angle of attack and sideslip angle are defined as

$$\alpha = \tan^{-1}(w'/u') \tag{26}$$

$$\beta = \tan^{-1}(v'/u') \tag{27}$$

(g) *Aerodynamic Forces and Moments*

$$F_{X_B} = -\bar{q}SC_D \tag{28}$$

$$F_{Y_B} = \bar{q}S(\partial C_N/\partial\beta)\beta \tag{29}$$

$$F_{Z_B} = \bar{q}S(\partial C_N/\partial\alpha)\alpha \tag{30}$$

$$M^F_{X_B} = F_{Z_B}\Delta_Y - F_{Y_B}\Delta_Z \tag{31}$$

$$M^F_{Y_B} = F_{Z_B}(\bar{X}_{c.p.} - \bar{X}_{c.g.}) + F_{X_B}\Delta_Z - C_{M_q}(\bar{q}Sb^2/u')q \tag{32}$$

$$M^F_{Z_B} = -F_{Y_B}(\bar{X}_{c.p.} - \bar{X}_{c.g.}) - F_{X_B}\Delta_Y - C_{M_r}(\bar{q}Sb^2/u')r \tag{33}$$

where $$\bar{q} = (1/2)\rho(V'_{c.g.})^2 \tag{34}$$

(h) *Bending Moment Equation*

A separate computer program solves for the bending moment in terms of the six-dimensional parameters, the mass distribution, and the quasi-steady aerodynamic properties. Let $M_{Y_B}(\bar{x}, t)$ and $M_{Z_B}(\bar{x}, t)$ represent the components of the bending moment at missile station $\bar{x}$ and flight time t; then

$$M_{Y_B}(\bar{x}, t) = M_{I\alpha}\alpha + M_{Iq}q + M_{I\dot{q}}\dot{q} + M_{IA_{Z_B}}A_{Z_B} + M^T_{Y_B}(\bar{x}, t) \tag{35}$$

$$M_{Z_B}(\bar{x}, t) = M_{I\beta}\beta + M_{Ir}r + M_{I\dot{r}}\dot{r} + M_{IA_{Y_B}}A_{Y_B} + M^T_{Z_B}(\bar{x}, t) \tag{36}$$

The terms $M^T_{Y_B}(\bar{x}, t)$ and $M^T_{Z_B}(\bar{x}, t)$ represent the contribution of the control system to the bending moment, and are zero for missile stations forward of the control elements. The unit moments appearing in Eqs. (35) and (36) are

$$M_{I\alpha}(\bar{x}, t) = \bar{q}S\int_0^{\bar{x}}\int_0^{\bar{x}_1} \frac{\partial C_N(\bar{x}_2)}{\partial\alpha}\,d\bar{x}_2\,d\bar{x}_1 \tag{37}$$

$$M_{I\beta}(\bar{x}, t) = \bar{q}S\int_0^{\bar{x}}\int_0^{\bar{x}_1} \frac{\partial C_N(\bar{x}_2)}{\partial\beta}\,d\bar{x}_2\,d\bar{x}_1 \tag{38}$$

$$M_{Iq}(\bar{x}, t) = M_{Ir}(\bar{x}, t) = \int_0^{\bar{x}}\int_0^{\bar{x}_1} m(\bar{x}_2)(\bar{x}_{c.g.} - \bar{x}_2)d\bar{x}_2\,d\bar{x}_1 \tag{39}$$

$$M_{I\dot{q}}(\bar{x}, t) = -\frac{\bar{q}s}{\mathbf{V}'_{c.g.}}\int_0^{\bar{x}}\int_0^{\bar{x}_1} \frac{\partial C_N(\bar{x}_2)}{\partial\alpha}\,(\bar{x}_2 - \bar{x}_{c.g.})d\bar{x}_2\,d\bar{x}_1 \tag{40}$$

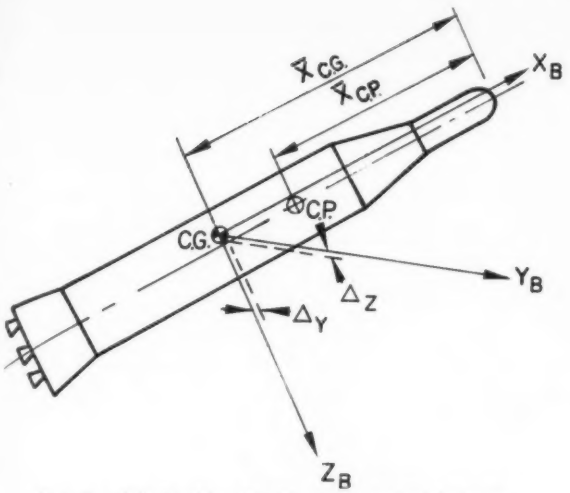

FIG. 2. Relationship of body axes to geometrical axes.

$$M_{I_F}(\bar{x}, t) = -\frac{\bar{q}s}{V'_{c.g.}} \int_0^{\bar{x}} \int_0^{\bar{x}_1} \frac{\partial C_N(\bar{x}_2)}{\partial \beta} (\bar{x}_2 - \bar{x}_{c.g.})\, d\bar{x}_2\, d\bar{x}_1 \quad (41)$$

$$M_{IA_{Y_B}}(\bar{x}, t) = M_{IA_{Z_B}}(\bar{x}, t) = \int_0^{\bar{x}} \int_0^{\bar{x}_1} m(\bar{x}_2)\, d\bar{x}_2\, dx_1 \quad (42)$$

where $\bar{x}_1$ and $\bar{x}_2$ are dummy variables.

(i) *Linearity Check*

The nonstationary statistical methods employed in this paper apply only to linear systems. An examination of the foregoing motion and bending moment equations indicates that they are nonlinear. However, owing to the linearized control system and the small motions involved, the bending moment response is essentially linear over a reasonable range of wind-velocity inputs. To verify this, the following linearity check was performed.

Let $M_1(\bar{x}, t)$ denote either the Y_B or Z_B component of the bending moment due to the one-dimensional wind input $U_1(h)$.

Let M_2 denote the corresponding response due to U_2.

By definition the system is linear if, for all combinations of U_1 and U_2, the input $U_1 + U_2$ produces the output $M_1 + M_2$. Obviously, only a finite number of combinations of U_1 and U_2 can actually be tried. Consequently, the missile system of Section 6 was subjected to inputs of the form $U_1 = a_1 \mathfrak{M}_U$ and $U_2 = a_2 \mathfrak{M}_U$, where $\mathfrak{M}_U$ is the average wind velocity at Patrick AFB (Table 1).

For inputs of this form, the rigid-body motion and the bending moment response were found to be essentially linear throughout the altitude region of interest (25,000 to 45,000 ft.) and over the range of wind inputs ($0 < a_1 + a_2 < 3.0$). Larger values of $a_1 + a_2$ were not tried. These results were construed as sufficient proof of linearity for purposes of the present study.

(5) Analysis

If it is assumed that the wind-velocity probability density function has the form of Eq. (A-10) (normally distributed), and if it is shown either analytically or experimentally that the equations of motion are linear, then it follows that the response is also normally distributed. Thus, it is only necessary to compute the average and covariance in order to define the probability distribution of the bending moment response. Throughout this section the bending moment response refers to the bending moment at a particular missile station.

(a) *Average*

For a linear system the average response is merely the response to the average input. On a high-speed computer this is a simple matter of making one run to obtain the performance parameters and an additional run per altitude to compute the bending moment distribution over the missile. However, to formulate the problem mathematically the unit-impulse response is introduced with the flight altitude as the independent variable.

Let $G(H, h)$ denote the bending moment response at altitude H due to a unit-impulse wind velocity at altitude h. Then

TABLE 4

Covariance of Resultant Wind Velocity (ft./sec.)² at Indicated Altitudes

Altitude (ft)	0	6,562	13,124	19,686	26,248	32,810	39,372	45,934	52,496	59,058	65,620	72,182	78,744	85,306
0	284.82	311.33	301.84	317.07	329.09	353.91	257.72	119.51	103.26	76.93	24.49	4.26	−8.53	16.43
6,562		1032.64	894.43	968.30	1065.30	1092.80	946.27	778.51	621.23	356.04	103.15	35.57	193.00	208.24
13,124			1619.48	1508.49	1674.82	1777.52	1565.70	1341.75	1044.89	662.41	283.59	143.12	232.15	342.72
19,686				2896.28	2460.97	2632.76	2619.62	1985.02	1502.25	971.77	366.11	229.75	226.59	440.55
26,248					4575.44	3794.65	3452.86	2795.11	2127.93	1396.22	542.75	188.15	285.19	563.77
32,810						7364.20	4665.77	3666.52	2541.39	1678.25	620.61	498.62	403.56	649.94
39,372							8448.36	4381.40	3054.86	1935.47	651.17	432.20	337.15	596.25
45,934								6559.73	3027.64	1928.61	639.53	269.18	317.84	381.32
52,496									4048.31	1786.00	863.43	514.55	384.64	416.21
59,058										2803.86	864.15	407.87	476.19	530.15
65,620											1746.14	647.41	623.66	684.86
72,182												1550.86	860.32	836.05
78,744													2036.60	1263.37
85,306														2105.07

TABLE 5

Square Root of Resultant Wind Velocity Covariance
(Table 4)

Altitude (ft)	0	6,562	13,124	19,686	26,248	32,810	39,372	45,934	52,496	59,058	65,620	72,182	78,744	85,306
0	14.98	5.42	3.57	2.69	2.19	2.14	1.09	−0.35	−0.15	0.22	0.14	0.04	−0.53	−0.28
6,562		26.96	9.94	7.66	6.80	5.48	3.83	3.27	3.13	1.22	−0.22	−0.65	1.95	1.29
13,124			32.09	12.27	10.74	9.20	6.51	6.20	5.29	3.08	1.50	0.41	1.45	2.23
19,686				43.99	15.62	13.36	12.87	8.77	7.02	4.44	1.44	1.17	0.66	2.57
26,248					56.17	20.52	15.92	12.73	10.46	6.79	2.61	−0.37	0.89	3.22
32,810						75.32	22.11	16.77	11.04	7.34	2.36	2.92	1.61	3.00
39,372							81.92	21.43	14.70	8.90	2.33	1.92	9.30	2.54
45,934								71.60	16.94	10.39	2.70	0.44	1.25	0.88
52,496									55.05	11.79	6.20	3.77	1.87	1.33
59,058										47.57	7.41	2.51	3.33	3.44
65,620											38.91	6.55	5.38	6.11
72,182												36.42	8.88	8.25
78,744													41.48	13.47
85,306														42.01

$$\mathfrak{M}_M(H) = \int_0^H G(H, h)\mathfrak{M}_U(h)\, dh \tag{43}$$

where $\mathfrak{M}_U(h)$ is the average one-dimensional wind velocity versus altitude (Table 1) and $\mathfrak{M}_M(H)$ is the average bending moment response at altitude H.

It should be remembered that Eq. (43) represents the rigid-body response due to the wind input and does not include the effects of (1) high-frequency turbulence which is beyond the frequency range of the wind measurement, and (2) structural elasticity.

Eq. (43) can be written in matrix form as

$$\{\mathfrak{M}_M\} = \Delta h[G]\{\mathfrak{M}_U\} \tag{44}$$

where $G_{rs} = G(H_r, h_s)$.

(b) *Covariance*

The covariance of the bending moment response is

$$R_{MM}(H_r, H_s) = \int_0^{H_r} G(H_r, h_r)\, dh_r \int_0^{H_s} G(H_s, h_s) \times R_{UU}(h_r, h_s)\, dh_s \tag{45}$$

where $R_{UU}(h_r, h_s)$ is the covariance of the one-dimensional wind velocity (Table 4). Eq. 45 is the integral form of a typical element of the covariance matrix

$$[R^{MM}] = \Delta h^2[G][R^{UU}][G]^T \tag{46}$$

Physically the covariance element $R_{MM}(H_r, H_s)$ represents the average product of the bending moment at altitude H_r with the bending moment at H_s. A more familiar statistical quantity is the variance. The variance at a particular altitude is given by the corresponding diagonal element of $[R^{MM}]$; e.g., $R_{rr}{}^{MM} = R_{MM}(H_r, H_r) = \sigma^2{}_{M(H_r)}$.

Unlike the average response, the solution of Eq. (46) for the covariance is difficult to obtain even with a high-speed computer. One possibility would be to apply a series of "pulses" to the system in order to generate the G matrix. Other schemes for solving Eq. (46) have also been proposed; one of the most interesting, if not the most practical, is described below.

The input covariance matrix $[R^{UU}]$ is factored into two identical and symmetrical matrices so that

$$[R^{UU}] = [R^{UU}]^{1/2}[R^{UU}]^{1/2} \tag{47}$$

Substituting into Eq. (46),

$$[R^{MM}] = \Delta h^2[G][R^{UU}]^{1/2}[R^{UU}]^{1/2}[G]^T \tag{48}$$

Since $[R^{UU}]^{1/2}$ is symmetrical,

$$[R^{UU}]^{1/2}[G]^T = \left[[G][R^{UU}]^{1/2}\right]^T \tag{49}$$

Let
$$[W] = \Delta h[G][R^{UU}]^{1/2} \tag{50}$$

then
$$[R^{MM}] = [W][W]^T \tag{51}$$

From Eq. (50) one can observe that the first column of the W matrix is the bending moment response to the first row or column of $[R^{UU}]^{1/2}$. The second column is the response to the second row or column, etc. From a computing standpoint the rows or columns of $[R^{UU}]^{1/2}$ closely resemble individual wind soundings; consequently, the computer program of reference 8 is well suited to solving for the rigid-body response. A separate computer program which solves the bending moment equation is then employed in completing the formulation of the W matrix. Finally, the covariance

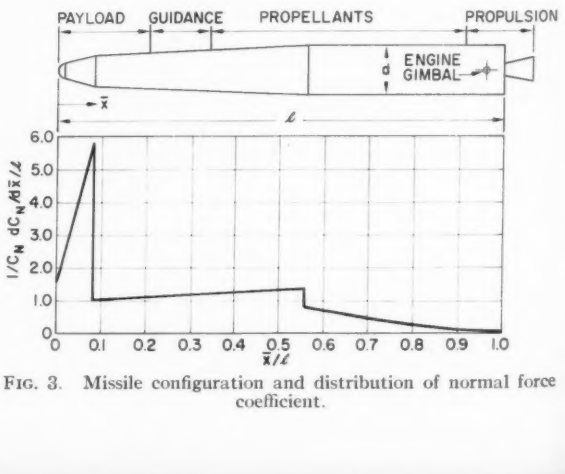

FIG. 3. Missile configuration and distribution of normal force coefficient.

of the bending moment is obtained by performing the matrix multiplication indicated by Eq. (51).

The derivation of the square-root matrix is shown in Appendix B. It turns out that the square-root matrix is a function of the eigenvalues and eigenvectors of the input covariance. (These eigenvalues and eigenvectors are not to be confused with the natural modes and frequencies of the system.) The square root of the Patrick AFB one-dimensional wind covariance matrix (Table 4) is shown in Table 5.

(c) *Extreme Values*

For obvious reasons, structures are usually designed to an extreme or infrequently occurring value of the applied load. Since the normality of the structural response in the present problem has already been established, the probability of not exceeding the extreme-value bending moment $\bar{M}$ at a particular altitude H_r is

$$P[M(H_r) < \bar{M}] = \int_{-\infty}^{\bar{M}} p_G[M(H_r)]\, dM(H_r) = \int_{-\infty}^{\bar{M}} \frac{1}{\sqrt{2\pi}\,\sigma_{M(H_r)}} \exp\left(\frac{-[M(H_r) - \mathfrak{M}_{M(H_r)}]^2}{2\sigma^2_{M(H_r)}}\right) \times dM(H_r) \quad (52)$$

where the average response $\mathfrak{M}_{M(H_r)}$ is give by Eq. (43) and the variance $\sigma^2_{M(H_r)}$ is the $R_{rr}{}^{MM}$ element of the covariance matrix as given by Eq. (46).

Letting

$$\bar{M} = \mathfrak{M}_{M(H_r)} + n_P \sigma_{M(H_r)} \quad (53)$$

the probability P associated with the coefficient n_P can be obtained from normal distribution tables;[7] e.g., for $P[\bar{M}(H_r) < \bar{M}] = 0.99$, $n_P = 2.33$. In the event that the probability of not exceeding the extreme value $\bar{M}$ at any of the altitudes $h_1, h_2, \ldots, h_n$ during a particular flight is required, then the integration problem becomes much more cumbersome, viz.:

$$P[M(H_1) < \bar{M}, \ldots, M(H_n) < \bar{M}] = \int_{-\infty}^{\bar{M}} \cdots \int_{-\infty}^{\bar{M}} p_G\,[M(H_1), \ldots, M(H_n)] \times dM(H_1) \ldots dM(H_n) \quad (54)$$

where the multivariate normal density function has the same form as Eq. (A-10):

$$p_G[M(H_1) \ldots M(H_n)] = \frac{1}{(\sqrt{2\pi})^n |R^{MM}|^{1/2}} \exp\left\{-\frac{1}{2}\sum_{r=1}^{r=n}\sum_{s=1}^{s=n}(R_{rs}{}^{MM})^{-1} \times [M(H_r) - \mathfrak{M}_{M(H_r)}]\,[M(H_s) - \mathfrak{M}_{M(H_s)}]\right\} \quad (55)$$

(d) *Design Criteria*

A special case of the extreme-value problem which is worthy of note occurs if the maximum response always occurs at the same flight time or altitude. In this event, the probability of not exceeding the extreme value $\bar{M}$ at any altitude reduces to the one-dimensional form of Eq. (52). Assuming that a critical altitude H_c exists, then

$$P[M(H) < \bar{M}] = \int_{-\infty}^{\bar{M}} p[M(H_c)]\, dM(H_c) \quad (56)$$

where $p[(M(H_c)]$ is the probability density function of the bending moment at H_c. For vertical-rising ballistic missiles launched at Patrick AFB, the load response does in fact possess a characteristic maximum in the region of 35,000 ft. This is due to the combination of maximum dynamic pressure (which also occurs in the region of 35,000 ft.) and the consistent characteristic profile of the jetstream-type winds. Consequently, the solution of extreme-value design loads by Eq. (56) is proposed as a design criterion for the Patrick AFB launch site. Since the critical altitude as originally defined does not actually exist, it is redefined as the altitude at which the maximum standard deviation occurs.

(6) Results

The methods developed in the previous section have been applied in obtaining the average, standard deviation, and extreme-value bending moments for an axially symmetric, vertical-rising ballistic missile of the IRBM class. For the one-dimensional input of this study (Section 3), and neglecting the minor effect of the earth's rotation at Patrick AFB, only motion in the vertical plane containing the wind velocity was excited. The computations involved were carried out using the digital-computer programs already mentioned.

A schematic of the vehicle configuration, along with a typical supersonic normal-force distribution, is shown in Fig. 3. Control in the plane of motion (pitch plane) is maintained by the gimballed booster engine. The percentage of the gross launch weight for each section is:

Payload	7.36
Guidance	0.96
Propellants	86.03
Propulsion	5.65

The performance parameters of Mach number, forward acceleration, and dynamic pressure are plotted versus flight time in Fig. 4, along with altitude and the average wind velocity at Patrick AFB. Maximum dynamic pressure is seen to occur at approximately 61 sec. and 33,000 ft.

The most significant parameters in Eq. (35) (bending moment equation) are angle of attack, booster-engine angle, and normal acceleration. The average and the standard deviation of these three parameters are plotted versus flight time in Figs. 5, 6, and 7. It is interesting to note that the maximum response occurs in the vicinity of maximum dynamic pressure (t = 61 sec.), even though the average wind input peaks a few seconds later (t = 67.5 sec.). Also, there is a marked similarity between the average and the standard deviation of each parameter.

By solving Eqs. (44) and (46) for a large number of missile stations, the average and the standard deviation

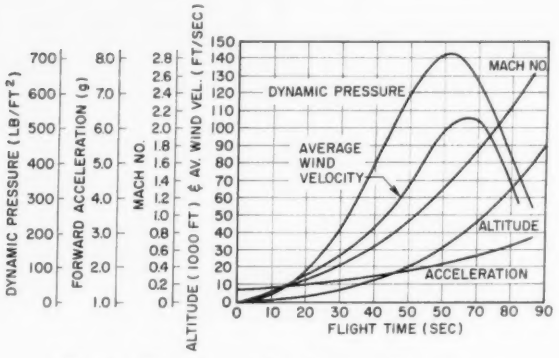

FIG. 4. Time history of performance parameters.

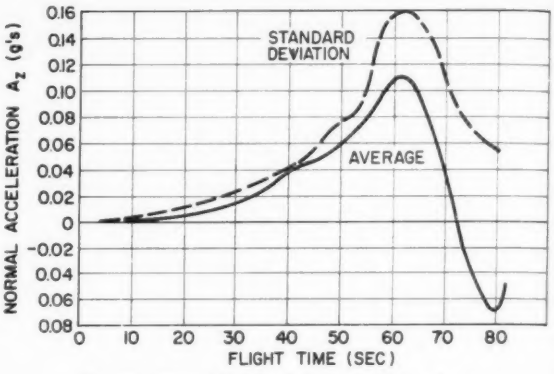

FIG. 7. Time history of normal acceleration.

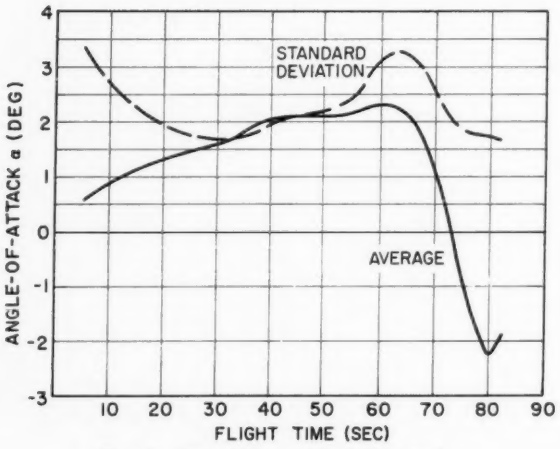

FIG. 5. Time history of angle of attack.

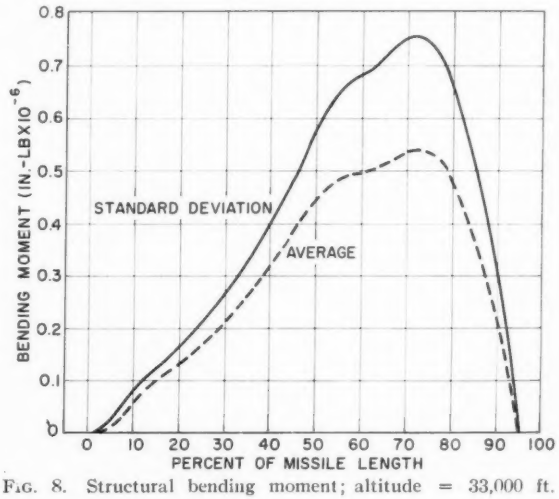

FIG. 8. Structural bending moment; altitude = 33,000 ft.

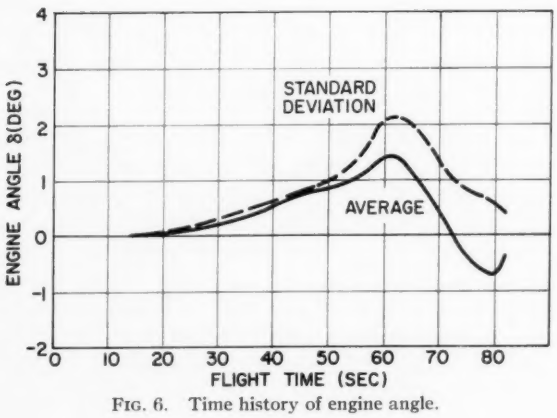

FIG. 6. Time history of engine angle.

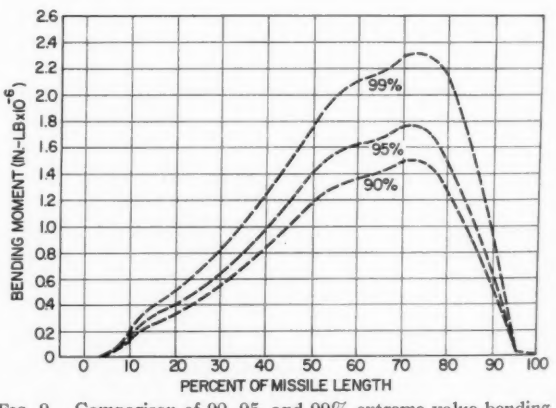

FIG. 9. Comparison of 90, 95, and 99% extreme value bending moments; altitude = 33,000 ft.

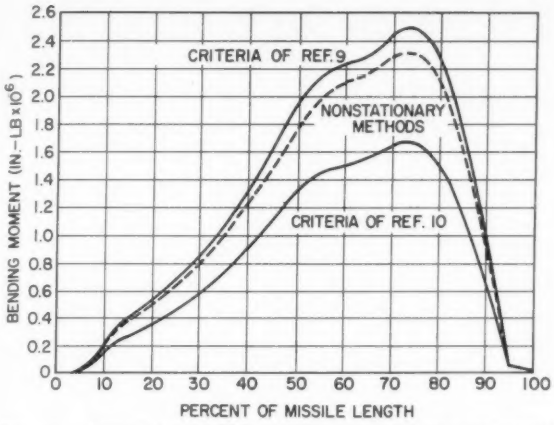

FIG. 10. Comparison of 99% extreme-value bending moments; altitude = 33,000 ft.

of the bending moment as functions of the percent of missile length were established. In Fig. 8 the average and the standard deviation at the critical altitude of 33,000 ft. are shown. The 90, 95, and 99% extreme-value design bending moments obtained by Eq. (56) are shown in Fig. 9 (i.e., from Fig. 8, the average plus n_P times the standard deviation).

In Fig. 10 the 99% design bending moments as obtained by the discrete profile design criteria of references 9 and 10 are compared with the 99% curve of Fig. 9. In reference 9, the extreme wind velocities are combined with extreme wind shears (rate of change of wind velocity with altitude) in a prescribed way in arriving at a critical wind profile. The criterion of reference 10 was intended primarily for guidance system design; however, the bending moment response due to the 99% Patrick AFB profile was computed for comparison purposes. No special significance should be attached to the close agreement between the results obtained by nonstationary methods and those obtained by the criterion of reference 9 (upper curve). For a different missile system, considerable disagreement could occur.

Appendix A
Statistical Description of Wind Velocity

A statistical description of the N-S and E-W components of the winter-season winds at Patrick AFB as given in reference 6 is reproduced in Tables 1, 2, and 3. The covariance of the one-dimensional wind discussed in Section 3 and the square root of this matrix as discussed in Section 5 are shown in Tables 4 and 5.

In order to illustrate the average techniques involved in reducing wind measurements to the form of average and covariance matrices, consider a set of one-dimensional wind soundings as shown in Fig. 11.

(a) *Average*

The sample average or expected value of the wind velocity at any altitude h is defined as

$$\tilde{\mathfrak{M}}_U(h) = \tilde{E}[U(h)] = \frac{1}{I}\sum_{i=1}^{i=I} U_i(h) \qquad \text{(A-1)}$$

whereas the true average is defined as

$$\mathfrak{M}_U(h) = E[U(h)] = \int_{-\infty}^{\infty} U(h)\, p[U(h)]\, dU(h) \qquad \text{(A-2)}$$

where $p[U(h)]$ is the probability density function of $U(h)$.

The sample average and true average will be used interchangeably, which implies that

$$\tilde{\mathfrak{M}}_U(h) \approx \mathfrak{M}_U(h) \qquad \text{(A-3)}$$

(b) *Covariance*

Let

$$U'(h) = U(h) - \tilde{\mathfrak{M}}_U(h) \qquad \text{(A-4)}$$

Then

$$\tilde{R}_{UU}(h_r, h_s) = \tilde{E}[U'(h_r)U'(h_s)] = \frac{1}{I}\sum_{i=1}^{i=I} U'_i(h_r)\, U'_i(h_s) \qquad \text{(A-5)}$$

Again, the sample covariance will be used interchangeably with the true covariance, i.e.,

$$\tilde{R}_{UU}(h_r, h_s) \approx R_{UU}(h_r, h_s) \qquad \text{(A-6)}$$

(c) *Variance and Standard Deviation*

The variance is a special case of the covariance and is usually denoted by σ^2, e.g.,

$$\sigma^2_{U(h_r)} = R_{UU}(h_r, h_r) \qquad \text{(A-7)}$$

The standard deviation is the square root of the variance:

$$\sigma_{U(h_r)} = \sqrt{R_{UU}(h_r, h_r)} \qquad \text{(A-8)}$$

(d) *Correlation Coefficient*

The correlation coefficient is a normalized covariance:

$$\rho_{UU}(h_r, h_s) = [R_{UU}(h_r, h_s)]/[\sigma_{U(h_r)}\sigma_{U(h_s)}] \qquad \text{(A-9)}$$

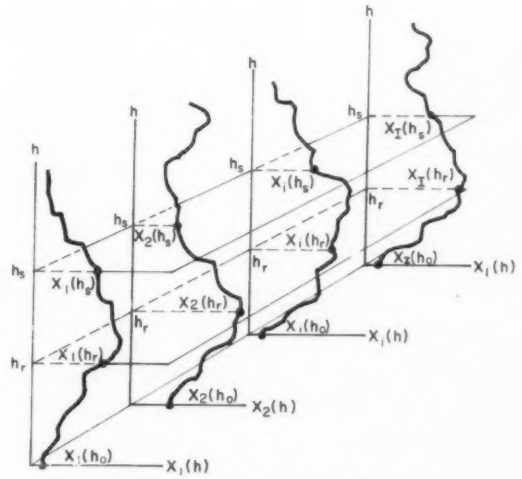

FIG. 11. Wind velocity sample space.

(e) *Normal Probability Distribution*

Assuming the model wind process is normally distributed, then the joint probability density function at altitudes $h_1, \ldots, h_n$ is given by

$$p_G[U(h_1), \ldots, U(h_n)] = \frac{1}{(\sqrt{2\pi})^n \left| R^{UU} \right|^{1/2}} \times \exp\left\{ -\frac{1}{2} \sum_{r=1}^{r=n} \sum_{s=1}^{s=n} (R_{rs}^{UU})^{-1} U'(h_r) U'(h_s) \right\} \quad \text{(A-10)}$$

where $\left| R^{UU} \right|^{1/2}$ is the square root of the determinate of the $n \times n$ covariance matrix $[R^{UU}]$, and $(R_{rs}^{UU})^{-1}$ is the rs element of the inverse covariance matrix $[R^{UU}]^{-1}$.

Appendix B
Derivation of Square Root Matrix

In Section 4, the input matrix $[R^{UU}]$ was factored into the product of two identical matrices $[R^{UU}]^{1/2}$. This derivation follows from the so-called modal matrix equations (e.g., reference 11).

If $[R]$ is a real and symmetrical matrix, then

$$[R][\Xi] = [\Xi]\lceil D \rfloor \quad \text{(B-1)}$$

where $\lceil D \rfloor$ is a diagonal matrix of the eigenvalues $d_1, d_2, \ldots, d_n$ obtained by solving the determinant

$$\left| [R] - d[I] \right| = 0 \quad \text{(B-2)}$$

$[\Xi]$ is a matrix of eigenvectors with columns $\Xi_1, \Xi_2, \ldots, \Xi_n$. The eigenvector corresponding to the d_i eigenvalue is

$$[R]\{\Xi_i\} = d_i\{\Xi\} \quad \text{(B-3)}$$

From Eq. (B-1) $$[R] = [\Xi]\lceil D \rfloor [\Xi]^{-1} \quad \text{(B-4)}$$

since $$[R] = [R]^T \quad \text{(B-5)}$$

It follows that Ξ is orthogonal:

$$[\Xi]^{-1} = [\Xi]^T \quad \text{(B-6)}$$

Substituting in Eq. (B-4),

$$[R] = [\Xi]\lceil D \rfloor [\Xi]^T \quad \text{(B-7)}$$

Introducing the matrices

$$\lceil D \rfloor^{1/2} \lceil D \rfloor^{1/2} = \lceil D \rfloor \quad \text{(B-8)}$$

where

$$\lceil D \rfloor^{1/2} = \begin{bmatrix} \sqrt{d_1} & & & \\ & \sqrt{d_2} & & \\ & & \ddots & \\ & & & \sqrt{d_n} \end{bmatrix} \quad \text{(B-9)}$$

and $$[R]^{1/2}[R]^{1/2} = [R] \quad \text{(B-10)}$$

Eq. (B-7) can now be written:

$$[R]^{1/2}[R]^{1/2} = [[\Xi]\lceil D \rfloor^{1/2}[\Xi]^T]\,[[\Xi]\lceil D \rfloor^{1/2}[\Xi]^T] \quad \text{(B-11)}$$

Thus $$[R]^{1/2} = [\Xi]\lceil D \rfloor^{1/2}[\Xi]^T \quad \text{(B-12)}$$

There are a number of square roots of $[R]$, since the square root of the eigenvalues can be positive or negative. In fact, there are at least 2^n matrices that will satisfy Eq. (B-10). The positive roots of d were used in computing the square-root matrix shown in Table 5. The eigenvalues and eigenvectors were obtained with the aid of a digital computer.

References

[1] Crane, H. L., *Measurement of Atmospheric Turbulence Over a Wide Range of Wavelengths for One Meteorological Condition*, NACA TN 3702, 1956.

[2] Press, H., *A Re-Evaluation of Data on Atmospheric Turbulence and Airplane Gust Loads for Application in Spectral Calculations*, NACA Report 1272, 1956.

[3] Liepmann, H. W., *On the Spectrum of Isotropic Turbulence*, NACA TN 2473, 1951.

[4] Weather Bureau, U.S. Department of Commerce, *Daily Series, Synoptic Weather Maps. Part II: Northern Hemisphere Data Tabulations.*

[5] Charles, B. N., *The U.S. Weather Bureau: Sandia Corporation Cooperative Project in Climatology*, Sandia Corporation TM 302-351 (51), 1957.

[6] Court, Arnold, *Vertical Correlation of Wind Components*, AFCRC-TN-57-292, March 29, 1957.

[7] Mood, A. M., *Introduction to the Theory of Statistics*, McGraw-Hill Book Co., Inc., New York, 1950.

[8] Williams, J. J., *Generalized Six Degrees of Freedom of Flight Loads Analysis*, LMSD-2923, 1958.

[9] Williams, J. J., *Design Wind Criteria for Air Force Missile Test Center*, LMSD-2933, 1958.

[10] Sissenwine, N., *Windspeed Profile, Windshear, and Gusts for Design of Guidance Systems for Vertical Rising Air Vehicles*, Air Force Surveys in Geophysics, No. 57, 1954.

[11] Bodewig, E., *Matrix Calculations*, North-Holland Publishing Co., Amsterdam, 1956.

An Authorized Binding for
Journal of the Aerospace Sciences

Arrangements have been made by the Institute of the Aerospace Sciences for members and subscribers to have their Journals bound carefully and economically. Simply write for details to:

Publishers' Authorized Bindery Service Ltd., 430 West Erie St., Chicago 10, Ill.

Vibration of Stepped Beams

N. J. TALEB* AND E. W. SUPPIGER**
Princeton University

Summary

Some results from the theory of integral equations, applicable to the problem of free lateral vibration of beams, are presented and the Cauchy function method is utilized in the solution, by successive approximations, for the lowest frequency and modal configuration of a stepped beam. The results are then compared to the exact solution based on the differential equation of motion.

Symbols

x, y	=	rectangular coordinates
E	=	modulus of elasticity
$I = I(x)$	=	moment of inertia of cross section
γ	=	weight per unit volume
$A = A(x)$	=	cross-sectional area
g	=	gravitational acceleration
t	=	time
l	=	span of beam
X	=	normal function for beam
T	=	function of time
p_i	=	circular frequency for the ith mode
$L(X)$	=	differential operator
$G(x,s)$	=	Green's function
$H(x,s)$	=	Cauchy's function
$f_0(x)$	=	generating function
$f_n(x)$	=	the nth iterated function of x
a, b, c, d, K	=	constants

(1) Formulation of the Problem

THE DIFFERENTIAL EQUATION[1] for the free lateral vibration of a beam is

$$\frac{\partial^2}{\partial x^2}\left(EI\frac{\partial^2 y}{\partial x^2}\right) = -\frac{\gamma A}{g}\frac{\partial^2 y}{\partial t^2}$$

One assumes $y = y(x,t) = X(x)T(t)$, with $T(t)$ a harmonic function of time; the problem then is to find the circular frequencies p and the functions X that satisfy

$$\frac{d^2}{dx^2}\left(EI\frac{d^2X}{dx^2}\right) = p^2\frac{\gamma A}{g}X \qquad (1)$$

and the boundary conditions, i.e., for built-in ends,

$$X = 0, \quad X' = dX/dx = 0 \qquad (x = 0,\ x = l)$$

for hinged ends,

$$X = 0, \quad IX'' = I\,(d^2X/dx^2) = 0 \qquad (x = 0,\ x = l)$$

for free ends,

$$IX'' = 0, \quad (d/dx)(IX'') = 0 \qquad (x = 0,\ x = l)$$

Eq. (1) may be written as

$$L(X) + \lambda m(x)X = 0 \qquad (2)$$

where $L(X)$ is the differential expression of Eq. (1), $\lambda = p^2$, and $m(x) = -\gamma A/g$. It is known that the only values of λ for which Eq. (2) has a solution $X(x)$ valid for $0 \le x \le l$, and satisfying the boundary conditions, are the eigenvalues λ of the integral equation

$$X(x) = \lambda\int_0^l G(x,s)\,m(s)\,X(s)\,ds \qquad (3)$$

where $G(x,s)$ is the Green's function of $L(X)$ and its boundary conditions. The $G(x,s)$ here is the deflection of the beam at section x due to the application of a unit load at section s, and it is evident that this function satisfies the boundary conditions. It is also known that the λ are positive, real, and infinite in number and that the eigenfunctions X that correspond to the λ are unique.

(2) Cauchy Function Method

Only the essential elements of this method are outlined here; for proofs and details the reader is referred to Temple.[2] Our purpose is to illustrate how the method may be applied, as a practical iteration method, in the solution of the beam vibration problem.

We may define

$$f_n(x) = (f_{n-1},G) = \int_a^b G(x,s)\,m(s)\,f_{n-1}(s)\,ds \qquad (4)$$

where (f_{n-1},G) is the solution of

$$L[f_n(x)] + m(x)f_{n-1}(x) = 0 \qquad (5)$$

The function $G(x,s)$ may be discontinuous and often necessitates tedious calculation. Another solution of Eq. (5), due to Cauchy,[3] is often simpler and proceeds as follows:

The solution of Eq. (5) may be written as

$$f_n(x) = \phi(x) + \int_{x_0}^x H(x,s)\,m(s)\,f_{n-1}(s)\,ds \qquad (6)$$

where

(i)	$L[\phi(x)] = 0$
(ii)	$L[H(x,s)] = 0$
(iii)	$H = H' = H'' = 0, \quad x = s$
(iv)	$H''' = -1, \quad x = s$

In Eq. (6), we may make every function of this set, with the possible exception of the generating function

Received August 14, 1959. Revised and received March 1, 1960.

* Consulting Engineer, Dar Al-Handasah, Beirut, Lebanon.
** Professor of Mechanical Engineering, Princeton University.

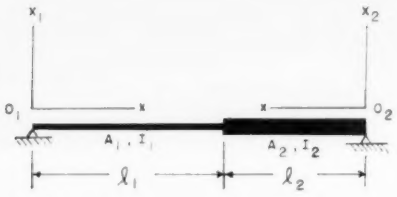

FIG. 1. Simply supported stepped beam.

$f_0(x)$, satisfy the boundary conditions and thus determine the constants in $\phi(x)$. The conditions imposed on $H(x,s)$ give the constants in $H(x,s)$.

In many engineering applications, the cross section of the beam is constant (or may so be assumed) for a certain length and then changes abruptly to another constant section. This allows us to solve $L[f_n(x)] = 0$, for each region. with relative ease. The Cauchy function method is therefore readily adaptable to stepped beams.

(3) Application to a Stepped Beam

Consider the stepped beam shown in Fig. 1. Cauchy's method will be used here only to obtain the approximate fundamental frequency and modal configuration. The method, of course, may be extended to multi-stepped beams, and to the higher modes.[4]

Eq. (1) may be written as:

$$\frac{d^2}{dx^2}\left(\frac{d^2X}{dx^2}\right) = p^2\,\frac{\gamma A_i}{EI_i g}\,X \tag{7}$$

where

$$A_i(x) = A_1, \quad I_i(x) = I_1, \quad i = 1 \qquad 0 \le x \le l_1$$

$$A_i(x) = A_2, \quad I_i(x) = I_2, \quad i = 2 \qquad 0 \le x \le l_2$$

The solution of $L(X) = d^4X/dx^4 = 0$ gives

$$X_1 = \frac{a_1x^3}{6} + \frac{b_1x^2}{2} + c_1x + d_1 \qquad 0 \le x \le l_1$$

$$X_2 = \frac{a_2x^3}{6} + \frac{b_2x^2}{2} + c_2x + d_2 \qquad 0 \le x \le l_2$$

$H(s,x)$ and $\phi(x)$ have the same form as X, as is evident from conditions (*i*) and (*ii*) of Section 2. Applying conditions (*iii*) and (*iv*), we obtain

$$H(s,s) = 0 = \frac{S_1s^3}{6} + \frac{S_2s^2}{2} + S_3s + S_4$$

$$[H'(s,x)]_{x=s} = 0 = (S_1s^2/2) + S_2s + S_3$$

$$[H'']_{x=s} = 0 = S_1s + S_2$$

$$[H''']_{x=s} = -1 = S_1$$

These four equations give

$$S_1 = -1, \quad S_2 = s, \quad S_3 = -s^2/2, \quad S_4 = s^3/6$$

hence

$$H(s,x) = -\frac{x^3}{6} + \frac{sx^2}{2} - \frac{s^2x}{2} + \frac{s^3}{6} \tag{8}$$

Eq. (6) yields

$$f_{ni}(x) = \left(\frac{a_{ni}x^3}{6} + \frac{b_{ni}x^2}{2} + c_{ni}x + d_{ni}\right) - \frac{\gamma A_i}{EI_i g}\int_0^x \left(-\frac{x^3}{6} + \frac{sx^2}{2} - \frac{s^2x}{2} + \frac{s^3}{6}\right) f_{n-1}(s)\,ds \tag{9}$$

where

$$m(s) = -\gamma A_i/EI_i g \qquad \begin{matrix} i = 1, & 0 \le x \le l_1 \\ i = 2, & 0 \le x \le l_2 \end{matrix}$$

For our choice of a generating function $f_0(x)$ we take $f_0(x) = 1$. This does *not* satisfy the boundary conditions, but the iterated calculations that follow are simple, and good accuracy is obtained after only two iterations.

Eq. (9) gives us

$$f_{1i}(x) = \frac{a_{1i}x^3}{6} + \frac{b_{1i}x^2}{2} + c_{1i}x + d_{1i} + \frac{\gamma A_i}{EI_i g}\,\frac{x^4}{24} \tag{10}$$

The boundary conditions (see Fig. 1) are

$$f_{1i}(x) = f''_{1i} = 0, \quad x = 0, \quad i = 1, 2$$

$$f_{11}(l_1) = f_{12}(l_2) \quad \text{and} \quad f'_{11}(l_1) = -f'_{12}(l_2)$$

$$I_1f''_{11}(l_1) = I_2f''_{12}(l_2)$$

and

$$(d/dx)[I_1f''_{11}]_{x=l_1} = -(d/dx)[I_2f''_{12}]_{x=l_2}$$

These eight conditions determine the eight constants in Eq. (10). The first four give

$$b_{11} = d_{11} = 0 \quad \text{and} \quad b_{12} = d_{12} = 0$$

The last four conditions give results that will be simplified by assuming from here on: $l_1 = l_2 = l/2 = h$, $A_2 = 2A_1$, $I_2 = 4I_1$ (note that for circular cross sections if $A_2/A_1 = 2$, then $I_2/I_1 = 4$). Therefore,

$$\frac{a_{11}h^3}{6} + c_{11}h + \frac{\alpha h^4}{24} = \frac{a_{12}h^3}{6} + c_{12}h + \frac{\alpha h^4}{48}$$

$$\frac{a_{11}h^2}{2} + c_{11} + \frac{\alpha h^3}{6} = -\left(\frac{a_{12}h^2}{2} + c_{12} + \frac{\alpha h^3}{12}\right)$$

$$I_1\left(a_{11}h + \frac{\alpha h^2}{2}\right) = I_2\left(a_{12}h + \frac{\alpha h^2}{4}\right)$$

$$I_1(a_{11} + \alpha h) = -I_2\left(a_{12} + \frac{\alpha h}{2}\right)$$

wherein $\alpha = \gamma A_1/EI_1g$. The solution yields

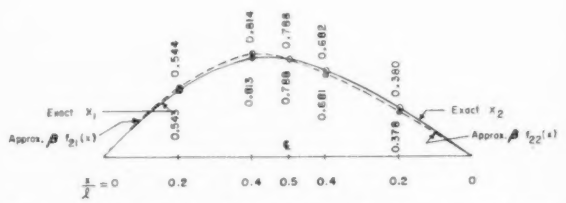

FIG. 2. First modal configuration. Exact vs. approximate solutions.

$$a_{11} = -1.2500\,\alpha h, \qquad a_{12} = -0.43750\,\alpha h$$

$$c_{11} = 0.35416\,\alpha h^3, \qquad c_{12} = 0.23958\,\alpha h^3$$

Eq. (10) becomes

$$f_{11}(x) = \alpha(-0.20833\,hx^3 + 0.35416\,h^3x + 0.04167\,x^4)$$

$$f_{12}(x) = \alpha(-0.07292\,hx^3 + 0.23958\,h^2x + 0.02083\,x^4)$$

We now calculate for this beam, using the generating function $f_0(x) = 1$:

$$(f_0, f_0) = \frac{\gamma}{g}\int_0^h A_1 f_0^2(x)\,dx + \frac{\gamma}{g}\int_0^h A_2 f_0^2(x)\,dx = \frac{3A_1\gamma l}{2g}$$

and

$$(f_0, f_1) = \frac{\gamma}{g}\int_0^h A_1 f_0(x) f_{11}(x)\,dx + \frac{\gamma}{g}\int_0^h A_2 f_0(x) f_{12}(x)\,dx = 0.01077\,\frac{A_1\gamma\alpha l^5}{g}$$

The number λ_{11} is defined as follows:

$$\lambda_{11} = (p_1^2)_1 = \frac{(f_0, f_0)}{(f_0, f_1)} = \frac{3A_1 l}{2(0.01077\,A_1\alpha l^5)} = \frac{139.3}{\alpha l^4}$$

and $\lambda_{11} > \lambda_1$ (the first eigenvalue).

The fundamental frequency (first approximation) is therefore

$$(p_1)_1/2\pi = (11.8/2\pi l^2)\sqrt{EI_1 g/\gamma A_1} \tag{11}$$

For the second approximation, we return to Eq. (9) and let $n = 2$. Thus

$$f_{2i}(x) = \left(\frac{a_{2i}x^3}{6} + \frac{b_{2i}x^2}{2} + c_{2i}x + d_{2i}\right) - \frac{\gamma A_i}{EI_i g}\int_0^x H(s,x) f_{1i}(s)\,ds \tag{12}$$

where $H(s,x)$ is given by Eq. (8) and $i = 1, 2$.

$$f_{21}(x) = \frac{a_{21}x^3}{6} + \frac{b_{21}x^2}{2} + c_{21}x + d_{21} + 0.00294\alpha^2h^3x^5 - 0.00025\alpha^2hx^7$$

$$f_{22}(x) = \frac{a_{22}x^3}{6} + \frac{b_{22}x^2}{2} + c_{22}x + d_{22} + 0.00100\alpha^2h^3x^5 - 0.00004\alpha^2hx^7$$

As before, we apply the eight boundary conditions to determine the constants. It follows that

$$\left.\begin{aligned} f_{21}(x) &= \alpha^2(-0.02544h^5x^3 + 0.04858h^7x + 0.00294h^3x^5 - 0.00025x^7) \\ f_{22}(x) &= \alpha^2(-0.00740h^5x^3 + 0.03227h^7x + 0.00100h^3x^5 - 0.00004hx^7) \end{aligned}\right\} \tag{13}$$

and

$$(f_0, f_2) = \frac{\gamma}{g}\int_0^h A_1 f_0(x) f_{21}(x)\,dx + \frac{\gamma}{g}\int_0^h A_2 f_0(x) f_{22}(x)\,dx = \frac{0.04727}{(2)^9}\,\frac{A_1\gamma\alpha^2 l^9}{g}$$

thus

$$\lambda_{12} = (p_1^2)_2 = \frac{(f_0, f_1)}{(f_0, f_2)} = \frac{0.01077(2)^9}{0.04727\alpha l^4} = \frac{116.6}{\alpha l^4}$$

or the fundamental frequency (second approximation) is

$$(p_1)_2/2\pi = (10.8/2\pi l^2)\sqrt{EI_1 g/\gamma A_1} \tag{14}$$

One may test the accuracy of this solution by substituting Eqs. (13) and (14) back into Eq. (7).

(4) Exact Solution and Comparison

The stepped beam of Fig. 1 may be solved by the exact (differential equation) method as follows, and the results compared to the above. We start with

$$l_2 \neq l_1, \quad A_2 = uA_1, \quad I_2 = vI_1$$

Eq. (1) may be written as

$$d^4X_i/dx^4 = K_i^4 X$$

where $K_i^4 = \gamma A_i p^2/EI_i g$ and $i = 1,2$. The general solution is

$$\left.\begin{aligned} X_1 &= C_1 \sin K_1x + C_2 \cos K_1x + C_3 \sinh K_1x + C_4 \cosh K_1x, \qquad 0 \le x \le l_1 \\ X_2 &= C_5 \sin K_2x + C_6 \cos K_2x + C_7 \sinh K_2x + C_8 \cosh K_2x, \qquad 0 \le x \le l_2 \end{aligned}\right\} \tag{15}$$

The boundary conditions are

$$X_1 = I_1X_1'' = 0, \quad x = 0 \qquad \therefore C_2 = C_4 = 0$$
$$X_2 = I_2X_2'' = 0, \quad x = 0 \qquad \therefore C_6 = C_8 = 0$$
$$(X_1)_{x=l_1} = (X_2)_{x=l_2} \quad \text{and} \quad (X_1')_{x=l_1} = -(X_2')_{x=l_2}$$
$$(I_1X_1'')_{x=l_1} = (I_2X_2'')_{x=l_2} \quad \text{and} \quad (d/dx)(I_1X_1'')_{x=l_1} = -(d/dx)(I_2X_2'')_{x=l_2}$$

Let: $$z = K_2/K_1 = \sqrt[4]{u/v}, \quad \sin_1 = \sin K_1l_1, \quad \sinh_1 = \sinh K_1l_1, \quad \text{etc.}$$

The last four conditions require

$$\left.\begin{aligned} &C_1 \sin_1 + C_3 \sinh_1 - C_5 \sin_2 - C_7 \sinh_2 = 0 \\ &C_1 \cos_1 + C_3 \cosh_1 + zC_5 \cos_2 + zC_7 \cosh_2 = 0 \\ &-C_1 \sin_1 + C_3 \sinh_1 + vz^2C_5 \sin_2 - vz^2C_7 \sinh_2 = 0 \\ &-C_1 \cos_1 + C_3 \cosh_1 - vz^3C_5 \cos_2 + vz^3C_7 \cosh_2 = 0 \end{aligned}\right\} \tag{16}$$

Either $C_1 = C_3 = C_5 = C_7 = 0$ (a trivial solution) or the determinant of the system must equal zero. Expanding this determinant gives the frequency equation

$$(v^2z^5 - 2vz^3 + z)(\sin_1 \sin_2 \cosh_1 \cosh_2 + \cos_1 \cos_2 \sinh_1 \sinh_2) - (v^2z^5 + 2vz^3 + z)(\cos_1 \sin_2 \sinh_1 \cosh_2 + \sin_1 \cos_2 \cosh_1 \sinh_2) - 4vz^4 \sin_1 \cos_2 \sinh_1 \cosh_2 - 4vz^2 \cos_1 \sin_2 \cosh_1 \sinh_2 = 0 \tag{17}$$

As before, we simplify the calculations from here on by assuming

$$l_1 = l_2 = l/2, \quad A_2 = 2A_1, \quad I_2 = 4I_1$$

i.e., $$u = 2, \quad v = 4, \quad z = 0.841, \quad \text{and} \quad K_2 = 0.841K_1$$

Let: $$k = K_1l_1 = K_1l/2 \quad \text{and} \quad k_0 = K_2l_2 = K_2l/2 = 0.841k$$

Eq. (17) becomes

$$2.801(1 + \cot k \cot k_0 \tanh k \tanh k_0) - 12.32 (\cot k \tanh k + \cot k_0 \tanh k_0) - 8 \cot k_0 \tanh k - 11.31 \cot k \tanh k_0 = f(k) = 0 \tag{18}$$

The differential equation method loses its charm at this point. However, the first root of Eq. (18) may be found to be $k_1 = 1.62$ and the fundamental frequency is

$$p_1/2\pi = (10.5/2\pi l^2)\sqrt{EI_1g/\gamma A_1} \tag{19}$$

Note that the *second* approximation to this frequency as computed for this beam, with a jump discontinuity, by the Cauchy function method with $f_0(x) = 1$ [see Eq. (14)] is about three per cent above the exact value given in Eq. (19). In design calculations, accuracy of this order may be acceptable. If greater accuracy is required, a third approximation may be made—or one may choose a better-fitting generating function $f_0(x)$.

Having determined the first root of Eq. (18), we may return to Eqs. (16) and obtain

$$C_3 = -0.088C_1, \quad C_5 = +0.623C_1, \quad C_7 = +0.099C_1$$

substituting these values in Eq. (15) we obtain the equation for the first normal mode:

$$\left.\begin{aligned} X_1 &= C_1 [\sin 3.24(x/l) - 0.088 \sinh 3.24(x/l)] \\ X_2 &= C_1[0.623 \sin 2.72(x/l) + 0.099 \sinh 2.72(x/l)] \end{aligned}\right\} \tag{20}$$

We now compare this exact configuration with the approximate solution given in Eqs. (13). We may choose $C_1 = 1$ and multiply Eqs. (13) by a suitable constant β so that

$$\beta(f_{21})_{x=l/2} = X_1$$

The results are shown in Fig. 2.

References

[1] Timoshenko, S., *Vibration Problems in Engineering*, D. Van Nostrand, New York, 1955.

[2] Temple, G., *The Computation of Characteristic Numbers and Characteristic Functions*, Proc London Math. Soc., Vol. 29, No. 2, 1929

[3] Goursat, E., *Cours d'Analyse Mathématique, Tome II*, Gauthier-Villars, Paris, 1949.

[4] Taleb, N. J., Ph.D. dissertation, Princeton University, 1955.

✦ ✦ ✦

Microcards for Volumes 1–5 Available

Microcards for Volumes 3–5 of the JOURNAL are now available (Vols. 1 and 2 were republished in this form earlier). All five volumes are priced at $5.50 each, and are obtainable through:

J. S. Canner & Company, Inc.
Boston, Roxbury 20, Mass.

Radiative Heat Transfer in Free-Molecule Flow†

SAUL ABARBANEL*

Massachusetts Institute of Technology

Summary

The effects of thermal radiation on the equilibrium temperatures in free-molecule flow are investigated. It is shown that when the temperature is nondimensionalized appropriately the problem possesses similitude properties. Solutions for this dimensionless temperature are found in terms of a similarity parameter. In the case of high-speed flow, the body temperature is given directly in terms of flight conditions, body geometry, and surface properties.

The effects of solar radiation and finite thermal conductivity of the body are studied both qualitatively and quantitatively.

Symbols

a = radius of a sphere or outer radius of spherical shell
a_n = coefficients in Legendre-polynomial expansion of $f(\mu)$ [see Eq. (35)]
A_n = coefficients of $P_n(\mu)$ in solution for the temperature distribution in a solid sphere of finite conductivity
b = inside radius of spherical shell
c_∞ = most probable molecular speed under free-stream conditions
C_n, D_n = coefficients of $P_n(\mu)$ in solution for the temperature distribution in a spherical shell
e = emissivity and absorptivity of a radiating solid surface
E = $E_t + E_j$ = total molecular-energy influx (ergs/sec./cm.²)
E_j = molecular-energy influx due to internal degrees of freedom
E_r = energy efflux carried by the re-emitted molecules (ergs/sec./cm.²)
E_s = energy influx due to solar radiation
E_t = translational energy flux in free-molecule flow
$\mathcal{E}$ = average dimensionless translational energy flux per molecule; defined in Eq. (2)
$f(\mu)$ = flux factor for spherical surfaces; defined by Eq. (34)
F = dimensionless overall energy-flux factor; defined by Eq. (18)
H = similarity parameter for bodies of finite thermal conductivity; defined by Eq. (25)
H_c = similarity parameter for perfect conductors; defined in Eq. (16)
H_n = similarity parameter for perfect insulators; defined in Eq. (10)
$\tilde{H}$ = similarity parameter for solid spheres; defined in Eqs. (31) and (33)
$\tilde{H}_\gamma$ = similarity parameter for spherical shell; defined in Eq. (39)
j = number of internal molecular degrees of freedom partaking in the energy exchange with a surface
J_s = solar constant = 1.46×10^6 ergs/sec./cm.² in vicinity of the earth
k = Boltzmann's constant = 1.38×10^{-16} ergs/°K.
K = thermal conductivity (ergs/cm./°K.-sec.)
l = thickness of flat plate
L = reference length
m = molecular mass
n_∞ = free-stream molecular number density (number of molecules per cc.)
N = dimensionless overall flux factor; defined in Eq. (17)
$\dot{Q}_1$ = total heat-transfer rate (ergs/sec.)
$\dot{Q}$ = dimensionless total heat-transfer rate (see Figs. 11 and 12)
r = dimensionless radial coordinate
R = dimensional radial coordinate
S = speed ratio (= U_∞/c_∞)
T = temperature (°K.)
T_b = constant temperature imposed on inner surface of spherical shell
T_c = temperature of perfect conductor
T_n = temperature of perfect insulator
U_∞ = flight speed
Z = dimensionless molecular number flux; defined by Eq. (1)
α = local angle of attack
β = semivertex angle of cone or wedge
γ = $a - b$ = thickness of spherical shell
ϵ = γ/a = ratio of spherical-shell thickness to outside radius
η = dimensionless temperature appropriate for similarity solutions
η_c = dimensionless temperature of perfect conductor appropriate for similarity solution
η_n = dimensionless temperature of perfect insulator appropriate for similarity solution
θ = polar angle in spherical coordinates
μ = $\cos\theta$
ν = molecular number flux (No. of molecules/sec./cm.²)
σ = Stefan-Boltzmann constant = 5.76×10^{-5} ergs cm.$^{-2}$ sec.$^{-1}$ °K.$^{-4}$
Φ = elevation of sun above horizon plane
χ = dimensionless parameter defined in Eq. (24)
ψ = azimuth angle of sun
ω = angle between direction of sun rays and normal to surface element
Ω = thermal accommodation coefficient of solid surface

Received January 12, 1960. Revised and received July 2, 1960.

† This research was supported by the Office of Scientific Research, USAF, whose sponsorship is gratefully acknowledged.

* Research Associate, Department of Aeronautics and Astronautics; presently a Research Fellow at the Weizmann Institute of Science, Israel.

(1) Introduction

THE PRESENT INVESTIGATION is concerned with the steady-state temperature of radiating objects in the free-molecule flow regime. There are two main reasons why radiation effects are important in free-molecule flow. The more obvious one is the fact that rarefied gases cannot support a large convective heat-

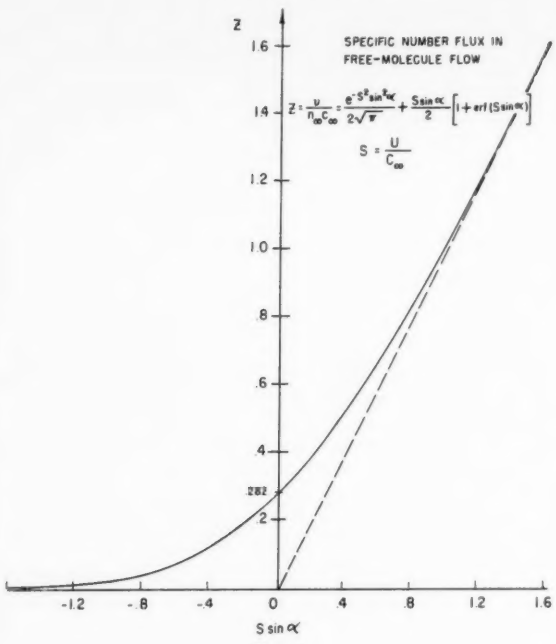

FIG. 1.

transfer rate and hence the alternate modes of energy exchange, namely, radiation and conduction, predominate. The second reason has to do with the resulting relatively low surface temperature. Recent studies by Willis[1] indicate that transitional corrections to free-molecule flow theory depend strongly on the surface temperature when the latter is low in comparison with the free-stream stagnation temperature. It is therefore of some interest to be able to predict the surface temperature and the effect of radiation on it.

The first calculations of radiation cooling in free-molecule flow were carried out by Sanger and Bredt.[2] Stalder and Jukoff[3] made numerical computations of the temperature of a radiating flat plate for various free-molecule flight conditions. In the present paper a similarity law is sought and applied to several body geometries. The form of the solution in the presence of solar radiation and finite thermal conductivity of the body is considered as well.

(2) Energy Fluxes in Free-Molecule Flow

Many of the results of this section are readily available in the literature. They are summarized briefly here in order to establish the various notations and their meanings.

Under the assumptions of free-molecule flow, the gas has a Maxwellian velocity distribution, and the number flux ν (the number of molecules incident on a unit area per second) is given by:

$$\nu = n_\infty c_\infty \left\{ [e^{-S^2 \sin^2 \alpha}/2\sqrt{\pi}] + (1/2)S \sin \alpha [1 + \mathrm{erf}\ (S \sin \alpha)] \right\} \equiv n_\infty c_\infty Z \quad (1)$$

where n_∞ is the molecular number density (cm.$^{-3}$), $c_\infty = \sqrt{2kT_\infty/m}$ is the most probable speed, k is Boltzmann's constant, m is the molecular mass, T_∞ is the free-stream temperature, α is the local angle of attack, and $S = U_\infty/c_\infty$ is the speed ratio. The parameter Z, defined by Eq. (1), is a dimensionless number flux.

The total energy influx (ergs/cm.^{2}/sec.), $E = E_t + E_j$, is composed of two parts: the translational energy flux, E_t, given by

$$E_t = \frac{mn_\infty c_\infty^3}{2} \left\{ \left(\frac{2 + S^2}{\sqrt{2\pi}} \right) e^{-S^2 \sin^2 \alpha} + \left(\frac{5 + 2S^2}{4} \right) \times S \sin \alpha \, [1 + \mathrm{erf}\ (S \sin \alpha)] \right\} \equiv (1/2) m c_\infty^2 \nu \mathcal{E} \quad (2)$$

and the energy influx due to the internal degrees of freedom, E_j,

$$E_j = (1/2) j k T_\infty \nu \quad (3)$$

where j is the number of *internal* degrees of freedom that partake in the energy exchange with the surface.

The dimensionless translational energy flux per molecule, $\mathcal{E}$, defined by Eq. (2), can be written as

$$\mathcal{E} = (5/2) + S^2 - (e^{-S^2 \sin^2 \alpha}/4\sqrt{\pi}Z) \quad (4)$$

Its asymptotic values can easily be shown to be

$$\mathcal{E} \xrightarrow[S \sin \alpha > 1]{S^2 \gg 1} S^2$$

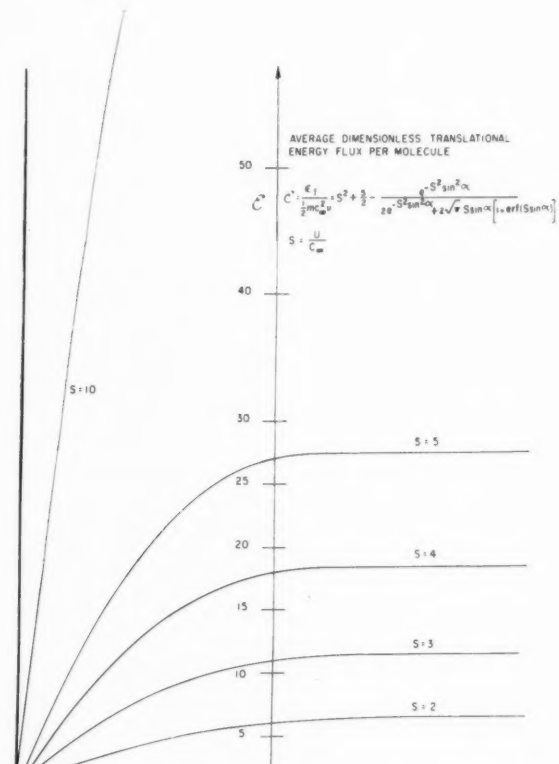

FIG. 2.

and $$\mathcal{E} \xrightarrow[S \sin\alpha < 1]{S^2 \gg 1} \frac{5}{2} + S^2 \cos^2 \alpha$$

Plots of Z and $\mathcal{E}$ are given in Figs. 1 and 2, respectively.

Following the accepted convention, it is assumed that a single thermal accommodation coefficient, Ω, governs the translational and internal degrees of freedom and is defined by

$$\Omega = (E - E_r)/(E - E_w) \tag{5}$$

where E_r is the actual energy efflux of the rebounding molecules and E_w is the energy flux that the re-emitted molecules would have carried away if they were at the wall temperature. With $E_w = (2 + 1/2\, j)kT_w\nu$, Eq. (5) can be rearranged in the form

$$E_r/E = 1 - \Omega\{1 - [(4 + j)/(2\mathcal{E} + j)](T_w/T_\infty)\} \tag{6}$$

Since, owing to radiation cooling, T_w/T_∞ is at most of order unity (see reference 3), it follows that for $S^2 \gg 1$ (and $\alpha \gtrsim 0$),

$$E_r/E \approx 1 - \Omega \tag{6a}$$

(3) Similarity Parameters for Insulated Surfaces

The surface temperature distribution of a thermally insulated object depends on the local heat fluxes only. The energy balance at a radiating surface element exposed to free-molecule flow can be written as

$$E = E_r + e\sigma T_n^4 \tag{7}$$

where T_n is the temperature of the insulated (nonconducting) surface and σ and e are the Stefan-Boltzmann constant and surface emissivity, respectively. Substitute for $E = E_t + E_j$ and E_r from Eqs. (2), (3), and (6), and define a dimensionless temperature

$$\eta_n = [2e\sigma/(4 + j)\Omega k n_\infty c_\infty Z]^{1/3} T_n \tag{8}$$

thereby transforming Eq. (7) into

$$\eta_n^4 + \eta_n = H_n \tag{9}$$

where

$$H_n = \left(\frac{2\mathcal{E} + j}{4 + j}\right)\left[\frac{2e\sigma}{(4 + j)\Omega k n_\infty c_\infty Z}\right]^{1/3} T_\infty = \left(\frac{2\mathcal{E} + j}{4 + j}\right)\eta_\infty \tag{10}$$

Since H_n is completely specified by the surface, free-stream and flight conditions, η_n and hence T_n is immediately available.

Notice that it is possible to formulate a similarity rule only for the dimensionless variable η_n rather than for T_n itself. The similitude, as expressed by Eq. (9), indicates that all surface elements that possess the same value of the parameter H_n will also have the same value of η_n. A plot of η_n vs. H_n is given in Fig. 3. It terminates at $H_n = 84$ since for values of $H_n \gg 1$ the solution

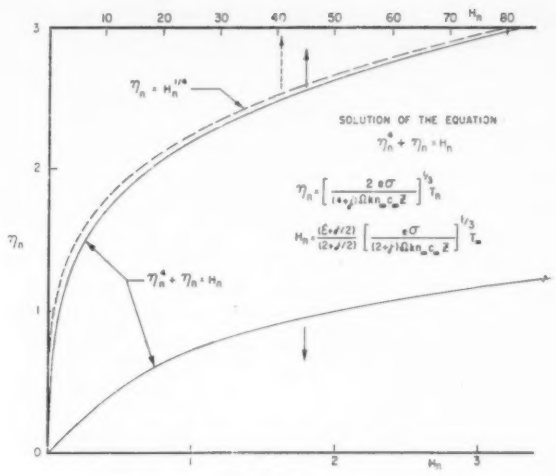

FIG. 3.

$$\eta_n = H_n^{1/4} \qquad (H_n \gg 1) \tag{11}$$

is an excellent approximation. It is easily demonstrated[4] that for free-molecule flight in the terrestrial atmosphere, $H_n \gg 1$ for hypersonic speeds ($S^2 \gg 1$). Thus, for the very important class of problems of high-speed flight an explicit solution for T_n is available; substitution of (8) and (10) into (11) yields:

$$T_n = [(2\mathcal{E} + j)\Omega n_\infty k^{3/2} T_\infty^{3/2} Z/\sqrt{2m}\, e\sigma]^{1/4} \qquad (S^2 \gg 1) \tag{12}$$

(4) Similarity Parameters for Perfect Conductors

The temperature of a perfect conductor, T_c, is uniform and is found by a procedure similar to that used in Section 3. One forms the total, rather than local, energy-flux balance:

$$\int\int E\, dA = \int\int E_r\, dA + \int\int e\sigma T_c^4\, dA \tag{13}$$

where dA indicates integration over the surface area of the object in question. Upon substitution for E and E_r, and defining

$$\eta_c = \left[\frac{2e\sigma \int\int dA}{(4 + j)\Omega k n_\infty c_\infty \int\int Z dA}\right]^{1/3} T_c \tag{14}$$

Eq. (13) becomes

$$\eta_c^4 + \eta_c = H_c \tag{15}$$

where

$$H_c = \left[\frac{\int\int (2\mathcal{E} + j) Z dA}{(4 + j)\int\int Z dA}\right] \times \left[\frac{2e\sigma \int\int dA}{(4 + j)\Omega k n_\infty c_\infty \int\int Z dA}\right]^{1/3} T_\infty \tag{16}$$

Notice that Eq. (15) has exactly the same form as Eq. (9) and hence its solution, for a given H_c, is also obtainable from Fig. 3. The various ratios such as $[\int\int (2\mathcal{E} + j) Z dA]/[(4 + j)\int\int Z dA]$ that appear

in Eq. (16) depend, of course, on the geometry in question. The results for several common shapes are presented in Section 5.

(5) Examples

Only cases of perfect conductors will be considered here, since the surface temperature distribution of an insulator is given by Eq. (12) [or Eqs. (8), (9), and (10) for the nonhypersonic cases]. Computation of the local angle of attack on simple shapes is a straightforward geometrical problem.

It was shown in Section 4 that in order to compute H_e and perform the transformation $\eta_e \leftrightarrow T_e$, it is necessary to evaluate the quantities

$$N \equiv \int\int ZdA / \int\int dA \tag{17}$$

and $$F \equiv \int\int (2\mathcal{E} + j)ZdA/(4 + j)\int\int ZdA \tag{18}$$

Eqs. (14) and (16) are thus rewritten, respectively, as:

$$\eta_e = [2e\sigma/(4 + j)\Omega k n_\infty c_\infty N]^{1/3}\, T_e \tag{19}$$

$$H_e = F[2e\sigma/(4 + j)\Omega k n_\infty c_\infty N]^{1/3} \square T_\infty = F\eta_\infty \tag{20}$$

The integrations involved in calculating F and N can be quite tedious and the details will be omitted here. The final expressions for F and N are tabulated below for several geometrical configurations, thus allowing one immediately to compute H_e and hence (from Fig. 3) η_e, leading to T_e. In the case of hypersonic flow ($S^2 \gg 1$) it can be easily demonstrated that regardless of body shape

$$F \xrightarrow[S^2 >> 1]{} \frac{2S^2}{4 + j}$$

and since $\eta_e = H_e^{1/4}$ $(S^2 \gg 1)$

it follows that

$$T_e = [2\Omega n_\infty k^{3/2} T_\infty^{3/2} S^2/\sqrt{m}\, e\sigma]^{1/4} N^{1/4} \quad (S^2 \gg 1) \tag{21}$$

In addition to the expressions F and N given in Table 1, plots of the dimensionless temperature

$$\left[\frac{T_e}{\sqrt{2}\,\Omega n_\infty k^{3/2} T_\infty^{3/2} S^2/\sqrt{m}\, e\sigma}\right]^{1/4}$$

are shown in Figs. 4 and 5.

In the formulas given in Table 1, I_0 and I_1 are the modified Bessel functions of the first kind of order zero and unity, respectively.

(6) The Effect of Solar Radiation

A surface element exposed to the sun's rays will absorb an energy flux of the amount

TABLE 1
Values of the Parameters $(4 + j)F$ and N for Some Perfect Conductors

Configuration \ Parameter	$(4+j)F = \frac{\iint (2\mathcal{E}+j) Z\, dA}{\iint Z\, dA}$	$N = \frac{\iint Z\, dA}{\iint dA}$
a) **Flat** plate at angle of attack α 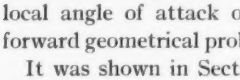 b) Symmetrical double wedge or double cone 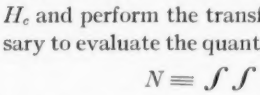	$2S^2 + 5 + j - \left(1 + \sqrt{\pi}\, \xi e^{\xi^2} \operatorname{erf} \xi\right)^{-1}$ $\xi = \begin{cases} S\sin\alpha & \text{for flat plate} \\ S\sin\beta & \text{for double cone or wedge} \end{cases}$	$\frac{e^{-\xi^2} + \sqrt{\pi}\, \xi \operatorname{erf} \xi}{2\sqrt{\pi}}$
Sphere	$2S^2 + 5 + j - \left(\frac{\sqrt{\pi}}{2} \operatorname{erf} S\right)\left[S e^{-S^2} + \sqrt{\pi}\left(1 + 2S^2\right) \operatorname{erf} S\right]^{-1}$	$\frac{2e^{-S^2} + \sqrt{\pi}\left[\frac{1}{S} + 2S\right] \operatorname{erf} S}{8\sqrt{\pi}}$
Infinite yawed cylinder 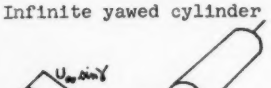	$2S^2 + 5 + j - \left\{1 + \xi^2\left[1 + \frac{I_1(\xi^2/2)}{I_0(\xi^2/2)}\right]\right\}^{-1}$ $\xi = S\sin\gamma$	$\frac{\xi e^{-\frac{\xi^2}{2}}}{2\sqrt{\pi}} I_0\left(\frac{\xi^2}{2}\right)\left[\frac{1}{\xi} + \xi + \frac{\xi I_1(\xi^2/2)}{I_0(\xi^2/2)}\right]$
Unyawed cone 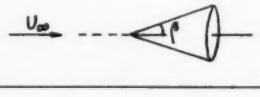	$2S^2 + 5 + j - \frac{e^{-\xi^2} + e^{-\xi^2 \csc\beta} \sin\beta}{e^{-\xi^2} + e^{-\xi^2 \csc\beta} \sqrt{\pi}\, \xi\left[\operatorname{erf} \xi + \operatorname{erf}(\xi \csc\beta)\right]}$ $\xi = S\sin\beta$	$\frac{e^{-\xi^2} + e^{-\xi^2 \csc\beta} \sin\beta + \sqrt{\pi}\, \xi\left[\operatorname{erf} \xi + \operatorname{erf}(\xi \csc\beta)\right]}{2\sqrt{\pi}\,(1 + \sin\beta)}$
Finite Yawed Cylinder 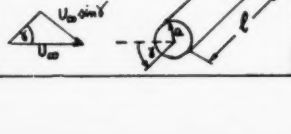	$(2S^2 + 5 + j) - \frac{e^{-\frac{\xi^2}{2}} I_0 + \left(\frac{a}{\ell}\right) e^{-\xi^2 \operatorname{ctn}^2\gamma}}{\xi e^{-\frac{\xi^2}{2}} I_0\left[\frac{1}{\xi} + \xi + \frac{\xi I_1}{I_0}\right] + \left(\frac{a}{\ell}\right)\left[e^{-\xi^2 \operatorname{ctn}^2\gamma} + \sqrt{\pi}\, \xi \operatorname{ctn}\gamma \operatorname{erf}(\xi \operatorname{ctn}\gamma)\right]}$ where $I_0 \equiv I_0\left(\frac{\xi^2}{2}\right)$, $I_1 \equiv I_1\left(\frac{\xi^2}{2}\right)$; $\xi = S\sin\gamma$	$\frac{1}{2\sqrt{\pi}\left(1 + \frac{a}{\ell}\right)}\left\{\xi e^{-\frac{\xi^2}{2}} I_0\left[\frac{1}{\xi} + \xi + \frac{\xi I_1}{I_0}\right] + \left(\frac{a}{\ell}\right)\left[e^{-\xi^2 \operatorname{ctn}^2\gamma} + \sqrt{\pi}\, \xi \operatorname{ctn}\gamma \operatorname{erf}(\xi \operatorname{ctn}\gamma)\right]\right\}$

$$E_s = eJ_s \cos \omega$$

where J_s is the local solar constant; e is the surface absorptivity (= emissivity) and ω is the angle between the direction of sun rays and the normal to the surface, $\mathbf{n}$. In the vicinity of the earth the solar constant is approximately 2 cal./min./cm.^{2} or 1.46×10^6 ergs/sec./cm.^{2}

It is desirable to express ω in terms of the flight coordinates. Let the horizon plane contain the free-stream velocity vector $\mathbf{U}_\infty$ and be normal to the plane defined by $\mathbf{U}_\infty$ and $\mathbf{n}$. The sun elevation Φ is measured from this horizon plane, and its azimuth ψ is measured from the flight direction. Then

$$\cos \omega = \cos \alpha \sin \Phi + \cos \Phi \sin \alpha \cos \psi$$

where α is the local angle of attack.

The dimensionless local energy-flux balance, Eq. (9), is now modified to read

$$\eta_n^4 + \eta_n = H_n + H_{s;n} = H_n[1 + (H_{s;n}/H_n)] \quad (22)$$

where

$$H_{s;n}/H_n = 2eJ_s \cos \omega/(2\mathcal{E} + j)\Omega n_\infty k c_\infty Z T_\infty$$

is the ratio of the net solar energy influx to the net free-molecule energy influx. Thus for given flight conditions the formulation of the problem remains essentially unchanged. In the case of perfect conductors, Eq. (15) becomes:

$$\eta_c^4 + \eta_c = H_c + H_{s;c} =$$

$$H_c\left[1 + \frac{2eJ_s \int\int \cos \omega \, dA}{\Omega k n_\infty c_\infty T_\infty \int\int (2\mathcal{E} + j) Z dA}\right] \quad (23)$$

To demonstrate the effect of solar radiation, consider the simple case of a perfectly conducting sphere (or spherical shell) at hypersonic speeds. For this case one has

$$\int\int \cos \omega \, dA = 1/2$$

and

$$\int\int (2\mathcal{E} + j) Z dA \xrightarrow[S^2 >> 1]{} S^3$$

and it follows that

$$(H_{s;c}/H_c)_{\text{sphere}} \xrightarrow[S^2 >> 1]{} eJ_s/\Omega k n_\infty c_\infty T_\infty S^3$$

A plot of this ratio vs. S, for several altitudes, is presented in Fig. 6. The necessary atmospheric data were obtained from reference 5. It is seen that the effect of solar radiation can be neglected only at the very lower altitudes and at extremely high speeds. Thus at 120 km. and $S = 17.5$, $H_{s;c} = H_c$, i.e., the effective heating rate is doubled and hence the temperature is about 20% above the value it would have in the absence of solar radiation.

(7) The Effect of Finite Thermal Conductivity

This section is concerned with the effect of thermal conductivity on the temperature distribution of a radiating object in high-speed free-molecule flow. It will be shown that similarity solutions are still available provided the nondimensionalization scheme differs from the one previously employed.

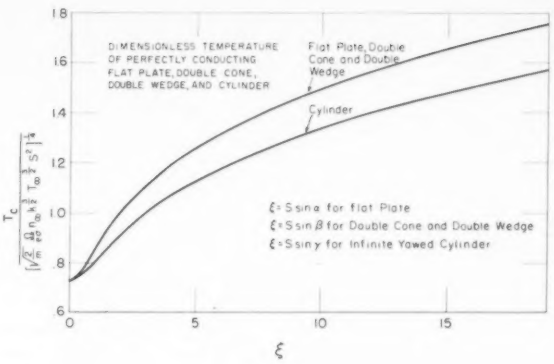
DIMENSIONLESS TEMPERATURE OF PERFECTLY CONDUCTING FLAT PLATE, DOUBLE CONE, DOUBLE WEDGE, AND CYLINDER
Flat Plate, Double Cone and Double Wedge
Cylinder
ξ = S sin α for Flat Plate
ξ = S sin β for Double Cone and Double Wedge
ξ = S sin γ for Infinite Yawed Cylinder
ξ

FIG. 4.

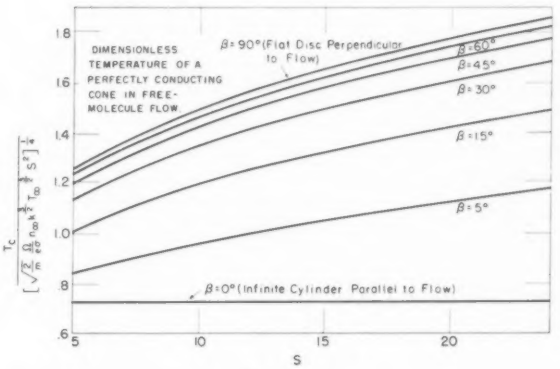
DIMENSIONLESS TEMPERATURE OF A PERFECTLY CONDUCTING CONE IN FREE-MOLECULE FLOW
β = 90° (Flat Disc Perpendicular to Flow)
β = 60°
β = 45°
β = 30°
β = 15°
β = 5°
β = 0° (Infinite Cylinder Parallel to Flow)
S

FIG. 5.

It will be assumed in the following that we are dealing with solid objects made of homogeneous material with constant thermal conductivity K (ergs/sec./cm.^{2}). Free use will be made of previous results, particularly those of Section 2.

The basic approach that will be taken is that the steady temperature distribution problem in a solid is to be solved, subject to certain nonlinear boundary conditions. The boundary condition then will include the heat fluxes due to radiation and free-molecule flow convection, as well as the conduction term. The formal statement of the problem is then:

$$\nabla^2 T = 0$$

$$K(\partial T/\partial n) + e\sigma T^4 + E_r = E \quad \text{(on external surfaces)}$$

where $\partial T/\partial n$ denotes the derivative in the direction of the outward normal. In some cases, for example, a spherical shell, an additional boundary condition must be specified on the internal surface.

Next we nondimensionalize the coordinates through division by some reference length L characteristic of the problem geometry (e.g., plate thickness, sphere radius, etc.), and introduce a dimensionless temperature

$$\eta = (e\sigma L/K)^{1/3} T$$

and use Eqs. (2) and (3) to transform the problem

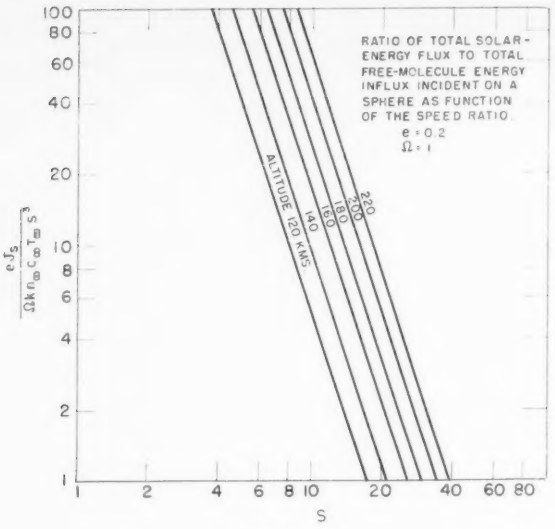

FIG. 6.

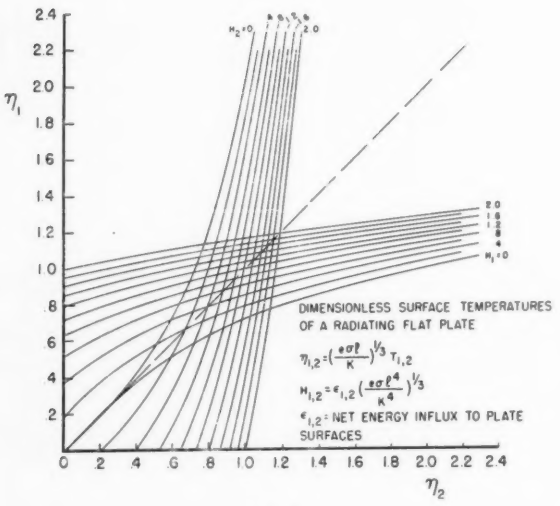
DIMENSIONLESS SURFACE TEMPERATURES OF A RADIATING FLAT PLATE
$\eta_{1,2} = (\frac{e\sigma l}{K})^{1/3} T_{1,2}$
$H_{1,2} = \epsilon_{1,2} (\frac{e\sigma l^4}{K^4})^{1/3}$
$\epsilon_{1,2}$ = NET ENERGY INFLUX TO PLATE SURFACES
η_1
η_2

FIG. 7.

statement into

$$\nabla^2\eta = 0$$

$$(\partial\eta/\partial n') + \eta^4 + \chi\eta = \mathrm{H}$$

(on external "dimensionless" surface)

where $\partial/\partial n' = \partial/\partial(n/L)$

$$\chi = \left(\frac{4+j}{2}\right)\left(\frac{\Omega k L \nu}{K}\right) \tag{24}$$

and $$H = \left(\frac{2\mathcal{E}+j}{2}\right)\left(\frac{e\sigma L^4}{K^4}\right)^{1/3} \Omega k \nu T_\infty \tag{25}$$

It can be demonstrated[4] that for the range of available solid materials [$10^{-4} < K \leqslant 0(1)$ cal./sec./cm.-°C.] and for reasonable free-molecule flow flight conditions (e.g., speeds not exceeding the escape velocity) the parameter χ is always small in comparison to unity. It follows that $\partial\eta/\partial n' \gg \chi\eta$ and the problem statement reduces to

$$\nabla^2\eta = 0 \tag{26}$$

$$(\partial\eta/\partial n') + \eta^4 = H \qquad \text{(on external surfaces)} \tag{27}$$

The physical significance of the simplification leading to Eq. (27) (i.e., $\chi \ll 1$) can be best understood by noting that χ is essentially the ratio of the rebounding energy flux to the conducted flux. Notice also that Eq. (27) can be derived directly from Eqs. (2) and (3) through the use of the relation $E_r/E \approx 1 - \Omega$ established in Section 2. Both of these observations emphasize the minor role of the rebounding molecules in establishing the energy balance.

The solution of (26) and (27) for some particular configurations will be summarized below.

(7a) *The Flat Plate*

Consider a conducting flat plate whose thickness l is much smaller than its length so that it is essentially a solid slab in which heat conduction is one-dimensional and the temperature distribution is linear. The boundary condition, Eq. (27), becomes

$$\eta_1^4 + \eta_1 - \eta_2 = H_1 \tag{28}$$

$$\eta_2^4 + \eta_2 - \eta_1 = H_2 \tag{29}$$

where the subscripts 1 and 2 refer to the pressure and suction sides of the plate, respectively.

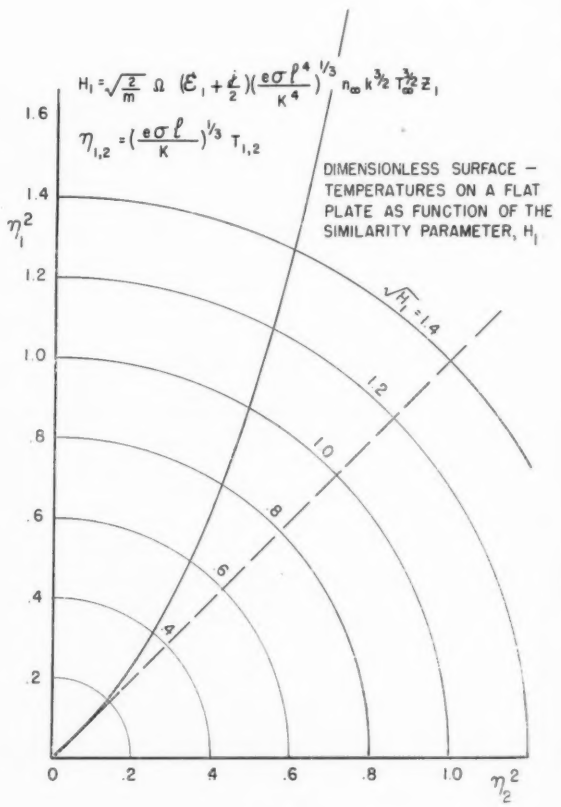

FIG. 8.

The solution for the dimensionless surface temperatures η_1 and η_2 will now be considered. A straightforward graphical method, illustrated in Fig. 7, consists of plotting the parametric curves indicated by Eqs. (28) and (29) for various values of H_1 and H_2. The intersection of the two curves for the proper H_1 and H_2 yields the two values of η_1 and η_2 that are sought.

Some special cases are detailed in reference 4. One of them is that of $|S \sin \alpha| > 1$, i.e., $H_2 \ll H_1$, which is demonstrated in Fig. 8 where η_1 and η_2 are given as functions of H_1 only.

When solar radiation is present, the quantity $H_s = eJ_s(e\sigma l^4/K^4) \cos \omega$ is added to either H_1 or H_2, depending on which side of the plate is exposed to the sun rays. The solution is then found from Fig. 7 as before. A special case of interest is that of flight outside the sensible atmosphere (i.e., $E_s \gg E_1$ and E_2). The equations for η_1 and η_2 become:

$$\eta_1^4 + \eta_1 - \eta_2 = H_s$$

$$\eta_2^4 + \eta_2 - \eta_1 = 0$$

where now the plate surface exposed to the sun is designated as side 1. One then uses Fig. 8 with $\sqrt{H_1}$ replaced by $\sqrt{H_s}$.

(7b) *The Solid Sphere*

Consider a solid sphere of radius a whose coordinate system is shown in Sketch 1. The dimensionless spherical coordinates of a point in the sphere are $r = R/a$, ϑ, φ where ϑ is the polar angle and is related to the angle of attack α through

$$\alpha = \vartheta - (\pi/2)$$

For high speeds ($S^2 \gg 1$) the problem statement (26) and (27) becomes:

$$\nabla^2 \eta = 0 \qquad (0 < r < 1) \tag{30}$$

$$(\partial \eta/\partial r) + \eta^4 = H \equiv \tilde{H} f(\mu) \quad (r = 1) \tag{31}$$

where $$\tilde{H} = \sqrt{2/m}\,(e\sigma a^4/K^4)^{1/3}\,\Omega n_\infty k^{3/2} T_\infty^{3/2} S^3 \qquad (S^2 \gg 1) \tag{33}$$

$$\mu = \cos \vartheta$$

and $$f(\mu) = \begin{cases} -\mu & -1 \leqslant \mu \leqslant 0 \\ 0 & 0 < \mu \leqslant 1 \end{cases} \tag{34}$$

Because of the axial symmetry the solution must be of the form

$$\eta(r, \mu) = \sum_{n=0}^{\infty} A_n r^n P_n(\mu)$$

where the coefficients A_n are to be determined from the boundary condition (31) which takes the form

$$\sum_{n=1}^{\infty} n A_n P_n(\mu) + \left[\sum_{n=0}^{\infty} A_n P_n(\mu)\right]^4 = \tilde{H} f(\mu) = \tilde{H} \sum_{n=0}^{\infty} a_n P_n(\mu) \tag{35}$$

The coefficients a_n are those used in the expansion of $(f\mu)$ in terms of the Legendre polynomials $P_n(\mu)$, and

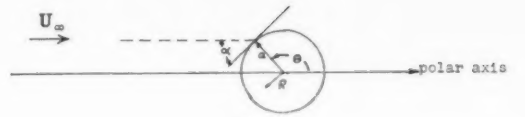

Sketch 1.

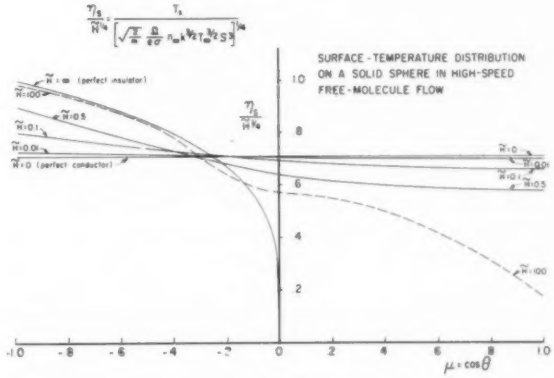

FIG. 9.

are given by

$$a_{2n} = (-)^{n+1}\,[(4n + 1)/(2n - 1)(n + 1)] \times [(2n)!/(2^{2n+2} n!n!)]$$

$$a_{2n+1} = \begin{cases} -1/2 & n = 0 \\ 0 & n \geqslant 1 \end{cases}$$

The nonlinearity of (35) rules out the usual procedure of matching coefficients of like order in P_n. However, methods of solution can be devised[4] for the three main classes of problems: (a) $\tilde{H} \ll 1$, (b) $\tilde{H} = 0(1)$, (c) $H \gg 1$. The details are omitted here and attention is called to Fig. 9 where the surface temperature distribution is plotted vs. μ for various values of $\tilde{H}$.* It should be noted that for $\tilde{H} = 0$ and ∞ the results reduce respectively to the correct form for the perfect conductor and insulator.

(7c) *The Thin Spherical Shell*

Two problems of interest suggest themselves when one considers the radiating spherical shell in high-speed free-molecule flow. In the first one the inner surface is maintained, through cooling or heating, at some desired constant temperature T_b.

In the second case, which might be designated as the "natural" configuration, equilibrium is established without any artificially imposed mechanism. Thus, in addition to conduction, internal cavity radiation also contributes to the energy fluxes at the inner surface. These two cases now will be considered separately.

The Spherical Shell With a Constant Inner-Surface Temperature

Consider a hollow sphere with an outer radius a and an inner radius b. The coordinate system and

* The dashed line in Fig. 9 for $\tilde{H} = 100$ represents only the zero-order result of an iterative procedure.

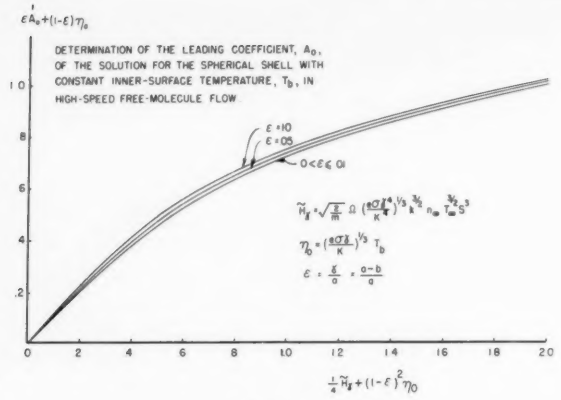
DETERMINATION OF THE LEADING COEFFICIENT, A_0, OF THE SOLUTION FOR THE SPHERICAL SHELL WITH CONSTANT INNER-SURFACE TEMPERATURE, T_b, IN HIGH-SPEED FREE-MOLECULE FLOW
ε = 10
ε = 05
0 < ε ≤ 01
$\tilde{H}_\gamma = \sqrt{\frac{1}{m}}\,\Omega\,(\frac{\epsilon\sigma\gamma}{K})^{1/3} k^{3/2} n_\infty T_\infty^{3/2} S^3$
$\eta_0 = (\frac{\epsilon\sigma\gamma}{K})^{1/3} T_b$
$\epsilon = \frac{\gamma}{a} = \frac{a-b}{a}$
$\frac{1}{4}\tilde{H}_\gamma + (1-\epsilon)^2\eta_0$

FIG. 10.

molecular energy fluxes are the same as for the solid sphere. Physical considerations indicate that the shell thickness, $\gamma = a - b$, is a meaningful reference length. This suggests the following dimensionless variables:

$$r = (R - b)/\gamma = (R - b)/(a - b)$$

and $$\eta = (e\sigma\gamma/K)^{1/3}T = (e\sigma\epsilon a/K)^{1/3}T$$

where $\epsilon = \gamma/a$ is the significant dimensionless ratio for the problem. The equation and boundary conditions become

$$\frac{\partial}{\partial r}\left[\left(r + \frac{1-\epsilon}{\epsilon}\right)^2 \frac{\partial \eta}{\partial r}\right] + \frac{\partial}{\partial \mu}\left[(1-\mu^2)\frac{\partial \eta}{\partial \mu}\right] = 0 \qquad (0 < r < 1) \quad (36)$$

$$(\partial\eta/\partial r) + \eta^4 = \tilde{H}_\gamma f(\mu) \qquad (r = 1) \quad (37)$$

$$\eta = \eta_0 = \text{constant} \qquad (r = 0) \quad (38)$$

The similarity parameter $\tilde{H}_\gamma$ is given by

$$\tilde{H}_\gamma = \sqrt{2/m}\,(e\sigma\gamma^4/K^4)^{1/3}\Omega n_\infty k^{3/2} T_\infty^{3/2} S^3 = \epsilon^{4/3}\tilde{H} \quad (39)$$

and $$\eta_0 = (e\sigma\gamma/K)^{1/3}T_b$$

The solution to (36) must be of the form

$$\eta(r, \mu) = \sum_{n=0}^{\infty}\left\{A_n\left[r + \frac{1-\epsilon}{\epsilon}\right]^n + B_n\left[r + \frac{1-\epsilon}{\epsilon}\right]^{-n-1}\right\} P_n(\mu) \quad (40)$$

Use of the inner boundary condition, Eq. (38), yields the relations:

$$B_0 = [(1-\epsilon)/\epsilon](\eta_0 - A_0) \quad (41)$$

$$B_n = -[(1-\epsilon)/\epsilon]^{2n+1} A_n \quad (n \geq 1) \quad (42)$$

If we restrict the analysis to thin shells ($\epsilon \ll 1$) it follows[4] that $\tilde{H}_\gamma \ll 1$. Under this condition it is found that the A_n's satisfy the following:

$$[\epsilon A_0 + (1-\epsilon)\eta_0]^4 + (1-\epsilon)[\epsilon A_0 + (1-\epsilon)\eta_0] = (\tilde{H}_\gamma/4) + (1-\epsilon)^2\eta_0 \quad (43)$$

and

$$A_n = \epsilon^n a_n \tilde{H}_\gamma \left\{n\epsilon\left[1 + \frac{n+1}{n}(1-\epsilon)^{2n+1}\right] + 4[\epsilon A_0 + (1-\epsilon)\eta_0]^3[1 - (1-\epsilon)^{2n+1}]\right\}^{-1} \quad (n \geq 1) \quad (44)$$

A graphical solution of Eq. (43) is given in Fig. 10, supplying us with A_0 for given ϵ, $\tilde{H}_\gamma$, and η_0. Having obtained A_0, all the A_n are available through Eq. (44).

With the complete solution being specified by Eqs. (40) through (44) it is now possible to compute the total heating or cooling rate $\dot{Q}_1$ (ergs/sec.) that is required to maintain the inner-surface constant temperature, $T_b = (K/e\sigma\gamma)^{1/4}\eta_0$. The result, in two nondimensional forms, is shown in Figs. 11 and 12.

Finally, one can inquire under what conditions there will be no net heat transfer at the inner surface. It is deduced[4] that $\dot{Q}_1 = 0$ when the imposed inner-surface temperature satisfies the condition

$$\eta_0^4 + \epsilon(1-\epsilon)\eta_0 = \tilde{H}_\gamma/4 \quad (45)$$

Solution of (45) for various values of ϵ is presented graphically in Fig. 13.

There remains to consider the case of the "natural" configuration.

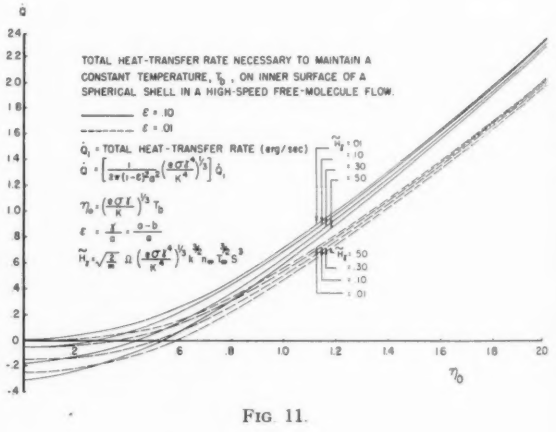
TOTAL HEAT-TRANSFER RATE NECESSARY TO MAINTAIN A CONSTANT TEMPERATURE, T_b, ON INNER SURFACE OF A SPHERICAL SHELL IN A HIGH-SPEED FREE-MOLECULE FLOW.
ε = 10
ε = 01
$\dot{Q}_1$ = TOTAL HEAT-TRANSFER RATE (erg/sec)
$\dot{Q} = \left[\frac{1}{2\pi(1-\epsilon)^2 a^2}\left(\frac{\epsilon\sigma\gamma^4}{K^4}\right)^{1/3}\right]\dot{Q}_1$
$\eta_0 = \left(\frac{\epsilon\sigma\gamma}{K}\right)^{1/3} T_b$
$\epsilon = \frac{\gamma}{a} = \frac{a-b}{a}$
$\tilde{H}_\gamma = \sqrt{\frac{1}{m}}\,\Omega\left(\frac{\epsilon\sigma\gamma^4}{K^4}\right)^{1/3} k^{3/2} n_\infty T_\infty^{3/2} S^3$
$\tilde{H}_\gamma$ = 01, 10, 30, 50
$\tilde{H}_\gamma$ = 50, 30, 10, 01
η_0

FIG. 11.

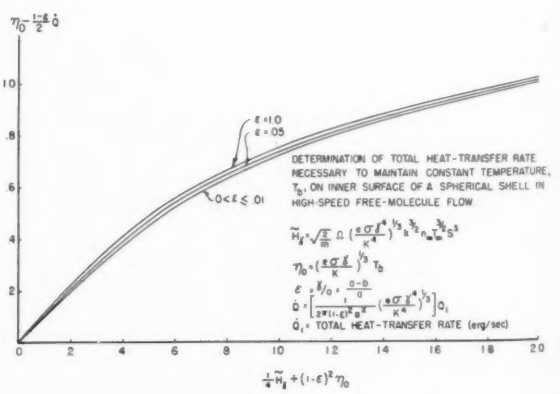
$\eta_0 - \frac{1-\epsilon}{2}\dot{Q}$
ε = 10
ε = 05
0 < ε ≤ 01
DETERMINATION OF TOTAL HEAT-TRANSFER RATE NECESSARY TO MAINTAIN CONSTANT TEMPERATURE, T_b, ON INNER SURFACE OF A SPHERICAL SHELL IN HIGH-SPEED FREE-MOLECULE FLOW
$\tilde{H}_\gamma = \sqrt{\frac{1}{m}}\,\Omega\,(\frac{\epsilon\sigma\gamma^4}{K^4})^{1/3} k^{3/2} n_\infty T_\infty^{3/2} S^3$
$\eta_0 = (\frac{\epsilon\sigma\gamma}{K})^{1/3} T_b$
$\epsilon = \frac{\gamma}{a} = \frac{a-b}{a}$
$\dot{Q} = \left[\frac{1}{2\pi(1-\epsilon)^2 a^2}\left(\frac{\epsilon\sigma\gamma^4}{K^4}\right)^{1/3}\right]\dot{Q}_1$
$\dot{Q}_1$ = TOTAL HEAT-TRANSFER RATE (erg/sec)
$\frac{1}{4}\tilde{H}_\gamma + (1-\epsilon)^2\eta_0$

FIG. 12.

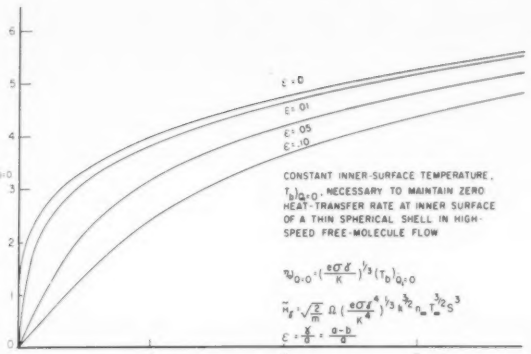
ε = 0
ε = .01
ε = .05
ε = .10
CONSTANT INNER-SURFACE TEMPERATURE, $(\tau_b)_{Q=0}$, NECESSARY TO MAINTAIN ZERO HEAT-TRANSFER RATE AT INNER SURFACE OF A THIN SPHERICAL SHELL IN HIGH-SPEED FREE-MOLECULE FLOW
$\eta_{Q=0}=(\frac{\epsilon\sigma\delta}{K})^{1/3}(\tau_b)_{Q=0}$
$\tilde{H}_\gamma=\sqrt{\frac{2}{\pi}}\,\Omega\,(\frac{\epsilon\sigma\gamma^4}{K^4})^{1/3}k^{3/2}n_\infty T_\infty^{3/2}S^3$
$\xi=\frac{X}{\delta}=\frac{a-b}{a}$
$(\eta_b)_{Q=0}$
$\tilde{H}_\gamma$

FIG. 13.

The Spherical Shell With Internal Cavity Radiation

This case differs from the preceding one in that there are no externally imposed restrictions on the inner boundary. Using the same nondimensionalization scheme, the problem statement becomes

$$\frac{\partial}{\partial r}\left[\left(r+\frac{1-\epsilon}{\epsilon}\right)^2\frac{\partial\eta}{\partial r}\right]+\frac{\partial}{\partial\mu}\left[(1-\mu^2)\frac{\partial\eta}{\partial\mu}\right]=0 \qquad (0<r<1) \quad (46)$$

$$(\partial\eta/\partial r)+\eta^4=\tilde{H}_\gamma f(\mu) \qquad (r=1) \quad (47)$$

$$(\partial\eta/\partial r)=(1/2)\int_{-1}^{1}[\eta^4(0,\mu)-\eta^4(0,\mu_1)]d\mu_1 \qquad (r=0) \quad (48)$$

The last boundary condition expresses the fact that each point on the inner surface receives and emits radiant energy as well as conductive heat flux. In its present form this boundary condition is quite troublesome. It can however be "linearized" if it is realized that the internal radiation tends to diminish temperature differences on the cavity wall. Thus Eq. (48) is replaced by

$$\frac{\partial\eta}{\partial r}=4\eta^4-2\eta^3\int_{-1}^{1}\eta(0,\mu_1)\,d\mu_1 \qquad (r=0) \quad (48a)$$

The general solution to (46) is

$$\eta(r,\mu)=\sum_{n=0}^{\infty}\left[C_n\left(r+\frac{1-\epsilon}{\epsilon}\right)^n+D_n\left(r+\frac{1-\epsilon}{\epsilon}\right)^{-n-1}\right]P_n(\mu) \quad (49)$$

where the coefficients C_n and D_n are to be determined from the boundary conditions. Again using the fact that $\tilde{H}_\gamma \ll 1$, the following expressions are obtained[4]:

$$D_0=0 \quad (50)$$

$$D_n=-\left(\frac{1-\epsilon}{\epsilon}\right)^{2n+1}\times\left[\frac{4C_0^3-(\epsilon/1-\epsilon)n}{4C_0^3+(\epsilon/1-\epsilon)(n+1)}\right]C_n \qquad (n\geqslant 1) \quad (51)$$

$$C_0=(\tilde{H}_\gamma/4)^{1/4} \quad (52)$$

$$C_n=\epsilon^n a_n\tilde{H}_\gamma\left\{n\epsilon\left[1+\frac{n+1}{n}(1-\epsilon)^{2n+1}\times\frac{4C_0^3-(\epsilon/1-\epsilon)n}{4C_0^3+(\epsilon/1-\epsilon)(n+1)}\right]+4C_0^3\left[1-(1-\epsilon)^{2n+1}\times\frac{4C_0^3-(\epsilon/1-\epsilon)n}{4C_0^3+(\epsilon/1-\epsilon)(n+1)}\right]\right\}^{-1} \qquad (n\geqslant 1) \quad (53)$$

Eq. (49) in conjunction with these expressions for C_0, C_n, and D_n constitute the formal solution to the problem (when $\tilde{H}\gamma \ll 1$, which is usually the case). It should be noted that the result $D_0 = 0$ does not depend on any approximation. It follows from the fact that the net integrated heat transfer at the inner surface must vanish.

Conclusions

(a) The procedure for determining the temperature of a perfect insulator is, in general, as follows: (1) Compute H_n from Eq. (10); (2) For this H_n obtain η_n from Fig. 3; (3) Use this value of η_n in Eq. (8) to find T_n.

In the special case of $S^2 \gg 1$ (i.e., $H_n \gg 1$), find T_n directly from Eq. (12).

(b) The procedure for the case of perfect conductors is basically the same as the one above. Determination of H_c is more involved than that of H_n. Some specific examples are tabulated in Section 5.

(c) It was seen that solar radiation does not affect the basic formulation of the similarity solution. The specific example of a perfectly conducting sphere (or spherical shell) was used to demonstrate that this effect is dominant at low speeds and high altitudes.

(d) The effect of finite thermal conductivity of the body is considered in Section 7. It is shown that the problem, though more complicated, is still susceptible to a similarity solution, H (or $\tilde{H}$) being the similarity parameter.

References

[1] Willis, D. R., *On the Flow of Gases Under Nearly Free Molecular Conditions*, Princeton University, Department of Aeronautical Engineering, Report No. 442(AFOSR TN-1093), December 1958.

[2] Sanger, E., and Bredt, J., *Über einen Raketenantrieb für Fernbomber*, Deutsche Luftfahrtforschung, Untersuchungen u. Mitteilen, No. 3538, pp. 141–173, Berlin, 1944.

[3] Stalder, J. R., and Jukoff, D., *Heat Transfer to Bodies Traveling at High Speeds in the Upper Atmosphere*, NACA TR 944, 1949.

[4] Abarbanel, S. S., *On Some Problems in Radiative Heat Transfer*, MIT Fluid Dynamics Research Group, Report No. 59-1 (AFOSR TN 59-531), April 1959.

[5] Hulburt, E. O., *Advances in the Physics of the Upper Air Since 1950*, NRL Report 4600, Washington, D. C., October 25, 1955.

Buckling of a Column With Random Initial Displacements†

WILLIAM E. BOYCE*
Rensselaer Polytechnic Institute

Summary

Elementary column-buckling theory assumes that the column is initially straight, and leads to an eigenvalue problem for the buckling load. For curved columns the phenomenon of buckling in a sense disappears, inasmuch as nonzero displacements occur for arbitrarily small loads. The purpose of this paper is to discuss the relation between the load and the mean transverse displacement of the column when the initial configuration of the column is random in nature.

Symbols

P	=	applied load, positive when compressive
l	=	length of column
EI	=	flexural rigidity
k	=	dimensionless load parameter
W	=	initial transverse column displacement
Y	=	transverse column displacement due to load P
G	=	Green's function
$E(\phi)$	=	mathematical expectation or mean of the random variable ϕ
$D^2(\phi)$	=	variance of the random variable ϕ
ρ	=	correlation function
μ^2	=	variance of W, assumed constant
I_h	=	integral used in computation of approximate value of $D^2[Y(x)]$
ρ^*	=	correlation function used to compute I_h
$I_h{}^*$	=	integral appearing in expression for I_h
k_{cr}	=	value of load parameter for which $D^2[Y] = D^2[W]$
σ	=	standard deviation of midspan displacement
m'	=	mean absolute midspan displacement
σ'	=	standard deviation of absolute midspan displacement
α	=	parameter appearing in correlation function

(1) MOST MATHEMATICAL ANALYSES OF MECHANICAL SYSTEMS involve idealized models, generally designed so as to produce linear mathematical problems. The literature dealing with such problems is vast. Actual physical systems deviate from the ideal model, however, and to take this into account, a great variety of problems have been considered involving prescribed, and frequently small, perturbations of the model. Unfortunately, sometimes the difference between the actual system and the model is random in character; in this case observations of the physical system also differ from predictions based on the model in a random manner. This leads to the question, studied by comparatively few investigators, of relating the random deviations from a mathematical model with the consequent random deviations from solutions based on it. Much of the existing work along this line has been in connection with electrical problems, and usually involves a Fourier-type approach. The present paper is concerned with this question from a different viewpoint; while much of the discussion is general, the problem of "buckling" of an initially curved column is given particular consideration.

(2) The elementary theory of columns under end loads originated with Euler about two centuries ago. This treatment involves several assumptions, including the following:

(i) the column is initially straight;
(ii) the loads are perfectly centered and parallel to the axis of the column;
(iii) the column is made of homogeneous isotropic elastic material;
(iv) the strains are small.

As a consequence one is led to the differential equation

$$Y^{IV} + k^2 Y'' = 0, \qquad 0 < x < 1 \tag{2.1}$$

together with suitable boundary conditions at $x = 0$ and $x = 1$. Here $Y(x)$ is the lateral displacement of the centerline, the primes and roman numerals denote differentiation with respect to x, and

$$k^2 = Pl^2/EI \tag{2.2}$$

where P is the applied load (positive when compressive), l the length of the column, and EI its flexural rigidity. The boundary conditions are linear and homogeneous in Y and its first three derivatives, leading to a typical eigenvalue problem. Nontrivial solutions for Y exist only for certain nonnegative values $k_1, k_2, \ldots$ of the parameter, the smallest of which defines the buckling load. When P is less than the buckling load, no lateral displacements occur.

The behavior of the column is quite different if a nonhomogeneous term in the differential equation is introduced through violation of assumption (i). The present paper concerns the situation when such a term is random in character.

If the column is not perfectly straight, as in Fig. 1, the differential equation becomes

$$Y^{IV} + k^2 Y'' = -k^2 W'', \quad 0 < x < 1 \tag{2.3}$$

Received March 10, 1960. Revised and received July 27, 1960.

† This research was supported by the United States Air Force through the Air Force Office of Scientific Research of the Air Research and Development Command, under Contract Number AF 18 (600)-1586.

* Associate Professor of Mathematics.

The author is indebted to Prof. W. Prager for calling his attention to this problem.

where $W(x)$ is the initial displacement of the centerline, and $Y(x)$ still represents the displacement resulting from the application of the load P. Now, well-behaved but nontrivial solutions exist for all values of k except the eigenvalues, and, in particular, displacements $Y(x)$ not identically zero occur for arbitrarily small loads P.

The solution is represented most conveniently for present purposes in terms of the Green's function $G(x,\xi)$ by the integral

$$Y(x) = k^2 \int_0^1 G(x, \xi) \frac{d^2W}{d\xi^2} (\xi)\, d\xi \qquad (2.4)$$

While the following analysis can be carried out for any reasonable boundary conditions, the calculations are simplest when both ends are simply supported so that the boundary conditions are

$$Y(0) = Y(1) = Y''(0) = Y''(1) = 0 \qquad (2.5)$$

The differential equation can then be integrated twice, leading to the new equation

$$Y'' + k^2 Y = -k^2 W, \quad 0 < x < 1 \qquad (2.6)$$

with the boundary conditions

$$Y(0) = Y(1) = 0 \qquad (2.7)$$

In this event (2.4) is replaced by

$$Y(x) = k^2 \int_0^1 G(x, \xi) W(\xi)\, d\xi \qquad (2.8)$$

where $G(x, \xi)$ is now the Green's function associated with (2.6) and (2.7); thus

$$G(x, \xi) = \begin{cases} \dfrac{\sin kx \sin k(1 - \xi)}{k \sin k}, & 0 < x < \xi \\ \dfrac{\sin k(1 - x) \sin k\xi}{k \sin k}, & \xi < x < 1 \end{cases} \qquad (2.9)$$

(3) Some of the statistical consequences of a relation such as (2.8) between random function have been discussed elsewhere (see references 1 or 6, for example); it can be shown, for instance that the operation of taking the mean** can be commuted with the Green's function integral, so that

$$E[Y(x)] = k^2 \int_0^1 G(x, \xi) E[W(\xi)]\, d\xi \qquad (3.1)$$

Thus the mean of $Y(x)$ can be computed whenever the mean of $W(\xi)$ is given. In particular, if $W(\xi)$ is distributed symmetrically about zero for all ξ, then $E[W(\xi)] \equiv 0$, and hence $E[Y(x)] = 0$ for all x.

Determination of the variance of $Y(x)$ requires a consideration of $Y^2(x)$, which may be written

$$Y^2(x) = k^4 \int_0^1 \int_0^1 G(x, \xi) G(x, \eta) W(\xi) W(\eta) d\xi d\eta \qquad (3.2)$$

** The necessary statistical terms are defined in the Appendix.

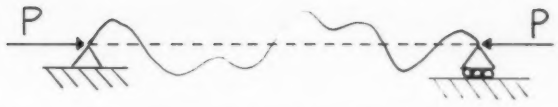

FIG. 1. Simply supported column with random initial configuration subject to axial load P.

Hence

$$E[Y^2(x)] = k^4 \int_0^1 \int_0^1 G(x, \xi) G(x, \eta) E[W(\xi) W(\eta)] d\xi d\eta \qquad (3.3)$$

Use of Eqs. (A.5) and (A.9) yields

$$D^2[Y(x)] = k^4 \int_0^1 \int_0^1 G(x, \xi) G(x, \eta) \rho(\xi, \eta) \{D^2[W(\xi)] \times D^2[W(\eta)]\}^{1/2} d\xi d\eta \qquad (3.4)$$

When $E[Y(x)] \equiv 0$, then $D^2[Y(x)] = E[Y^2(x)]$. Eq. (3.4) can be substantially simplified provided $W(\xi)$ is assumed to be a stationary function. In this case the statistical parameters of W are independent of the space variable; that is,

$$D^2[W(\xi)] = D^2[W(\eta)] = \mu^2$$

independent of ξ or η. Moreover, $\rho(\xi, \eta)$ is not a function of ξ and η separately, but only of their difference, $\rho = \rho(\xi - \eta)$. Under this assumption

$$D^2[Y(x)] = k^4 \mu^2 \int_0^1 \int_0^1 G(x, \xi) G(x, \eta) \rho(\xi - \eta) d\xi d\eta \qquad (3.5)$$

In principle, the distribution function for $Y(x)$ could be obtained as a series* involving statistical moments of all orders for $Y(x)$, which in turn would require the computation of $E[Y^n(x)]$ for all values of n. In practice this does not appear feasible.

However, if $Y(x)$ is a normal variable, then its distribution function depends only on the mean and variance; these quantities are more amenable to calculation than the higher moments. In general the normality of $Y(x)$ cannot be established conclusively, but the integral representation of $Y(x)$ can of course be replaced by a finite sum,

$$Y(x) = \sum_{i=1}^{n} G(x, \xi_i) W(\xi_i) \Delta\xi_i$$

each of whose terms makes a negligible contribution. Since the individual terms are not independent, the central limit theorem cannot in general be applied directly, but it nonetheless suggests that $Y(x)$ is approximately normal, provided that the values of $W(\xi_i)$ are only weakly dependent in some sense. At least, this assumption can serve as a basis for further work.

(4) Now consider again (2.8) and (2.9) describing the behavior of an initially curved simply supported

* See reference 2. p. 177.

column. Assume that $W(\xi)$ is a stationary function, so that $E[W(\xi)] = 0$ and $D^2[W(\xi)] = \mu^2$ independent of ξ. Thus $E[Y(x)] = 0$ also, but some further hypothesis concerning $\rho(\xi - \eta)$ is necessary in order to compute $D^2[Y(x)]$. The correlation function is unity when $\xi = \eta$ and presumably decreases in absolute value, not necessarily monotonically, as $|\eta - \xi|$ increases. Experience in other areas** suggests the use of a damped oscillatory function such as

$$\frac{\sin \alpha(\eta - \xi)}{\alpha(\eta - \xi)} \quad \text{or} \quad e^{-\alpha|\eta-\xi|} \cos \beta(\eta - \xi)$$

Neither of these choices permits the evaluation of (3.5) in closed form. However, an approximate value of $D^2[Y(x)]$ can be obtained by assuming $\rho(\xi - \eta)$ to be a step function approximating either of these functions. For instance, the calculations below are based on such an approximation to $[\sin \alpha(\eta - \xi)]/\alpha(\eta - \xi)$. First note that the zeros of this function are $\eta - \xi = n\pi/\alpha$, $n = \pm 1, \pm 2, \ldots$. The region of integration in (3.5) is the square with corners at (0,0), (1,0), (1,1), (0,1) in the $\xi\eta$-plane. This region is divided into diagonal strips by the lines $\eta - \xi = n\pi/\alpha$. In each strip $[\sin \alpha(\eta - \xi)]/\alpha(\eta - \xi)$ is of the same sign; $\rho(\xi - \eta)$ is defined so as to be constant in each strip as follows:

$$\rho(\xi - \eta) = \rho_1 = 1, \quad |\eta - \xi| < \pi/\alpha$$

$$\rho(\xi - \eta) = \rho_n = (-1)^{n+1}/(2n - 1)(\pi/2),$$

$$(n - 1)\pi/\alpha < |\eta - \xi| < n\pi/\alpha, \quad n \geq 2 \quad (4.1)$$

These definitions stem from assigning to $\rho(\xi - \eta)$ the value assumed by $[\sin \alpha(\eta - \xi)]/\alpha(\eta - \xi)$ on the centerline of the strip in question. The evaluation of (3.5) can now be accomplished in terms of the integral

$$I_h(x) = k^4\mu^2 \int_0^1 \int_0^1 G(x, \xi)G(x, \eta)\rho^*(\xi - \eta)d\xi d\eta \quad (4.2)$$

where $$\rho^*(\xi - \eta) = \begin{cases} 1, & |\eta - \xi| \leq h \\ 0, & |\eta - \xi| > h \end{cases} \quad (4.3)$$

For the midpoint ($x = 1/2$) it turns out that

$$I_h(1/2) = \frac{[1 - \cos (k/2)]^2}{\cos^2 (k/2)} - I_h^* \quad (4.4)$$

where

$$I_h^* = 2 \frac{\sin^2 (k/2)}{\sin^2 k} \left\{ -4 \cos \frac{k}{2} + \frac{3}{2} \cos kh + \frac{1}{2} \cos k(1 - h) + 1 + \cos \frac{k}{2} \cos k\left(\frac{1}{2} - h\right) - \frac{1}{2} kh \sin k(1 - h) - k\left(\frac{1}{2} - h\right) \sin kh \right\},$$

$$0 \leq h \leq 1/2 \quad (4.5)$$

** See reference 3.

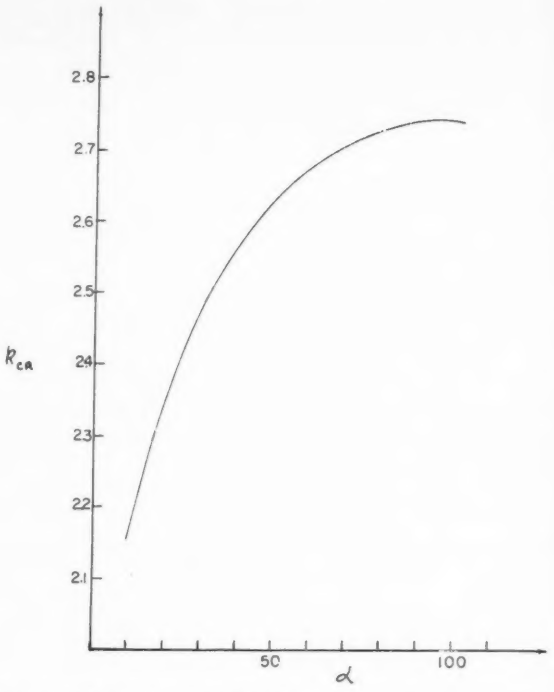

FIG. 2. Plot of k_{cr}, the critical load parameter, versus α, the correlation parameter.

$$I_h^* = 2 \frac{\sin^2 (k/2)}{\sin^2 k} \left\{ 1 - \frac{1}{2} k(1 - h) \sin k(1 - h) - \cos k(1 - h) \right\}, \quad \frac{1}{2} \leq h \leq 1 \quad (4.6)$$

$I_h(x)$ can be evaluated for other values of x, but the resulting expressions are even more bulky. If now $h_n = n\pi/\alpha$ and $\rho(\xi - \eta)$ is defined by (4.1), then

$$D^2[Y(x)] = I_{h_1}(x) + \rho_2[I_{h_2}(x) - I_{h_1}(x)] + \ldots + \rho_n[I_{hn}(x) - I_{hn-1}(x)] + \ldots \quad (4.7)$$

A finite sum of this form will suffice to cover the region of integration. If $x = 1/2$, then (4.4)–(4.6) are used.

Of primary interest is the relation between the applied load and the midspan displacement. In particular, the following two questions naturally arise.

(1) For what ranges of loading is the scatter in the additional displacement respectively less and greater than that in the initial displacement?

(2) For a given load, what is the probability that the absolute value of the midspan displacement lies between given bounds? Or, conversely, given the absolute midspan displacement, what is the probability that the load required to produce it lies between given bounds?

The first question can be answered as follows. For small loads the resulting displacements will also be small, and so will their dispersion; on the other hand, for loads near the Euler load the opposite will be the case. The boundary between the two ranges is best defined as that load for which

$$D^2[Y(x)] = D^2[W(x)] \tag{4.8}$$

although measures of dispersion other than the variance are possible, they are not so convenient. Once the integral in (3.5) is known as a function of k, this critical load is trivially determined. It of course depends on α and x; for $x = 1/2$ the variation of k_{cr} with α is shown in Fig. 2.

This information can also be used for the purpose of ascertaining reasonable values of α by comparing the critical load with that obtained in some simpler cases. For example, if

$$W(x) = A \sin \pi x$$

where A is a random variable, then

$$Y(x) = [k^2/(\pi^2 - k^2)]W(x)$$

Thus $D^2[Y(1/2)] = D^2[W(1/2)]$ when $k^4 = (\pi^2 - k^2)^2$, which leads to $k_{cr} = \pi/\sqrt{2} \approx 2.22$.

Likewise, assuming $W(x) = Ax(1 - x)$, one is led to

$$Y(x) = A \frac{2}{k^2} \left\{ \frac{1 - \cos k}{\sin k} k \cos kx - k \sin kx - \frac{k^2}{2}(1 - 2x) \right\}$$

and eventually to $k_{cr} \approx 2.205$. It is clear from Fig. 2 that similar values of k_{cr} are obtained in the general case for $\alpha \approx 10$.

Reduction of the original displacement $W(x)$ to a one-parameter family involves considerable restriction on the behavior of the column, since then its configuration is completely determined by a single value; in other words, its displacement might be said to be "completely dependent." Ordinarily, this would not seem to be a reasonable assumption, and hence the conclusion that such small values of α do not accurately reflect the physical situation.

The second question is more difficult; the following remarks are based on the assumption that $Y(1/2)$ is normally distributed. For any other given distribution, however, the same lines could be followed. In the first place, although $Y(1/2)$ is a normal random variable, $|Y(1/2)|$ is not. Letting $\sigma^2 = D^2[Y(1/2)]$ denote the variance of $Y(1/2)$, it readily follows that

$$m' = E[|Y(1/2)|] = \frac{1}{\sigma}\sqrt{\frac{2}{\pi}} \int_0^\infty t e^{-t^2/2\sigma^2}\, dt = \sqrt{\frac{2}{\pi}}\,\sigma \tag{4.9}$$

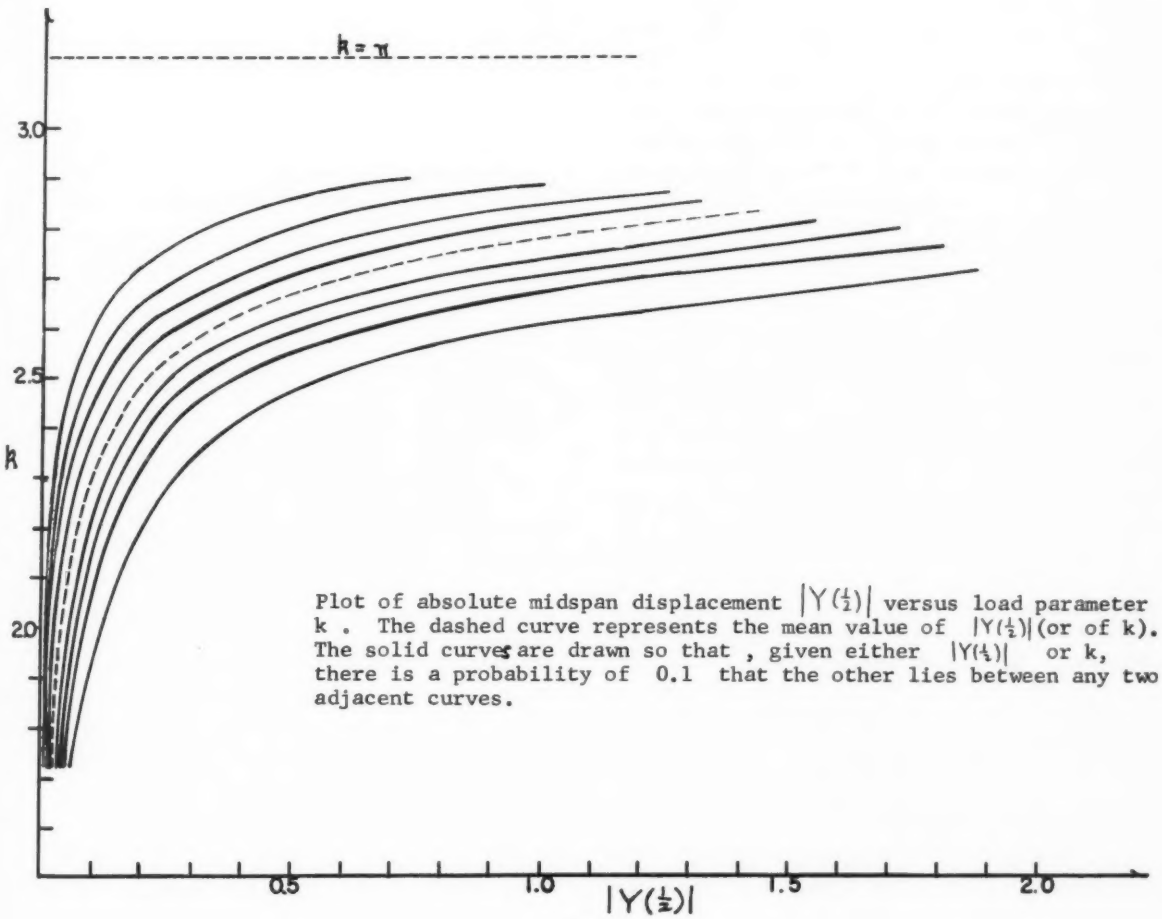

Plot of absolute midspan displacement $|Y(\frac{1}{2})|$ versus load parameter k . The dashed curve represents the mean value of $|Y(\frac{1}{2})|$ (or of k). The solid curves are drawn so that , given either $|Y(\frac{1}{2})|$ or k, there is a probability of 0.1 that the other lies between any two adjacent curves.

FIG. 3.

$$\sigma'^2 = D^2[\,|Y(1/2)|\,] = E[Y^2(1/2)] - (m')^2 = [1 - (2/\pi)]\sigma^2 \quad (4.10)$$

It is clear that

$$Pr\{m' < |Y| \leq m' + \beta\sigma\} = Pr\{Y \leq m' + \beta\sigma\} - Pr\{Y < m'\} + Pr\{Y \leq -m'\} - Pr\{Y < -m' - \beta\sigma\} \quad (4.11)$$

Letting
$$H(x) = \frac{2}{\sqrt{\pi}} \int_0^x e^{-u^2}\, du^* \quad (4.12)$$

and if $a > 0$, then

$$\left.\begin{aligned} Pr\{Y \leq a\} &= (1/2)[1 + H(a/\sqrt{2}\,\sigma)] \\ Pr\{Y \leq -a\} &= (1/2)[1 - H(a/\sqrt{2}\,\sigma)] \end{aligned}\right\} \quad (4.13)$$

Thus (4.11) becomes

$$Pr\{m' < |Y| \leq m' + \beta\sigma\} = H\left(\frac{1}{\sqrt{\pi}} + \frac{\beta}{\sqrt{2}}\right) - H\left(\frac{1}{\sqrt{\pi}}\right) \quad (4.14)$$

Similarly,

$$Pr\{m' - \beta\sigma < |Y| \leq m'\} = H\left(\frac{1}{\sqrt{\pi}}\right) - H\left(\frac{1}{\sqrt{\pi}} - \frac{\beta}{\sqrt{2}}\right), \quad \beta < \sqrt{\frac{2}{\pi}} \quad (4.15)$$

The information implicit in (4.14) and (4.15) can be presented graphically in the following manner. First m' is plotted against k, showing the relation between the mean or expected value of the absolute midspan displacement and the load. Next a small parameter δ is chosen and β is computed so that

$$H\left(\frac{1}{\sqrt{\pi}} + \frac{\beta}{\sqrt{2}}\right) - H\left(\frac{1}{\sqrt{\pi}}\right) = \delta$$

Using this value of β, the quantity $m' + \beta\sigma$ is then plotted against k. These two curves have the property that for a given value of the load parameter k, there is a probability of δ that the value of the absolute midspan displacement $|Y(1/2)|$ lies between them. Alternatively, given $|(Y(1/2)|$ the probability that k lies between the curves is also δ. Proceeding in the same way, as many curves of this family as are required can be drawn. Fig. 3 is typical of the end result, and was constructed using the correlation function defined in (4.1) with $\alpha = 100$ and $\delta = 0.1$. Thus given either k or $|Y(1/2)|$ there is a probability of 0.1 that the other lies between any two adjacent curves. By interpolation the answer to question (2) above is readily found.

(5) This paper deals with the effect of random initial displacements on the load–deflection relation of an otherwise uniform column.

The principal result, at least for the designer, lies in the possibility of arriving at estimates for the answer to the following question: given either the load or absolute midspan displacement, what is the probability that the other lies between preassigned bounds? In carrying out the necessary calculations, some assumptions about the statistical nature of the initial displacement are required. In particular, the mean, variance, and correlation of that random function must be specified, though they do not necessarily have to take the form used here. The assumption of stationarity made above, while reasonable in many cases, is not essential to the argument, and can be dropped at the cost of more extended computations.

It is clear that the method outlined here is applicable to a much wider class of problems. An obvious generalization is to columns with other end conditions. Such problems will require considerably more elaborate computations since the Green's functions are then much more complicated.

More important is the observation that the results of Section 3 are valid for any boundary-value problem, whether in ordinary or partial differential equations, whose solution can be represented by a Green's function integral. Thus, results qualitatively similar to those in Section 4 can be achieved, at least in principle, for any such problem. Indeed, the general ideas involved may be used in any situation where one random function depends on another by means of an appropriate integral.

Appendix

A random variable ϕ is characterized by its distribution function $F(t)$ or its frequency function $f(t) = F'(t)$. These are defined so that $F(t)$ is the probability that $\phi \leq t$, i.e.,

$$\Pr\{\phi \leq t\} = F(t) = \int_{-\infty}^{t} f(\tau)d\tau \quad (A.1)$$

This and all similar integrals appearing later are to be considered in the Lebesgue-Stieltjes sense.

The mean or expected value of ϕ is defined by

$$m = E(\phi) = \int_{-\infty}^{\infty} \tau dF(\tau) = \int_{-\infty}^{\infty} \tau f(\tau)\, d\tau \quad (A.2)$$

It can easily be shown that

$$E(\phi_1 + \ldots + \phi_n) = E(\phi_1) + \ldots + E(\phi_n) \quad (A.3)$$

and that, if c is a constant,

$$E(c\phi) = cE(\phi) \quad (A.4)$$

The most important parameter measuring the dispersion of a distribution is its variance, defined as

$$\sigma^2 = D^2(\phi) = E[(\phi - m)^2] = E(\phi^2) - m^2 \quad (A.5)$$

The quantity σ is called the standard deviation. If c is a constant,

(*Continued on page 320*)

* The function $H(x)$ is tabulated in reference 4.

Supersonic Boom of Wing-Body Configurations

I. L. RYHMING* AND Y. A. YOLER**

Boeing Scientific Research Laboratories

Summary

The supersonic boom in steady, level flight of a wing-body configuration is due to the effects of body volume, wing volume, wing incidence or lift, and wing-body interference. The contribution in the far field of each of these factors can, in any given azimuthal plane, be represented as that of an equivalent body of revolution. This concept is developed to investigate the possibilities of using interference among the components of a wing-body configuration to reduce or suppress the boom due to lift. Results of wind tunnel experiments are also presented and discussed in light of the theoretical indications.

Symbols

A	=	aspect ratio
B	=	boom intensity on the ground
C	=	chord length (ft.)
C_L	=	lift coefficient
C_D	=	drag coefficient
d	=	body diameter (ft.)
E	=	elliptic integral of the second kind
F	=	function defined by Eq. (2)
f_R	=	reflection factor
f_v	=	volume shape-factor
f_L	=	lift shape-factor
$f(\gamma)$	=	$2^{1/4}\gamma/(\gamma+1)^{1/2}$
H	=	Heaviside step function
h	=	flight altitude (ft.)
L	=	lift per unit axial foot of aircraft (lbs./ft.)
M	=	free-stream Mach number
N	=	nose length (ft.)
p	=	pressure (lbs./ft.^{2})
q	=	dynamic pressure $(\gamma p_\infty/2)M^2$ (lbs./ft.^{2})
r	=	radial coordinate measured from the body axis (ft.)
R	=	radius of the body (ft.)
S	=	cross-sectional area (ft.^{2})
t	=	wing thickness (ft.)
W	=	total weight of aircraft (lbs.)
x, y, η	=	axial coordinates (ft.)
α	=	angle of attack (radians)
β	=	$(M^2-1)^{1/2}$
γ	=	ratio of specific heats
λ	=	length of aircraft (ft.)
θ	=	meridian plane
σ	=	shock intensity $(p-p_\infty)/p_\infty$

(I) General Considerations

THE THEORETICAL METHODS for the determination of the pressure fields due to volume at large distances from three-dimensional bodies were developed by Whitam.[1, 2] For a pointed, slender body of revolution, the intensity of the bow shock is given by the familiar formula

$$\sigma = \frac{\Delta p}{p_\infty} = \frac{f(\gamma)\beta^{1/4}}{r^{3/4}}\left[\int_0^{y_0} F(y)\,dy\right]^{1/2} \qquad (1)$$

where $f(\gamma) = 2^{1/4}\gamma/(\gamma+1)^{1/2}$, $y_0 > 0$ is a certain zero† of the F-function given by

$$F(y) = \frac{1}{2\pi}\int_0^y \frac{S''(\eta)}{\sqrt{y-\eta}}\,d\eta \quad [F(y)=0;\quad y<0] \qquad (2)$$

r is the radial distance from the axis, y is the characteristic variable‡ $y = x - \beta r$, and S is the cross-sectional area of the body $S = \pi R^2$.

Whitham showed further that, for three-dimensional bodies, the intensity of the bow shock due to volume is dependent on both the radial distance r and the meridian plane θ, but that in any meridian plane θ the pressure field can be interpreted as being due to a certain body of revolution. This principle was demonstrated by Walkden[3] to be valid for complete aircraft configurations including the effects of body volume, wing volume, incidence, and wing-body interference—namely, in any meridian plane θ it is possible to define a body of revolution which, in the far field, has a pressure signature identical to that of the actual aircraft in that direction.

With respect to the effects of volume, the intensity of the boom in the far field of a body of length λ and maximum equivalent body diameter d_{e_v} may be expressed in the form

$$B_v = \Delta p_{v_G}/P_{\text{ref.}} = f_v f_R[f(\gamma)/\sqrt{3}][\beta^{1/4}d_{e_v}(\theta)/\lambda^{1/4}r^{3/4}] \qquad (3)$$

where Δp_{v_G} is the pressure jump across the nose shock and its reflection on the ground. The reflection factor f_R is equal to unity across the incident shock. It is very close to two for a shock reflected by a smooth, level plane and somewhat less than two for reflections over rough terrain or on inclined surfaces. The reference pressure $P_{\text{ref.}}$ is equal to the free-stream pressure p_∞ in a homogeneous, isothermal atmosphere, but is modified by the pressure and temperature gradients in a nonhomogeneous atmosphere.[7] The approximate ex-

Presented at the Aerodynamics Session, IAS 28th Annual Meeting, New York, January 25–27, 1960. Revised and received April 30, 1960.

* Staff Member, Flight Sciences Laboratory. Presently at Convair, San Diego.

** Head, Flight Sciences Laboratory.

† The determination of the proper y_0 is discussed in the next section.

‡ This representation of the characteristic variable is a first-order approximation which is satisfactory in the vicinity of the body.

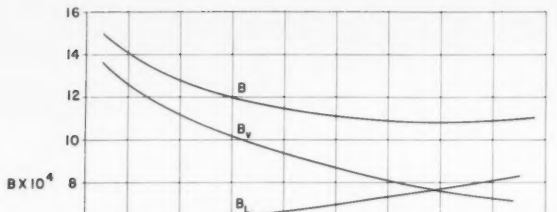

FIG. 1.

pression $P_{\text{ref.}} = \sqrt{p_\infty p_G}$, where p_G is the atmospheric pressure at the ground level and p_∞ the free-stream pressure at the flight altitude, is satisfactory for engineering purposes for flight in the troposphere.[4] To this approximation, the relation between B and Δp is given by

$$\Delta p = p_G B \exp(-h/46{,}000) \tag{4}$$

where h is the altitude of flight with respect to the ground, in feet.

Although, according to (1) and (2), the boom due to volume is, in principle, dependent on the geometry of the body (i.e., on the distribution of cross-sectional area in the axial direction) it has been known that f_v, the volume shape-factor, is approximately equal to unity and highly insensitive to the body geometry once the maximum diameter of the equivalent body of revolution due to volume and its length are given.[5, 6]

The determination of the boom due to lift is particularly simple in the case of a flat triangular wing with subsonic leading edges.[3] The equivalent body of revolution due to lift* in this case is a cone of length C equal to the maximum chord and with semiapex angle given by[6]

$$\theta_{c_e} = (A/4)\sqrt{\alpha\beta/E(k)} \tag{5}$$

where A is the aspect ratio, α the angle of attack, $E(k)$ the elliptic integral of the second kind with modulus $k = \sqrt{1 - (\beta A/4)^2}$.

In the more general case[3] the derivative with respect to the axial coordinate x of the cross-sectional area of the equivalent body of revolution due to lift, S_{e_L}, is related to the lift distribution $L(x)$ per foot of axial length of aircraft in the following form:

$$S_{e_L}' = \beta L/2q \tag{6}$$

where $q = (\gamma p_\infty/2)M^2$ is the dynamic pressure.

Integration of Eq. (6) with respect to the axial coordinate gives the maximum diameter of the equivalent body of revolution due to lift as

$$d_{e_L} = \left[\frac{2\beta}{\pi q}\int_0^{x_0} L(x)\,dx\right]^{1/2}$$

where x_0 is a certain zero of the lift distribution L and is determined by the same rules which apply to the determination of y_0 corresponding to the proper zero of the F-function in the volume case. In particular, if $L \geqslant 0$ everywhere, then

$$d_{e_L} = \left[\frac{2\beta W}{\pi q}\right]^{1/2} = \frac{2\sqrt{W}}{\sqrt{\pi\gamma p_\infty}}\frac{\beta^{1/2}}{M} \tag{7}$$

where W is the total weight of the aircraft. In this case the distribution of lift does not influence the maximum diameter of the equivalent body of revolution due to lift but can be accounted for by a "shape factor" as in the volume case.

Although the boom due to lift is thus dependent on the distribution of lift in the axial direction, or on the distribution of the cross-sectional area of the equivalent body of revolution, in view of the remarks made previously with respect to the boom due to volume it is reasonable to expect that the boom due to lift should be relatively insensitive to the distribution of lift over the wing once its length and total lift have been specified. These conclusions appear to be substantially correct and, by substituting Eq. (7) for the diameter in Eq. (3) and using a shape factor due to lift, the boom due to lift can be expressed as

$$B_L = \frac{2f_L f_R f(\gamma)}{\sqrt{3\pi\gamma p_\infty}}\frac{\beta^{3/4}}{M}\frac{W^{1/2}}{C^{1/4}\gamma^{3/4}} \tag{8}$$

The difference in the Mach number dependence of the boom due to lift and due to volume may be noted. The lift shape-factor f_L is equal to one for the triangular wing with subsonic leading edges, and is insensitive to other distributions of lift.

It follows from the principle of equivalence that the total boom of a configuration of given boom due to volume B_v and boom due to lift B_L is at most roughly of the order of

$$B_{max} \approx (B_v^2 + B_L^2)^{1/2} \tag{9}$$

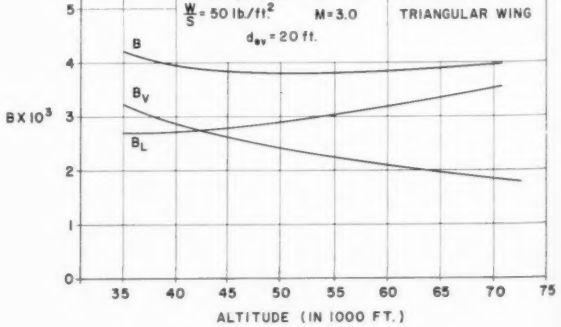

FIG. 2.

* The boom due to lift is a maximum under the wing in the plane of the lift vector and the free-stream velocity vector ($\theta = -\pi/2$). All equations related to lift in this paper refer to the boom in this plane.

It may be noted that, in general, for operation at the lower altitudes of relatively small aircraft the boom due to volume makes the major contribution to the total boom. Because of this fact, coupled with the simplicity of the equation predicting the boom due to volume, it has become common practice to represent aircraft by a nose shape[8] and to correlate the supersonic boom of aircraft by equations related to the volume effect.[9] That this is justified is evident from Fig. 1 which shows the boom of an aircraft possessing roughly the characteristics of those reported in reference 9. For altitudes below 45,000 ft., at which the passes were made, the boom due to volume makes the major contribution to the total boom.*

It can be seen from Eq. (7), however, that for large aircraft operating at higher altitudes, the diameter of the equivalent body due to lift may become much larger than that due to volume. Even for the supersonic transport type of aircraft of relatively low slenderness ratio and wing loading considered in Fig. 2, the boom due to lift is seen to make the major contribution to the total boom for altitudes above roughly 50,000 ft.

These considerations have prompted the present study of the boom due to lift of aircraft. Although such unconventional techniques as thrust vectoring (partial or total support of the aircraft by propulsive thrust) may be effective in this connection, the present study is limited to a consideration of the possibilities of interference to reduce the boom due to lift. The underlying principle is that if the effect in the far field in any direction of a lifting wing-body combination can be expressed as that of an equivalent body of revolution, the problem of minimizing the boom of an aircraft of given length consists essentially of minimizing the diameter of the equivalent body of revolution.

It follows that, for a given body diameter fixed by operational considerations, the maximum diameter of the equivalent body of revolution of the lifting wing-body configuration can be no smaller than the maximum diameter of the equivalent body due to volume of the aircraft. From Eq. (7), the condition $d_{e_T} \geqslant d_{e_L}$ is expressed by

$$d_{e_T} \geqslant \left(\frac{2\beta W}{\pi q}\right)^{1/2} = \frac{2\sqrt{W}}{\sqrt{\pi\gamma p_\infty}} \frac{\beta^{1/2}}{M} \tag{10}$$

If this inequality is satisfied, the boom due to lift can, in principle, be made to contribute nothing in addition to the boom due to volume. This concept is developed further in the next section.

(II) Theoretical Considerations

We introduce a cylindrical coordinate system x, r, θ. The x-axis is in the streamwise direction and the origin is placed at the intersection of the wing leading edge and the x-axis in the plane of symmetry of the airplane (see Fig. 3).

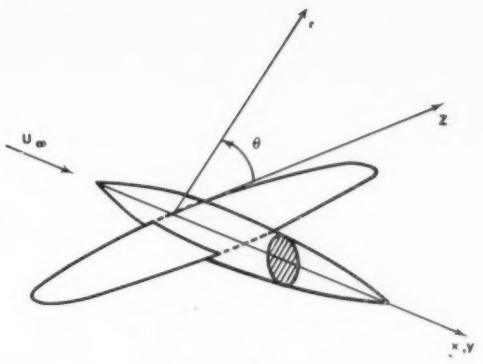

FIG. 3.

The asymptotic value of the bow shock strength for the airplane configuration as $r \to \infty$ is[3]

$$\sigma = \frac{p - p_\infty}{p_\infty} = 2^{1/4}\gamma(\gamma + 1)^{-1/2}\beta^{1/4}r^{-3/4} \times \left[\int_0^{y_0} F(y;\theta)\, dy\right]^{1/2} \tag{11}$$

If it is assumed that the equivalent bodies of revolution for wing thickness and wing lift are centered on the x-axis, the function $F(y;\theta)$ has the following form:

$$2\pi F(y;\theta) = H(y+N)\int_{-N}^{y} \frac{S''(\eta)}{\sqrt{y-\eta}}\, d\eta - H(y)\int_0^y \frac{S_1''(\eta)}{\sqrt{y-\eta}}\, d\eta + H(y)\int_0^y \frac{S_2''(\eta)}{\sqrt{y-\eta}}\, d\eta - H(y)\,(1/2)\beta\sin\theta\int_0^y \frac{S_3''(\eta)}{\sqrt{y-\eta}}\, d\eta \tag{12}$$

The variable y appearing in the above formulas is a function of x and r and describes the characteristics in a plane θ = constant. The four integrals in Eq. (12) give the contribution to $F(y;\theta)$ of body volume, wing-body interference, wing volume, and wing lift, respectively. $S(y)$ is defined as the body cross-sectional area $\pi R^2(y)$, where $R(y)$ is the body radius. $S_1(y)$ is defined as the cross-sectional area of a certain body of revolution which accounts for the interference effects. Also $S_1'(y) = -4R(y)t'(y)$, where $t(y)$ is the wing thickness in the central section of the symmetrical wing.[3] $S_2(y) = \pi R_2^2(y)$ is the cross-sectional area of the equivalent body of revolution for wing volume, and $S_3(y) = \pi R_3^2(y)$ is the cross-sectional area of the equivalent body of revolution for wing lift.† H is the Heaviside step function taking into account the proper location of the body nose ($y = -N$) and the intersection of the wing leading edge with the x-axis at $y = 0$.

The upper limit y_0 in the integral in Eq. (11) is defined as the first zero of the F-function apart from $y = 0$ itself. However, if the F-function exhibits

* Note that for purposes of comparison the boom defined as $\Delta p/P_{ref.}$, rather than the pressure jump Δp, is plotted in Figs. 1 and 2. Thus, although B_L is increasing with flight altitude, the shock intensity on the ground decreases with altitude by virtue of Eq. (4).

† For the determination of $S_2(y)$ and $S_3(y)$, see reference 3.

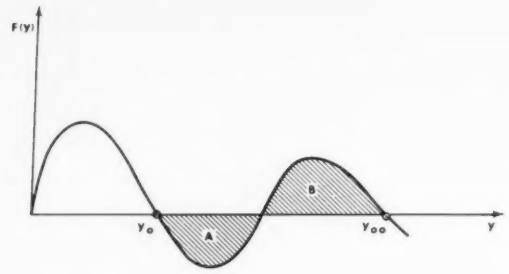

FIG. 4.

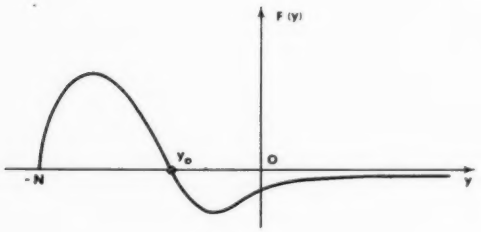

FIG. 5.

several zeros, the proper y_0 value must be chosen as follows:[1] Suppose that the F-curve is of the form shown in Fig. 4, and consider the two expansive zeros y_0 and y_{00}. If the area B is greater than the area A, the upper limit in Eq. (11) is y_{00}. Otherwise, y_0 is the proper limit.

In Eqs. (11) and (12) no discontinuities in the S-function or its first or second derivatives are allowed. However, in the following we wish to consider wing-body configurations which may possess discontinuities in the first or second derivatives of their cross-sectional area distributions. As shown by Whitham,[1] the Riemann integral of the type

$$F(y) = \frac{1}{2\pi}\int_0^y \frac{S''(\eta)}{\sqrt{y-\eta}}\,d\eta \qquad (13)$$

is then to be replaced by the Stieltjes integral:

$$F(y) = \int_0^\infty \left[\frac{2}{\beta R(\eta)}\right]^{1/2} h\left(\frac{y-\eta}{\beta R(\eta)}\right)\frac{dS'(\eta)}{2\pi} \qquad (14)$$

where $h[(y-\eta)/\beta R(\eta)]$ is a function defined in reference 1. Therefore, whenever an S-function occurs in Eq. (12) which has discontinuities in the first or second derivatives, the integrals of the type given by Eq. (13) will be replaced by Eq. (14).

For a conventional lifting configuration, the F-curve for $\theta = -\pi/2$, which is the case we wish to treat in this paper, will have a form shown in Fig. 4. Generally, if the wing apex is upstream of y_0, the area A will be small or can even be made to disappear. Therefore, the integral over the F-function will take on a fairly large value compared to that for the isolated body, even for small angles of attack.

In order to make the area under the F-curve as small as possible for a wing-body combination given the body, wing plan form, and wing thickness distribution, we can first conclude that the wing apex should be so placed relative to y_0 of the body F-curve that the area A will be as large as possible. That is, we shall allow the aerodynamic interference effects between the body and the wing to act in a most favorable way. Once the form of the aircraft components are known, this can best be studied by means of the F-curves of the components, because the individual F-curves describe the flow pattern of each component. In this way, the most favorable location of the wing apex relative to the body can be determined. However, by modifying the area distribution of the body along the wing-body juncture, a considerable reduction of the F-curve area, and hence the boom intensity, can be obtained.

Consider a wing-body combination in which the body consists of a nose section in the interval $-N < y < 0$ and a cylindrical section for $y > 0$. For simplicity, we suppose that the nose cross-sectional area $S(y)$ is a continuous function with continuous first and second derivatives. We also impose these conditions on S_1, S_2, and S_3. Since $S''(0) = 0$ for $y > 0$, the first integral in Eq. (12) has the following form for this combination:

$$\int_{-N}^{y} \frac{S''(\eta)}{\sqrt{y-\eta}}\,d\eta \qquad \text{for} \quad -N < y < 0 \qquad (15)$$

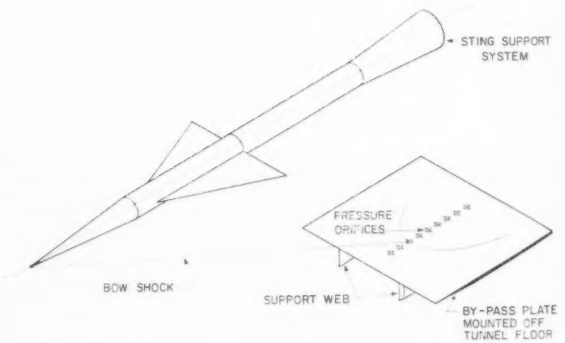

FIG. 6. Schematic illustration of the experimental setup.

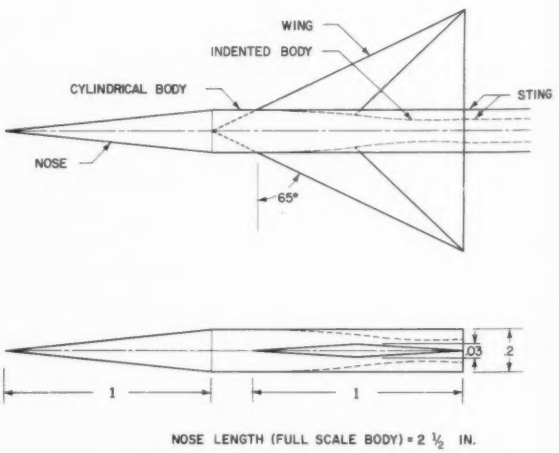

FIG. 7. Wing-body model configurations.

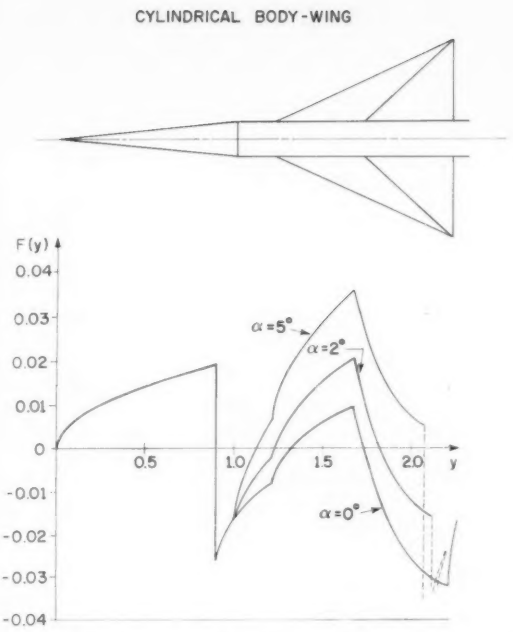

FIG. 8. The F-curves for the cylindrical body-wing ($M = 1.41$)

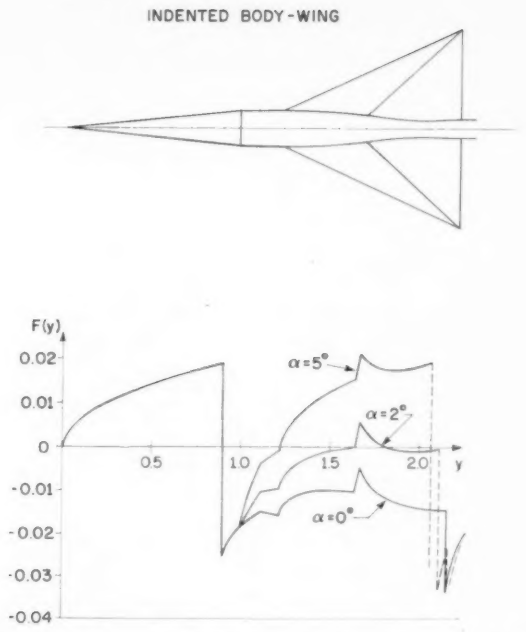

FIG. 9. The F-curves for the indented body-wing ($M = 1.41$).

$$\int_{-N}^{0} \frac{S''(\eta)}{\sqrt{y-\eta}}\,d\eta \qquad \text{for} \quad y > 0 \tag{16}$$

The F-curve for the body has only one zero at y_0, and may have a form like that shown in Fig. 5. Now, by adding the F-curves for the wing thickness, wing lift, and wing-body interference starting at $y = 0$, we will have a situation very much like that shown in Fig. 4. However, suppose that we replace the cylindrical portion of the body by an indented section $S^*(y)$ for $y > 0$. By virtue of Eq. (16) for $\theta = -\pi/2$, Eq. (12) has the form

$$2\pi F\left(y; -\frac{\pi}{2}\right) = \int_{-N}^{0} \frac{S''(\eta)}{\sqrt{y-\eta}}\,d\eta + \int_{0}^{y} \frac{S^{*\prime\prime}(\eta)}{\sqrt{y-\eta}}\,d\eta - \int_{0}^{y} \frac{S_1''(\eta)}{\sqrt{y-\eta}}\,d\eta + \int_{0}^{y} \frac{S_2''(\eta)}{\sqrt{y-\eta}}\,d\eta + (1/2)\beta \int_{0}^{y} \frac{S_3''(\eta)}{\sqrt{y-\eta}}\,d\eta \tag{17}$$

If, for a given Mach number and angle of attack, the function $S^*(y)$ is chosen so that the F-curve for the combination for $y > 0$ reduces to

$$2\pi F\left(y; -\frac{\pi}{2}\right) = \int_{-N}^{0} \frac{S''(\eta)}{\sqrt{y-\eta}}\,d\eta \tag{18}$$

(that is, if it has the same form as for the isolated body itself), then the area B does not appear at all. Therefore, in such a case the boom of the configuration is determined only by the nose geometry of the configuration. In order to achieve this result, the function $S^*(y)$ has to be chosen so that:

$$S^{*\prime\prime}(y) - S_1''(y) + S_2''(y) + (1/2)\beta S_3''(y) = 0 \tag{19}$$

Integrating Eq. (19) once gives

$$S^{*\prime}(y) - S_1'(y) + S_2'(y) + (1/2)\beta S_3'(y) = 0 \tag{20}$$

since for $y = 0$, $S^{*\prime}(0) = S_1'(0) = S_2'(0) = S_3'(0) = 0$. Introducing

$$S^*(y) = \pi R^{*2}(y) \qquad S_1'(y) = -4R^*(y)t'(y)$$
$$S_2(y) = \pi R_2^2(y) \qquad S_3(y) = \pi R_3^2(y)$$

we arrive at the following equation for the unknown function $R^*(y)$:

$$R^*(y)[R^{*\prime}(y) + (2/\pi)t'(y)] + R_2(y)R_2'(y) + (1/2)\beta R_3(y)R_3'(y) = 0 \tag{21}$$

This is a so-called Abel differential equation of the second kind, the solution of which, in general, is not known in closed form.* However, for thin wings the function $t'(y)$ is nowhere large, and a first approximation to the solution of Eq. (21) for $t'(y) = 0$ can be written down immediately:

$$R^{*2}(y) + R_2^2(y) + (1/2)\beta\, R_3^2(y) = \text{constant}$$

For $y = 0$, $R^{*2}(0) = R_0^2$, say, and $R_2(0) = R_3(0) = 0$. Therefore**

$$R^{*2}(y) = R_0^2 - R_2^2(y) - (1/2)\beta R_3^2(y) \tag{22}$$

Eq. (22) can be used as a first approximation in an iterative solution of Eq. (21). In order to get a physically valid solution, it is necessary that $R^*(y) > 0$. This leads to limitations on wing plan form, wing thickness distribution, and angle of attack. For a thin wing, an approximate expression for the maximum

* See, for example, reference 10, p. 26.

** Note that Eq. (22) contains the Area Rule.

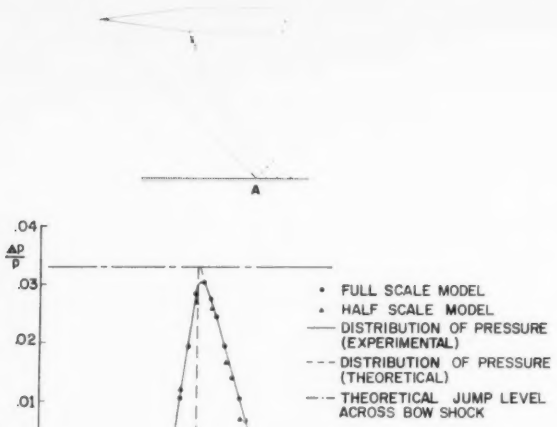

FIG. 10. Pressure signature of a cone-cylinder on a plane passing through A.

lift coefficient to suppress the boom due to lift is readily derived from Eq. (22) by setting $R^*(C) = 0$ and $R_2(y) = 0$, and is given by

$$C_{L_{max}} \leqslant (2\pi/\beta A)(d_{ep}/C)^2 \qquad (23)$$

The condition (10) is readily derived from Eq. (23) (see reference 6).

(III) Experimental Investigations

To obtain experimental evidence of the effect of interference with respect to the boom due to lift in the far field, a series of experiments were performed with triangular wing-body configurations in the Boeing 4 × 4 ft. supersonic blowdown wind tunnel. A schematic layout of the tests is shown in Fig. 6. The static pressure field of the model was measured, by a bank of manometers, on a smooth flat plate close to one of the tunnel walls. The runs were made at Mach numbers of 1.41 and 2.00.

Wing-Body Configurations

The wing-body configurations consisted of a conical nose of fineness ratio equal to 5.0, a cylindrical or an indented body, and a triangular wing sweptback at 65 degrees (Fig. 7). The aspect ratio of the wing was 1.87, and the symmetrical double-wedge section was 3 per cent thick. The models were supported by stings whose diameters were tapered gently from the base diameter of the after-body to the wind-tunnel model support system. The stings may be assumed to represent roughly the wake or the jet trailing the body. Tests at angle of attack were performed with stings which were bent to the appropriate angle.

The cylindrical body has a constant diameter equal to the maximum diameter of the nose. The indented body was designed to produce no additional boom due to lift up to an angle of attack of 2° at $M = 1.41$. The F-curves for the cylindrical and indented configurations at various angles of attack are shown in Figs. 8 and 9. These F-curves account for the boom due to body volume, wing volume, wing lift, and wing-body interference.*

Boundary-Layer Effects

Whereas in the actual case the pressure signature of the aircraft on the ground is not affected by a boundary

* For the lifting cases, the shape of the F-curves downstream of the wing trailing edge is difficult to estimate owing to the trailing vortex system. It may be noted also that since the equivalent bodies of revolution due to body volume and wing volume exhibit discontinuities in S' and S'', the F-curves have been calculated using Eq. (14) instead of Eq. (13).

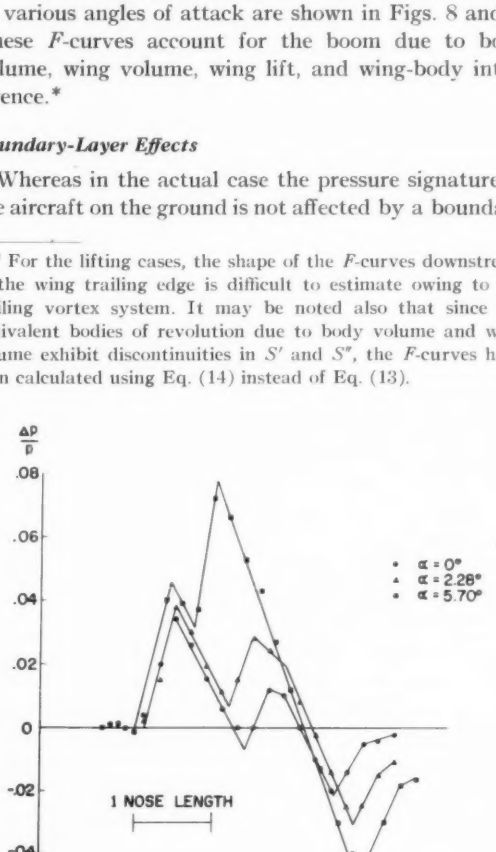

FIG. 11(a). The effect of angle of attack on the pressure signature of the cylindrical body-wing configuration at 11 nose lengths ($M = 2.0$).

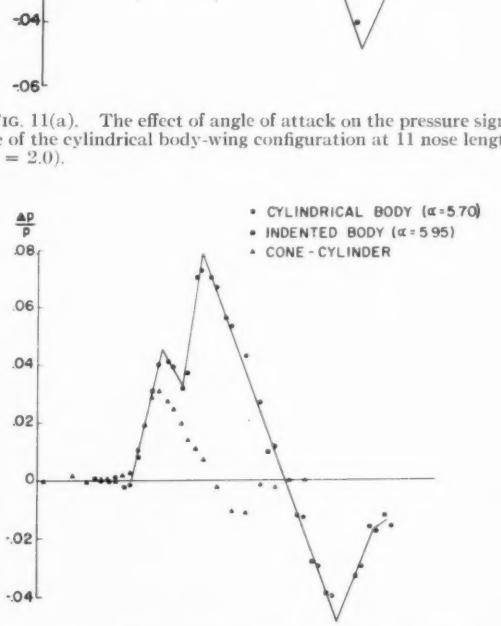

FIG. 11(b). The pressure signatures at 11 nose lengths of the cylindrical and indented body-wing configurations at $\alpha \cong 6°$ compared with that of a cone-cylinder at $\alpha = 0°$, $M = 2.0$.

layer on the ground, the pressure distribution on the plate in the wind tunnel is influenced by the boundary layer. Investigations on pressures due to shock wave–boundary layer interactions are to be found in the literature[12] in cases where the inviscid pressure upstream and downstream of the shock wave is constant. In the present case, however, the inviscid pressure behind the shock wave has a strong gradient, and the amplitude of the N-wave may be modified by the boundary layer.

To identify the effect of the boundary layer on the inviscid pressure distributions in the present experiments, two devices were employed. First, from Figs. 8 and 9 it is evident that for the cylindrical body at $\alpha = 0$ and for the indented body at $\alpha = 0°$, 2°, the strength of the bow shock should be determined by the conical nose. Hence the pressure distribution of the wing-body configurations were compared to that of a cone-cylinder body of revolution which had the same nose length and maximum diameter as those of the wing-body configurations and was tested at the same positions above the plate. Secondly, the intersection point of the bow shock and the first characteristic of the expansion fan from the shoulder of the cone-cylinder was determined by a numerical and graphical process from Kopal's tables,[11] and the inviscid pressure rise on the plate was calculated at that point.[6] The calculated pressure difference was compared to that measured in the tunnel for the same height of the body above the plate (Fig. 10).

(V) Results and Discussion

The results of the investigation on boundary-layer effects are shown in Fig. 10. The amplitude of the bow wave is rounded out and reduced by the boundary layer. The reduction (which should depend on the Reynolds number) does not appear to be large (roughly 10 per cent) under the conditions of the present experiments and is not significantly greater than the range of experimental inaccuracy. The sharp profile of the jump, on the other hand, is smeared by the boundary layer.

Representative results of wind tunnel measurements of the pressure signatures of cylindrical and indented body-wing configurations and of a cone-cylinder body of revolution at $M = 1.41$ and $M = 2.00$ at a radial distance equal to eleven nose lengths are presented in Figs. 11 and 12.* The accuracy of measurements made at much larger distances (with much smaller models) were not satisfactory with the particular wind tunnel facility and instrumentation used. Hence, although at distances of the order of eleven nose lengths the pressure distribution is not representative of the "far field," salient features of the effects of interference and body indentation on the boom due to lift are nevertheless brought out.

From Fig. 11(a), the rise to prominence of the pressure peak due to lift with increasing angle of attack

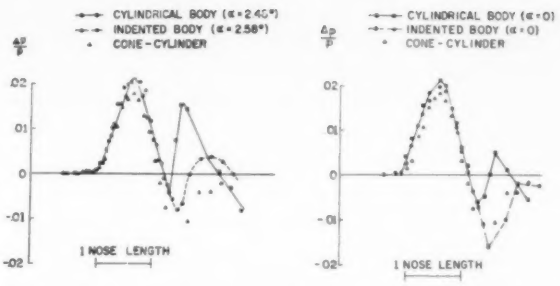

FIG. 12(a), *left;* (b), *right.* The pressure signatures at 11 nose lengths of the cylindrical and indented body-wing configurations compared with that of a cone-cylinder at $\alpha = 0°$, $M = 1.41$.

is evident. In fact, it is seen from Fig. 11(b) that the effect of the indentation at high angles of attack, in cases where the boom due to lift dominates over that due to volume, is negligible as expected. The pressure field due to lift is already reinforcing the pressure field of the nose, resulting in an initial peak which is substantially greater than the peak pressure for the cone-cylinder body of revolution which has the same equivalent diameter due to volume.

The effect of interference becomes more apparent at the design Mach number and near the design angle of attack of 2° [Fig. 12(a)] at which the boom due to lift should, theoretically, be suppressed completely. The pressure pulse due to lift is seen to be substantially smaller for the indented body, and the reinforcement in the far field of the first peak by the second should similarly be of lesser consequence. At zero angle of attack the indented body, designed to compensate for the pressure rise due to both wing volume and lift up to 2° angle of attack, should overcompensate the pressure pulse due to wing volume alone. That this is so is shown in Fig. 12(b) in which the indented body has a larger negative pulse than the cone-cylinder body of revolution, while the cylindrical body-wing at zero angle of attack has a positive pulse due to wing volume. The pressure pulse due to lift in Fig. 12(a) of the indented body-wing at 2.58° angle of attack is no larger than the peak due to wing volume in Fig. 12(b) of the cylindrical body-wing at $\alpha = 0$ which, according to the F-curve given in Fig. 8, should not contribute significantly to the boom due to the nose volume in the far field.

(VI) Conclusions

The representation of the components of lifting wing-body configurations contributing to the boom in the far field by equivalent bodies of revolution offers a simple concept whereby the possibilities of utilizing interference in suppressing the boom of wing-body combinations can be evaluated. For large, slender aircraft operating at high altitudes, the boom due to lift assumes importance. The boom due to lift can be suppressed by aerodynamic interference so long as the boom due to lift alone is of the order of the boom due to vol-

* Additional measurements have been reported in references 6 and 7.

ume of the body. When the boom due to lift is much larger than the boom due to volume, interference becomes ineffective. These conclusions are substantiated by wind tunnel experiments with wing-body configurations.

References

[1] Whitham, G. B., *On the Propagation of Weak Shock Waves*, J. Fluid Mech., Vol. 1, p. 290, September, 1956.

[2] Whitham, G. B., *The Flow Pattern of a Supersonic Projectile*, Comm. in Pure and Appl. Math., Vol. 5, p. 290, August, 1952.

[3] Walkden, F., *The Shock Pattern of a Wing-Body Combination far from the Flight Path*, The Aeronautical Quarterly, Vol. 9, p. 164, May, 1958.

[4] Warren, C. H. E., *An Estimation of the Occurrence and Intensity of Sonic Bangs*, RAE TN Aero. 2334, September, 1954.

[5] Ryhming, I. L., *The Supersonic Boom of a Projectile Related to Drag and Volume*, Boeing Document No. DI-82-0023, October, 1959. Journal of the Aerospace Sciences, Vol. 28, No. 2, pp. 113–118, February 1961.

[6] Ryhming, I. L., and Yoler, Y. A., *Supersonic Boom of Wing-Body Configurations*, IAS 28th Annual Meeting, Preprint 60-20, New York, January, 1960. Also, Boeing Document DI-82-0034, 1959.

[7] Ryhming, I. L., Yoler, Y. A., and Aoki, Y., *Shock-Wave Noise of Supersonic Aircraft*, SAE National Aeronautic Meeting, Preprint 166B, New York, April, 1960.

[8] Struble, R. A., et al., *Theoretical Investigations of Sonic Boom Phenomena*, WADC TR 57-412, August, 1957.

[9] Maglieri, D. J., et al., NASA TN D-48, September, 1959.

[10] Kamke, E., *Differentialgleichungen*, Vol. 1, Chelsea Publishing Co., New York, 1948.

[11] Kopal, Z., *Tables of Supersonic Flow around Cones*, MIT Cambridge, 1947.

[12] Barry, F. W., Shapiro, A. H., and Neumann, E. P., Journal of the Aeronautical Sciences, Vol. 18, pp. 229–238, 1951.

✦ ✦ ✦

Buckling of a Column (*Continued from page 312*)

$$D^2(c\phi) = c^2D^2(\phi) \tag{A.6}$$

If $\phi_1, \ldots, \phi_n$ are independent random variables, i.e., if

$$E(\phi_i\phi_j) = E(\phi_i)E(\phi_j) \tag{A.7}$$

then

$$D^2(\phi_1 + \ldots + \phi_n) = D^2(\phi_1) + \ldots + D^2(\phi_n) \tag{A.8}$$

For random variables which are not independent,

$$E(\phi_i\phi_j) = E(\phi_i)E(\phi_j) + \rho(i, j)\{D^2(\phi_i)D^2(\phi_j)\}^{1/2} \tag{A.9}$$

where $\rho(i, j)$ is the correlation function. A consequence of this definition is that $|\rho| \leq 1$.

Many distributions are in common use. Of particular interest is the normal distribution defined by its frequency function

$$f(t) = (1/\sigma\sqrt{2\pi})e^{-(t-m)^2/2\sigma^2} \tag{A.10}$$

One important property of a normally distributed random variable is that its distribution is completely determined by only two parameters, the mean and variance. Another source of the importance of this distribution is the central limit theorem, which states, roughly speaking, that a random variable which is defined as a sum of many terms, all independent and each negligibly small, is in the limit normally distributed.

Several excellent books, for example those by Feller[5] and Cramér[2] among others, provide more extended discussions of these concepts.

References

[1] Boyce, W. E., *Linear Differential Equations With Random Nonhomogeneities*, AFOSR TN 59-1260, Department of Mathematics, Rensselaer Polytechnic Institute, 1959.

[2] Cramér, H., *Mathematical Methods of Statistics*, Princeton University Press, Princeton, N.J., 1946.

[3] Bendat, J. S., *Principles and Applications of Random Noise Theory*, John Wiley & Sons, Inc., New York, 1958.

[4] National Bureau of Standards, *Tables of the Error Function and its Derivative*, Applied Mathematics Series, Number 41, U.S. Government Printing Office, Washington, D.C., 1954.

[5] Feller, W., *An Introduction to Probability Theory and Its Application*, 2nd ed., John Wiley & Sons, Inc., New York, 1957.

[6] Davenport, Jr., W. B., and Root, W. L., *An Introduction to the Theory of Random Signals and Noise*, McGraw-Hill Book Company, Inc., New York, 1958.

Change of Address

Since the Post Office Department does not as a rule forward magazines to forwarding addresses, it is important that the Institute be notified of changes in address 30 days in advance of publishing date to ensure receipt of every issue of the JOURNAL and AEROSPACE ENGINEERING. Notices should be printed legibly and sent to:

Circulation Department
Institute of the Aerospace Sciences, Inc.
2 East 64th Street, New York 21, N.Y.

On the Aerodynamic Noise of a Turbulent Jet†

SIN-I CHENG*

Princeton University and General Applied Science Laboratories, Inc.

Summary

A new model is advanced for analyzing the broad-spectrum noise of a turbulent jet. The shear layer bounding the turbulent jet is assumed to play an important role in modifying the "quadrupole sound radiation" from the interior. To the sound-emitting, small-scale turbulent eddies (with frequencies much higher than those of large-scale eddies), the laminar shear layer has an irregular contour, as if the large-scale turbulent motions were frozen. The linearized analysis is then applied to the laminar shear layer to relate the acoustic oscillations across it.

The concept of geometrical acoustics is generalized to represent the passage of an acoustic ray through a laminar shear layer. Acoustic rays may be traced across the shear layer as transmission and refraction, but they may also be apparently "absorbed" or "generated" by the laminar layer. This "generation" is visualized as the schematic representation, within the framework of geometrical acoustics, of the action of the Reynolds stress in transferring energy from the shearing mean flow to the acoustic waves. Such action of the Reynolds stress can be neglected in ordinary acoustics when the acoustic medium is not moving at speeds comparable to the speed of sound in the medium. However, this action is of crucial importance in the aerodynamic noise of high-speed turbulent jets where the Reynolds stress is the fundamental element of the radiating quadrupoles, according to Lighthill.

Those acoustic waves that become "stationary" with respect to the local mean flow somewhere in the interior of the shear layer are significantly modified by the viscous action through the critical layer. The shear layer therefore serves as a selective amplifier of the acoustic waves passing through it. Kinematically, the shear layer brings about the preferred downstream emission. Dynamically, the shear-layer augmentation significantly increases the polar peak noise level. The acoustic power output per unit solid angle for such downstream emissions augmented by the shear layer (including the polar peak) varies as U_j^8, as predicted by Lighthill, but without Lighthill's convective corrections. On the other hand, the acoustic power output per unit solid angle nearly normal to the jet, due to the transmitted downstream-propagating waves, varies roughly as U_j^8. Heating the jet gas increases the shear-layer augmentation and may increase the polar peak noise level by several db. The silencing action of the edge notches and edge teeth may also be interpreted as due apparently to the result of possible distortion of the shear-layer profiles.

(1) Introduction to the Physical Model

THE PRESENT INVESTIGATION concerns only the sound field in an unbounded, uniform acoustic medium at rest, produced by a high-speed jet in the absence of any resonating mechanisms; the discrete-frequency noise often observed in supersonic jets is not considered here. Lighthill[1, 2] pointed out the quadrupole nature of aerodynamic sound radiation with amplitudes proportional to the square of the frequencies (the Stokes effect). For a turbulent jet, Lighthill proposed a model (Fig. 1) whereby the jet may be replaced by a volume of quadrupole radiation centers, moving with some convective velocity in the ambient acoustic medium, which is assumed to be at rest everywhere, including inside the jet. The density field in the acoustic medium is the integrated result of the individual contributions from all these quadrupoles, which are not emitted simultaneously owing to the finite speed of sound propagation. With the assumption of a representative frequency proportional to the ratio of the characteristic velocity to the length scale of the turbulent jet (i.e., of the turbulence field), the total acoustic power output is found to be $P_{total} \sim U_j^8$. Extensive experimental tests show that this law is generally satisfactory. Nevertheless, Lighthill considered it "hardest of all to explain . . . (that) the acoustic output varies as U_j^8," since the convective correction necessary to account for the preferred downstream sound emission "implies a further increase of power output with Mach number over and above the U_j^8 law" (reference 2, p. 5).

It is also known that the presence of teeth or notches on the circumference of the solid boundary of the jet exit changes the noise level by several decibels.[3] These teeth modify only the shear layer of the jet. Since the

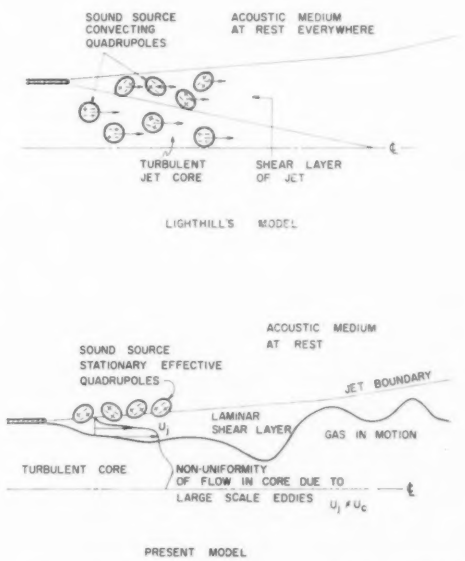

FIG. 1. Schematic diagrams of the present model and Lighthill's.

Received September 29, 1959. Revised and received June 2, 1960.

† This research was sponsored by the Office of Scientific Research, ARDC, under Contract AF 49(638)-194.

* Consultant, General Applied Science Laboratories, Inc.; Professor, Princeton University, Department of Aeronautical Engineering.

shear layer contributes only "a fair portion, perhaps one third" of the total power output (reference 2, footnote, p. 27), a complete elimination of the shear-layer contribution would lead to a reduction in the noise level of not more than 1.75 db.

The concept of quadrupole radiation is based upon the observation that the negative of the instantaneous stress

$$T_{ij} = \rho v_i v_j + (p - a_0^2\rho)\delta_{ij} \qquad i,j = 1,2,3 \quad (1.1)$$

enters into the approximation equation for the density field in a uniform acoustic medium at rest as

$$(\partial^2\rho/\partial t^2) - a_0^2\nabla^2\rho = (\partial^2/\partial x_i \partial x_j)T_{ij} \qquad (1.2)$$

so that $\partial^2 T_{ij}/\partial x_i \partial x_j$ may be identified as an equivalent but fictitious fluctuating mass source, $\partial Q/\partial t$, exciting the sound field. Eq. (1.2) is valid in a uniform medium at rest and can be corrected for the presence of a uniform convective velocity of the sound sources relative to the medium. Wherever the variations of the mean flow properties in the medium over a wavelength are not negligibly small, Eq. (1.2) may be seriously in error. By giving the sound-emitting quadrupoles a "predominant orientation" (reference 2, p. 17) in the presence of a large shear, one might possibly neglect some essential feature of the shear layer.

It is known since the time of Reynolds that in a layer of sheared mean flow there is an exchange of energy between the mean flow and the disturbance motion. Such an energy exchange is ignored in ordinary acoustics (reference 4, p. 61) because in turbulent flow fields of low velocities the frequencies of the sound waves are much larger than, and not related to, the turbulent fluctuations. The turbulent fluctuations are essentially frozen during the passage of acoustic waves. Hence, the concept of turbulent or Reynolds stress is fortuitous, and the energy exchange between the turbulent fluctuations and the mean flow has little bearing on the sound waves of the ordinary acoustic field. The turbulence exerts only the kinematic effect of dispersion. For aerodynamic noise, which is emitted by the turbulent fluctuations themselves in a high-speed jet, the frequencies of the sound waves and of the Reynolds stress components must be comparable. Thus, the mean Reynolds stress is as significant in aerodynamic noise as other mean acoustic quantities such as intensities and power output. The energy exchange between the mean flow and the disturbance motion is important in the balance of the disturbance energy, and is proportional to the temporal average of the sound-emitting quadrupoles. The following model is therefore proposed for analyzing the aerodynamic noise of a jet.

The entire field is divided into three regimes: the ambient air at rest, the turbulent jet core, and the shear layer separating the two (Fig. 1). The air flow in the turbulent core of the jet carries with it the sound-emitting quadrupole cells in the form of fine-scale turbulent eddies. The mean flow velocity is essentially uniform across the jet and may vary slowly in the direction of the flow. Throughout this region, Lighthill's model with convective correction will apply if wave reflection from the shear layer is ignored. Acoustic waves from quadrupoles throughout the turbulent core from upstream to downstream infinity will be incident upon the inner boundary of the shear layer. These will be represented by a distribution of the quadrupole cells along the boundary of the shear layer and the turbulent core.

The shear layer is characterized by the rapid decrease of the mean flow velocity (large shear in the mean flow) normal to the flow direction. The kinematic and dynamic behavior of acoustic waves crossing this layer is the essential part of the following investigation. The acoustic waves emerging from the shear layer into the ambient air may again be represented by a distribution of the quadrupoles along the outer boundary of the shear layer, consistent with Lighthill's model without convective correction. The relation between the quadrupole strengths distributed on the two sides of the shear layer is of crucial interest.

Recent studies[5, 6] on the structure of low-speed turbulent flows have revealed the sharp lateral transition from the turbulent core flow to the bounding laminar shear flow, although the boundary changes from time to time under the influence of the large-scale eddies. The frequency of the large-scale eddies is very low, corresponding to those waves in the pseudo-sound range, as was indicated in reference 7. During the passage of an acoustic wave through the shear layer, it is well justified to consider the shear-layer boundary as frozen, although the long-time average of the noise level taken in the far field is actually an average over the large-scale eddies. The Strouhal number of the large-scale eddies based upon the jet diameter and the mean flow velocity is less than 10^{-1}. The successive eruptions of the large-scale eddies will be spaced at many times the jet diameter. Hence, except for the brief period at the peak of the occasional eruption, the shear layer is essentially a region of parallel mean flow. The linearized analysis for the propagation of the small disturbances in a parallel shear flow may then be adopted to provide useful information at least for the mean acoustic quantities.

The density fluctuation $\rho - \rho_0$, the acoustic intensity I, and the power output P per unit solid angle at a point x_i in the ambient air will be given by the same formulas as were given in reference 2:

$$\Delta\rho = \rho - \rho_0 \sim \frac{1}{4\pi a_0^2}\frac{\partial^2}{\partial x_i \partial x_j}\int T_{ij}\left(Y, t - \frac{|X-Y|}{a_0}\right)\frac{dY}{|X-Y|} \sim$$
$$\frac{1}{4\pi a_0^2}\int \frac{(x_i - y_i)(x_j - y_j)}{|X-Y|^3}\,\frac{1}{a_0^2}\frac{\partial^2}{\partial t^2}\,T_{ij}\left(Y, t - \frac{|X-Y|}{a_0}\right)dY \quad (1.3)$$

$$I(X) \sim \frac{1}{16\pi^2 \rho_0 a_0^5} \iint \frac{(x_i - y_i)(x_j - y_j)(x_k - z_k)(x_l - z_l)}{|X - Y|^3 \, |X - Z|^3} \left\langle \frac{\partial^2}{\partial t^2} T_{ij}\left(Y, t - \frac{|X-Y|}{a_0}\right) \frac{\partial^2}{\partial t^2} T_{kl}\left(Z, t - \frac{|X-Z|}{a_0}\right) \right\rangle dY\,dZ \quad (1.4)$$

$$P(X) \sim \frac{1}{60\pi \rho_0 a_0^5} \iint \left\{ \left\langle \frac{\partial^2}{\partial t^2} T_{ii}\left(Y, t - \frac{|X-Y|}{a_0}\right) \frac{\partial^2}{\partial t^2} T_{kk}\left(Z, t - \frac{|X-Z|}{a_0}\right) \right\rangle + 2\left\langle \frac{\partial^2}{\partial t^2} T_{ij}\left(Y, t - \frac{|X-Y|}{a_0}\right) \frac{\partial^2}{\partial t^2} T_{ij}\left(Z, t - \frac{|X-Z|}{a_0}\right) \right\rangle \right\} dY\,dZ \quad (1.5)$$

where $\langle\ \rangle$ indicates the proper mean pertaining to the turbulent fluctuations. Here, the integrals extend only throughout the acoustic field at rest, including the outer boundary of the shear layer. Since the integrand vanishes everywhere except on the boundary, where quadrupole cells are distributed, these integrals degenerate into surface integrals over that portion of the shear-layer boundary from whence the acoustic emissions travel to the point x_i under consideration. The quadrupoles under consideration are fixed on the frozen boundary of the large-scale eddies, but their magnitudes and orientations vary with time in response to the fine-scale turbulent fluctuations in the interior. If the mean product is expressed as

$$\left\langle \frac{\partial^2}{\partial t^2} T_{ij}(Y) \frac{\partial^2}{\partial t^2} T_{kl}(Z) \right\rangle F_{ijkl}(Y, Z)$$

and if the correlation coefficients F_{ijkl} are assumed to be geometric characteristics, the quantity of direct interest is the magnitude $\langle(\partial^2/\partial^2)T_{ij}\rangle$ on the outer edge of the shear layer, which will have to be related to similar quantities distributed over the inner boundary of the shear layer. The T_{11}'s distributed over the inner boundary of the shear layer represent the resultant acoustic oscillations of all the quadrupoles in the turbulent jet core. They may be determined with Eqs. (1.3)–(1.5), corrected for the convective motion of the quadrupoles in the jet core, if necessary.

Although $\langle(\partial^2/\partial t^2)T_{ii}\rangle$ is nonlinear in terms of the acoustic disturbance velocity components, it can be evaluated, accurate to the squared magnitude, with the disturbance quantities determined from the linearized analysis for each of the three regions—i.e., the jet core in uniform mean motion, the shear layer, and the air at rest. The possibility of resolving the acoustic disturbances into planar waves, or sound rays, propagating in different directions leads to the notion of geometrical acoustics. This possibility is well known for mediums at rest or in uniform motion. Insofar as the linearized analysis may be carried out through the shear layer, we would like to see first how far geometrical acoustics will lead us. This analysis is given in Section 2, where the dynamic role of the shear layer is revealed. In Section 3, the relation between the quadrupoles across the shear layer will be given. Practical implications as to the dimensional dependence of the outer noise field will then be discussed and illustrated with some interesting experimental results.

It may be pertinent to repeat here that the present consideration is limited to the cases in which the sound sources are not coupled to, nor influenced by, the resulting sound field. We shall consider only the aerodynamic noise of quadrupole nature which is of predominant importance at high jet velocities. Other noises, such as those induced by mass-source fluctuations, etc., which depend on the mean flow velocity to lower powers are ignored. The turbulent velocity fluctuations of the gas are assumed to be small compared with the mean flow velocity and the mean speed of sound in the jet. The thickness Δ of the shear layer is taken to be much smaller than the jet diameter D and the wavelength λ of the sound wave. Other assumptions of less general nature are mentioned in the text when needed. Finally, we are concerned only with the average quantities in the acoustic field at distances L sufficiently far away from the jet exit, i.e., $L/D \gg 1$.

(2) Geometrical Acoustics in Shear Layer

The linearized acoustics for an individual frequency component of a sound wave are the same as the linearized treatment of the propagation of a small periodic disturbance in a flow field that is either subsonic or supersonic, uniform or under shear. Geometrical acoustics implies, in addition to linearization, the local approximation by planar waves. This is not always possible, even in uniform flow fields. The difficulty is more severe in a shear layer. In the extensive treatment by Blokhinstev,[4] the dispersion of sound by wind in low atmosphere, which is taken as a shear layer with small gradients, has been considered. Ribner[8] tried to approach the problem of a thin shear layer by considering the shear layer a rippled interface so that the law of refraction could be inferred across it. In what follows, the geometrical acoustics will be considered in a thin shear layer of parallel mean flow with larger gradients of the mean flow properties across it. The assumption of a parallel mean flow in the shear layer between the ambient quiescent atmosphere and the turbulent jet core appears to be a rather strong postulate, because the size of the large-scale eddies (or, roughly, the radius of curvature of the shear-layer boundary) is comparable to the jet diameter and therefore to the wavelength of the sound. This assumption is considered to be adequate, however, since in the following discussion the qualitative or at most the dimensional aspect is of greatest interest.

The system of conservation equations, being linearized with respect to the disturbance quantities, will

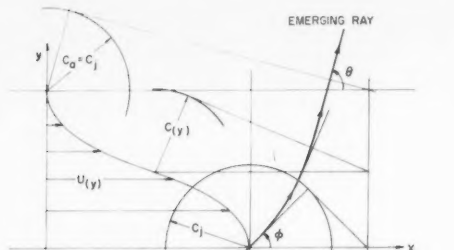

FIG. 2. Transmission of acoustic ray through the shear layer.

clearly admit of time-dependent exponential solutions [exp $(-i\omega t)$], even if all the dissipative terms originating from viscosity, heat conductivity, etc., are included. Since the mean properties such as $U(y)$, $T(y)$, etc., appearing as coefficients in the system of differential equations for the disturbance quantities are independent of x, the system of equations will admit of solutions with exponential x-dependence. That is, for any disturbance quantity Q, solutions of the following form will be obtained:

$$Q = R\{q(y) \exp [i\alpha(x - c_r t)]\} \tag{2.1}$$

It should be noted here that α and c_r may take any real values forced upon the shear layer by the oscillations from the turbulent jet core. In Eq. (2.1), R indicates the real part of the quantity in braces; $q(y)$ is the complex amplitude function; and α is the angular wave number, equal to 2π times the number of complete waves contained within distances equal to the shear-layer thickness Δ along the x-axis (i.e., the direction of mean motion). The spatial coordinate axes x,y will be fixed with the ambient quiescent atmosphere. c_r is the apparent phase velocity in the x-direction due to the component wave motion. Both α and c_r are real quantities since the acoustic oscillations are neutral on the long-time average. $\omega = \alpha c_r$ is the angular frequency of the component oscillation. Any two of the three quantities α, c_r, and ω will specify completely the mode of oscillation under consideration.

That both ω and c_r may be arbitrarily selected and are independent of the spatial coordinate y during the propagation of the wave across the shear layer implies an important geometric characteristic of the "sound ray." A sound wave propagating in the direction of the mean motion, $U(y)$, but inclined to it at an angle θ (see Fig. 2), leads to

$$c_r = U(y) + c(y)/\cos\theta(y) \tag{2.2}$$

where c the local speed of sound $= (\gamma p/\rho)^{1/2}$ and θ is the angle included between the **c** vector (tangent to the sound ray) and the positive x-axis, with positive angles measured counterclockwise from this axis. This expression of c_r is general for planar sound waves propagating in any direction with respect to the wind. Since c_r is an invariant property, the local direction of the sound ray, θ, measured in the counterclockwise sense from the positive x-axis, is uniquely determined by the local value of $U(y)$ and $c(y) = (\gamma p/\rho)^{1/2}$. Eq. (2.2) offers a convenient means of graphically constructing the path of the sound ray or rays, as illustrated in Fig. 2 for the cases $c_r > U_j + c_j > c_a$ and $0 > -c_a > c_r$. For application across a discontinuity of U and/or c, however, Eq. (2.2) may be put into a more convenient form:

$$\tilde{\mu} = \frac{\cos\theta_1}{\cos\theta_2} = \frac{c_1 + U_1\cos\theta_1}{c_2 + U_2\cos\theta_2} \tag{2.3}$$

where $\tilde{\mu}$ designates the index of refraction and $c_i + U_i\cos\theta_i$ stands for the "effective propagating speed" of the wave front or ray in the ith medium.

The result (2.2) is simple. Its derivation is based only on the linearization and the assumption that all the mean profiles are independent of x. Nevertheless, it has far-reaching consequences. In Fig. 3, a typical situation encountered when $(U_j - c_j) > c_r > c_a$ is illustrated. A band inside the shear layer, centered around $U(y) = c_r$, is prohibited for the incident and the emerging rays. This aspect of geometrical acoustics inside a shear layer is not unique. Let us consider the solution of the wave equations in two dimensions in an acoustic medium at rest:

$$\exp [i\alpha(x + \beta y) - i\alpha c_r t] = \exp\left\{i\omega\left[\frac{x}{c_r} + \left(1 - \frac{c^2}{c_r^2}\right)^{1/2}\frac{y}{c} - t\right]\right\} \tag{2.4}$$

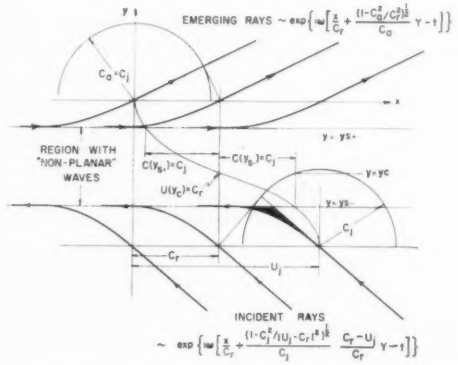

FIG. 3. Absorption and generation of acoustic rays by the shear layer.

where $\alpha = \omega/c_r$ and $\beta^2 = (c_r^2/c^2) - 1$. Here c_r may take on any real value from $-\infty$ to $+\infty$. When $c_r^2 > c^2$ (the square of the local speed of sound), then β is real and Eq. (2.4) represents periodic planar waves or sound rays. When $c_r^2 < c^2$, β is imaginary, and (2.4) represents a one-dimensional wave in the x-direction that decays exponentially or amplifies in the y-direction. This kind of acoustic wave cannot be described by sound rays. For outer acoustic mediums unbounded for positive y, $i\alpha\beta$ must be negative and real when $|c_r| < c_a$, corresponding to waves decaying exponentially with increasing y. Such waves will have no influence on the far sound field and are often ignored. For the turbulent core with uniform velocity U_j, the wave equation refers to the moving coordinate system with $(c_r - U_j)^2 = (1 + \beta^2)c_j^2$. Thus β is imaginary when $|c_r - U_j| < c_j$. Since the jet core is finite in extent, and contains actual sound sources such that the amplitudes of the local oscillations may be much larger than those at the edge of the jet core, $i\alpha\beta$ may take on negative as well as positive values. It is clear, then, the absence of sound rays in geometrical acoustics when $|c_r - U_j| < c_j$ does not imply the absence of acoustic waves and is not devoid of physical meaning.

For a given c_r the circumstances $|c_r - U| < c$ may be brought about by the variation of c or U or both, when a ray of a given c_r with $U_j - c_j > c_r > c_a$ penetrates the shear layer. When $|c_r - U| = c$, the wave is "locally sonic," propagating along or against the mean flow with $\beta = 0$. If we expand the inviscid approximation of the linearized equations about this point, the amplitude function $\varphi(y)$ is found to be locally

$$\varphi(y) \sim \exp\left(\left|\frac{U'}{U - c_r}_{*}\right| y\right), \qquad \varphi'(y) = \left|\frac{U'(y)}{U - c_r}_{*}\right| \varphi(y) \tag{2.5}$$

indicating that the amplitude of the wave motion in the x-direction is decaying or growing exponentially with increasing y. This substantiates the correspondence of the physical situations in the shear flow and in the uniform flow. In Fig. 3, $\varphi(y)$ is decaying exponentially or decreasing near $y = y_{s-}$, and is growing exponentially near $y = y_{s+}$ as y increases. The situation inside the prohibited band, except in the immediate vicinity of $U(y) = c_r$, is essentially the same as that in a uniform flow with varying c_j.

The eventual exponential decay of an incident wave conveys the notion of its absorption by the shear layer. The exponential amplification prior to the formation of the emerging waves suggests that the emerging rays may be fundamentally different from the corresponding incident rays.

The prohibited band may include one of the shear-layer boundaries when either $|c_r - U_j| < c_j$ or $|c_r| < c_a$. Thus the geometrical acoustics will not reveal either incident rays or emerging rays. Hence they leave stronger impression of shear-layer emission and total absorption respectively. In Fig. 4 are illustrated the different situations encountered. The downstream propagating, emerging waves (III and IV) are clearly

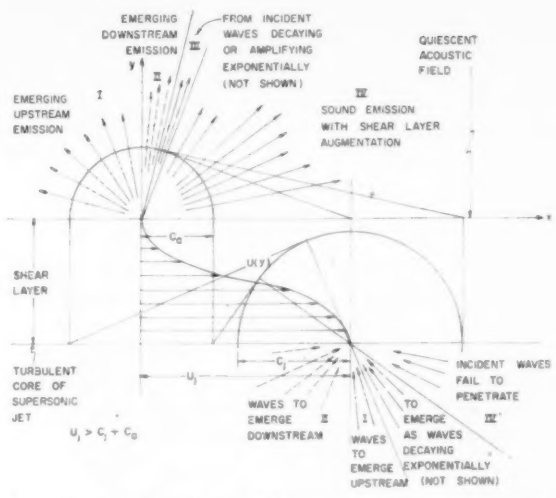
EMERGING DOWNSTREAM EMISSION
FROM INCIDENT WAVES DECAYING OR AMPLIFYING EXPONENTIALLY (NOT SHOWN)
QUIESCENT ACOUSTIC FIELD
EMERGING UPSTREAM EMISSION
SOUND EMISSION WITH SHEAR LAYER AUGMENTATION
SHEAR LAYER
TURBULENT CORE OF SUPERSONIC JET
INCIDENT WAVES FAIL TO PENETRATE
WAVES TO EMERGE DOWNSTREAM
TO EMERGE AS WAVES DECAYING EXPONENTIALLY (NOT SHOWN)
WAVES TO EMERGE UPSTREAM

FIG. 4(a). Patterns of the incident and the emerging acoustic rays. $U_j > c_j + c_a$.

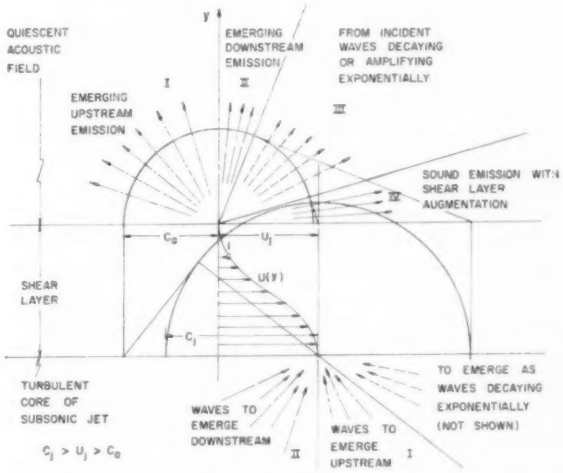
QUIESCENT ACOUSTIC FIELD
EMERGING DOWNSTREAM EMISSION
FROM INCIDENT WAVES DECAYING OR AMPLIFYING EXPONENTIALLY
EMERGING UPSTREAM EMISSION
SOUND EMISSION WITH SHEAR LAYER AUGMENTATION
SHEAR LAYER
TURBULENT CORE OF SUBSONIC JET
TO EMERGE AS WAVES DECAYING EXPONENTIALLY (NOT SHOWN)
WAVES TO EMERGE DOWNSTREAM
WAVES TO EMERGE UPSTREAM

FIG. 4(b). Patterns of the incident and the emerging acoustic rays. $c_j > U_j > c_a$.

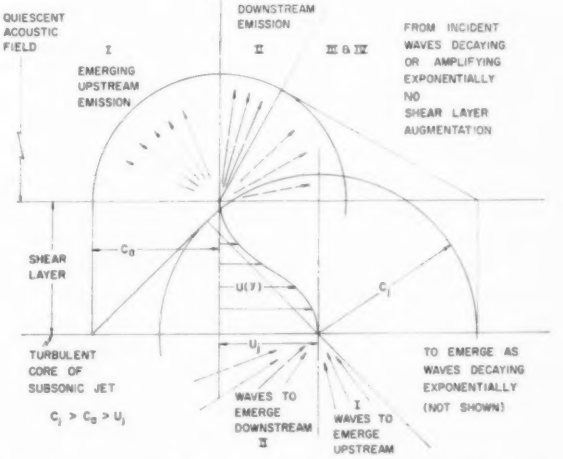
QUIESCENT ACOUSTIC FIELD
EMERGING DOWNSTREAM EMISSION
FROM INCIDENT WAVES DECAYING OR AMPLIFYING EXPONENTIALLY NO SHEAR LAYER AUGMENTATION
EMERGING UPSTREAM EMISSION
SHEAR LAYER
TURBULENT CORE OF SUBSONIC JET
TO EMERGE AS WAVES DECAYING EXPONENTIALLY (NOT SHOWN)
WAVES TO EMERGE DOWNSTREAM
WAVES TO EMERGE UPSTREAM

FIG. 4(c). Patterns of the incident and the emerging acoustic rays. $c_j > c_a > U_j$.

affected by the shear layer. The transmitted waves (I and II) are primarily confined to the upstream region and the region nearly normal to the mean flow direction of the jet. In the next section, the role of the shear layer in different regimes will be examined.

(3) Relation Between Quadrupoles Across Shear Layer

The acoustic energy density in a medium at rest, accurate to the square of the disturbance amplitudes, is $I = (c^2/\rho_0)(\Delta\rho)^2$, where $\Delta\rho$ is the variation of the medium density from its average value ρ_0. The density fluctuation $\Delta\rho = \rho - \rho_0$, the sound intensity I, and the acoustic power output P in the ambient medium can be represented by Eqs. (1.3), (1.4), and (1.5), if all the T_{ij} are those distributed on the outer edge of the shear-layer boundary.

Before considering the three-dimensional problems, and in keeping with the spirit of taking the "shear layer" as a parallel flow, we shall investigate only the planar problem, with $\langle\rho u^2\rangle$, $\langle\rho v^2\rangle$, and $\langle\rho uv\rangle$ nonvanishing, to illustrate the physical mechanisms operating to relate these quadrupoles across the shear layer. Each of these long-time averages may be resolved into a frequency spectrum, and each frequency component may be resolved into a c_r spectrum corresponding to waves propagating in different directions. This is possible because the analysis of the present forced-oscillation problem is linearized. If all the individual components of $\langle\rho u^2\rangle$, $\langle\rho v^2\rangle$, and $\langle\rho uv\rangle$ in the elementary ranges of ω and c_r are specified at the outer edge of the turbulent jet core (for analytical purposes), the linearized equations of motion will permit us to calculate these values at the outer edge of the shear layer, when the "mean profiles" of the "laminar" shear layer are specified.

The analysis is largely the same as that for the stability of the compressible laminar boundary layer as outlined in reference 9. The only important difference is that the present problem is a nontrivial boundary-value problem of forced oscillation, rather than an eigenvalue problem for the investigation of stability. The following two conclusions are of fundamental importance in the present investigation:

(1) For boundary-layer types of flow (large Reynolds number) the waves are governed essentially by the inviscid equations (obtained formally by dropping all terms involving some negative power of Re) everywhere except in a thin viscous layer called the "critical layer" in the interior of the shear flow where $U(y_c) = c_r$. The thickness of this critical layer is $O(\alpha Re)^{-1/3}$. There is no solid boundary in the present problem.

(2) The Reynolds stress component $\langle\rho uv\rangle$ of the disturbance motion remains essentially constant within each inviscid layer and undergoes an almost discontinuous jump across the critical viscous layer, the magnitude of the discontinuity being determined by the local profiles of the mean flow.

For the present purpose, we shall first express the quadrupoles T_{ij} at the shear-layer boundaries in terms of the small disturbance quantities treated in the linearized analysis within the inviscid framework. The linearized results for the shear layer will then relate the T_{ij} across the shear layer. Accordingly, each of the disturbance quantities will be written as the real part of the product of $\exp[i\alpha(x - c_r t)]$ and its complex amplitude function. Since the mean motion on either side of the shear-layer boundary is uniform, the complex amplitude functions take particularly simple forms. Let

$$\varphi(y) = \varphi_0 \exp[i\alpha\beta y] \tag{3.1}$$

with $1 + \beta^2 = (U - c_r)^2/c^2$ and $\alpha = \omega/c_r$, and where U is the uniform velocity of mean motion, c is the local speed of sound and c_r is the wave velocity in the x-direction, all expressed as fractions of the mean turbulent jet velocity U_j at the core. The complex amplitude functions are as follows:

for the x-component of the disturbance velocity,

$$f(y) = -\varphi'(y)/\beta = -i\alpha\varphi(y)/\beta \tag{3.2}$$

for the y-component of the disturbance velocity,

$$g(y) = -i\alpha\varphi(y) \tag{3.3}$$

for the pressure, the density and the temperature, respectively,

$$\left.\begin{aligned} \pi(y) &= -(\gamma/c)[(1+\beta^2)^{1/2}/\beta]i\alpha\varphi(y) \\ r(y) &= (1/\gamma)\langle\rho\rangle\pi(y) \\ \theta(y) &= (\gamma - 1)/\gamma\langle T\rangle\pi(y) \end{aligned}\right\} \tag{3.4}$$

and

$$\langle uv\rangle = fg^* = (\alpha^2/\beta)\varphi_0^2 \qquad (\beta \text{ real}) \tag{3.5}$$

The mean gas pressure $\langle p\rangle$ is unity (to the first order) everywhere. The mean gas density $\langle\rho\rangle$ and the mean temperature $\langle T\rangle$ are expressed in terms of their respective values in the center of the jet core. Now take the temporal average of (1.1) for each individual component after ω and c_r resolution, and let the acoustic oscillations be isentropic (to the square of the amplitude) with purely sinusoidal density oscillation. Then, for real β we have

$$\left.\begin{aligned} \langle T_{ij}\rangle &= \langle\rho uv\rangle(\tau_{ij}) \\ (\tau_{11}) &= \left[\frac{1}{\beta} + \frac{(1+\beta^2)^{1/2}}{c\beta} + \frac{\gamma-1}{2}\frac{1+\beta^2}{\beta}\right] \\ (\tau_{22}) &= \left[\beta + 0 + \frac{\gamma-1}{2}\frac{1+\beta^2}{\beta}\right] \\ (\tau_{12}) &= \left[1 + \frac{(1+\beta^2)^{1/2}}{c\beta} + 0\right] \end{aligned}\right\} \tag{3.6}$$

Similar relations for (τ_{ij}) may be obtained for imaginary β. The second term in (τ_{ij}) of Eqs. (3.6) originates from the correlation of the density and the velocity fluctuations. The third term is due to $\langle p\rangle - 1$ evaluated to the square of the acoustic wave magnitude. They are not important insofar as dimensional results are concerned, and are included only to achieve the correct limiting behavior of τ_{ij} when $\beta \to 0$ (i.e., for

waves propagating along the mean flow direction) and when $\beta \to \infty$ (i.e., $c_r \to \infty$ with ω constant for waves propagating normal to the jet flow direction). The parameter β is the tangent of the angle θ between the acoustic ray and the jet flow direction with $\theta = (\cos^{-1}c)/(U - c_r)$. The τ_{ij} given in Eqs. (3.6) is for the component in the range of unit ω and unit c_r. The component in unit ω and unit angular range (θ) is $dc_r/d\theta = c\beta(1 + \beta^2)^{1/2}$ times that given in (3.6). It can be verified that $\tau_{ij}dc_r/d\theta$ is well behaved for both limiting conditions. We shall therefore ignore these limiting cases in the following discussions, to avoid unnecessary complications.

From Eqs. (3.6), the importance of the variation of $\langle\rho uv\rangle$ within the shear layer in relating the quadrupole strength across the shear layer is evident. For the waves incident on the inner boundary of the shear layer ($y = -1$) near the jet exit, we have $U = 1$ and $1/c_{-1} = M_j$, the Mach number of the jet. For the waves emerging from the outer boundary ($y = 0$), we have $U = 0$ and $1/c_0 = U_j/a_0$, where a_0 is the speed of sound in the ambient air. Two different cases need to be considered.

(1) Transmitted waves, $c_r \geq (1 + c_j)$ or $c_r < -c_0$ (the minus sign indicating waves propagating in the direction opposite to the mean flow, as illustrated in Fig. 2). For these waves, there is no critical viscous layer with $\langle\rho uv\rangle$ substantially constant throughout the shear layer. With subscripts 0 and -1 designating quantities evaluated at the outer and the inner edges of the shear layer, where $y = 0$ or -1 respectively, we may write

$$(\tau_{ij})_t = [\partial^2\langle T_{ij}\rangle/\partial t^2]_0/[\partial^2\langle T_{ij}\rangle/\partial t^2]_{-1} = (\tau_{ij})_0/(\tau_{ij})_{-1} \tag{3.7}$$

where $(\tau_{ij})_0$ and $(\tau_{ij})_{-1}$ are defined in Eqs. (3.6) which are independent of ω for a given value of c_r. The quantity $(\tau_{ij})_t$ may be identified as the transmission coefficient for the quadrupole component T_{ij}, constant for a given frequency component but different for waves propagating in different directions. This transmission coefficient $(\tau_{ij})_t$ depends on the uniform conditions on both sides of the shear layer but not on the details of the shear layer which brings about the change of the uniform conditions.

(2) Shear-layer emission ($1 > c_r > c_0$), as illustrated in Fig. 3 and the emerging waves in region IV of Fig. 4. For waves in this range, there is a critical viscous layer across which a discontinuous change of the stress component $\langle\rho uv\rangle$ takes place. The jump may be estimated from the inviscid approximation.[9] Thus

$$\frac{[(\partial^2/\partial t^2)\langle T_{ij}\rangle]_0}{[(\partial^2/\partial t^2)\langle T_{ij}\rangle]_{-1}} = (\tau_{ij})_t\left\{1 + \frac{D_j^2}{\Delta^2}\zeta_\omega\right\} \tag{3.8}$$

where
$$\zeta_\omega(\omega,c_r) = -\frac{\pi c_r}{\omega}\frac{(\rho U')'_c}{|\rho U'|_c}\frac{[\langle\rho uv\rangle]_c}{[\langle\rho uv\rangle]_{-1}} \tag{3.9}$$

is the dimensionless coefficient representing the discontinuous jump. The factor $(D_j/\Delta)^2$ arises because the reference length of the outer field is the jet diameter D_j, while throughout the shear-layer analysis the unit length is the shear-layer thickness Δ. The subscript c in Eq. (3.9) indicates quantities evaluated at the critical point y_c where $U(y_c) = c_r$. The function $\zeta_\omega(\omega)$ depends to some extent on the details of the mean velocity and temperature profiles across the shear layer, but largely on the quantity evaluated at the critical point,

$$-\frac{(\rho U')'_c}{|\rho U'|_c} = \left(\frac{U''}{U'} - \frac{T'}{T}\right)_c \tag{3.10}$$

the general variation of which is shown schematically in Fig. 5 for different c_r. Thus, the coefficient $\zeta_\omega(\omega)$ for a given frequency band around ω is generally positive for practically all the waves in this range of c_r. The term $(D_j/\Delta)^2\zeta_\omega(\omega,c_r)$ is therefore the shear-layer augmentation to the transmitted waves. Since (D_j/Δ) is usually very large, the shear-layer augmentation will be much more significant than the transmitted waves, at least when ζ_ω is O(1).

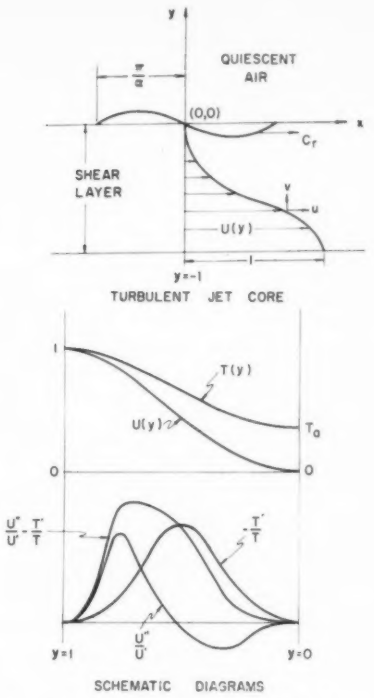

FIG. 5. Schematic diagrams of the profiles of some mean flow properties in the shear layer.

Eqs. (3.7)–(3.9) may be integrated over all the frequencies to yield relations between the integrated results of acoustic waves of all frequencies for a given c_r. Since the transmission coefficient $(\tau_{ij})_t$ is independent of ω, it remains so for the integrals of $(\tau_{ij})_t$ over all ω. In Eq. (3.8), the shear-layer augmentation will then be replaced by $(D_j/\Delta)^2\zeta(c_r)$ with

$$\zeta(c_r) = \int_{0+}^{\infty}\zeta_\omega(\omega, c_r)d\omega \tag{3.11}$$

which is primarily a function of c_r (i.e., the direction of the acoustic wave) and the profiles within the shear layer. Both ζ_ω and ζ can be evaluated with results

from reference 9. The precise values of ζ or ζ_ω are not important in the later discussions.

There are two ranges of c_r that have not yet been considered. The first one, $|c_r| < |c_0|$ corresponding to those emerging waves that decay exponentially, is of little importance to the far acoustic field. The second one, $(1 + c_j) > c_r > 1$, corresponds to incident waves that amplify exponentially and eventually emerge as planar waves. Although there is no critical viscous layer for these waves, the geometrical acoustics show emerging rays without corresponding incident rays, and convey the impression that these waves may belong to the shear-layer emission.

When the acoustic waves incident on the inner boundary of the shear layer are given, Eqs. (3.6) and (3.7) enable us to calculate the detailed distribution of the emerging, transmitted waves. When, in addition, the profiles inside the shear layer are prescribed, Eqs. (3.8)–(3.11) with the necessary information from reference 9 will determine the shear-layer emissions. The latter determination will not be attempted here; we shall be concerned primarily with the overall dimensional implications. Accordingly, the quadrupoles for the transmitted waves will be considered as essentially unchanged across the shear layer, and hence they should follow the dimensional relation given by Lighthill,[1] but there will be no need for a convective correction for the quadrupoles. The effect of the shear layer on these transmitted waves is essentially kinematic, i.e., to bring these waves to emerge in the direction upstream or nearly normal to the laminar mean flow. The quadrupoles for waves with shear-layer augmentation will be increased, possibly by orders of magnitude, when D_j/Δ is large. Kinematically, the shear layer brings these waves to emerge in the downstream direction of the local laminar mean flow. Dynamically, the strength of these downstream propagating waves will depend dimensionally on the ratio D_j/Δ.

(4) Outer Noise Field of the Jet

The outer noise field with air at rest as the medium will be divided into three different regions with different dimensional dependences:

(1) The upstream region of the turbulent jet will be reached only by the waves transmitted through the shear layer without shear-layer augmentation. Hence, with the dependence of the transmission coefficient $(\tau_{ij})_t$ on U_j, c_j, etc., neglected, the acoustic intensity I and the acoustic power output P per unit solid angle at a given point at distance r from the exit, will depend dimensionally as

$$r^2 I \sim P \sim (\rho_j D_j^2 U_j^3)(\rho_j/\rho_0)(U_j/a_0)^5 \qquad (4.1)$$

where the incident quadrupole $\langle \rho uv \rangle$ has been replaced dimensionally by $\rho_j U_j^2$ at the exit of the turbulent jet. This is the same as the dimensional result given by Lighthill.[1]

(2) The downstream region of the turbulent jet will be reached only by acoustic emissions from quadrupoles with shear-layer augmentation. Hence

$$r^2 I \sim P \sim (\rho_j D_j^2 U_j^3)(\rho_j/\rho_0)(U_j/a_0)^5 \{1 + \zeta (D_j/\Delta_0)^2\}^2$$
$$\sim (\rho_j D_j^2 U_j^3)(\rho_j/\rho_0)(U_j/a_0)^5 (D_j/\Delta_0)^4 \qquad (4.2)$$

The last simplification is valid when the typical shear-layer thickness Δ_0 is sufficiently small compared with jet diameter D_j.

(3) The transition region downstream of but nearly normal to the turbulent jet flow is covered largely by the transmitted acoustic waves of positive $c_r > (1 + c_j)$, corresponding to downstream-propagating incident waves. However, there will be some waves with shear-layer augmentation emitted from those parts of the shear-layer boundary where the local laminar flow directions are inclined away from the flow direction of the jet core. Since these waves carry considerably more energy than the transmitted waves, the angular variation of the acoustic intensity in this region may indicate the relative frequency of arrival of waves with shear-layer augmentation. It can be shown that the total acoustic power output of all the transmitted waves in this region increases dimensionally as U_j^6, in contrast to the dependence on U_j^8 of the shear-layer emissions. In view of the complicated shape of the shear-layer contour and its temporal variation under the influence of the large-scale eddies in the turbulent jet core, the angular extent of this transition region may be quite large. It will join the downstream region near $\theta = \tan^{-1} U_j/a_0$ and the upstream region around $\theta = \pi/2$, with considerable overlap.

Throughout the outer noise field, the local acoustic intensity varies as U_j^8, as does also the total acoustic output. Since D_j/Δ_0 is usually large, the downstream region will show a considerably higher noise level and will make a large contribution to the total acoustic power output. The angular distribution of the noise level in the downstream region, however, cannot be identified strictly with the dependence of the shear-layer augmentation on c_r, owing to the smearing effect of the large-scale eddies. The polar plot of the noise level will not show any sharp peak. The general orientation of the maximum polar noise level will correspond roughly to

$$\theta \sim \cos^{-1} (2U_j/3a_0)$$

Heating the turbulent jet will increase the level of the shear-layer augmentation through an increase in ζ [Eqs. (3.9) and (3.10)]. A 5–6 db increase of the downstream noise level may be produced when a jet at room temperature is heated to, say, three times the ambient temperature. Some change of the transmission coefficient $(\tau_{ij})_t$ may result, but its effect on the upstream noise level is relatively small and uncertain [Eqs. (3.1) and (3.6)].

According to the shear-layer analysis, the factor most significant for the downstream noise level is $(D_j/\Delta_0)^4$ in Eq. (4.2). It is this factor that brings about a downstream noise level much higher than the upstream

noise level, since in the present model there is no convective correction factor.

Eq. (4.2) indicates that the ratio D_j/Δ_0 is almost as important as U_j/a_0 in determining the change of the downstream noise level when the jet thrust power $(\rho_j D_j^2 U_j^3)$ is kept constant while U_j and D_j are varied. For the noise fields of turbulent jets from several different fully developed turbulent pipe flows, the ratio D_j/Δ_0 in all cases is essentially the same. Accordingly, the U_j^8 law is expected to hold fairly well for experimental results with test configurations of this general category. The importance of other factors may appear under other test conditions.

Besides the factor $(D_j/\Delta_0)^4$ it should be noted also that the dimensional relations (4.1) and (4.2) require that the quadrupole $\langle \rho uv \rangle$ on the inner boundary of the shear layer be represented dimensionally by $\rho_j U_j^2$ at the jet exit. This is appropriate for experiments involving turbulent jets from pipe flows where U_j is the maximum velocity. For configurations like the diffuser-silencer to be discussed in the next section, the velocity of the turbulent jet in the upstream region is considerably larger than that at the diffuser exit. The acoustic emissions from the quadrupoles in the upstream region may be more important in determining the strength of the acoustic waves incident on the shear layer and therefore $\langle \rho uv \rangle$. The relative importance of the upstream region may be estimated with the help of Eq. (1.4) when assumptions on the variation of the local mean jet velocity and the variation or the similarity of the turbulent fluctuation inside the turbulent jet core are made. The dimensional rules (4.1) and (4.2) must be corrected accordingly when applied to these configurations.

(5) Diffuser-Silencers and Other Practical Considerations

Practical interest in jet noise arises from the need to reduce the noise produced by modern high-thrust jet engines. In view of Lighthill's result that the outer noise field depends on U_j^8, the reduction of jet exit velocity by diffusion appears most attractive. Hence, many diffuser-silencers have been designed and tested. The noise reduction achieved in many cases has been substantial, although far short of what may be expected from U_j^8 law. In the following, a representative successful diffuser-silencer (CF100 Orenda 11/R) and an anomalous laboratory test model (UTIA wide-angle diffuser) are discussed. Some explanation of the observed results, and illustration of the importance of some other factors in practical devices, are attempted.

The experimental conditions did not, in general, correspond to the idealized conditions postulated in the theories. For the above examples, the presence of solid boundaries such as the diffuser liner, baffles, and screens in the turbulent core of the jet may raise the question of the applicability of the theoretical results. It is felt that when the aeolian tones and the possible resonance of the solid boundaries are neglected, the important

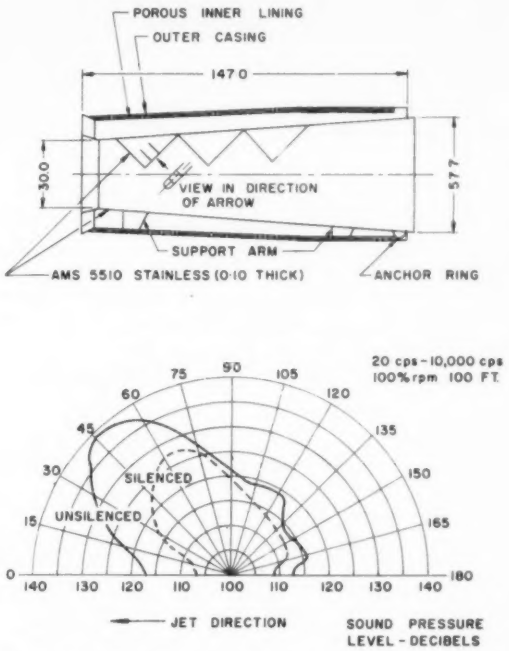

FIG. 6. The polar diagram of the noise field of the CF 100 Orenda 11/R diffuser-silencer.

role of the added solid boundaries is to change the turbulent flow conditions of the jet gas, as was remarked at the end of the last section. Thus the experimental observations in practical systems may be discussed within the framework of the theories.

We shall first look into these cases according to Lighthill's model. The configuration of the Orenda diffuser and the polar diagrams of the noise fields are shown in Fig. 6, which is reproduced from reference 10. The velocity and density of the gas at the diffuser exit are estimated in reference 12. The density may not be assumed constant across the diffuser. According to Lighthill's model, the dimensional rule (4.1) should apply in all directions if the convective correction is ignored. A reduction of 22–24 db would be expected in all directions. The actual reduction, as indicated in Fig. 6, is 14–16 db downstream and 2–4 db upstream.

If the upstream or background noise were due to some upstream noise source (for example, the combustion chamber) it would be difficult to understand why the addition of a diffuser should decrease the background noise intensity by 50 per cent (~2–4 db). The aerodynamic noise from the jet must constitute an essential part of the upstream noise. The large difference in the noise reduction in the upstream and the downstream fields may be accounted for by the corrections for the decrease in the convective velocity of the quadrupoles and the increase of the local turbulence level accompanying the velocity diffusion. The effects of the two factors are additive in the decibel (logarithmic) scale, being of opposite sign in the downstream region but of the same sign upstream. The effects of the two factors need not compensate each other in the downstream direction

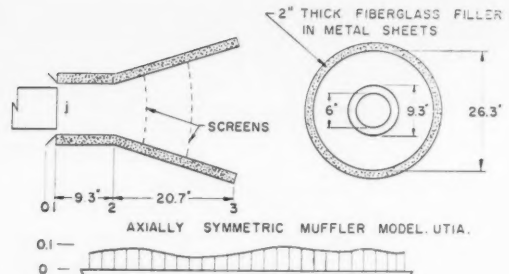

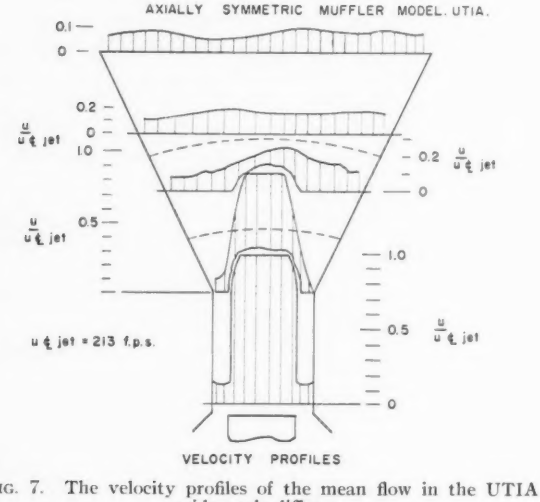

FIG. 7. The velocity profiles of the mean flow in the UTIA wide-angle diffuser.

(as was proposed in reference 2). To account for the difference in the reduction of the noise level achieved and the reduction expected from the U_j^8 rule, the increase in turbulence level ($\langle \rho u_i u_j \rangle / \rho_j U_j^2$) should be capable of causing an increase of 14–15 db in all directions, and the decrease in the convective velocity should bring about a 7–8 db reduction downstream and a 4–5 db increase upstream. This means that the turbulence level increases sixfold and the absolute magnitudes of turbulent fluctuations are increased by ~25 per cent with the mean velocity $U_2 = U_1/2.6$. If the convective correction should be less effective in reducing the upstream noise level (as indicated in reference 1), the required increase of the turbulence level would be larger.

The UTIA wide-angle ground muffler is similar to Orenda diffuser only in that two screens are introduced to achieve uniform diffusion to a much smaller jet velocity at the diffuser exit. The geometrical configuration and the mean velocity profiles are given in Fig. 7 (reproduced from reference 10). According to the U_j^8 law [Eq. (4.1)], a reduction of 70 db would be expected. Test results[10,13] show, on the other hand, a startling increase of 10–15 db. The sound pressure levels on the muffler wall are ~25 db below those on the edge of the jet without the muffler. The suggestion[10] that the noise increase is due to the inadequate acoustic design of the muffler wall cannot be a valid explanation of the anomaly. Let us attempt an explanation within Lighthill's model as for the previous case. The jet velocity in the test is too low to require any appreciable convective correction. The turbulence intensity would have to increase sufficiently to produce an 80–85 db increase of the outer noise field. To achieve this, the turbulence level would have to increase more than 10^4-fold, and the magnitude of turbulent fluctuations would have to increase more than a hundredfold. If such a large increase is regarded as unlikely, one would either have to dismiss this experimental result as erroneous, or reconsider the validity of the simple dimensional rule and its modification.

An attempt now will be made to explain these two cases on the basis of the present model. In both cases the diffuser exit is five diameters downstream of the jet exit, a distance comparable to the axial extent of the nondecaying turbulent core of the exit jet. Hence, in evaluating $\langle \rho uv \rangle$ distributed along the inner edge of the shear layer over the diffuser exit, the upstream high-speed region must not be ignored, as was explained at the end of the previous section.

According to the present model, the effect of the shear layer on the noise level in the upstream region of the outer noise field is negligible. The change in the noise level in this region due to the addition of a diffuser will therefore reflect the ratio of the integral of the square of the quadrupole strengths over the inner surfaces of the shear layers with and without the diffuser. In the case of Orenda diffuser, a 2–4 db reduction is effected in the upstream field when the exit diameter of the diffuser is about twice that of the jet. Thus, the ratio of the effective quadrupole radiation intensities with and without the diffuser is

$$\frac{\langle \rho uv \rangle_{\text{diffuser}}}{\langle \rho uv \rangle_{\text{jet}}} = 10^{\Delta \text{db}/20} \left(\frac{D_{\text{jet}}}{D_{\text{diffuser}}} \right) \sim \frac{1}{2.5} \quad \text{to} \quad \frac{1}{3.2}$$

This may be checked by assuming different distributions of ρ and U in evaluating the integrals (1.3) and (1.4). For points at corresponding positions on the edges of the shear layers with and without the diffuser, the ratio of the integrals generally falls in the above range.

The downstream, outer noise field will be considered as essentially due to the shear-layer augmentation which depends on both $(D_j/\Delta_0)^4$ and $\langle \rho uv \rangle$. With 2–4 db due to the reduction in $\langle \rho uv \rangle$, the reduction of 12–14 db will be accounted for by the decrease in the factor $(D_j/\Delta_0)^4$. This 12 db reduction will be effected by $(\Delta_{\text{diffuser}}/\Delta_{\text{jet}}) = 4$. If for example the Δ_{jet} of the full-scale motor is 1 in., then the shear-layer thickness at the diffuser exit must be 4 in. The 4-in. shear layer does not appear to be large in a diffuser with an exit diameter of ~60 in. and with air induced into the turbulent core of the jet through baffles that extend almost to the jet axis.

The test results of the UTIA diffuser did not include the noise level in the upstream field. The relative strengths of the effective quadrupoles on the edges of the shear layers with and without the diffuser will have to be estimated from (1.3). The effective $\langle \rho uv \rangle$ with diffuser is found to lie between $^1/_{14}$ to $^1/_{25}$ of the value without the diffuser, corresponding to a 15–20 db reduction of the noise level in the upstream region. Near-field measurements indicated a 25–30 db reduction[13] on

the diverging part of the diffuser wall which is shaded from the noise emission from the jet. The estimate of 15–20 db reduction in the far upstream field may be too low, but is probably on the conservative side.

To account for the 10 db increase in the downstream noise field, along with the 15–25 db decrease in the upstream region, there must be a 25–35 db increase due to a change in the parameter D_j/Δ_0. With the jet diameter increased 4.4 times, the mean shear-layer thickness at the diffuser exit should be about 1 to 0.6 times that at the jet exit. The mean velocity profile of the jet flow (Fig. 7) indicates an initial shear-layer thickness of $\sim 1/2$ in. at the jet exit but no shear layer at the diffuser exit. If it is assumed that the fine screens used in the UTIA diffuser destroyed the upstream turbulent boundary layer completely, then the growth of the turbulent boundary layer after the second screen would give rise, at the diffuser exit, to a turbulent boundary layer about $1/2$ in. thick. This would lead to a laminar shear layer (not a sublayer) about $1/4$ in. thick under the sweep of the large-scale eddies. The requirements of the physical situation again appear to be reasonable and consistent. The increase of the downstream noise field in spite of the large decrease of the jet velocity at the exit of the UTIA diffuser is not anomalous in the present model.

The most significant differences between the present model and Lighthill's are:

(1) The shear layer is considered important both dynamically and kinematically for the outer noise field in the present model, while it is ignored in Lighthill's model. However, the correction for the convective motion of the quadrupoles in Lighthill's model may be interpreted as representing effects of a similar nature and origin, if the convective velocity is properly selected and if the relative population of the lateral and the longitudinal convecting quadrupoles is properly selected.

(2) The change of the turbulence intensity relative to the local mean flow properties is neglected in the present model, but it is emphasized that the effective quadrupoles distributed over the shear-layer edges are the integrated effect of all the radiating quadrupoles throughout the turbulent jet core. (The distribution of the turbulence intensity in different parts of the turbulent core, if known, may be included in evaluating the integral.)

The variation suggested by Lighthill,[2] of the turbulence level at the jet exit may be interpreted as representing the variation of the integrated results over the physical extension of the turbulent jet core, with different distributions of the mean velocity and/or the turbulence level, etc.

The following remark is also of practical importance. The shear-layer augmentation need not predominate if D_j/Δ_0 is not sufficiently large—for example, in small-scale laboratory tests. Under such circumstances, the simplified form of the dimensional relation (4.2) will overemphasize the dynamic role of the shear layer. Furthermore, a slight increase of the mean jet velocity U_j will often accompany an increase of the shear-layer thickness in a given test jet. This will counterbalance to a large extent the silencing effect of a larger Δ_0. A small effect of the shear layer may then be observed in such small-scale tests, despite the fact that for large test units or full-scale engines even a small change, such as in edge teeth at the jet exit, may produce noticeable effects.

From the practical point of view, the present model demonstrates, among other things, that to strive for the lowest possible jet velocity, as indicated by the U_j^8 law, may not always be desirable in the design of an effective noise silencer. It also points out the need for caution in applying the laboratory test results for small-scale models to full-scale equipment.

References

[1] Lighthill, M. J., *On Sound Generated Aerodynamically, Part I—General Theory*, Royal Soc. (London) Proc., Ser. A, Vol. 211, pp. 564–587, 1952.

[2] Lighthill, M. J., *On Sound Generated Aerodynamically, Part II—Turbulence as a Source of Sound*, Royal Soc. (London) Proc., Ser. A, Vol. 222, pp. 1–32, 1954.

[3] Richards, E. J., *Research on Aerodynamic Noise from Jets and Associated Problems*, J. Royal Aero. Soc., pp. 332–335, May, 1953.

[4] Blokhinstev, D. L., *Acoustics of a Non-homogeneous Moving Medium*, NACA TM 1399 (Translation from Russian, 1946).

[5] Townsend, A. A., *Local Isotropy in the Turbulent Wake of a Cylinder*, Australian J. Sci. Res., Ser. A, Vol. 2, pp. 451–468, December, 1949.

[6] Grant, H. L., *The Large Eddies of Turbulent Motion*, J. Fluid Mech., pp. 149–190, June, 1958.

[7] Howes, L. L., *Similarity of Far Noise Field of Jets*, NASA TR R-52, 1959 (with fairly complete bibliography of recent works on the subject).

[8] Ribner, H. S., *Reflection, Transmission and Amplification of Sound of a Moving Medium*, J. Acoust. Soc. Amer., Vol. 29, No. 4, pp. 435–441, 1957.

[9] Lin, C. C., *Theory of Hydrodynamic Stability*, Cambridge Monographs on Mechanics and Mathematics, Cambridge Univ. Press, 1955.

[10] Neely, K. K., Etkin, B., and Ribner, H. S., *Noise Research in Canada: Physical and Bio-Acoustic*, Advances in Aeronautical Sciences, Proc. of the First International Congress in Aeronautical Sciences, Madrid, Spain, September, 1958, Vol. I, pp. 393–426, Pergamon Press, London, 1959.

[11] Cheng, S. I., *On the Aerodynamic Noise of a Jet*, Report submitted to General Applied Science Laboratory, Inc., OSR TN 59-1308, April, 1959.

[12] Cheng, S. I., *Note on the Broad-Spectrum Noise of a Jet and its Silencer*, Report submitted to General Applied Science Laboratory, Inc., OSR TN 59-1309, November, 1959.

[13] Cambell, A. J., *Investigation of a Wide-Angle Diffuser With an Augmentation for Use as a Jet Muffler*, Univ. of Toronto Institute of Aerophysics, TN 15, 1957.

✦ ✦ ✦

Readers' Forum

BRIEF REPORTS of investigations in the aerospace sciences and discussions of papers published in the JOURNAL are presented in this special department. Entries must be restricted to a maximum of 1,300 words or the equivalent of one JOURNAL page including formulas and illustrations. Publication is completed as soon as possible after receipt of the material. The Editorial Committee does not hold itself responsible for the opinions expressed by the correspondents.

Contents

Comment on "A Note for Finding Complex Roots of a Special Kind of Quartic Equation" ..... JAMES SHENG 332
Additional Comment ..... RALPH PAPIRNO 332
Additional Comment ..... ARTHUR W. LEISSA 333
Author's Reply ..... F. A. LEE 333
Comments on "Rarefaction Effects in Low-Speed Turbulence" ..... S. CORRSIN 333
Authors' Reply ..... HAROLD S. MICKLEY AND ANTHONY TURANO, JR. 334
Turbine-Nozzle Wake Prediction ..... R. HIRSCHKRON AND J. M. HEALZER 334
On Skin Friction in the Slip-Flow Regime ..... H. A. HASSAN 335
One-Dimensional Heat Conduction With Arbitrary Heating Rate ..... SHIH-YUAN CHEN 336
On the Gradient Functions for Nonequilibrium Dissociative Flow Behind a Shock ..... CHENG-TING HSU 337
On Moderately Separated Viscous Flows ..... MARTIN H. BLOOM 339
Vortex Shedding From Thin Flat Plates Parallel to the Free Stream ..... ANDREW B. BAUER 340
Thermal Buckling of Rectangular Plates ..... KORYO MIURA 341
High-Heat-Flux Effects in Wire Heat Gages ..... JOHN C. CUTTING AND JAMES A. FAY 342
Concerning the Integral Equation of Unsteady Motion of a Delta Wing in Supersonic Flight by Means of the Acceleration-Potential Method ..... M. M. STANIŠIĆ 343
Heat Transfer to Sharp and Blunt Yawed Plates in Hypersonic Airflow ..... J. GORDON HALL AND T. C. GOLIAN 345
Free-Convection Magnetohydrodynamic Flow Past a Porous Flat Plate ..... PAU-CHANG LU 346
The Redesign of Redundant Structures Having Undesirable Stress Distributions ..... E. D. POPPLETON 347
On Column Behavior ..... S. SERGEV 348
On the Feasibility of Using Aerodynamic Control on Vehicles Operating in Regions of Slip Flow and Free-Molecule Flow ..... ROBERT L. SWAIM 349
A Method of Obtaining An Approximate Solution of the Laminar Boundary-Layer Equations ..... WILLIAM B. BUSH 350
Atmospheric Entry With Small L/D ..... PAUL D. ARTHUR AND HANS K. KARRENBERG 351

Comment on "A Note for Finding Complex Roots of a Special Kind of Quartic Equation"

James Sheng
Dynamics Research Staff, Research and Development Department, The Martin Company, Baltimore, Md.

September 9, 1960

IN A RECENT PAPER,[1] a method described in detail was proposed for the solution of the quartic equation. However, this method is commonly known as Descartes' method, given in 1637, which may be found in standard textbooks used in high schools and first-year colleges.

REFERENCE

[1] Lee, F. A., *A Note for Finding Complex Roots of a Special Kind of Quartic Equation*, Journal of the Aerospace Sciences, Readers' Forum, Vol. 27, No. 9, pp. 714–715, September, 1960.

Additional Comment

Ralph Papirno
Research Scientist, Research Division, College of Engineering, New York University, N.Y.

September 10, 1960

IN A NOTE in the Readers' Forum in the September 1960 issue (see reference 1 above), F. A. Lee proposes an explicit method for finding the complex roots of the quartic equation:

$$x^4 + A_2x^2 + A_1x + A_0 = 0$$

It should be pointed out that this is the method proposed by L. Ferrari some 400 years ago and which may be found described in various handbooks and in texts on the Theory of Equations—(see for example L. E. Dickson, "New First Course in the Theory of Equations," pp. 51–52, Wiley, 1939).

Contributors Please Note

Readers' Forum items must be confined to the equivalent of one page in the *journal*. Contributions that exceed this limit will be returned to the authors for condensation and rewrite. To avoid inconvenience and delay, please adhere to the following specifications:

(1) Five, double-spaced, typewritten, manuscript pages (8½ by 11 in.), including wide margins, formulas, and headings, equal one printed page.

(2) For every illustration, deduct at least one-half or as much as one manuscript page, depending on the size of the illustration.

In addition, it should be noted that Ferrari's method may also be used on the general form of the quartic—i.e., a quartic with the cube term present.

Additional Comment

Arthur W. Leissa
Assistant Professor of Engineering Mechanics, The Ohio State Univ. Also, Research Specialist, Columbus Div., North American Aviation, Inc.
September 13, 1960

IN THE PAPER BY LEE (see reference 1 above), an explicit method is presented for finding the roots of a quartic in the form

$$x^4 + A_2x^2 + A_1x + A_0 = 0 \qquad (1)$$

As is shown by Burington[1] and many others, any general quartic of the form

$$y^4 + py^3 + qy^2 + ry + s = 0 \qquad (2)$$

can be reduced to the normal form of Eq. (1) by the substitution of

$$y = x - (p/4) \qquad (3)$$

However, the explicit method of solution is generally quite tedious. In the writer's experience it has been found that for most types of quartics encountered, and for the type of accuracy usually required by engineering calculations, it is usually easier to solve a fourth-degree equation by trial-and-error or by means of another approximate method.

REFERENCE

[1] Burington, R. S., *Handbook of Mathematical Tables and Formulas*, 3rd Ed., p. 9, Handbook Publishers, Inc., 1948.

Author's Reply

F. A. Lee
Structural Dynamics Group, Structural Research Unit, Boeing Airplane Company, Transport Div., Renton, Wash.
September 13, 1960

I HAVE ATTEMPTED TO DETERMINE the overlap between my proposed method[1] as published in Readers' Forum of last September and that of Ferrari, Descartes, or others, and have found the following which might be of interest.

(1) Ferrari's method and the method proposed are not identical. Ferrari's method involves the concept of completion of perfect squares, while mine rests on consideration of quadratic factors. Also, Ferrari's "resolvent cubic" form (based on omission of the cubic term from the quartic equation) is different from mine because of the basic difference in initial mathematical approach.

(2) The method suggested by Descartes is indeed the same as that proposed. I have conducted quite an extensive literature search in the University of Washington Library in an effort to determine the nature of Descartes' method, however, I have been unable to find any reference to such a method in any of the available textbooks on college algebra. This method does appear in "Theory of Equations" (see reference 2).

(3) Professor Leissa's comments are interesting in providing another approach to the solution of a more general type of quartic equation. However, the method listed in Burington's Handbook differs again in that it is described as Euler's method (see reference 2) and involves the assumption of the explicit irrational form of roots.

Upon review of my initial Readers' Forum article, I find that an implication as to nonexistence of any other methods of solution could be drawn although such was not my intent. The Descartes' method is new to me and I hope my reviewers will excuse this oversight.

REFERENCES

[1] Lee, F. A., *A Note for Finding Complex Roots of a Special Kind of Quartic Equation*, Journal of the Aerospace Sciences, Readers' Forum, Vol. 27, No. 9, pp. 714–715, September, 1960.

[2] Burnside, W. S., and Panton, A. W., Theory of Equations, Vol. I, Chapt. VI and Note A, Dublic University Press, 1918.

Comments on "Rarefaction Effects in Low-Speed Turbulence"[1]

S. Corrsin
Professor of Fluid Mechanics, Mechanics Department, The Johns Hopkins University, Baltimore, Md.
August 8, 1960

THE MEASUREMENTS of turbulence at low density given in reference 1 are interesting and important, but I should like to comment on the authors' heroic assertion: "These results are a *refutation*† of a fundamental premise of turbulence theory that for all practical conditions the fluid may be regarded as a continuum, and hence the validity of the Navier-Stokes equations may be assumed, even when applied to the smallest scale components of the motion."

In fact, the use of the Navier-Stokes equations in turbulence theory is regarded by turbulence-research people as simply a *restriction* to cases in which the Navier-Stokes equations are applicable—e.g., to gas flows in which the Kolmogorov microscale is much larger than the mean free path.

Thus, nothing has been refuted; the authors have, however, pushed forward the frontiers to give us an empirical estimate of a qualitatively known restriction.

The usual criterion for estimating whether a particular turbulent gas flow fulfills the continuum restriction is derived from the identity which states that the Kolmogorov Reynolds number is unity:

$$\eta v^*/\nu \equiv 1 \qquad (1)^*$$

where

$$\eta \equiv (\nu^3/\epsilon)^{1/4} \quad \text{and} \quad v^* \equiv (\nu\epsilon)^{1/4} \qquad (1a,b)$$

are the Kolmogorov microscale and velocity, respectively. ν is kinematic viscosity; ϵ is time rate of viscous dissipation of turbulent kinetic energy per unit mass.

With a gas-kinetic estimate for ν,

$$\nu \backsimeq lc \qquad (2)$$

[l = mean free path; c = rms molecular velocity or sound velocity], Eq. (1) gives

$$l/\eta \backsimeq v^*/c \qquad (3)^*$$

the Mach number of the "small eddies."

An equation in more accessible variables follows from Eq. (1b) and G. I. Taylor's form for ϵ in isotropic turbulence,

$$\epsilon = \nu\overline{(\partial u_i/\partial x_k)(\partial u_i/\partial x_k)} = 15\,\nu(u'^2/\lambda^2) \qquad (4)$$

Here $u' \equiv \sqrt{\overline{u^2}}$, the rms turbulent velocity component; λ is a Taylor microscale, actually defined by Eq. (4). Then Eq. (3) becomes

$$l/\eta \backsimeq (0.5/\sqrt{R_\lambda})(u'/c) = (0.5/\sqrt{R_\lambda})M \cdot (u'/\bar{U}) \qquad (5)^*$$

$R_\lambda \equiv u'\lambda/\nu$ is a turbulence Reynolds number,[2] M is Mach number, $\bar{U}$ is mean velocity.

† Italics mine.

* The interpretation of a Reynolds number as the ratio of a Mach number and a Knudsen number is apparently due to von Kármán: *Gastheoretische Deutung der Reynoldsschen Kennzahl*, ZAMM., Vol. 3, pp. 395–396, 1923. I am uncertain who originally devised this particular relation for turbulent motion; I first heard it, in 1950, at a lecture by J. von Neumann.

Eq. (3) of reference 1 appears to be incomplete. Its basis is not indicated there, but a more appropriate form follows from Eq. (5): first introduce the theoretical relation

$$R_\lambda \sim \sqrt{R_L} \tag{6}$$[2]

where $R_L \equiv u'L/\nu$, and L is an integral scale of the turbulence. Empirically, it is observed that for given geometry

$$L \sim D \tag{7}$$[4]

D is a characteristic dimension of the system.

With these, Eq. (5) becomes

$$l/\eta \sim (M/R_D{}^{1/4})(u'/\bar{U})^{5/4} \tag{8}$$

$[R_D \equiv \bar{U}D/\nu]$.

This permits estimating $u'/\bar{U}$ as a function of l/η provided the Mach number and Reynolds number are kept constant. An important aspect is that Mach-number effects cannot be ignored in Eq. (8) no matter how small M is.

Finally, it is obvious that Eq. (8) can be valid only for "small" amounts of slip because the basic relations come from continuum theory.

REFERENCES

[1] Mickley, H. S., and Turano, A., Jr., *Rarefaction Effects in Low-Speed Turbulence*, Journal of the Aerospace Sciences, Vol. 27, No. 8, pp. 629–630, August, 1960.

[2] Batchelor, G. K., *The Theory of Homogeneous Turbulence*, Cambridge University Press, 1953.

[3] Corrsin, S., *Outline of Some Topics in Homogeneous Turbulent Flow*, J. Geophys. Res., Vol. 64, No. 12, pp. 2134–50, December, 1959.

[4] Corrsin, S., *Simple Theory of an Idealized Turbulent Mixer*, J. AIChE, Vol. 3, Section 3, (see "for example"): pp. 329–30, September, 1957.

Authors' Reply

Harold S. Mickley* and Anthony Turano, Jr.**

Department of Chemical Engineering, Massachusetts Institute of Technology, Cambridge, Mass.

September 26, 1960.

As Professor Corrsin points out, it has indeed long been recognized that the Navier-Stokes equations are not always valid. Dr. G. K. Batchelor (reference 2, page 5) states: "It has occasionally been speculated in the literature of the subject that since turbulence is a mixture of many different length scales, there may exist some subsidiary motions whose length scales are so small as to be comparable with the mean free path (for a gaseous medium), and if this were true, the Navier-Stokes equation certainly would not apply to these small-scale motions." Dr. Batchelor goes on to remark: "However, the action of viscosity is to suppress strongly the small-scale components of the turbulence, and we shall see that for all practical conditions the spectral distribution of energy dies away effectively to zero long before length scales comparable with the mean free path are reached. As a consequence we can ignore the molecular structure of the medium and regard it as a continuous fluid." In reference 1 it was our desire to point out that "significant rarefaction effects do occur in practical systems at pressures far higher than previously have been suspected."

Eq. (3) of reference 1 is actually an extension of Professor Corrsin's Eq. (8). Space limitations prevented its derivation and extended discussion. The intermediate steps in our derivation of Eq. (3), reference 1 are very similar to his development of his Eq. (8). We extended the treatment in order to obtain a relation which would be more immediately useful in the problem of modelling, recognizing that in many cases measurements of turbulent intensity would not be available. Our basic additional assumption was that as long as continuum relations were valid, the turbulence intensity in the wake of the turbulence-generating device would be of the form

$$u'/\bar{v} = \varphi(C_D)/f(\mathbf{R}/D) \tag{1}$$

where C_D is the drag coefficient of the turbulence generator, $\mathbf{R}$ the downstream position vector, and D a characteristic system dimension. For sufficiently high Reynolds numbers and in the absence of significant slipflow, presumably $\varphi(C_D)$ and $f(\mathbf{R}/D)$ are functions of the system geometry only. This is borne out, for example, by measurements of turbulent intensity behind grids in the early decay period. We then substituted Eq. (1) above into the equivalent of Corrsin's Eq. (8); giving Eq. (3) of reference 1:

$$l/\eta \sim \left(\frac{u'}{\bar{v}}\right)^{3/4} \frac{M}{R_D{}^{1/4}} = \left[\frac{\varphi(C_D)}{f(\mathbf{R}/D)}\right]^{3/4} \frac{M}{R_D{}^{1/4}}$$

$$= \Lambda M/R_D{}^{1/4}$$

(To avoid confusion we use l here to denote the mean free path.) It then follows that if a device exhibits rarefaction effects beginning at a given value of $M/R_D{}^{1/4}$, a geometrically similar device should do so also provided the continuum and Reynolds-number limitations are observed.

REFERENCES

[1] Mickley, H. S., and Turano, A., Jr., *Rarefaction Effects in Low-Speed Turbulence*, Journal of the Aerospace Sciences, Vol. 27, No. 8, pp. 629–630, August, 1960.

[2] Batchelor, G. K., *The Theory of Homogeneous Turbulence*, Cambridge University Press, Cambridge, Mass., 1953.

Turbine-Nozzle Wake Prediction

R. Hirschkron* and J. M. Healzer**

General Electric Co., Lynn, Mass., and Technical Education, Schenectady, N.Y., Respectively.

August 12, 1960

SYMBOLS

d_0	=	nozzle throat
K_1	=	6.502×10^{-5}, constant

* Manager, Turbine Aerodynamics Small Aircraft Engine Dept.

** Engineer.

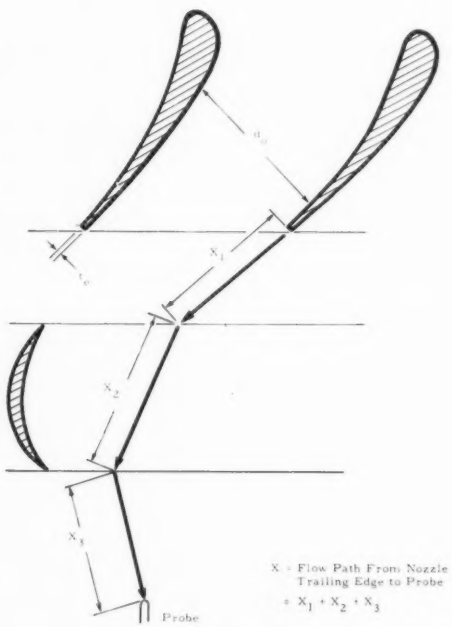

FIG. 1. Nozzle wake flow path.

* Professor of Chemical Engineering.

** Now employed by the Esso Standard Oil Company, Baton Rouge. La.

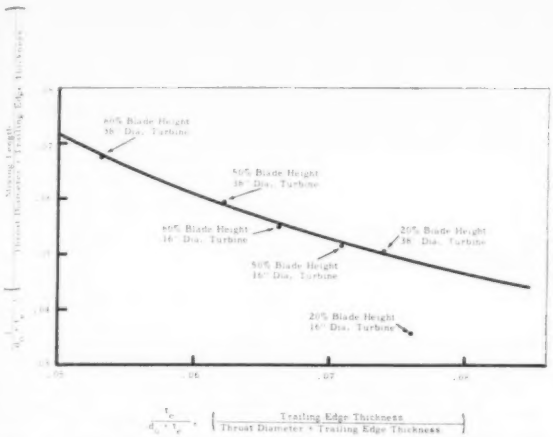

FIG. 2. Mixing lengths calculated from two air turbine tests.

l = mixing length
P_S = static pressure
P_{TA} = average total pressure
ΔP_{TW} = total pressure difference, max.-min.
t_e = nozzle trailing-edge thickness
X = streamline distance from nozzle trailing edge to point of interest (see Fig. 1)
u_1 = perturbation velocity
U = mean velocity
Y = coordinate axis perpendicular to streamline

THE PERSISTENCE of nozzle wakes through the downstream rotor has been long appreciated. The following test results show that the decay and extent of the wakes can be predicted.

From Prandtl's mixing-length theory, an expression for the velocity perturbation u_1 can be derived if a mixing length l is postulated proportional to $(d_0 + t_e)$, the nozzle spacing in the streamline direction normal to the flow[1]:

$$u_1 = \frac{U}{8\pi^3}\left(\frac{t_e + d_0}{l}\right)^2\left(\frac{t_e + d_0}{X}\right)\cos\left(\frac{2\pi Y}{t_e + d_0}\right) \tag{1}$$

Circumferential traverse data obtained behind the rotors of two completely different turbines were reduced to compute a mixing-length ratio. The total and static pressure measured on a wedge probe in one case, and a cobra probe in the other case, were used in an expression derived from (1) above:

$$\frac{\Delta P_{TW}}{P_{TA} - P_S} = K_1\left(\frac{d_0 + t_e}{X}\right)^2\left(\frac{d_0 + t_e}{l}\right)^4 \tag{2}$$

From Eq. (2) a mixing length l was found for each radial station where a circumferential traverse was accomplished.

Fig. 2 shows the resulting mixing-length ratios $l/(d_0 + t_e)$ plotted against $t_e/(d_0 + t_e)$. There is a clear empirical correlation between the mixing length and trailing-edge blockage parameter. For a large trailing-edge blockage, the mixing length is small and hence, from Eq. (2), the wake will persist further downstream.

REFERENCE

[1] Olsson, R. Gran, *Geschwindigkeits und Temperaturverteilung hinter einem Gitter bei turbulenter Strömung*, ZAMM, Vol. 16, pp. 257–274, 1936.

On Skin Friction in the Slip-Flow Regime

H. A. Hassan
Associate Professor, Department of Aeronautical Engineering, Virginia Polytechnic Institute, Blacksburg, Va.
August 19, 1960

THE OBJECT OF THIS NOTE is to give an expression for the shearing stress in the slip-flow regime for a certain class of outer pressure distributions. It is shown that, for the class of outer pressure distributions considered, the governing equations have a series solution whose coefficients are governed by second-order linear differential equations which have known solutions. The resulting expression for the skin-friction coefficient shows that the pressure gradient has a second-order effect. The problem in the absence of pressure gradient has been discussed by Schaaf and Sherman[1] and Hasimoto.[2]

The governing equations are assumed to be the laminar boundary-layer equations for an incompressible flow. These equations can be written as

$$uu_x + vu_y = VV_x + \nu u_{yy} \tag{1}$$

$$u_x + v_y = 0 \tag{2}$$

where V is the free-stream velocity and ν is the kinematic viscosity. The slip-flow boundary conditions, assuming reflection, are

$$u = Lu_y, \quad v = 0 \text{ at } y = 0, \quad u \to V \text{ as } y \to \infty \tag{3}$$

where L is the mean free path.

The boundary conditions can be simplified by introducing von Mises' transformation. This transformation reduces the governing equations and boundary conditions to

$$uu_x = VV_x + \nu u(uu_\psi)_\psi \tag{4}$$

and $$u^\psi = 1/L \text{ at } \psi = 0, \quad u \to V \text{ as } \psi \to \infty \tag{5}$$

Introducing the dimensionless quantities

$$s = x/L, \quad \sigma = \psi/\nu, \quad V = (\nu/L)h(s), \quad u = (\nu/L)\chi(s, \sigma) \tag{6}$$

one obtains $$\chi[\chi\chi_\sigma]_\sigma - \chi\chi_s + hh' = 0 \tag{7}$$

and $$\chi_\sigma = 1 \text{ at } \sigma = 0, \quad \chi \to h(s) \text{ as } \sigma \to \infty \tag{8}$$

It will be assumed that h has a power-series representation. As a result of this assumption, it has been found useful to introduce the transformation

$$\xi = \sqrt{s}, \quad \eta = \sigma f(s) \tag{9}$$

$$h(\xi) = \sum_0^\infty a_n\xi^n, \quad \chi = h(s)\varphi(\xi, \eta)$$

where $$f(\xi) = 1/\xi h \quad \text{and} \quad a_0 \neq 0 \tag{10}$$

Substituting Eqs. (9) and (10) into Eqs. (7) and (8), one finds

$$\varphi[\varphi\varphi_\eta]_\eta - (\varphi/2)[\xi h'(\varphi - 1/\varphi) + \xi h\varphi_\xi - (h + \xi h')\eta\varphi_\eta] = 0 \tag{11}$$

and $$\varphi_\eta = \xi \text{ at } \eta = 0, \quad \varphi \to 1 \text{ as } \eta \to \infty \tag{12}$$

The solution of Eq. (11) is assumed as

$$\varphi = 1 + \sum_{n=1}^\infty \varphi_n(\eta)\xi^n \tag{13}$$

with the functions φ_n satisfying the following boundary conditions:

$$\varphi_1' = 1, \quad \varphi_n' = 0, \quad n \geq 2 \text{ at } \eta = 0, \quad \varphi_n' \to 0 \text{ as } \eta \to \infty \tag{14}$$

Substituting Eq. (13) into Eq. (11) and letting

$$\xi h'/h = \sum_0^\infty b_n\xi^n, \quad b_0 = 0 \tag{15}$$

one finds that the functions φ_n satisfy the following linear equations:

$$\varphi_n'' + (a_0/2)[\eta\varphi_n' - n\varphi_n] = R_{n-1} \tag{16}$$

where

$$R_0 = 0 \tag{17a}$$

$$R_{n-1} = -2\sum_{k=1}^{n-1}\varphi_k\varphi_{n-k}'' - \sum_{k=1}^{n-1}\sum_{m=1}^{n-k}\varphi_m\varphi_k\varphi_{n-m-k}'' - \sum_{k=1}^{n-1}\varphi_k'\varphi_{n-k}' - \sum_{k=1}^{n-1}\sum_{m=1}^{n-k}\varphi_m\varphi_k'\varphi_{n-m-k}' + (1/2)\left\{n\sum_{k=1}^{n-1}a_k\varphi_{n-k} + a_0\sum_{k=1}^{n-1}(n-k)\varphi_k\varphi_{n-k} + \sum_{=1}^{n-1}\sum_{m=1}^{n-k}(n-m)a_k\varphi_m\varphi_{n-m-k} - \eta\sum_{k=1}^{n-1}a_k(1+k)\varphi_{n-k}' - a_0\eta\sum_{k=1}^{n-1}\varphi_k\varphi_{n-k}' - \eta\sum_{k=1}^{n-1}\sum_{m=1}^{n-k}a_k(1+k)\varphi_m\varphi_{n-m-k}'\right\} \quad (17b)$$

Letting $\varphi_n = \beta^2 F_n, \quad \eta = \beta Z, \quad \beta^2 = 4/a_0$ (18)

Eq. (16) reduces to

$$F_n'' + 2ZF_n' - 2nF_n = R_{n-1}(Z) \quad (19)$$

It is known that the homogeneous part of Eq. (19) is satisfied by the repeated integrals of the error function; these integrals are defined as

$$E_n(z) = \int_Z^\infty E_{n-1}(\xi)\alpha\xi,$$

$$E_0(z) = erfcz = (2/\sqrt{\pi})\int_Z^\infty \exp(-\xi^2)d\xi \quad (20)$$

Therefore, the solution of Eq. (19) can be written as

$$F_1 = E_1/\beta \quad (21a)$$

and

$$F_n = c_nE_n + E_n\int_Z^\infty [\exp(-\eta^2)/E_n^2] \times \left\{\int_\eta^\infty \exp(\xi^2)E_nR_{n-1}d\xi\right\} d\eta \quad (21b)$$

where c_n is a constant to be determined from the condition $F_n'(0) = 0, \quad n \geq 2$.

Both numerical and analytical methods can be employed in carrying out the integration in Eq. (21b). The latter approach is used here and it has been possible to give a closed-form expression only for $n = 2$. However, for $n \geq 3$ the integrals can be expressed in terms of convergent power series.

Using Eqs. (14), (17), (18), (20), and (21b), one obtains

$$F_2 = (1/2)\{(7/2)E_2 - (E_1^2 + E_0E_2)\} + (a_1\beta/4)[E_1 - \sqrt{\pi}E_2 + 2\exp(-Z^2)/3\sqrt{\pi}] \quad (22a)$$

$$F_3 = -\beta\{2(1+1/\pi)E_3 - (7/8)(3E_1E_2 + E_0E_3) + E_1^3/4 + (3/2)E_2E_1E_0 - [\exp(-Z^2)/2\sqrt{\pi}][E_2^2 + 4E_2^2 + 32E_1^2 + \ldots] - (\beta^2a_1/2)\{\sqrt{\pi}(1 + 47/6\pi)E_3 + (7E_0/24) + (\sqrt{\pi}/4)(3E_1E_2 + E_0E_3) - 11E_2E_0/15 - [\exp(-Z^2)/2\sqrt{\pi}]E_1 - Z[\exp(-Z^2)/2\sqrt{\pi}][E_2 - 13E_1^2/30 + (3/10)(E_2^2 - E_2^2) + \ldots]\} + (\beta^3a_1^2/4)\{-E_3 + \sqrt{\pi}E_0/12 - E_1/8 - [\exp(-Z^2)/9\sqrt{\pi}][Z^2 + 23/8]\} + (\beta a_2/2)[E_1/4 + 3\exp(-Z^2)/8\sqrt{\pi} - E_3] \quad (22b)$$

Therefore, using Eqs. (13), (18), (21a), and (22), one obtains the following expression for local skin-friction coefficient:

$$C_f = (2\beta^2/h)\{(1/\beta^2) - (\xi/\beta\sqrt{\pi}) + [5/16 - 1/2\pi + a_1\beta\sqrt{\pi}(5/12\pi - 1/16)]\xi^2 + [-\beta(19/36\pi\sqrt{\pi} - 17/64\sqrt{\pi}) - (\beta^2a_1/4)(1 + 1/\pi) + (\beta^3a_1^2\sqrt{\pi}/48)(1 - 22/3\pi) + 11\beta a_2/48\sqrt{\pi}]\xi^3 + \ldots\} \quad (23)$$

In conclusion, it should be remembered that the assumptions introduced are rather restrictive because the range of Knudsen number that defines the slip-flow regime requires a large Mach number or a small Reynolds number or both. Therefore, the results obtained are expected to give first-order estimates in the low-Mach-number range.

References

[1] Schaaf, S. A., and Sherman, F. S., *Skin Friction in Slip Flow*, Journal of the Aeronautical Sciences, Vol. 21, No. 2, pp. 85–90, 144, February, 1953.

[2] Hasimoto, H., *Boundary-Layer Slip Solutions for a Flat Plate*, Journal of the Aeronautical Sciences, Readers' Forum, Vol. 25, No. 1, pp. 68–69, January, 1958.

One-Dimensional Heat Conduction With Arbitrary Heating Rate

Shih-Yuan Chen
Chief, Aerothermodynamics Unit, Aero-Space Division, Boeing Airplane Company, Seattle, Wash.

August 14, 1960

ONE-DIMENSIONAL HEAT CONDUCTION with arbitrary heating rate at one boundary while the other boundary is insulated has become a problem of interest in recent years in hypersonic-vehicle design. The problem with variable coefficient of heat transfer and variable adiabatic wall temperature without phase change was given by Chen.[1] However, when a vehicle re-enters the earth's atmosphere, its surface temperature is small compared with the gas temperature and can be neglected. For this case, the heating rate at one boundary becomes a time function $q(t)$. Sutton[2] has presented solutions for the case where $q(t)$ is represented by a power series. The solutions presented here are for an arbitrary time function $q(t)$.

Consider the general case of transient one-dimensional heat conduction as shown in Fig. 1. The material is assumed to have constant properties and the heat flux is time-dependent. For this case, the basic differential equation for heat conduction and the initial and boundary conditions are:

$$\frac{\partial T(x,t)}{\partial t} = \alpha\frac{\partial^2 T(x,t)}{\partial x^2} \qquad 0 \leq x \leq a \quad (1)$$

$$T(x,0) = T_i = \text{constant} \quad (2)$$

$$\frac{\partial T(0,t)}{\partial x} = 0 \quad (3)$$

$$k\frac{\partial T(a,t)}{\partial x} = q(t) \quad (4)$$

where $q(t)$ is the heat flux at the boundary $x = a$. Only aerodynamic heating effects such as gas convection and gas radiation from the shock layer are considered. Surface radiation to space has been neglected for simplicity, since it is at least one order of magnitude smaller than the aerodynamic heating rate or can be included by iteration methods. Let

$$x = a\xi \quad (5)$$

$$t = (a^2/\alpha)\tau \quad (6)$$

$$\theta(\xi,\tau) = T(x,t) - T_i \quad (7)$$

$$(a/k)q(t) = Q(\tau) \quad (8)$$

Introducing these definitions into Eqs. (1)–(4), we have

$$\partial\theta/\partial\tau = \partial^2\theta/\partial\xi \qquad 1 \leq \xi \leq 1 \quad (9)$$

$$\theta(\xi,0) = 0 \quad (10)$$

$$\frac{\partial\theta(1,\tau)}{\partial\xi} = Q(\tau) \quad (11)$$

$$\frac{\partial\theta(-1,\tau)}{\partial\xi} = -Q(\tau) \tag{12}$$

Let $\bar{\theta}(\xi, s)$ and $\bar{Q}(s)$ be Laplace transforms of the temperature $\theta(\xi, \tau)$ and $Q(\tau)$ respectively, where s is the Laplace-transform parameter. Then Eqs. (9) to (12) become

$$s\bar{\theta} = d^2\bar{\theta}/d\xi \tag{13}$$

$$\frac{d\bar{\theta}(1,s)}{d\xi} = \bar{Q}(s) \tag{14}$$

$$\frac{d\bar{\theta}(-1,s)}{d\xi} = -\bar{Q}(s) \tag{15}$$

The solution of the transformed problem becomes

$$\bar{\theta} = \frac{\bar{Q}(s)\cosh\sqrt{s}\,\xi}{\sqrt{s}\sinh\sqrt{s}} \tag{16}$$

Let $v(\xi, \tau)$ denote the temperature distribution when $Q(\tau) = 1$. The solution of this transformed problem equals $V(\xi, s)$ or

$$V(\xi, s) = \frac{\cosh\sqrt{s}\,\xi}{s^{3/2}\sinh\sqrt{s}} \tag{17}$$

or

$$v(\xi,\tau) = \tau + \frac{3\xi^2-1}{6} + \frac{2}{\pi^2}\sum_{n=1}^{\infty}\frac{(-1)^{n+1}}{n^2}e^{-n^2\pi^2\tau}\cos n\pi\xi \tag{18}$$

Assume that $Q(\tau)$ is continuous, that $Q'(\tau)$ is sectionally continuous, and that these functions are of exponential order; then

$$\bar{\theta}(\xi, s) = [L\{Q(\tau)\} + Q(0)]V(\xi, s) \tag{19}$$

Consequently, one has the solution:

$$\begin{aligned} Q(\xi,\tau) &= Q(0)v(\xi,\tau) + \int_0^\tau Q'(\tau-t)v(\xi,t)\,dt \\ &= \frac{3\xi^2-1}{6}Q(\tau) + \int_0^\tau Q(\tau-t)\,dt \\ &\quad - \frac{2Q(0)}{\pi^2}\sum_{n=1}^{\infty}\frac{(-1)^n}{n^2}e^{-n^2\pi^2\tau}\cos n\pi\xi \\ &\quad - \frac{2}{\pi^2}\sum_{n=1}^{\infty}\frac{(-1)^n}{n^2}\cos n\pi\xi\int_0^\tau Q'(\tau-t)e^{-n^2\pi^2\tau}\,dt \end{aligned} \tag{20}$$

Hence

$$\begin{aligned} T(x,t) &= T_i + \frac{3x^2-a^2}{6ak}q(t) - \frac{\alpha}{ak}\int_0^t q(t-\tau)d\tau \\ &\quad - \frac{2a}{k\pi^2}q(0)\sum_{n=1}^{\infty}\frac{(-1)^n}{n^2}e^{-n^2\pi^2(\alpha/a^2)t}\cos n\pi\frac{x}{a} \\ &\quad - \frac{2a}{k\pi^2}\sum_{n=1}^{\infty}\frac{(-1)^n}{n^2}\cos n\pi\frac{x}{a}\int_0^t q'(t-\tau)e^{-n^2\pi^2(\alpha/a^2)\tau}d\tau \end{aligned} \tag{21}$$

for $0 \le x \le a$ and $T(a, t) < T_{ab}$.

The convergence of the series of Eq. (21) is rapid for large time. For small time the exact solution of Eq. (1) can be rewritten into a different form, namely

$$\begin{aligned} T(x,t) &= \frac{\sqrt{\alpha}}{k\sqrt{\pi}}\sum_{k=0}^{\infty}\int_0^t q(t-\tau)\frac{1}{\sqrt{\tau}}e^{-\frac{[(2k+1)a+x]^2}{4\alpha\tau}}d\tau \\ &\quad + \frac{\sqrt{\alpha}}{k\sqrt{\pi}}\sum_{k=0}^{\infty}\int_0^t q(t-\tau)\frac{1}{\sqrt{\tau}}e^{-\frac{[(2k+1)a+x]^2}{4\alpha\tau}}d\tau \end{aligned} \tag{22}$$

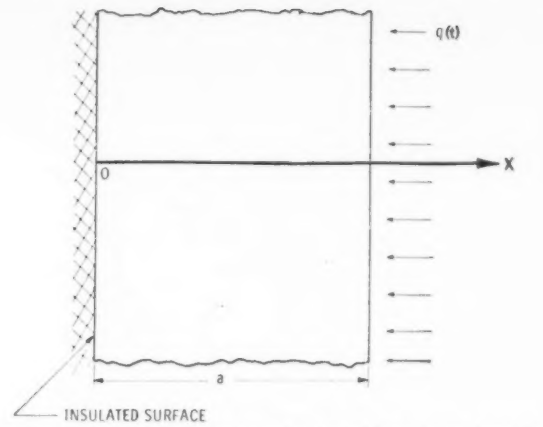

FIG. 1. One-dimensional heat conduction with arbitrary heating rate.

REFERENCES

[1] Chen, Shih-Yuan, *Transient Temperature and Thermal Stresses in Skin of Hypersonic Vehicle with Variable Boundary Conditions*, Trans. ASME, Vol. 80, October 1958.

[2] Sutton, G. W., *On One-Dimensional Heat Conduction With an Arbitrary Heating Rate*, Journal of the Aeronautical Sciences, Readers' Forum, Vol. 24, No. 11, pp. 854–855, November 1957.

On the Gradient Functions for Nonequilibrium Dissociative Flow Behind a Shock

Cheng-Ting Hsu
Associate Professor, Dept. of Aeronautical Engineering, Iowa State University, Ames, Iowa
October 17, 1960

THE GRADIENT FUNCTIONS of flow variables behind a curved shock in a vibrational relaxing flow were evaluated by Sedney.[1] The present note deals with those functions in the case of a nonequilibrium dissociative flow.

The dynamic equations of motion[1] in a steady isoenergetic flow using natural coordinates (see Fig. 1) are

Continuity
$$\frac{1}{\rho}\frac{\partial\rho}{\partial s} + \frac{1}{q}\frac{\partial q}{\partial s} + \frac{\partial\theta}{\partial n} + \frac{\epsilon\sin\theta}{y} = 0 \tag{1}$$

Momentum
$$\rho q\frac{\partial q}{\partial s} = -\frac{\partial p}{\partial s} \tag{2}$$

$$\rho q^2\frac{\partial\theta}{\partial s} = -\frac{\partial p}{\partial n} \tag{3}$$

Energy
$$dh + qdq = 0 \tag{4}$$

where p, ρ, h, q, and θ are the pressure, density, enthalpy, velocity and flow inclination, respectively, s and n are the distances along the streamline and its normal direction, respectively. $\epsilon = 1$ is for axisymmetrical flow and $\epsilon = 0$ is for two-dimensional flow. y is the distance from the axis of symmetry.

The thermodynamic aspect of a nonequilibrium dissociated gas (e.g., N_2) is treated below. Consider the dissociation of a unit mass of the mixture, the chemical equation is represented as $N_2 \rightleftharpoons 2N$. Let α be the degree of dissociation, m_1 and m_2 the masses of the reacting N and N_2, respectively; then $dm_i = \nu_i d\alpha$ where $\nu_1 = 1$ and $\nu_2 = -1$. If the enthalpy of a mixture of perfect gases is chosen as a function of p, S and m_i, the second law of thermodynamics may be written as

$$dh = TdS + (dp/\rho) + \sum_i \mu_i\nu_i d\alpha \tag{5}$$

where S is the specific entropy and μ_i is the chemical potential.

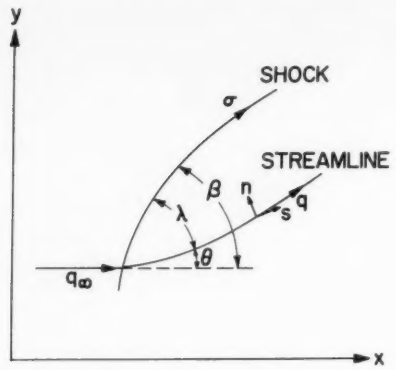

FIG. 1.

In terms of Gibbs free energy,[2] we have

$$\sum_i \mu_i \nu_i = (\partial G/\partial \alpha)_{p,T} \tag{6}$$

Combination of Eqs. (4), (5), and (6) results in

$$TdS = -qdq - (dp/\rho) - (\partial G/\partial \alpha)_{p,T}\, d\alpha \tag{7}$$

The Gibbs function[3] for a mixture of thermally perfect gases may be written as

$$G = \alpha[\omega_1(T) + R_1 T \ln p_1] + (1-\alpha)[\omega_2(T) + R_2 T \ln p_2] \tag{8}$$

where

$$p_1 = 2\alpha p/(1+\alpha), \quad p_2 = (1-\alpha)p/(1+\alpha), \quad p = (1+\alpha)\rho R_2 T \tag{9}$$

and

$$\omega_i(T) = \int c_{p_i} dT - T \int c_{p_i} \frac{dT}{T} + h_{0_i} - S_{0_i} T \tag{10}$$

The subscripts 1 and 2 indicate atomic and molecular nitrogen, respectively. R is the gas constant and $R_1 = 2R_2$. Substituting Eq. (9) into Eq. (8), and differentiating Eq. (8) with respect to α for constant p and T, we obtain

$$(\partial G/\partial \alpha)_{p,T} = \omega_1(T) - \omega_2(T) + R_2 T \ln 4\alpha^2 p/(1-\alpha^2) \tag{11}$$

Substituting Eq. (11) into Eq. (7), it gives

$$TdS = -qdq - \frac{dp}{\rho} - \left[\omega_1(T) - \omega_2(T) + R_2 T \ln \frac{4\alpha^2}{1-\alpha^2} p\right] d\alpha \tag{12}$$

The bracket term indicates the degree of flow nonequilibrium. For equilibrium flow this bracket term vanishes[3] while for frozen, flow $d\alpha = 0$. Taking the directional derivatives of Eq. (12) along the streamline and its normal directions respectively and making use of Eqs. (2) and (3), we have

$$T\frac{\partial S}{\partial s} = -\left[\omega_1(T) - \omega_2(T) + R_2 T \ln \frac{4\alpha^2}{1-\alpha^2} p\right] \frac{\partial \alpha}{\partial s} \tag{13a}$$

$$T\frac{\partial S}{\partial n} = q^2 \frac{\partial \theta}{\partial s} - g\frac{\partial q}{\partial n} - \left[\omega_1(T) - \omega_2(T) + R_2 T \ln \frac{4\alpha^2}{1-\alpha^2} p\right] \frac{\partial \alpha}{\partial n} \tag{13b}$$

Multiplying Eq. (2) by $q/\Gamma p$ and combining with Eq. (1) it gives

$$(M_0^2 - 1)\frac{\partial q}{\partial s} + q\left[\frac{1}{\Gamma p}\frac{\partial p}{\partial s} - \frac{1}{\rho}\frac{\partial \rho}{\partial s}\right] - q\frac{\partial \theta}{\partial n} - \frac{\epsilon q \sin\theta}{y} = 0 \tag{14}$$

where $M_0^2 = q^2/(\Gamma p/\rho)$ is the frozen Mach number and

$$\Gamma = c_{p_0}/c_{v_0} = \left(\frac{dQ}{dT}\right)_{p,\alpha} \Big/ \left(\frac{dQ}{dT}\right)_{v,\alpha} = \frac{\alpha c_{p_1} + (1-\alpha)c_{p_2}}{\alpha c_{v_1} + (1-\alpha)c_{v_2}} \tag{15}$$

which is the ratio of specific heats at frozen condition. In order to eliminate p and ρ from Eq. (14), we need the entropy function, which may be written[3] as

$$S = \alpha\left\{\int c_{v_1}\frac{dp_1}{p_1} - \int c_{p_1}\frac{d\rho_1}{\rho_1} + (S_0')_1\right\} + (1-\alpha)\left\{\int c_{v_2}\frac{dp_2}{p_2} - \int c_{p_2}\frac{d\rho_2}{\rho_2} + (S_0')_2\right\} \tag{16a}$$

or

$$S = \alpha\left\{\int c_{p_1}\frac{dT}{T} - R_1 \ln p_1 + S_{0_1}\right\} + (1-\alpha)\left\{\int c_{p_2}\frac{dT}{T} - R_2 \ln p_2 + S_{0_2}\right\} \tag{16b}$$

since

$$\frac{\partial S}{\partial s} = \left(\frac{\partial S}{\partial p}\right)_{\rho,\alpha}\frac{\partial p}{\partial s} + \left(\frac{\partial S}{\partial \rho}\right)_{p,\alpha}\frac{\partial \rho}{\partial s} + \left(\frac{\partial S}{\partial \alpha}\right)_{p,\rho}\frac{\partial \alpha}{\partial s} \tag{17}$$

with the use of Eq. (9), it is easy to obtain from Eq. (16a) that

$$(\partial S/\partial p)_{\rho,\alpha} = c_{v_0}/p, \quad (\partial S/\partial \rho)_{p,\alpha} = -c_{p_0}/\rho \tag{18}$$

using the relation obtained by Wood and Kirkwood[2]

$$\left(\frac{\partial S}{\partial \alpha}\right)_{p,\rho} = \left(\frac{\partial S}{\partial \alpha}\right)_{p,T} - c_{p_0}\left(\frac{\partial v}{\partial \alpha}\right)_{p,T} \Big/ T\left(\frac{\partial v}{\partial T}\right)_{p,\alpha} \tag{19}$$

together with Eqs. (9) and (16b), we have

$$\left(\frac{\partial S}{\partial \alpha}\right)_{p,\rho} = \int (c_{p_1} - c_{p_2})\frac{dT}{T} - R_2 \ln \frac{4\alpha^2 p}{1-\alpha^2} + S_{0_1} - S_{0_2} - \frac{c_{p_0}}{1+\alpha} \tag{20}$$

Substituting Eqs. (18) and (20) into Eq. (17), and using Eq. (13a), we obtain

$$\frac{1}{\Gamma p}\frac{\partial p}{\partial s} - \frac{1}{\rho}\frac{\partial \rho}{\partial s} = \left(\frac{1}{1+\alpha} - \frac{1_D}{c_{p_0}T}\right)\frac{\partial \alpha}{\partial s} \tag{21}$$

where $1_D = h_1 - h_2$ is the heat of dissociation. Eq. (21) is valid for a mixture of calorically imperfect gases which, in other words, is in vibrational equilibrium. Further substitute Eq. (21) into Eq. (14); this yields

$$(M_0^2 - 1)\frac{\partial q}{\partial s} + \left(\frac{1}{1+\alpha} - \frac{1_D}{c_{p_0}T}\right) q\frac{\partial \alpha}{\partial s} - q\frac{\partial \theta}{\partial n} - \frac{\epsilon q \sin\theta}{y} = 0 \tag{22}$$

Let σ be the distance along a curved shock. The derivative along the shock is

$$\partial/\partial\sigma = \cos\lambda(\partial/\partial s) + \sin\lambda(\partial/\partial n) \tag{23}$$

where $\lambda = \beta - \theta$ is the angle between the shock and the streamline (see Fig. 1). Since $\partial/\partial\sigma = (\partial\beta/\partial\sigma)(\partial/\partial\beta) = K_w(\partial/\partial\beta)$ where K_w is the shock curvature, we have

$$\partial/\partial n = [K_w(\partial/\partial\beta) - \cos\lambda(\partial/\partial s)]/\sin\lambda \tag{24}$$

Substituting Eq. (24) into Eqs. (22) and (13b) and using Eq. (13a) and the frozen condition along the shock $\partial\alpha/\partial\beta = 0$, the above equations become, respectively,

$$(M_0^2 - 1)\frac{\partial q}{q\partial s} + \cot\lambda\frac{\partial \theta}{\partial s} = \frac{\epsilon \sin\theta}{y} + f_1 + \frac{K_w}{\sin\lambda}K_2 \tag{25}$$

$$\cot\lambda\frac{\partial q}{\partial s} + q\frac{\partial \theta}{\partial s} = K_w(f_2 + qK_1)/q\sin\lambda \tag{26}$$

where

$$K_1 = \partial g/\partial\beta, \quad K_2 = \partial\theta/\partial\beta$$

$$f_1 = \left(\frac{1_D}{c_{p_0}T} - \frac{1}{1+\alpha}\right)\frac{\partial\alpha}{\partial s} = \frac{1}{\tau q}\left(\frac{1_D}{c_{p_0}T} - \frac{1}{1+\alpha}\right)[\alpha_e(p,T) - \alpha]$$

$$f_2 = T(\partial S/\partial\beta)$$

where τ is the relaxation time and α_e the equilibrium value at p and T. Eqs. (25) and (26) are similar to the corresponding equations of Sedney's, except for the different meaning of f_1. All the terms on the right-hand side of Eqs. (25) and (26) are known from the given boundary conditions behind the shock, which may be evaluated from the frozen conditions. Solving Eqs. (25) and (26) for $\partial q/\partial s$ and $\partial\theta/\partial s$, one obtains

$$\frac{\partial\theta}{\partial s} = F_1 K_w + \frac{\epsilon}{y} F_2 + f_1 \cot\lambda/D \tag{27}$$

$$\frac{1}{q_\infty}\frac{\partial q}{\partial s} = F_3 K_w + \frac{\epsilon}{y} F_4 - q f_1/q_\infty D \tag{28}$$

where

$$F_1 = [(1 - M_0^2)(K_1 + f_2/q) + qK_2 \cot\lambda]/qD \sin\lambda$$

$$F_2 = \sin\theta \cot\lambda/D$$

$$F_3 = [(K_1 + f_2/q)\cot\lambda - qK_2]/q_\infty D \sin\lambda$$

$$F_4 = -q \sin\theta/q_\infty D$$

$$D = 1 - M_0^2 + \cot^2\lambda$$

By the use of Eqs. (2), (1), and (4), the gradients of p, ρ, and T can be obtained. For nonequilibrium vibration, both D and f_1 are positive.[1] The effect of vibrational relaxation[1] is to increase the streamline curvature and decrease the velocity gradient. For nonequilibrium dissociation, the sign of f_1 depends on the value of $(1_D/c_{p_0}T) - 1/(1 + \alpha)$ which, in general, is positive.

References

[1] Sedney, Raymond, *Some Aspects of Nonequilibrium Flows*, IAS Preprint No. 60–4, January 1960; Journal of the Aerospace Sciences, Vol. 28, No. 3, pp. 189–196, March 1961.

[2] Wood, W. W., and Kirkwood, J. G., *Hydrodynamics of a Reacting and Relaxing Fluid*, J. Appl. Phys., Vol. 28, No. 4, pp. 395–398, April 1957.

[3] Liepmann, H. W., and Roshko, A., *Elements of Gasdynamics*, Chapt. 1; John Wiley and Sons, Inc., 1957.

On Moderately Separated Viscous Flows†

Martin H. Bloom*
General Applied Science Laboratories, Inc., Westbury, N.Y. and Polytechnic Institute of Brooklyn

August 19, 1960

Symbols

A	shape parameter, $(\rho_e u_{ex}/\mu_e)(\rho_e/\rho_w)\delta_n^2/C$ (analogous to A of reference 4)
b	index, = 0 for two-dimensional flow; = 1 for axially-symmetric flow
B	see Eq. (4a)
C	$(\rho\mu)_w/(\rho u)_e$
D	shear-stress parameter $\tau_w(R_N^{1/2}/\rho_e u_e^2)_0(\delta R_N^{1/2} u_{ex}/u_e)_0 = 2(u_e/u_{e0})(\delta_0/\delta)(1 - A/A_0)$
f_i	$\equiv H_i$
f_2	see Eq. (2b)
$F(K)$	see Fig. 2
h	enthalpy
H	form factor, δ^*/θ
H_i	constant-density form factor ($\equiv f_1$), $(\delta^*/\theta)_i$
K	$(\theta/\delta_n)^2 A$, a function of A
N	transformed normal coordinate $(1/\delta_n)\int_0^y (\rho/\rho_e)dy$
R_N	Reynolds number, $[(\rho_e u_e/\mu_e)(u_e/u_{ex})]$
δ	boundary-layer thickness
δ_n	boundary-layer thickness, transformed $\int_0^\delta (\rho/\rho_e)\,dy$
δ^*	displacement thickness $\int_0^\delta (1 - \rho u/\rho_e u_e)\,dy = \delta_n \int_0^1 (\rho_e/\rho - u/u_e)dN$

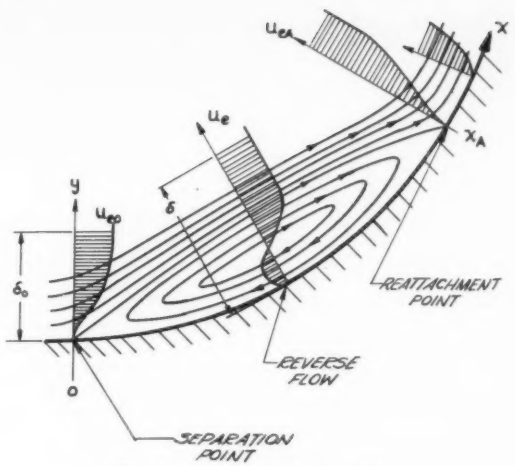

FIG. 1. Separation-flow model.

θ	momentum thickness $\int_0^\delta (\rho u/\rho_e u_e)(1 - u/u_e)dy = \delta_n \int_0^1 (u/u_e)(1 - u/u_e)dN$
τ_w	surface shear stress, $\mu_w u_y$

Subscripts

A	denotes reattachment point
e	local inviscid flow
i	constant density
o	initial (separation) point
w	surface
x, y	partial differentiation

ANALYSES OF SEPARATED FLOWS connected with surface concavities, forward- or rearward-facing steps, spikes, base flows, and shock-boundary-layer interactions, usually involve assumptions concerning aspects of the flow geometry such as the shape and location of a bounding streamline.[1, 2] In shock-boundary-layer interactions,[3] separated or not, the viscous-flow geometry is defined by viscous-inviscid coupling through streamline deflections, and prescription of the pressures corresponding to shock compression at bounding upstream and downstream stations.

This note presents a relatively simple procedure for estimating viscous characteristics of a class of separated flows describable in terms of the boundary-layer approximations, in particular, with negligible pressure variations normal to the surface. The use of boundary-layer coordinates obviates assumptions concerning surface or flow geometry. Such flows, designated "moderately separated," may occur at flare-junctions, in shallow concavities, or in shock-boundary-layer interactions. For present purposes, the usually-increasing streamwise pressures are assumed to be prescribed, more complex coupling not being considered.

In the flow model shown in Fig. 1,* the initial station is taken at a separation point, however, it may be taken anywhere prior to this point. Subsequent velocity profiles indicate reverse flow and imply a separated bubble. Reattachment, if it occurs, is assumed to take place when reverse flow vanishes at some downstream station so that a profile of separation-point type exists there. Downstream of the reattachment point, the usual type of forward-flow profiles may be reinstated. In accordance with the conservation of mass, the streamline which emerges from the separation point terminates at the reattachment point, thus delineating a bubble.

An integral method analysis along well-known lines,[4] but with emphasis on reverse-flow profiles, is utilized. Here the method in reference 4 is extended to take into account surface heat transfer and bodies of revolution. However, in this paper emphasis is placed on the velocity field, which is virtually uncoupled from the thermal field by means of the well-known density transformation. The thermal characteristics can be determined without undue complication.

† This study is part of a project sponsored by the Re-entry Body Section, Special Projects Office, Dept. of Navy, Bureau of Naval Weapons, under Contract No. NOrd-18053.

* The author expresses appreciation for discussions with Dr. Lu Ting in connection with this model.

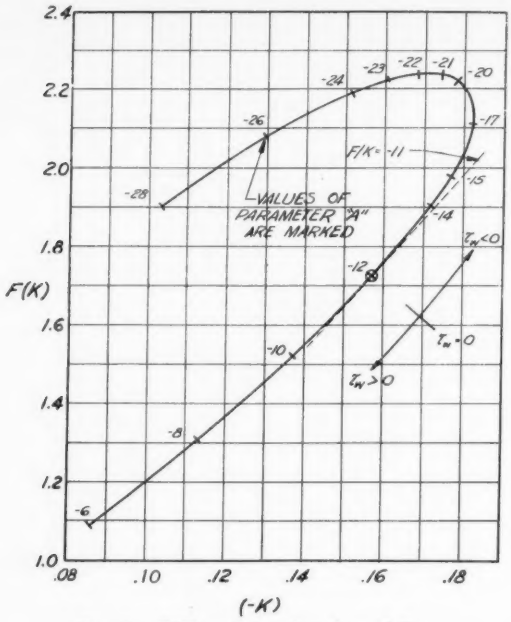

FIG. 2. $F(K)$ and A as functions of K.

The momentum integral equation is

$$\theta_x^2/2 + \theta^2[(H+2)(u_{ex}/u_e) + \rho_{ex}/\rho_e + br_x/r] = \tau_w\theta/\rho_e u_e^2 \quad (1)$$

where: u is streamwise velocity, ρ density, r body radius, $\tau_w = \mu u_y$ is surface shear stress, μ viscosity, x and y streamwise and normal coordinates, and other notation is given in the separate list.

Assumption of a fourth-degree polynomial profile yields[4]

$$u/u_e = (2N - 2N^3 + N^4) + (A/6)(N - 3N^2 + 3N^3 + N^4) \quad (2a)$$

where

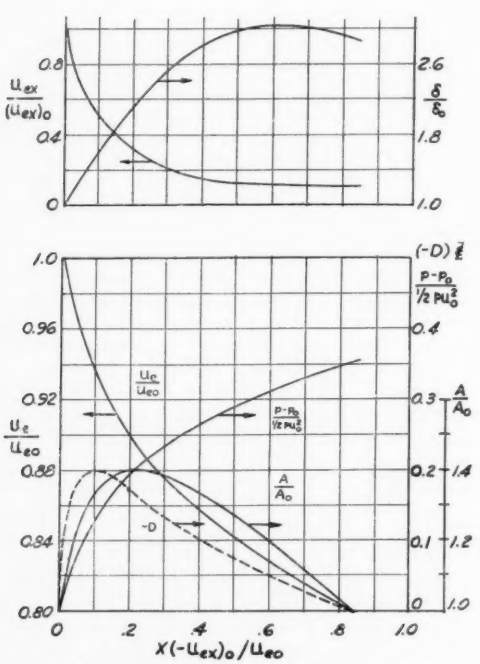

FIG. 3. Typical variations of flow parameters.

$$\tau_w\theta/\rho_e\mu_e^2 = (C\,\mu_e/\rho_e\,\mu_e)f_2(K), \quad f_2 = \theta/\delta_n(2 + A/6),$$
$$\theta/\delta_n = 37/315 - A/945 - A^2/9{,}072 \quad (2b)$$

Eqs. (1) and (2) may be rearranged in the following form:

$$\frac{d}{dx}\ln\left[\frac{K\mu_e\rho_w C r^{2b}}{u_{ex}}\right] + \left[2(H - H_i) - \frac{F(K)}{K}\right]\frac{u_{ex}}{u_e} + 2\left(1 - \frac{\rho_e}{\rho_w}\right)\frac{f_2(K)}{K}\frac{u_{ex}}{u_e} = 0 \quad (3)$$

where $F(K)$ is plotted in Fig. 2, for the extended range $A \geq -28$. The functions $F(K)$, H_i, and $f_2(K)$ are tabulated in reference 4, Table 2.12 for $A \geq -15$.

The momentum Eq. (3) is coupled to the energy equation (not given here) through H. However, it may be integrated together with the energy equation by straightforward numerical means.

To permit the simplified integration of Eq. (3) for a representative class of problems, the following approximation, which uncouples (3) from the energy equation may be considered reasonable:

$$2(H - H_i) - F/K \equiv B = \text{a constant average value} \quad (4)$$

Furthermore, for the case where $\rho_w = \rho_e$, Eq. (3) becomes

$$d/dx\,\ln\,[K\,\mu_e\rho_w C\,r^{2b}\,u_e^B/u_{ex}] = 0 \quad (5)$$

An estimate for B may be obtained with the following approximations:

$$H - H_i \cong (h_w - h_e/h_e)H_i + u_e^2/2h_e \cong \text{a constant average value} \quad (6a)$$

$$F/K \cong \text{constant } (\cong -11 \text{ for } -18 \leq A \leq 12) \quad (6b)$$

When Eq. (5) is integrated and the integration constants are evaluated at $x = 0$, the separation station, the following expressions are obtained:

$$(K/K_0)[(\rho\mu)_w/(\rho\mu)_{w0}](\rho_{w0}/\rho_e)[(u_{ex})_0/u_{ex}](u_e/u_{e0})^B(r/r_0)^{2b} = 1 \quad (7a)$$

$$(\theta/\theta_0)(\rho_e/\rho_{e0})(u_e/u_{e0})^{B/2}(r/r_0)^b = 1 \quad (7b)$$

From Eq. (7a), the variation in K/K_0 and the physical parameters dependent upon K may be calculated along the flow for the prescribed inviscid flow. If reattachment occurs, the value of K/K_0, which first exceeds unity, would return to unity. An analogous deviation and return to unity occurs for A/A_0 (see Eqs. 2).

For two-dimensional constant-density flow, a typical inviscid velocity distribution which would lead to the reattachment of a separated flow is shown in Fig. 3. Also shown are the corresponding variations of velocity gradient, pressure, boundary-layer thickness, shape parameter A, and shear-stress parameter D.

REFERENCES

[1] Chapman, D. R., *A Theoretical Analysis of Heat Transfer in Regions of Separated Flows*, NACA TN 3792, October, 1956.

[2] Carlson, W. O., *Heat Transfer in Laminar Separated and Wake Flow Regions*, Heat Transfer and Fluid Mechanics Institute, Stanford University Press, June, 1959.

[3] Cheng, S. I., and Bray, K. N. C., *On the Mixing Theory of Crocco and Lees and Its Application to the Interaction of Shock Wave and Laminar Boundary Layer* (Part I), Princeton University Press, AFOSR TN 57-283, AD 132354, May, 1957.

[4] Schlichting, H., *Boundary Layer Theory*, pp. 206, 289; McGraw-Hill Book Co. Inc., New York, 1955.

Vortex Shedding From Thin Flat Plates Parallel to the Free Stream

Andrew B. Bauer
Aerodynamics Engineer, Douglas Aircraft Co., Santa Monica, Calif.

August 22, 1960

FLAT-PLATE vortex-shedding frequency measurements have been made recently,[1] supplementing the earlier work by

Roshko[2] on bluff bodies. The tests were run in the GALCIT 20-in. low-turbulence wind tunnel. Hot-wire equipment was used to measure shedding frequencies and flow speed.[1]

It is well known that the vortex-shedding characteristics of bluff bodies are related to the distance between the thin vortex sheets which separate from the body.[2] In the case of a long body, such as a flat plate, the thickness of the boundary layer at the trailing edge, and hence the separated layer, may be large compared to the base thickness. One would then expect the ratio of boundary-layer thickness to base height to have an important effect on the vortex shedding, as was found to be the case.

Two different flat places of 12-in. chord and an NACA airfoil of 9-in. chord were tested. Both plates had round leading edges and blunt trailing edges. The "thick" plate was 0.250 in. thick; the "thin" plate was 0.040 in. thick. Fig. 1 shows the experimental Strouhal number S for the three models plotted as a function of the model-chord Reynolds number.

Fig. 2 shows the experimental Strouhal number plotted as a function of δ^*/d, the ratio of the ideal Blasius boundary-layer displacement thickness to the plate thickness. This clearly shows the dependence of S on δ^*/d.

The relation

$$S = \frac{(0.225 + 0.056\sqrt{1 - \epsilon/\sqrt{2}})\epsilon}{1.54\,(\delta^*/d) - C_p}$$

where ϵ is the fraction of boundary-layer vorticity that goes into the Kármán Vortex Street, may be derived by equating the well-known Kármán Vortex Street drag formula to the sum of the (assumed) Blasius friction drag and the base-pressure drag. This is also shown in Fig. 2, using an experimentally determined pressure coefficient C_p of approximately -0.3. It is seen that this gives an experimental ϵ of about 0.5, which is near the value of 0.43 found for cylinders by Roshko[2] using a different method.

A "wake Strouhal number," similar to that of reference 2, is shown in Fig. 3. This is defined as

$$S^* = n(d + 2\delta^*)/U_s$$

where $U_s = \sqrt{1 - C_p}\,U$. Here $(d + 2\delta^*)$ is used as an effective and wake width, and U_s represents the "free-streamline" velocity[2] assumed to exist in the potential flow at the edge of the wake. Fig. 3 shows the leveling effect of using S^*, but the values of S^* are considerably greater than those for the several models of reference 2, where $S^* \doteq 0.16$ was obtained.

Several interesting features of the flow may be seen in Fig. 1. At large Reynolds numbers, the thick plate showed a marked decrease in Strouhal number. At the same time the hot-wire signal indicated turbulent bursts in the flow immediately aft of the plate, becoming more pronounced as Reynolds number increased. Thus, it appears that the transition to a turbulent boundary

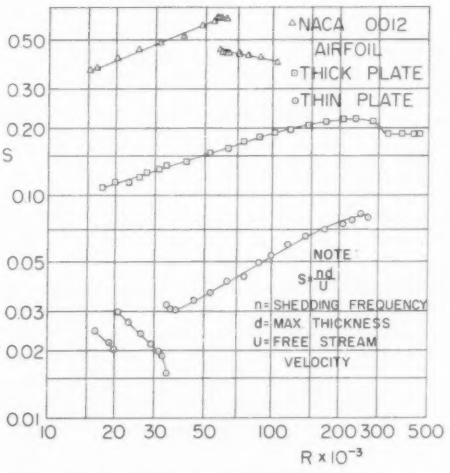

FIG. 1. Strouhal number vs. Reynolds number.

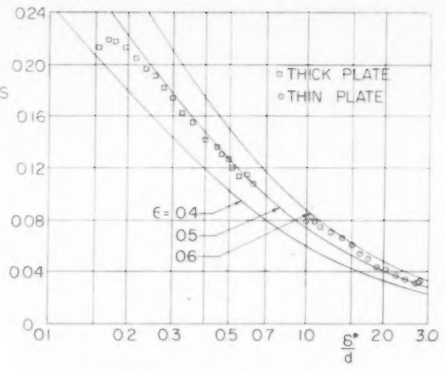

Fig. 2. Strouhal number vs. δ^*/d.

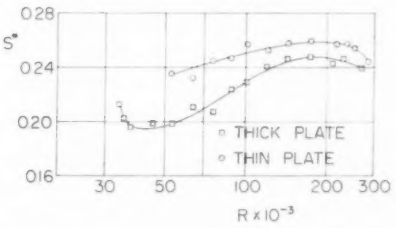

FIG. 3. Wake Strouhal number vs. Reynolds number.

layer affects the Strouhal number. Since Fig. 2 was computed on the basis of a Blasius profile, the data taken at Reynolds numbers greater than 282,000 are omitted from Fig. 2.

The odd behavior of the thin plate at low Reynolds number is not understood. Here the shedding frequency in cps was constant except for the discrete jumps shown.

As also shown in Fig. 1, an abrupt change in Strouhal number of the airfoil occurred at a Reynolds number of about 60,000. In fact, in this region it was observed that the Strouhal number would change between these two values at random, with no apparent disturbance being introduced into the tunnel operation. It is also interesting to note that this Reynolds number corresponds, as nearly as can be determined, to that for the "knee" in the curve of drag coefficient versus Reynolds number of the 12 per cent airfoils of reference 3.

It is interesting to note that a recent paper by Tritton[4] shows jumps in the shedding frequency for the case of a circular cylinder at low Reynolds number.

REFERENCES

[1] Bauer, A. B., *Vortex Formation and Shedding From a Two-Dimensional, Thin, Flat Plate Parallel to the Free Stream*, California Institute of Technology Thesis, June, 1959.

[2] Roshko, Anatol, *On the Drag and Shedding Frequency of Two-Dimensional Bluff Bodies*, NACA TN 3169, July, 1954.

[3] Hoerner, S. F., *Fluid-Dynamic Drag*, Fig. 6-2 (published by the author), Midland Park, N.J.

[4] Tritton, D. J., *Experiments on the Flow past a Circular Cylinder at Low Reynolds Numbers*, *J. Fluid Mech.*, Vol. 6, Part 4, pp. 547–567, Nov. 1959.

Thermal Buckling of Rectangular Plates

Koryo Miura

Aeronautical Research Institute, University of Tokyo, Tokyo, Japan

August 22, 1960

THERMAL BUCKLING of a plate simply supported by the web is analyzed when the system is subjected to an arbitrary symmetrical temperature distribution over the plate. The

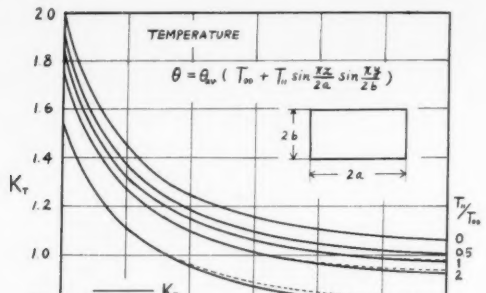

FIG. 1. Thermal-buckling parameter for rectangular plate (rigid boundary). K_T' is the approximate buckling parameter given by Eqs. (3)–(5) of the text with $s = t = i = j = 1$.

buckling criterion is established and, furthermore, a simple formula for buckling criterion with reasonable accuracy for engineering purposes is obtained. Special attention is paid to exactly satisfying the boundary conditions, and the solution thus obtained is compared with that of Klosner and Forray.[1] This paper is a brief report on reference 2.

The ideas and the principles of the author's method are: first, by the use of Duhamel's analogy, the thermal-stress problem can be converted into the isothermal problem subjected to an appropriate imaginary hydrostatic pressure and imaginary body forces; secondly, two-dimensional plane-stress problems involving body forces can be solved rigorously by the principle of virtual displacements provided the displacements are given at the edges; and finally, these displacements expressing the boundary conditions can be so defined that the conservation of the straightness of the edges after heating may be satisfied. The stresses obtained in this manner can be used in calculating the buckling criterion of the plate.

The displacements in the plane of the plate may be expressed as

$$\left.\begin{aligned} u(x, y) &= u_1(x) + \sum_{m\ \text{even}}^{\infty}\sum_{n\ \text{odd}}^{\infty} A_{mn}\sin(m\pi x/2a)\sin(n\pi y/2b) \\ v(x, y) &= v_1(y) + \sum_{m\ \text{odd}}^{\infty}\sum_{n\ \text{even}}^{\infty} B_{mn}\sin(m\pi x/2a)\sin(n\pi y/2b) \end{aligned}\right\} \quad (1)$$

where $u_1(x)$ and $v_1(y)$ are the unknown functions of x only or y only, respectively, $2a$ and $2b$ are the dimensions of the plate. From this it follows that the requirement about the conservation of straightness of the web after heating can be satisfied in all cases, since the second terms on the right hand of Eqs. (1) vanish at the boundary. Assuming the forms of $u_1(x)$ and $v_1(y)$ include two unknown coefficients which are to be determined by equating resultant displacements of the plate and the web, and taking virtual displacements in the form

$$\left.\begin{aligned} \delta u &= \delta A_{mn}\sin(m\pi x/2a)\sin(n\pi y/2b) \\ \delta v &= \delta B_{mn}\sin(m\pi x/2a)\sin(n\pi y/2b) \end{aligned}\right\} \quad (2)$$

we obtain the necessary equations for calculating the thermal stresses by the use of the principle of virtual displacements.

The Rayleigh-Ritz procedure is used in calculating the thermal-buckling criterion and results in the set of simultaneous equations that constitute a characteristic-value problem. A most representative example calculated is shown in Fig. 1. In the example, the boundary conditions about stress and deformation are satisfied exactly, and thus the solution is the exact one.

After due consideration of the results, it is possible to construct a compact formula for buckling criterion with reasonable accuracy. In brief, generally this result can be written in the form

$$K_T = \frac{(b/a)[s^2i^2(b/a) + t^2j^2(a/b)]^2}{s^2i^2(b/a)\mathbf{I}_{xx}(s, s, t, t) + 2stij\mathbf{I}_{xy}(s, s, t, t) + t^2j^2(a/b)\mathbf{I}_{yy}(s, s, t, t)} \quad (3)$$

where s and t are arbitrary odd integers, i and j are 1 or 2, and I are values easily calculable from the temperature distribution in the plate.

Example (1). Uniform temperature distribution:

$$\mathbf{I}_{xx} = \mathbf{I}_{yy} = 1, \qquad \mathbf{I}_{xy} = 0 \quad (4)$$

Example (2). $\theta = \theta_{av}(T_{00} + T_{11}\sin(\pi x/2a)\sin(\pi y/2b))$:

$$\left.\begin{aligned} \mathbf{I}_{xx} &= \mathbf{I}_{yy} = T_{00} \\ \mathbf{I}_{xy} &= \frac{8}{9\pi^2}\left[2\left(\frac{b}{a} + \frac{a}{b}\right) + \frac{4(b/a)^2 - 3\nu + 1}{4(b/a) + [(1-\nu)/2](a/b)} + \frac{4(a/b)^2 - 3\nu + 1}{4(a/b) + [(1-\nu)/2](b/a)}\right]T_{11} \end{aligned}\right\} \quad (5)$$

In the second example, the formula and the calculated buckling parameter is shown in Fig. 1 as K_T' compared with more accurate values. The effect of finite rigidity and the thermal expansion of the web can easily be included in this method.

Comparison With Klosner and Forray's Solution

By inspecting the boundary conditions imposed on the problem, the validity of the solutions by Klosner–Forray and the author can be shown. The Klosner–Forray solution will be exact when the tensile rigidity of the web is zero, while the author's solution will be exact when it is infinitely large. In the region located between these two limiting cases, both solutions give approximate values. From the fact that the thermal buckling of rectangular plate simply supported by the web is mainly due to the restriction of expanding plate by the web of lower temperature than the plate, and that even if the web is weak and the buckling is due mainly to the nonuniformity of the temperature distribution in the plate, such distribution may not happen in such a weak web or, in other words, a weak-heat-sink structure; the author's solution may be suitable in the case of buckling of supersonic wing panels. In the example calculated, the buckling parameter of the author's solution is somewhat lower than the Klosner–Forray value.

References

[1] Klosner, J. M., and Forray, M. J., *Buckling of Simply Supported Plates Under Arbitrary Symmetrical Temperature Distributions*, Journal of the Aeronautical Sciences, Vol. 25, No. 3, pp. 181–184, March, 1958.

[2] Miura, Koryo, *Thermal Buckling of Rectangular Plates*, Aeronautical Research Institute, University of Tokyo, Report 353, May, 1960.

High-Heat-Flux Effects in Wire Heat Gages*

John C. Cutting and James A. Fay
Department of Mechanical Engineering, Massachusetts Institute of Technology, Cambridge, Mass.
August 19, 1960

IN A RECENT REPORT,[1] the laminar heat-transfer rate in dissociated combustion gases was theoretically predicted and experimentally measured using thin-wire heat gages. The energy transport to the cold wall was considered to consist of the transport of kinetic, rotational, and vibrational energy through collision and the diffusion of dissociated particles possessing potential energy of recombination. Since accurate values of the

* This research was supported by the Air Force Office of Scientific Research under Contract No. AF 49(638)-643.

molecular-collision cross sections, and hence the transport coefficients, in a dissociated combustion gas are not known, the comparison of experimental and theoretical heat transfer is primarily a comparison of experimental and estimated transport coefficients. On this basis, the results reported in reference 1 would require cross sections four times larger than those extrapolated from low-temperature data. Subsequent measurements have been made[2] which reveal the source of this discrepancy.

The heat-transfer gage circuit consisted of a 1/2-in. length of a thin (2 to 4 mil diameter) platinum wire connected in series with a large ballast resistor to insure constant current, and a battery. The wire gage was placed transversely in a $1^1/_2$-in. ID shock tube and subjected to the stoichiometric hydrogen-oxygen detonation. The voltage increase across the wire, due to its increasing resistance with temperature, was then measured on an oscilloscope. These voltage-time responses were then utilized to calculate the heat-transfer rate to the wire by using Ohm's law and the temperature coefficient of resistivity.

The original results[1] were all obtained for the same value of the circuit current. By varying this current, the calculated heat-transfer rate was found to vary as shown in Fig. 1 (where the heat-transfer rate is plotted versus circuit current). It can be readily seen that, for very low currents or thin wires, the calculated rate approaches a limit. This limit will subsequently be shown to be almost that theoretically predicted in reference 1.

For our experiments, the electrical heating, even at the highest experimental currents, is a negligible fraction of the aerodynamic heating. It is thus expected that the heating of the wire should be independent of current. If Ohm's law then applies, the resistance of the wire should also be independent of current, and the heat-transfer rate inferred from the resistance change should be the same for all current values. Since this is not the case, we may infer that Ohm's law is not strictly applicable under these test conditions.

The most distinguishing factor present in these experiments is a very large temperature gradient established in the wire probe due to heat fluxes of the order of 100 kw. per cm². For platinum, this results in a temperature gradient in the metal of 2×10^5 °K./cm. It is, therefore, suspected that Ohm's law breaks down in regions of extremely high-temperature gradients perpendicular to the current flow.

A possible explanation of such a phenomenon may be found in the study of the degenerate electron gas in the metal. Mayer and Mayer[3] show that the electrical conductivity may be calculated for a degenerate electron gas under the simple assumption that the electrons come to equilibrium after every collision. From the Boltzmann equation, it has been found that equilibrium may exist after each collision if

$$(\partial \ln f^0/\partial x) \ll 1/\bar{l}$$

$$f^0 = (m^3\beta/h^3)[1/(1 + Ae^{mc^2/2kT})]$$

where f^0 is the velocity distribution function, β is the statistical weight of electrons, m is the mass, h is Planck's constant, C is the velocity of electrons, K is Boltzmann's constant, and $\bar{l}$ is the electron mean free path. For this highly degenerate gas,[4] A is small compared with unity and may be expressed as

$$A = e^{-(mW^2/2kT)}$$

where W is the velocity of the electrons at the Fermi brim. Upon substitution of numerical values for $T = 300$°K.

$$\partial \ln f^0/\partial x = 4.4 \times 10^4 \text{ cm.}^{-1}$$

Since the mean free path for platinum is about 5×10^{-6} cm., it is obvious that equilibrium is not established in the radial direction, even after many collisions. It is not surprising that Ohm's law may break down in the presence of such large radial temperature gradients.

Observing Fig. 1 again, and noting that gold has a thermal diffusivity four times larger than that of platinum, it can be readily seen that for decreasing current, decreasing wire diameter, and increasing thermal diffusivity, the experimental heat-transfer rate approaches a value close to the theoretical prediction of reference 1 which assumed an extrapolated collision cross section of 17×10^{-16} cm². This may be explained by noting that increasing thermal diffusivity and smaller diameter result in a reduced temperature gradient. These results then demonstrate the importance of a large radial temperature gradient upon the flow of current in a wire.

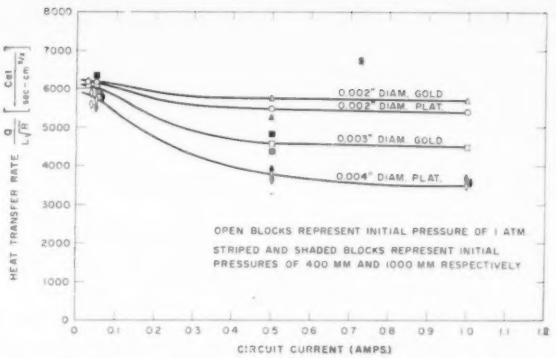

FIG. 1. Measured heat-transfer rates in stoichiometric hydrogen-oxygen mixtures. Different initial pressures were used as shown, and the 400 mm. and 1,000 mm. runs have been scaled to an initial pressure of 1 atm. The value of the heat-transfer rate calculated according to the theory reported in reference 1 for a collision cross section of 17×10^{-16} cm.² is 5,900 cal./sec. cm.$^{3/2}$.

REFERENCES

[1] Cutting, J. C., Fay, J. A., Hogan, W. T., and Moffatt, W. C., *Heat Transfer in Dissociated Combustion Gases*, Office of Scientific Research, Air Research and Development Command, U.S. Air Force (AFOSR-TR-59-78), 1959.

[2] Cutting, J. C., *Heat Transfer in Dissociated Combustion Gases*, S.M. Thesis, Department of Mechanical Engineering, Massachusetts Institute of Technology, Cambridge, Mass., 1960.

[3] Mayer, J., and Mayer, M., *Statistical Mechanics*, John Wiley & Sons, New York, 1940.

[4] Chapman, S., and Cowling, T. G., *The Mathematical Theory of Non-Uniform Gases*, Cambridge University Press, London, 1953.

Concerning the Integral Equation of Unsteady Motion of a Delta Wing in Supersonic Flight by Means of the Acceleration-Potential Method

M. M. Stanišić
Associate Professor, Division of Engineering Sciences, Purdue University, West Lafayette, Ind.

August 11, 1960

MATHEMATICAL FORMULATION

IN A PREVIOUS PAPER[1] the velocity and acceleration potentials were obtained for the motion of a delta wing with subsonic leading edges in supersonic flow. Furthermore, a relation between velocity potential and acceleration potential has already been established.[2] It has been shown that the velocity potential method leads to an integral equation [reference 2, Eq. (26)] of complicated form, the solution to which is hopeless. The object of this paper is to extend the results obtained in reference 1 using the acceleration-potential method.

If $\chi(x,y,z,t)$ is an acceleration potential given by reference 1, Eq. (17),

$$\chi(x,y,z,t) = -\frac{e^{-i\omega t}}{\pi}\frac{\partial}{\partial x}\iint_{\pi^*} A(x_1,y_1,0)K(x,y,z;\,x_1,y_1,0)\,dx_1dy_1 \quad (1)$$

then

$$dw/dt = \lim_{z \to 0} \partial\chi/\partial z \quad (2)$$

where [reference 2, Eq. (24)]

$$w = e^{-i\omega t}[Ug_x(x,y) - i\omega g(x,y)] \tag{3}$$

However, applying linearized theory,

$$dw/dt = (\partial w/\partial t) + U(\partial w/\partial x) \tag{4}$$

Thus, Eqs. (1), (2), (3), and (4) lead to

$$\int_{|y_1/m|}^{x} \{U^2 g_{xx}(x,y) - 2i\omega U g_x(x,y) - \omega^2 g(x,y)\}dx = -\frac{1}{\pi}\lim_{z=0}\frac{\partial}{\partial z}\iint_{\pi^*} A(x_1,y_1,0)K(x,y,z;\,x_1,y_1,0)dx_1dy_1 \tag{5}$$

where the region π^* is given in Fig. 1, references 1 and 2. Now Eq. (5) has to be solved for $A(x_1,y_1,0)$.

However, before going into the solution of Eq. (5), we must carefully examine it, since $K(x,y,z;\,x_1,y_1,0)$ represents a singular kernel. In short, we cannot undertake any differentiation procedure of a function under an integral sign which possesses singularities of any order, until the singularity is removed from the integrand.

Therefore, letting

$$\sqrt{(y-y_1)^2+z^2}\sinh\theta = \xi \tag{6}$$

then

$$K(x,y,z;\,x_1,y_1,0) = \frac{(x-x_1)z}{\beta[(y-y_1)^2+z^2]}\left\{\frac{\beta\cos\{\Lambda\sqrt{(x-x_1)^2-\beta^2[(y-y_1)^2+z^2]}\}}{\sqrt{(x-x_1)^2-\beta^2[(y-y_1)^2+z^2]}} + \Lambda\sin\{\Lambda\sqrt{(x-x_1)^2-\beta^2[(y-y_1)^2+z^2]}\} - \frac{z\Lambda^2\beta}{[(y-y_1)^2+z^2]}\int_0^{(1/\beta)\sqrt{(x-x_1)^2-\beta^2[(y-y_1)^2+z^2]}} \frac{}{\sqrt{\xi^2+(y-y_1)^2+z^2}\cos(\Lambda\beta\xi)d\xi}\right\} \tag{7}$$

Denote

$$y - y_1 = z\tan\phi \tag{8}$$

Then, Eqs. (5), (7) and (8) lead to

$$G(x_1y_1\Lambda) = \lim_{z\to 0}\sum_{i=1}^{3}\frac{\partial \Pi_i}{\partial z} \tag{9}$$

where the expressions for Π_i are given by the following:

$$\Pi_1 = \frac{1}{\pi}\iint_{\pi^*} A(x,y-z\tan\phi,0)\times \frac{(x-x_1)\cos\{\Lambda\sqrt{(x-x_1)^2-\beta^2z^2\sec^2\phi}\}}{\sqrt{(x-x_1)^2-\beta^2z^2\sec^2\phi}}\,dx_1\,d\phi \tag{10}$$

$$\Pi_2 = \frac{\Lambda}{\pi\beta}\iint_{\pi^*} A(x_1,y-z\tan\phi,0)\times (x-x_1)\sin(\Lambda\sqrt{(x-x_1)^2-\beta^2z^2\sec^2\phi})\,dx_1\,d\phi \tag{11}$$

$$\Pi_3 = -\frac{\Lambda^2\beta}{\pi}\iint_{\pi^*}\left\{A(x_1,y-z\tan\phi,0)\times \int_0^{(1/\beta)\sqrt{(x-x_1)^2-\beta^2z^2\sec^2\phi}} \frac{}{\sqrt{\xi^2+z^2\sec^2\phi}\cos(\Lambda\beta\xi)\,d\xi}\right\}dx_1\,d\phi \tag{12}$$

and

$$G(x,y,\Lambda) = \int_{|y_1/m|}^{x}\{U^2g_{xx}(x,y) - 2i\omega Ug_x(x,y) - \omega^2 g(x,y)\}dx \tag{13}$$

The problem is to prove that the limits of $\partial\Pi_i/\partial z$ as $z\to 0$ exist, and then to find these limits respectively. Here we will merely demonstrate $\lim_{z\to 0}\partial\Pi_1/\partial z$, since the other two terms in Eq. (9) can be developed in a similar manner.

Integrating by parts over the region π^* (see Fig. 1, reference 2), Eq. (11) leads to

$$\Pi_1 = -\frac{1}{\pi\Lambda}\int_0^{y_1^*} A\left(\frac{y_1}{m},y_1,0\right)\sin\left\{\Lambda\sqrt{\left(x-\frac{y_1}{m}\right)^2-\beta^2[(y-y_1)^2+z^2]}\right\}\frac{zdy_1}{(y-y_1)^2+z^2} - \frac{1}{\pi\Lambda}\int_{y_2^*}^{0} A\left(-\frac{y_1}{m},y_1,0\right)\sin\left\{\Lambda\sqrt{\left(x+\frac{y_1}{m}\right)^2-\beta^2[(y-y_1)^2+z^2]}\right\}\frac{zdy_1}{(y-y_1)^2+z^2} - \frac{1}{\pi\Lambda}\iint_{\pi^*}\frac{\partial A(x_1,y_1,0)}{\partial x_1}\sin\left\{\Lambda\sqrt{(x-x_1)^2-\beta^2[(y-y_1)^2+z^2]}\right\}\frac{zdx_1dy_1}{(y-y_1)^2+z^2} \tag{14}$$

Note that y_1^* and y_2^* are obtained by intersection of the cone, $(x-x_1)^2-\beta^2[(y-y_1)^2+z^2]=0$, with the boundary of the wing, $y_1 = \pm mx_1$.

Clearly,

$$y_1^* = \frac{m(\beta y + x)}{1+m\beta}; \qquad y_2^* = \frac{m(\beta y - x)}{1+m\beta} \tag{15}$$

Now suppose

$$\left.\begin{aligned} F(x,y,z;\,y_1,\Lambda) &= A(|y_1/m|,y_1,0)\sin\left\{\Lambda\sqrt{(x-|y_1/m|)^2-\beta^2[(y-y_1)^2+z^2]}\right\} \\ \text{and} \\ L(x,y,z;\,y_1,\Lambda) &= [\partial A(x_1,y_1)/\partial x]\sin\left\{\Lambda\sqrt{(x-x_1)^2-\beta^2[(y-y_1)^2+z^2]}\right\} \end{aligned}\right\} \tag{16}$$

Then, since F and L are regular functions everywhere, they can be expanded in series with respect to y_1.

Thus expanding Eqs. (16), differentiating the terms under the integral with respect to z, and letting $z\to 0$, one obtains after rearranging terms an expression for the complete sum for $z\to 0$ in the Hadamard sense; thus Eq. (5) yields

$$G(x,y) = -\frac{1}{\pi\beta}\,{}^{*}\iint_{\pi^*} A(x_1,y_1,0)K^*(x,y,0;\,x_1,y_1,0)dx_1\,dy_1 \tag{17}$$

where the asterisk (*) before the integral signifies that integration is to be considered in the Hadamard sense, with

$$K^*(x,y,0;\,x_1,y_1,\Lambda) = \frac{(x-x_1)}{(y-y_1)^2}\left[\frac{\beta\cos\{\Lambda\sqrt{(x-x_1)^2-\beta^2(y-y_1)^2}\}}{\sqrt{(x-x_1)^2-\beta^2(y-y_1)^2}} + \Lambda\sin\{\Lambda\sqrt{(x-x_1)^2-\beta^2(y-y_1)^2}\}\right] - \frac{\Lambda^2\beta^2}{(y-y_1)^2}\int_0^{(1/\beta)\sqrt{(x-x_1)^2-\beta^2(y-y_1)^2}} \frac{}{\sqrt{\xi^2+(y-y_1)^2}}\cos(\Lambda\beta\xi)\,d\xi \tag{18}$$

Let

$$\left.\begin{aligned} A(x_1,y_1,0) &= \sum_{n=0}^{N} A_n(x_1,y_1)\Lambda^n \\ K^*(x,y,0;\,x_1,y_1,\Lambda) &= \sum_{n=0}^{N} K_n(x,y;x_1,y_1)\Lambda^n \end{aligned}\right\} \quad (19)$$

and

$$G(x,y,\Lambda) = \sum_{n=0}^{2} G_n(x,y)\Lambda^n \quad (20)$$

Evidently,

$$G_0(x,y) = -\frac{1}{\pi}\,{}^{*}\!\iint_{\pi^*} \frac{A_0(x_1,y_1)(x-x_1)\,dx_1dy_1}{(y-y_1)^2\sqrt{(x-x_1)^2-\beta^2(y-y_1)^2}} \quad (21)$$

$$G_1(x,y) = -\frac{1}{\pi}\,{}^{*}\!\iint_{\pi^*} \frac{A_1(x_1,y_1)(x-x_1)dx_1dy_1}{(y-y_1)^2\sqrt{(x-x_1)^2-\beta^2(y-y_1)^2}} \quad (22)$$

The integral equation (21) represents the solution for steady flow. All other equations, Eq. (22), etc., are of the same type as Eq. (21). Note that $A_1(x_1,y_1)$ represents the coefficients of the source function for the expansion in powers of Λ. Moreover, if we can solve Eq. (22), we can solve the complete system for all $A_n(x_1,y_1)$. However, for the solution of Eq. (22) we cannot use the method used for Eq. (24) in reference 3. A new method[2] in the theory of integral equations has been developed for the solution of the singular integral equation (22).

References

[1] Stanišić, M. M., *On the Unsteady Motion of a Delta Wing in Supersonic Flight*, Journal of Aero/Space Sciences, Readers' Forum, Vol. 27, No. 5, pp. 399–400, May, 1960.

[2] Stanišić, M. M., *A Remark Concerning the Vibration of a Delta Wing in Supersonic Flight*, Journal of Aerospace Sciences, Readers' Forum, Vol. 26, No. 10, pp. 679–681, October, 1959.

[3] Stanišić, M. M., *On the Solution of an Integral Equation Appearing in the Delta-Wing Theory;* to appear in the near future in Zeitschrift für angewandte Mathematik und Mechanik, Band 40, Heft 9, pp. 397–415, September, 1960.

Heat Transfer to Sharp and Blunt Yawed Plates in Hypersonic Airflow†

J. Gordon Hall* and T. C. Golian**
Cornell Aeronautical Laboratory, Inc., Buffalo, N.Y.

August 19, 1960

A STUDY OF COMBINED EFFECTS of boundary-layer displacement, leading-edge bluntness, and angle of attack in hypersonic airflow over flat plates was reported at the IAS 28th Annual Meeting, January, 1960.[1] This study included development of a rational theory accounting for these combined effects, as well as experimental investigations of cold-wall heat transfer and shock shape over a wide range of density and leading-edge thickness. The experiments were conducted in the C.A.L. 11 × 15-in. shock tunnel at air Mach numbers around 12, stagnation temperatures from about 2,000°K. to 4,000°K., with plate surface temperatures close to 300°K. For leading-edge Reynolds numbers from about 2 (dominant viscous interaction) to 15,000 (dominant bluntness), the experimental data are quite well correlated by viscous hypersonic similitude[4] extended to include bluntness. Agreement with the leading (zero-order) approximation of the theory for $\gamma \to 1$ is reasonably good.

† Supported by U.S. Air Force Office of Scientific Research, Mechanics Division, Contract No. AF 18(603)-10.

* Principal Aerodynamicist.

** Associate Mechanical Engineer.

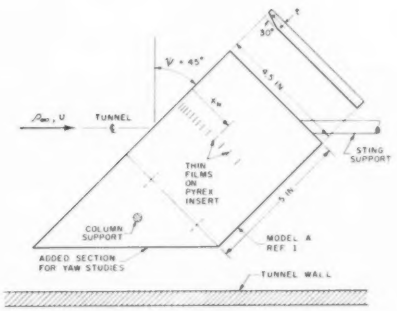

FIG. 1. Model configuration for yaw studies.

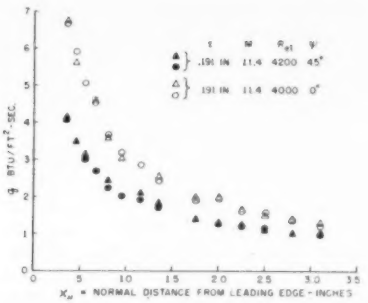

FIG. 2. Yawed and nonyawed heat transfer on blunt plate.

The purpose of the present note is to report recent experimental results for heat-transfer distributions over sharp and blunt plates at yaw with zero angle of attack. Heat-transfer tests were conducted in the C.A.L. 11 × 15-in. shock tunnel with a model yawed at 45° (Fig. 1) obtained by modification of flat plate "A" described in reference 1. Tests were also made to obtain comparable data for zero angle of yaw. General test conditions and thin-film measurement techniques were as in reference 1. Nominal values of airflow Mach number, M, and stagnation temperature, T_0, were 11.4 and 1,950°K., respectively. The ratio of wall temperature, T_w, to stagnation temperature was about 0.15 ($T_w \simeq 300$°K.). A nominal stagnation pressure of 1,150 psi, and leading-edge thicknesses, t, of 0.0005 and 0.191 in. provided leading-edge Reynolds numbers, Re_t, of approximately 10 and 4,000, respectively.

Typical results for measured heat-transfer rate, q, versus distance, x_N, measured normal to the plate leading edge are shown in Fig. 2 for zero yaw and 45° yaw with $t = 0.191$ in., and $Re_t = 4{,}000$. The distribution and magnitude of q characterize a laminar boundary layer.

If cross-flow effects are neglected, the two-dimensional zero-order theory of Cheng,[1] which requires a strong shock wave, small-flow deflection, and $\gamma \to 1$, may be applied. For sufficiently large Re_t resulting in pure bluntness effect, this gives

$$M^3C_H \doteq 0.119\sqrt{\gamma}\,K_\epsilon^{1/3}\,\bar{\chi} \quad (1)$$

as the heat transfer at yaw angle ψ, where

$C_H = q/\rho_\infty U_\infty(H_\infty - H_w)$
$K_\epsilon = (M^3\epsilon k_N t\cos^4\psi)/x_N$
$\bar{\chi} = M^3\sqrt{C\cos\psi}/\sqrt{Re_{xN}}$
$Re_{xN} = \rho_\infty U_\infty x_N/\mu_\infty$
$H_{\infty,w}$ = free-stream or wall total enthalpy
k_N = leading-edge drag coefficient for $\psi = 0$
C = constant in linear viscosity-temperature relation
$\epsilon = (\gamma-1)/(\gamma+1)$

The equivalent result for very small Re_t giving pure boundary-layer displacement effect[1] is

$$M^3C_H = 0.219\sqrt{\epsilon\gamma[0.664 + 1.73(H_w/H_\infty)]}\,\bar{\chi}^{3/2} \quad (2)$$

As regards the present experiments, Eq. (1) should be reasonably applicable for the case $t = 0.191$ in. and Eq. (2) for $t =$

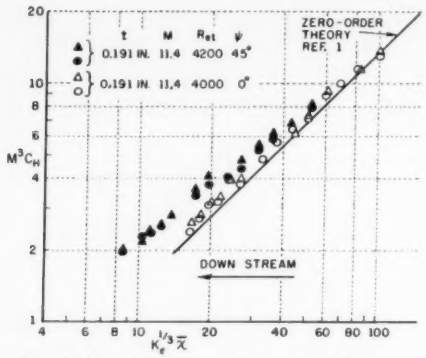

FIG. 3. Correlation of yawed and nonyawed heat transfer for large Re_t.

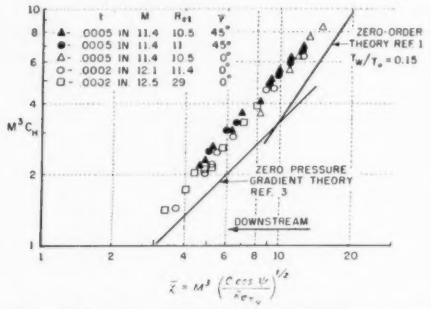
t M R_{et} ψ
0005 IN 11.4 10.5 45°
0005 IN 11.4 11 45°
0005 IN 11.4 10.5 0°
0002 IN 12.1 11.4 0°
0002 IN 12.5 29 0°
ZERO-ORDER THEORY REF 1
$T_w/T_\infty = 0.15$
ZERO PRESSURE GRADIENT THEORY REF. 3
DOWNSTREAM
M^3C_H

FIG. 4. Correlation of yawed and nonyawed heat transfer for small Re_t.

0.0005 in. Correlation of M^3C_H in terms of $K_e^{1/3}\bar{\chi}$ in Eq. (1) requires the condition of a strong shock wave as well as that of no viscous interaction. Correlation in terms of χ in Eq. (2), however, does not require the strong shock condition provided Re_t is sufficiently small.

Correlations of the experimental heat transfer for $\psi = 0$ and 45°, and comparisons with the predictions of Eqs. (1) and (2) are shown in Figs. 3 and 4, respectively. Some previous data[1] for $\psi = 0$ is also included in Fig. 4.

In Fig. 3 for large Re_t, the correlation of the yaw and zero-yaw data is seen to be best for the upstream data points. Divergence of the data in the downstream direction could result from two effects of yaw: reduction of shock strength, and increase in the relative importance of viscous interaction through reduction of effective bluntness. The correlation in Fig. 4 for the sharp plate and small Re_t is generally good. In this case, as noted above, the strong shock condition is not required for correlation provided Re_t is sufficiently small.

The correlations obtained indicate the effects of cross flow on heat transfer to be quite small. This supports the prediction given in reference 5 and also the numerical results of reference 2 obtained for the sharp-edged plate. Agreement of experiment with the zero-order theory has been discussed in reference 1 for $\psi = 0$.

REFERENCES

[1] Cheng, H. K., Hall, J. G., Golian, T. C., and Hertzberg, A., *Boundary-Layer Displacement and Leading-Edge Bluntness Effects in High-Temperature Hypersonic Flow*, IAS 28th Annual Meeting, January 1960; also, Cornell Aeronautical Laboratory Report AD-1052-A-9, AFOSR TN 59-1193. (To be published in Journal of the Aerospace Sciences.)

[2] Whalen, Robert J., *Boundary-Layer Interaction on a Yawed Infinite Wing in Hypersonic Flow*, Readers' Forum, Journal of the Aero/Space Sciences, Vol. 26, No. 12, pp. 839–841, December, 1959.

[3] Howarth, L., *Modern Developments in Fluid Dynamics: High-Speed Flow*, Vol. 1, p. 422, Oxford Univ. Press, London, 1953.

[4] Hayes, W. D., and Probstein, R. F., *Viscous Hypersonic Similitude*, Journal of the Aero/Space Sciences, Vol. 26, No. 12, pp. 815–824, December, 1959.

[5] Moore, F. K., and Cheng, H. K., *The Hypersonic Aerodynamics of Slender and Lifting Configurations*, IAS Summer Meeting, Los Angeles, Calif., 1959.

Free-Convection Magnetohydrodynamic Flow Past a Porous Flat Plate

Pau-Chang Lu
Graduate Assistant, Department of Mechanical Engineering, Case Institute of Technology, Cleveland, Ohio

August 22, 1960

THE INCOMPRESSIBLE FLOW of an electrically conducting fluid past a porous plate $y = 0$ with constant suction velocity in the presence of a transverse uniform strength H_0 has recently been investigated by Gupta.[1] In this note, the problem is generalized to take into account the effect of free convection, when a body force g per unit mass is acting in the negative x-direction parallel to the wall. The fluid is assumed to be semi-incompressible as usual. In addition to the obvious practical significance, this problem is also interesting in the sense that it provides another exact solution of the magnetohydrodynamic equations, since the only electromagnetic assumptions involved are constant properties and freedom from excessive charges.

Similar to the analysis of Gupta, we assume that all the variables, except the pressure p, are functions of y only. The following system is then obtained:

$$v = \text{constant} = -v_0 \tag{1a}$$

$$-\rho v_0(du/dy) = -(\partial p/\partial x) - \rho g + \mu(d^2u/dy^2) + \mu_e H_y(dH_x/dy) \tag{1b}$$

$$0 = -(\partial p/\partial y) + \mu_e H_x(dH_x/dy) \tag{1c}$$

$$-\rho c v_0(d\theta/dy) = k(d^2\theta/dy^2) + \mu(du/dy)^2 + (1/\sigma)(dH_x/dy)^2 \tag{1d}$$

$$(d/dy)(uH_y + v_0H_x) + (1/\mu_e\sigma)(d^2H_x/dy^2) = 0 \tag{1e}$$

$$d^2H_y/dy^2 = 0 \tag{1f}$$

where (H_x, H_y) and (u, v) are the components, parallel and perpendicular to the plate, of the magnetic-field strength and velocity; θ is the temperature difference that refers to the free-stream value; ρ, μ, c, k, μ_e, and σ are the density, viscosity, specific heat capacity, thermal conductivity, magnetic permeability, and electric conductivity, respectively. The subscript 0 refers to conditions at $y = 0$. The rationalized mks system is employed.

The boundary conditions to be satisfied are

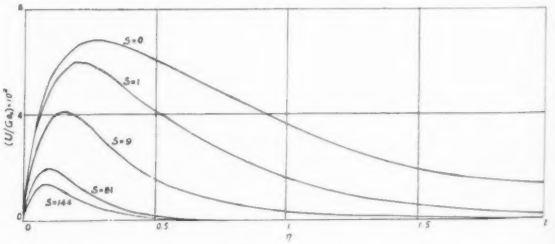

FIG. 1. Effect of magnetic field on free convection.

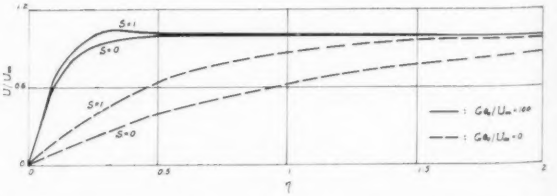

FIG. 2. Comparison of effects of free convection and magnetic field.

$$u(0) = 0, \quad \theta(0) = \theta_0, \quad H_y(0) = H_0 \tag{2a}$$

$$\theta(\infty) = 0 \tag{2b}$$

$$u(\infty) = u_\infty, \quad H_x(\infty) = 0, \quad \text{asymptotically} \tag{2c}$$

where the subscript ∞ refers to conditions in the free stream.

From Eq. (1c), we see that $\partial p/\partial x$ must be a function of x alone. Therefore, from Eq. (1b)

$$\partial p/\partial x = \text{constant} = -\rho_\infty g$$

Under the assumption of semi-incompressibility

$$\rho - \rho_\infty = -\rho\beta\theta$$

where β is the thermal coefficient of volumetric expansion. Otherwise, ρ is to be treated as constant. Eq. (1b) finally becomes

$$\mu(d^2u/dy^2) + \rho v_0(du/dy) + \mu_e H_y(dH_x/dy) + \rho\beta g\theta = 0 \tag{3a}$$

Eqs. (1e) and (1f), which are obtained by eliminating the electric-field strength among Maxwell's equations and Ohm's law,[1] immediately give

$$H_y = \text{constant} = H_0 \tag{3b}$$

$$uH_0 + v_0 H_x + (1/\mu_e\sigma)(dH_x/dy) = u_\infty H_0 \tag{3c}$$

The key equations of the problem are then the Eqs. (1d), (3a), and (3c). In general, they must be solved numerically.

However, if the viscous energy dissipation is negligible because of small u, and the electric energy dissipation is negligible because of small u and large σ, Eq. (1d) becomes uncoupled and gives

$$\theta/\theta_0 = \exp(-Pr\,\eta) \tag{4}$$

where Pr is the Prandtl number and $\eta = \rho v_0 y/\mu$. Here it is obvious that suction is necessary—i.e., v_0 must be greater than zero.

Using primes to denote differentiation with respect to η, we may integrate Eq. (3a) once and obtain

$$(U - U_\infty)' + (U - U_\infty) + Sh_x = G\theta_0 \exp(-Pr\,\eta)/Pr \tag{5a}$$

where $U = u/v_0$, $h_x = H_x/H_0$, $S = \mu_e H_0^2/\rho v_0^2$ and $G = \mu\beta g/\rho v_0^3$. Then h_x is eliminated between Eqs. (3c) and (5a)*:

$$\epsilon(U - U_\infty)'' + (1 + \epsilon)(U - U_\infty)' - (S - 1)(U - U_\infty) = (1/Pr - \epsilon)G\theta_0 \exp(-Pr\,\eta) \tag{5b}$$

where $\epsilon = \rho/\mu_e\sigma\mu$.

The solution for U is then, when $S \geq 1$,

$$U - U_\infty = -U_\infty \exp(-\alpha\eta) + \{(1/Pr - \epsilon)G\theta_0[\exp(-Pr\,\eta) - \exp(-\alpha\eta)]/[\epsilon Pr^2 - (1 + \epsilon)Pr - (S - 1)]\} \times [S \neq \epsilon Pr^2 - (1 + \epsilon)Pr + 1] \tag{6a}$$

$$= -U_\infty \exp(-Pr\,\eta) + (1/Pr - \epsilon)G\theta_0\eta \exp(-Pr\,\eta)/[(1 + \epsilon) - 2\epsilon Pr] \quad [S = \epsilon Pr^2 - (1 + \epsilon)Pr + 1] \tag{6b}$$

where $\alpha = \{(1 + \epsilon) + [(1 + \epsilon)^2 + 4\epsilon(S - 1)]^{1/2}\}/2\epsilon$.

It is interesting to note that when $S < 1$, the problem is indeterminate just as in the incompressible case. Another peculiarity is that the free-convection effect vanishes completely for a fluid with $Pr\,\epsilon = 1$. It is also seen that increasing S decreases the effect of free convection.

In Fig. 1, the effect of S on free convection is clearly shown for a hypothetical fluid with $Pr = 10$ and $\epsilon = 1$. A comparison of the pure forced and the combined flow with $S = 1$ is presented for the same fluid in Fig. 2. Nonmagnetic cases ($S = 0$) are also included.

REFERENCE

[1] Gupta, A. S., *Flow of an Electrically Conducting Fluid Past a Porous Flat Plate in the Presence of a Transverse Magnetic Field*, ZAMP., Vol. 11, No. 1, pp. 43–50, January 1960.

* One must not neglect h'_x in Eq. (3c) since $1/\sigma$ is a singular perturbation parameter there.

The Redesign of Redundant Structures Having Undesirable Stress Distributions

E. D. Poppleton
Assistant Professor of Aeronautical Engineering, University of Toronto, Institute of Aerophysics, Canada

August 22, 1960

METHODS for determining the effect of structural modifications on the stress distribution in a redundant structure have been given in references 1 and 2, but the use of these methods in the rectification of deficiencies in an existing structure leads to a trial-and-error procedure. The purpose of the present note is to point out a simple extension of reference 2, which enables the stress to be specified in a number of structural members (not greater than the number of redundancies), and the necessary modifications to the stiffness of these members to be calculated directly.

Using the notation of reference 2, we denote the generalized loads in the structural members (including the redundancies), the external loads, and the generalized loads in the redundant members by the column matrices S, R, and X, respectively. If the members have initial displacements (due to thermal effects or lack of fit) H, then the following relationships hold:

$$S = b_0 R + b_1 X - cH$$

$$X = -D^{-1}D_0 R$$

in which

$$D = b_1' f b_1$$

$$D_0 = b_1' f b_0$$

$$c = b_1 D^{-1} b_1' \tag{1}$$

and f = diagonal matrix of flexibilities of the unassembled elements (total strain energy of structure = $1/2 S' f S$).

In the above, the prime denotes a transposed matrix.

As indicated in reference 2, if the redundancies are judiciously chosen, b_0 and b_1 are readily written down from equilibrium considerations so that it is a relatively simple matter to write Eq. (1) in the form

$$S = bR - cH \tag{2}$$

The generalized displacements of the structural members are given by

$$v = fS + H \tag{3}$$

We now suppose that the application of Eq. (2) to a given structure (with $H = 0$) gives undesirable values for the stresses in some members. We, therefore, require to modify these members in such a way that the desired stresses are realized. Following the method of reference 2, we state that the stress distribution in the modified structure could be produced in the original structure if suitable initial displacements were imposed on the members which are to be modified.

We introduce subscripts g and h to indicate unmodified and modified sections of the structure, and a further subscript m to denote conditions in the modified structure, then we can rearrange and partition Eqs. (2) and (3) to obtain

$$\begin{bmatrix} S_{gm} \\ \hline S_{hm} \end{bmatrix} = bR - \left[\begin{array}{c|c} c_{gg} & c_{gh} \\ \hline c_{hg} & c_{hh} \end{array}\right] \begin{bmatrix} 0 \\ \hline H_h \end{bmatrix} = \begin{bmatrix} S_g \\ \hline S_h \end{bmatrix} - \left[\begin{array}{c|c} c_{gg} & c_{gh} \\ \hline c_{hg} & c_{hh} \end{array}\right] \begin{bmatrix} 0 \\ \hline H_h \end{bmatrix}$$

$$\left[\begin{array}{c|c} f_g & 0 \\ \hline 0 & f_{hm} \end{array}\right] \begin{bmatrix} S_{gm} \\ \hline S_{hm} \end{bmatrix} = v_m = v = \left[\begin{array}{c|c} f_g & 0 \\ \hline 0 & f_h \end{array}\right] \begin{bmatrix} S_{gm} \\ \hline S_{hm} \end{bmatrix} + \begin{bmatrix} 0 \\ \hline H_h \end{bmatrix}$$

From these we have

$$S_{hm} = S_h - c_{hh}H_h$$
$$H_h = \lfloor f_{hm} - f_h \rfloor S_{hm} \quad (4)$$
$$S_{hm} = S_h - c_{hh}\lfloor f_{hm} - f_h \rfloor S_{hm}$$

For structures consisting of an assembly of flanges carrying linearly-varying axial loads only, and thin sheets carrying constant shear flows on their edges, the flexibility matrix may be written

$$f = gA^{-1}$$

where g is a symmetrical matrix; A is a diagonal matrix of the cross-sectional areas resisting the loads.

Eq. (4) may thus be written

$$S_{hm} = S_h - c_{hh}g\sigma_{hm} + c_{hh}f_hS_{hm} \quad (5)$$

where σ_{hm} is a column of stresses in the modified members. Some of the stresses σ_{hm} may not be specified, however. This is because the column contains *all* stresses in the modified part of the structure, including those at both ends of those flanges in which the stress is specified at one end only.

Eq. (5) is thus conveniently solved directly only when all the elements of σ_{hm} are known, as would be the case, for example, in the analysis of a pinjointed framework. In such cases, we have

$$S_{hm} = [I - c_{hh}f_h]^{-1}\{S_h - c_{hh}g\sigma_{hm}\}$$

In other, more usual cases, Eq. (5) is solved by an iteration process in which initial values are assumed for S_{hm} ($= S_h$ say) and for the unknowns in σ_{hm}. Improved values of S_{hm}, and hence of the unknowns in σ_{hm} are then found by substitution in the right-hand side of Eq. (5), and the process is repeated until convergence is satisfactory.

It should be noted that Eq. (5) is not linear in the unknowns and, consequently, difficulties may arise in the iterative solution if two solutions exist in close proximity. A somewhat fuller discussion of the above analysis is given in reference 3, together with a few simple examples. The case where stresses are specified in members which are not modified is also investigated.

References

[1] Michielsen, H. F., and Dijk, A., *Structural Modifications in Redundant Structures*, Journal of the Aeronautical Sciences, Readers' Forum, Vol. 20, No. 4, pp. 286–288, April, 1953.

[2] Argyris, J. H., and Kelsey, S., *The Matrix Force Method of Structural Analysis and Some New Applications*, Gt. Brit., ARC R&M 3034, February, 1956.

[3] Poppleton, E. D., *A Note on the Design of Redundant Structures*, University of Toronto, UTIA TN 36, July, 1960.

On Column Behavior

S. Sergev
Professor, Department of Civil Engineering, University of Washington, Seattle, Wash.

August 22, 1960

THE BEHAVIOR of pressurized slender columns seems to have an air of mystery about it. Here we present the problem in a way that seems to point to better understanding of column behavior under different conditions of loading. The two cases we wish to discuss are: (a) the pressurized column with open ends, and (b) the pressurized column with closed ends. The problem in each case is the determination of the lateral instability criterion which, incidentally, turns out to be entirely different for the two cases.

The lateral instability of pressurized columns, while theoretically obvious, has not been observed until recently when use of thin-wall pipes and tubes became prevalent, especially, in airplane structures.* The complete understanding of column behavior is found in the elastic equilibrium of a differential length of the column.[1] Let us suppose, for definiteness, that we have a straight, slender, round tube which is used as a column and as a pressure vessel—separately, or in combination. Further, let us assume that we have simple (Hooke's joint) ends, but this limitation does not in any way affect the general philosophy of the analysis. If the column (tube) is unstable in the straight configuration, there will be a change of state and the tube will assume equilibrium in the curved configuration, as in Fig. 1(a). In this state, we draw an equilibrium sketch of an element of the column between sections normal to the column axis and located at x and $x + dx$ distances from the origin, Fig. 1(b). The displacement of this element from the straight configuration (x-axis) is v and the absolute value of the curvature to first approximation is d^2v/dx^2. Now, a variation in the shearing-force function requires a lateral load, which in a column comes from the forces N acting tangentially to the column axis and toward each other, Fig. 2. The forces, in this case, are essentially the same for all elements if we consider the displacements v to be small. Due to the curvature of the axis, these forces, not being parallel, have a resultant component acting in the positive direction of v and equal to $N|d^2v/dx^2|dx$.

From equilibrium and the geometry of deformation of the element, we have the well-known relationship:** $EI(d^4v/dx^4) = q$, q being the intensity of the lateral load per unit length, which in our case is $-Nd^2v/dx^2$. The minus sign is used because the curvature is negative. Substituting this lateral load for q and putting $N/EI = m^2$, the above equation becomes

$$(d^4v/dx^4) + m^2(d^2v/dx^2) = 0 \quad (1)$$

The integral of Eq. (1) is

$$v = A + Bx + C \sin mx + D \cos mx \quad (2)$$

where A, B, C, and D are constants. Eq. (2) contains enough arbitrary constants for the solution of any column of constant cross section and length L, if the proper boundary conditions are imposed. For a column that has freedom of rotation but not

** This formula can be found in most Strength of Materials textbooks.

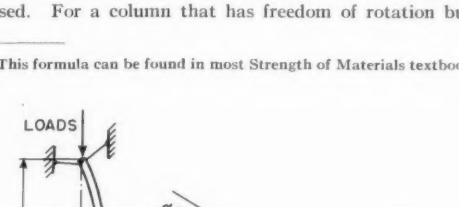

FIG. 1

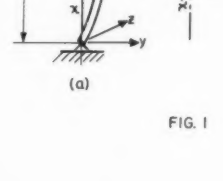

FIG. 2

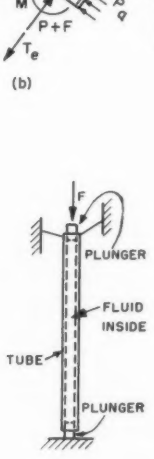

FIG. 3

* A solution was transmitted to O. T. Ritchie, Head of Structural Research and Development Group, Boeing Airplane Co., Seattle, Washington in June, 1956.

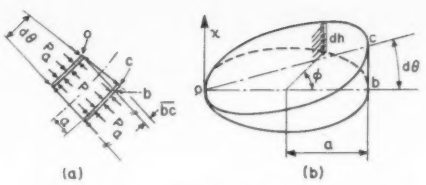

FIG. A. Open ends column.

lateral displacement at the ends, the four boundary conditions will be:

$$(v)_{x=0} = (v)_{x=L} = (d^2v/dx^2)_{x=0} = (d^2v/dx^2)_{x=L} = 0 \qquad (3)$$

These boundary conditions require that $A = B = D = 0$, and $C \sin mL = 0$. If $C = 0$, we have a trivial solution—i.e., the column axis before and after loading remains straight. If $C \neq 0$, then $\sin mL = 0$, from which it follows that $mL = 0, \pi, 2\pi, \ldots, n\pi$; and the first nontrivial root gives $m^2L^2 = \pi^2$, or a critical value of

$$N = \pi^2EI/L^2 \qquad (4)$$

Now, we inquire into the nature of the tangential forces N in the open-ends case.†

(a) Suppose these forces N emanate from loads P applied to the ends of the tube and transmitted along the walls of the tube, Fig. 1(b). In such a case, we have the necessary condition for an Euler column with the buckling (critical) load $N = P = \pi^2EI/L^2$.

(b) On the other hand, suppose we have pressure p *in* the column resulting from a force $F = Ap$, where A denotes internal cross-sectional area, applied to freely sliding plungers at the ends with $P = 0$, Fig. 3. Under this condition, there will be hoop but not axial stresses in the column wall and the forces necessary to maintain the bent configuration are $N = F = \pi^2EI/L^2$. However, if $P = 0$, but tensile forces T_e are applied to the ends, then the column will become unstable when $N = F - T_e$ approaches π^2EI/L^2, or the critical compressive fluid force $F = \pi^2EI/L^2 + T_e$. If practicable, this is a way to increase the lateral stability of the open-ends pressurized column.

(c) Lastly, we assume that the tube is capped (closed) at both ends and the column then pressurized, giving us a self-contained system. In this case with $P = 0$, $N = F - T_e = 0$ because the tensile forces T_e in the column wall are exactly equal to the fluid forces F. Thus, we see that the bent configuration cannot be maintained ($N = 0$), or conversely, the straight configuration is stable. With P critical ($F > 0$), we again have the Euler column, and conclude that instability of a pressurized slender column with closed ends is independent of the internal pressure.‡ If the pressure p is less than atmospheric—i.e., $p < 0$ and $P \neq 0$, there will be compressive forces on the ends of the column with $N = P + p_aA_e$, where p_a denotes atmospheric pressure and A_e the external area of the column cross section. Instability under this condition, with $P = 0$, is not possible since the external lateral force of the atmosphere $p_aA_e d\theta$ equals $Nd\theta$—see Appendix.

In all above discussions, bursting and local buckling (crippling) is assumed to be precluded.

APPENDIX

It may be of interest to approach the force $Fd\theta$ from another viewpoint. Let us remove the fluid from inside the element of the column in Fig. 1(b), and show the resulting pressure p (gage) acting on the wall of the column, as in Fig. A(a). Force F is absent, and we see that there is a resultant force acting toward the convex side of the column because the convex side is longer than the concave side by the amount $\overline{bc}$. Since the pressure acts with equal intensity on the wall of the tube (in case of gas), this resultant force will be—see Fig. A(b) (we assume thin wall)

$$dF_1 = \int_0^{2\pi} pa\, d\varphi dh \cos\varphi$$

where,

$$dh = d\theta\, a(1 + \cos\varphi)$$

Then,

$$dF_1 = pa^2d\theta \left[\sin\varphi + (\varphi/2) + (1/4)\sin 2\varphi\right]_0^{2\pi} = p\pi a^2 d\theta$$

which is exactly equal to $Fd\theta$. If $p < 0$, then the force dF_1 acts inward, which is equivalent to taking F with a minus sign in the previous discussion and A_e instead of A.

REFERENCE

[1] Timoshenko, S., *Theory of Elastic Stability*, McGraw-Hill Book Co., Inc., New York, 1936.

† The effect of atmospheric pressure p_a is not considered since force F is due to gage pressure p—i.e., above atmospheric. If p is less than atmospheric, F should be taken with minus sign.

‡ Experiments performed by D. A. Walton, Graduate Student in Civil Engineering, bore out exactly the theoretical prediction. Pressures up to 6,000 psi were used.

On the Feasibility of Using Aerodynamic Control on Vehicles Operating in Regions of Slip Flow and Free-Molecule Flow

Robert L. Swaim
1/Lt., USAF, Flight Control Laboratory,
Wright Air Development Division, Wright-Patterson AFB, Ohio
August 24, 1960

AT PRESENT there are no adequate theories for predicting aerodynamic coefficients and forces in slip flow. However, the lack of an adequate slip-flow theory will not prevent the determination of the feasibility, or lack thereof, of using aerodynamic control in the slip-flow regime, as will be shown below.

A criterion is needed on which to base any judgment of feasibility. Consider only longitudinal motion in a vertical plane of symmetry, where the vehicle is in equilibrium flight along any arbitrary flight path in this vertical plane. Equilibrium flight, in this analysis, means all angular and linear accelerations with respect to an axis system fixed on the vehicle are zero. Now, a realistic criterion for determining controllability is the rate of pitch $\dot{\theta}$ following a control-surface deflection and establishment of the new equilibrium flight condition. Using this angular-velocity criterion, maximum altitudes for vehicle controllability will be calculated for various changes in equilibrium lift coefficient, ΔC_L, due to a control-surface deflection.

A change in the equilibrium lift will result in a change in the equilibrium flight path, with a resultant centripetal acceleration towards the new center of curvature (Fig. 1) given by

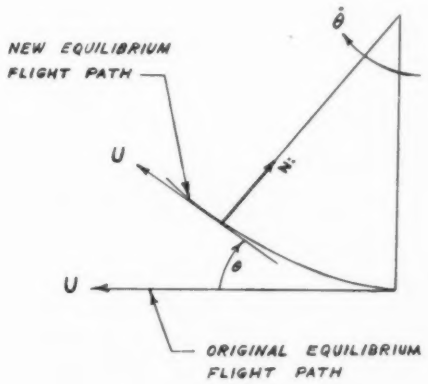

FIG. 1.

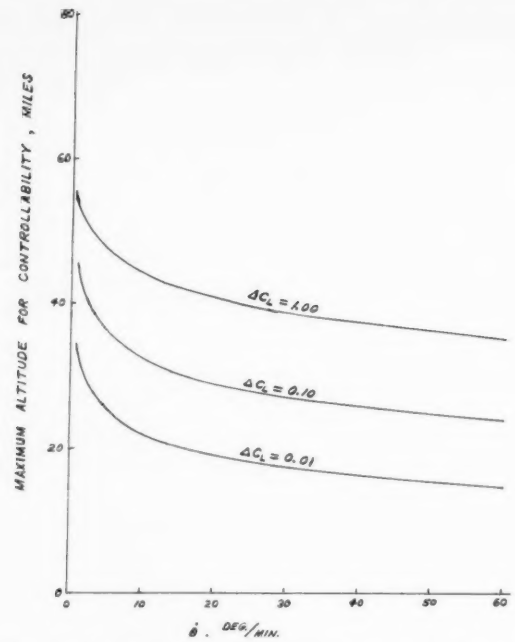

FIG. 2. Maximum altitude for control vs. change in pitch rate for various changes in equilibrium C_L [U = 12,875 ft./sec., $S = 300$ ft^2, $m = 106$ slugs].

$$\Delta L = m\ddot{z} = m\dot{\theta}U \tag{1}$$

$$\dot{\theta} = (\Delta C_L\, {}^1\!/_2 \rho U S)/m \tag{2}$$

Now, consider a representative vehicle with $m = 106$ slugs, and $S = 300$ ft.^{2}

$$\dot{\theta} = 1.407\ \Delta C_L\, \rho U \tag{3}$$

The condition for satisfactory controllability based on a desired change in pitch rate $\dot{\theta}$ is

$$\dot{\theta} \leq 1.407\ \Delta C_L\, \rho U \tag{4}$$

$$\rho \geq \dot{\theta}/(1.407\ \Delta C_L U) \tag{5}$$

Eq. (5) is shown graphically in Fig. 2 for three values of ΔC_L and a representative flight velocity, where ρ has been converted to altitude in statute miles.

It is seen that given a desired change in rate of response $\dot{\theta}$ to a control deflection and calculating the resultant change in equilibrium lift coefficient ΔC_L, the maximum altitude is then known, above which this rate of response cannot be attained with the aerodynamic control surface. Lift coefficients of the order shown are known to be attainable in free-molecule flow, and it justly follows that they can be attained in the higher-density slip flow.

It is evident from Fig. 2 that aerodynamic control is not feasible in the free-molecule regime (above 80 miles), since changes in C_L greater than 1.00 are not likely to be attained with a control surface. But aerodynamic control does appear to be feasible in slip-flow regions (20 to 60 miles); although, in the upper altitudes of the regime, the rate of response may become too slow to be practical. It might be mentioned that lower flight velocities, even as low as 6,000 ft./sec., do not lower the boundaries appreciably.

It is also evident from the results that for a given altitude and ΔC_L, the rate of response to control deflection decreases with decreasing flight velocity. However, for a vehicle on an atmospheric re-entry flight path, the altitude is decreasing as well as the vehicle velocity, and it may be possible to maintain relatively constant rates of control response.

A Method of Obtaining An Approximate Solution of the Laminar Boundary-Layer Equations*

William B. Bush**
Graduate Student, California Institute of Technology, Pasadena, Calif.
August 25, 1960

(I) The Incompressible Boundary-Layer Equation

It has been shown[1] that the incompressible laminar boundary-layer equations can be written in the form:

$$\frac{\partial^3 f}{\partial \eta^3} = -f\frac{\partial^2 f}{\partial \eta^2} - \beta(\xi)\left[1 - \left(\frac{\partial f}{\partial \eta}\right)^2\right] + 2\xi\left[\frac{\partial f}{\partial \eta}\frac{\partial^2 f}{\partial \xi \partial \eta} - \frac{\partial f}{\partial \xi}\frac{\partial^2 f}{\partial \eta^2}\right] \tag{1.01}$$

with the boundary conditions

$$f(\xi, 0) = (\partial f/\partial \eta)(\xi, 0) = 0, \quad (\partial f/\partial \eta)(\xi, \infty) = 1 \tag{1.02}$$

Introducing the new independent variables

$$s = \xi, \qquad t = a(\xi)\,\eta = a(s)\eta \tag{1.03}$$

and denoting $(\partial f/\partial \eta)$ by w, Eq. (1.01) takes on the form:

$$a^2\frac{\partial^2 w}{\partial t^2} = -\left[1 - \frac{2s}{a}\frac{da}{ds}\right]\left(\frac{\partial w}{\partial t}\right)\int_0^t w d\bar{t} - \beta\,[1 - w^2] + 2s\left[w\frac{\partial w}{\partial s} - \frac{\partial w}{\partial t}\int_0^t \left(\frac{\partial w}{\partial s}\right) d\bar{t}\right] \tag{1.04}$$

This equation may be solved by iteration by introducing a suitable approximation for w in the right-hand side. If the approximation for w in the right-hand side is a function of t alone, then the equation W, the resulting solution, is

$$a^2(s)\frac{\partial^2 W}{\partial t^2} = -\left[1 - \frac{2s}{a}\frac{da}{ds}\right]\left(\frac{dw}{dt}\right)\int_0^t w(\bar{t})d\bar{t} - \beta(s)\,[1 - w^2] \tag{1.05}$$

The first integral of this equation is

$$a^2\frac{\partial W}{\partial t} = \left[1 - \frac{2s}{a}\frac{da}{ds}\right]\int_t^\infty \frac{dw}{dt_1}\left[\int_0^{t_1} w(t_2)dt_2\right] dt_1 + \beta\int_t^\infty [1 - w^2]\, dt_1 \tag{1.06}$$

since it is required that $(\partial W/\partial t)(s, \infty) = 0$.

The second integral of this equation is

$$a^2 W = \left[1 - \frac{2s}{a}\frac{da}{ds}\right]\int_0^t dt_1\left[\int_{t_1}^\infty \frac{dw}{dt_2}\left\{\int_0^{t_2} w(t_3)dt_3\right\} dt_2\right] + \beta\int_0^t dt_1\left\{\int_{t_1}^\infty (1 - w^2)\, dt_2\right\} \tag{1.07}$$

satisfying the boundary condition $W(s, 0) = 0$.

Since the function W must also satisfy the boundary condition $W(s, \infty) = 1$, it follows that a, the function of s that was introduced in Eq. (1.03), must be the solution of the equation

$$a^2 = \left[1 - \frac{2s}{a}\frac{da}{ds}\right]\int_0^\infty dt_1\left[\int_{t_1}^\infty \frac{dw}{dt_2}\left\{\int_0^{t_2} w dt_3\right\} dt_2\right] + \beta\int_0^\infty dt_1\left[\int_{t_1}^\infty \{1 - w^2\}\, dt_2\right] \tag{1.08}$$

To illustrate this method, the approximating function $w = u(t) = \mathrm{erf}(t)$ was considered. Introducing this function into Eq. (1.08) and performing the indicated integrations yields the following:

* Prepared for the Air Force Ballistic Missile Division, Headquarters Air Research and Development Command, under Contract AF 04(647)-309, Magnetoaerodynamic Research.

** Formerly associated with Physical Research Laboratory, Space Technology Laboratories, Inc., Los Angeles, Calif.

$$[s/(a^2)]\,[d(a^2)/ds] + 4a^2 = 1 + \beta(s)[1 + (2/\pi)] \quad (1.09)$$

The shear function at the wall is

$$\frac{\partial W}{\partial \eta}(\xi, 0) = a(s)\frac{\partial W}{\partial t}(s, 0) = \frac{[1 - (2s/a)(da/ds)](\sqrt{2} - 1) + \sqrt{2}\beta}{a\sqrt{\pi}} \quad (1.10)$$

For "similar" solutions where $W = W(t)$ and a and β are constants, Eqs. (1.09) and (1.10) reduce to

$$a^2 = 1/4 + \beta[(1/4) + (1/2\pi)] \quad (1.11)$$

$$\frac{dW}{d\eta}(0) = \frac{\sqrt{2}\,(1 + \beta) - 1}{a\sqrt{\pi}} \quad (1.12)$$

The solutions of Eqs. (1.11) and (1.12) are given in Table 1 along with the exact solutions determined by Hartree.[2]

(II) The "Similar" Compressible Boundary-Layer Equations

Cohen and Reskotko[3] have shown that the partial differential equations governing the flow in the compressible laminar boundary layer by means of the Stewartson transformation (with slight modifications) and Faulkner-Skan similarity arguments can be reduced to two simultaneous nonlinear ordinary differential equations. These equations are

$$\frac{d^3f}{d\eta^3} = -f\frac{d^2f}{d\eta^2} - \beta g_w(1 - \phi) - \beta\left(\phi - \left\{\frac{df}{d\eta}\right\}^2\right) \quad (2.01)$$

$$d^2\phi/d\eta^2 = -f(d\phi/d\eta) \quad (Pr = 1) \quad (2.02)$$

with the boundary conditions

$$(0) = (df/d\eta)(0) = \phi(0) = 0; \qquad (df/d\eta)(\infty) = \phi(\infty) = 1 \quad (2.03)$$

In order to use the method of the previous section, Eqs. (2.01) and (2.02) must be rewritten in the following form:

$$\frac{d^2W}{d\eta^2} = -\frac{dw}{d\eta}\int_0^\eta w d\eta_1 - \beta g_w(1 - \phi) - \beta(\phi - w^2) \quad (2.04)$$

$$\frac{d^2G}{d\eta^2} = -\frac{d\phi}{d\eta}\int_0^\eta w d\eta_1 \quad (2.05)$$

If the approximating functions w and ϕ are

$$w = \text{erf}\,(a\eta), \qquad a = \text{constant} \quad (2.06a)$$

$$\phi = \text{erf}\,(b\eta), \qquad b = \text{constant} \quad (2.06b)$$

Then, the first integration of Eqs. (2.04) and (2.05) yields

$$\frac{dW}{d\eta}(0) = \frac{\sqrt{2}\,(1 + \beta) - 1 - m\beta(1 - g_w)}{a\sqrt{\pi}}, \qquad m = a/b \quad (2.07)$$

$$\frac{dG}{d\eta}(0) = \frac{\sqrt{1 + m^2} - 1}{a\sqrt{\pi}} \quad (2.08)$$

The second integration yields

Table 1

"Similar" Incompressible Boundary-Layer

β	a	$A = \frac{dW}{d\eta}(0)$, w = erf(t)	$B = \frac{dW}{d\eta}(0)$, exact	$\frac{A}{B}$
-0.1	0.4573	0.337	0.319	1.056
0	0.5000	0.467	0.470	0.994
0.1	0.5394	0.581	0.587	0.990
0.2	0.5760	0.683	0.687	0.994
0.3	0.6106	0.775	0.775	1.000
0.4	0.6432	0.860	0.854	1.007
0.5	0.6742	0.938	0.928	1.011
0.6	0.7039	1.012	0.996	1.016
0.8	0.7599	1.148	1.120	1.025
1.0	0.8119	1.271	1.233	1.031

Table 2

"Similar" Compressible Boundary-Layer

β	g_w	$A = \frac{dW}{d\eta}(0)$	$B = \frac{dW(0)}{d\eta}$ exact	$\frac{A}{B}$	$C = (1-g_w)\frac{dG}{d\eta}(0)$	$D = (1-g_w)\frac{dG}{d\eta}(a)$ exact	$\frac{C}{D}$
0	0	0.467	0.470	0.994	0.467	0.470	0.994
	0.2	0.467	0.470	0.994	0.374	0.376	0.995
	0.6	0.467	0.470	0.994	0.187	0.188	0.995
	1.0	0.467	0.470	0.994	0	0	1.000
	2.0	0.467	0.470	0.994	-0.467	-0.470	0.994
0.5	0	0.564	0.581	0.971	0.482	0.495	0.974
	0.2	0.663	0.655	1.012	0.389	0.403	0.965
	0.6	0.805	0.795	1.013	0.199	0.209	0.952
	1.0	0.938	0.928	1.011	0	0	1.000
	2.0	1.231	1.235	0.997	-0.544	-0.573	0.949

$$W(\infty) = 1 = \frac{1}{a^2}\left[\frac{1}{4} + \beta\left(\frac{1}{4} + \frac{1}{2\pi}\right) - \frac{m^2\beta(1 - g_w)}{4}\right] \quad (2.09)$$

$$G(\infty) = 1 = [m^2\tan^{-1}(m)]/a^2\pi \quad (2.10)$$

Table 2 compares the approximate solutions obtained by this method with the exact solutions of Cohen and Reskotko and again the agreement is good.

References

[1] Meksyn, D., *The Laminar Boundary-Layer Equations*, Proc. Royal Soc. (London), Ser. A., Vol. 192, p. 545, 1948.

[2] Hartree, D. R., *On the Equation Occurring in Falkner and Skan's Approximate Treatment of the Equations of the Boundary Layer*, Proc. Cambridge Philos. Soc., Vol. 33, p. 223, 1937.

[3] Cohen, C. B., and Reskotko, E., *Similar Solutions for the Compressible Laminar Boundary Layer with Heat Transfer and Pressure Gradient*, NACA TR 1293, 1956.

Atmospheric Entry With Small L/D

Paul D. Arthur and Hans K. Karrenberg
Systems Corporation of America, Los Angeles, Calif.

September 1, 1960

The "straight-line-trajectory" atmospheric-entry analysis of Allen and Eggers[1] has been very useful for zero-lift entries at angles greater than five or ten degrees.[2] This note extends their analysis to include a constant but small lift/drag ratio.

Derivation of Equations

The lift and drag component equations of motion of a body in the atmosphere of a planet with an inverse-square central force field are:

$$L/W = V(\dot\gamma/g) + [1 - (V^2/gr)]\cos\gamma$$
$$(D/W) + (\dot V/g) + \sin\gamma = 0$$

where γ is the elevation angle above the local horizon, and is negative during entry. As in Allen and Eggers study[1] the assumptions are: γ not too small, weight neglected, flat Earth ($r \to \infty$) and constant g. Thus, the equations reduce to:

$$L/W = V(\dot\gamma/g) \quad (1)$$

$$D/W = -\dot V/g \quad (2)$$

For $L = 0$ Eq. (1) shows that γ is a constant. However, lift causes γ to increase along the trajectory from its entry value, γ_E. Taking $\gamma = \gamma_E + \phi$, it is presumed that ϕ is small for small L/D. Thus, the kinematic relation, $V\sin\gamma = \dot h$ is approximated by:

$$V\sin\gamma_E(1 + \phi\cot\gamma_E) = \dot h \quad (3)$$

Eq. (1) may be integrated to obtain ϕ:

$$\phi = \dot\gamma = (g/V)(L/W) \quad (4)$$

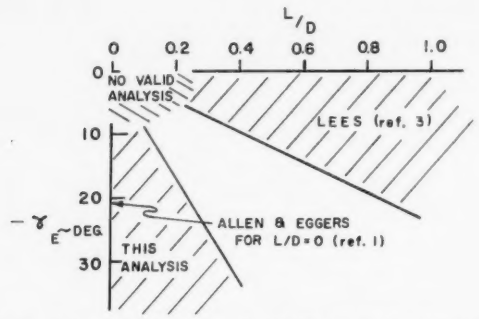

FIG. 1. Approximate regions of validity for various atmospheric entry analyses.

$$\phi = \int (L/D)\rho V/2\Delta)dt \quad \text{where } \Delta \text{ is defined as mass}/C_D A \tag{5}$$

Using the exponential atmospheric-density relation,

$$\rho = \rho_1 e^{-h/h_0} \quad \text{where } h_0 \text{ is the scale height} \tag{6}$$

and Eq. (3):

$$\phi = \frac{L}{D}\frac{\rho_1}{2\Delta \sin \gamma_E}\int_{h_E}^{h}\frac{e^{-h/h_0}\,dh}{1+\phi\cot\gamma_E} \tag{7}$$

Since $-\phi \cot \gamma_E \ll 1$, the integration is only taken to first order in ϕ:

$$\phi = -(L/D)(\rho h_0/2\Delta \sin \gamma_E) \tag{8}$$

As in the analysis of reference 1, the independent variable of the drag equation, Eq. (2), may be changed from time to altitude by the kinematic relation, Eq. (3). The first-order solution for ϕ, Eq. (8), then yields:

$$\left(1+\frac{L}{D}\frac{\rho h_0 \cot\gamma_E}{2\Delta\sin\gamma_E}\right)\rho dh = -2\Delta\sin\gamma_E\frac{dV}{V} \tag{9}$$

Using Eq. (6) and assuming that

$$\frac{L}{D}\frac{\rho h_0\cot\gamma_E}{2\Delta\sin\gamma_E} \ll 1$$

Eq. (9) may be integrated to yield:

$$\rho = \frac{2\Delta\sin\gamma_E}{h_0}\left(1-\frac{L}{D}\frac{\cot\gamma_E}{2}\ln\frac{V}{V_E}\right)\ln\frac{V}{V_E} \tag{10}$$

Maximum deceleration, heating, dynamic pressure, and Reynolds number can now be determined by the method of reference 1.

Considering the maximum deceleration,

$$-\frac{\dot V}{g} = \frac{D}{W} = \frac{\rho V^2}{2g\Delta} = \frac{\sin\gamma_E}{gh_0}\left(\frac{V}{V_E}\right)^2 V_E^2 \times \left(1-\frac{L}{D}\frac{\cot\gamma_E}{2}\ln\frac{V}{V_E}\right)\ln\frac{V}{V_E} \tag{11}$$

$\dot V_{max}$[or $(\rho V^2/2)|_{max}$] requires:

$$\ln\frac{V}{V_E} = -\frac{1}{2}\left(1+\frac{L}{D}\frac{\cot\gamma_E}{4}\right) \tag{12}$$

$$\frac{V}{V_E} = 0.606\left(1-\frac{L}{D}\frac{\cot\gamma_E}{8}\right) \tag{13}$$

Substituting into Eq. (11) and retaining only first-order terms:

$$-\frac{\dot V}{g}\bigg|_{max} = -\frac{V_E^2\sin\gamma_E}{2h_0 eg}\left(1+\frac{L}{D}\frac{\cot\gamma_E}{4}\right) \tag{14}$$

Since $\gamma_E < 0$, the maximum deceleration is decreased by lift. The density at maximum deceleration is

$$-\frac{\Delta\sin\gamma_E}{h_0}\left(1+\frac{L}{D}\frac{\cot\gamma_E}{2}\right)$$

indicating that an $L/D > 0$ causes the maximum deceleration to occur at a lower density (i.e., higher altitude) than that for zero lift.

The total acceleration felt by the body is the vector sum of $-\dot V = (D/M)$ and L/M:

$$a = -\dot V[1+(L/D)^2]^{1/2} \tag{15}$$

$$\frac{a}{g}\bigg|_{max} = -\left(\frac{V_E}{2030}\right)^2\sin\gamma_E\left[1+\frac{L}{D}\frac{\cot\gamma_E}{4}\right]\left[1+\left(\frac{L}{D}\right)^2\right]^{1/2} \tag{16}$$

where $h_0 = 23{,}500$ ft. has been assumed for the Earth. As the $(L/D)(\cot\gamma_E)/4$ term is negative, the effect of $L/D > 0$ is to decrease a/g.

Validity of Analysis

The basic assumption made in the above analysis is that

$$-\phi\cot\gamma_E = (L/D)\cot\gamma_E \ln(V/V_E) \ll 1$$

A 10 per cent accuracy requirement in the second-order term may be expressed as:

$$[(L/D)\cot\gamma_E \ln(V/V_E)]^2 \le 0.10 \tag{17}$$

The velocity range of interest, $|\ln(V/V_E)| < 1/2$ may be incorporated to produce the following region of validity:

$$|\tan\gamma_E| \ge 1.58\,L/D \tag{18}$$

Approximate regions of validity for various atmospheric-entry analyses are presented in Fig. 1. The analysis of reference 3 is limited to near circular velocities.

Comparison With Other Investigations

Entry investigations at small L/D and relatively steep entry angles are so rare that the only investigation which could be found for comparative purposes was Lees.[3] Lees' machine-calculated values which most closely approach the region of applicability of the above analysis are:

$$L/D = 1/4 \quad \text{and} \quad \gamma_E = -12°$$

giving $a/g|_{max} = 28(25)$ for $V_E = 26{,}000$ fps

and $a/g|_{max} = 39(45)$ for $V_E = 35{,}000$ fps

The values of the above analysis are given in parentheses, and are well within the 35 per cent accuracy limit dictated by $L/D = 1/4$ and $\gamma_E = -12°$.

For $L/D = 0$, the above analysis reduces to that of reference 1. Analyses similar to the above may be made for radiative and convective heating and Reynolds number.

References

[1] Allen, H. J., and Eggers, A. J., Jr., *A Study of the Motion and Aerodynamic Heating of Ballistic Missiles Entering the Earth's Atmosphere at High Supersonic Speeds*, NACA Report 1381, 1958.

[2] Riddell, F. R., and Teare, J. D., *The Differences Between Satellite and Ballistic Missile Re-entry Problems*, AVCO Res. Report 31, September, 1958.

[3] Lees, L., Hartwig, F. W., and Cohen, C. B., *Use of Aerodynamic Lift During Entry into the Earth's Atmosphere*, J. ARS, Vol. 29, No. 9, September, 1959.

✦ ✦ ✦

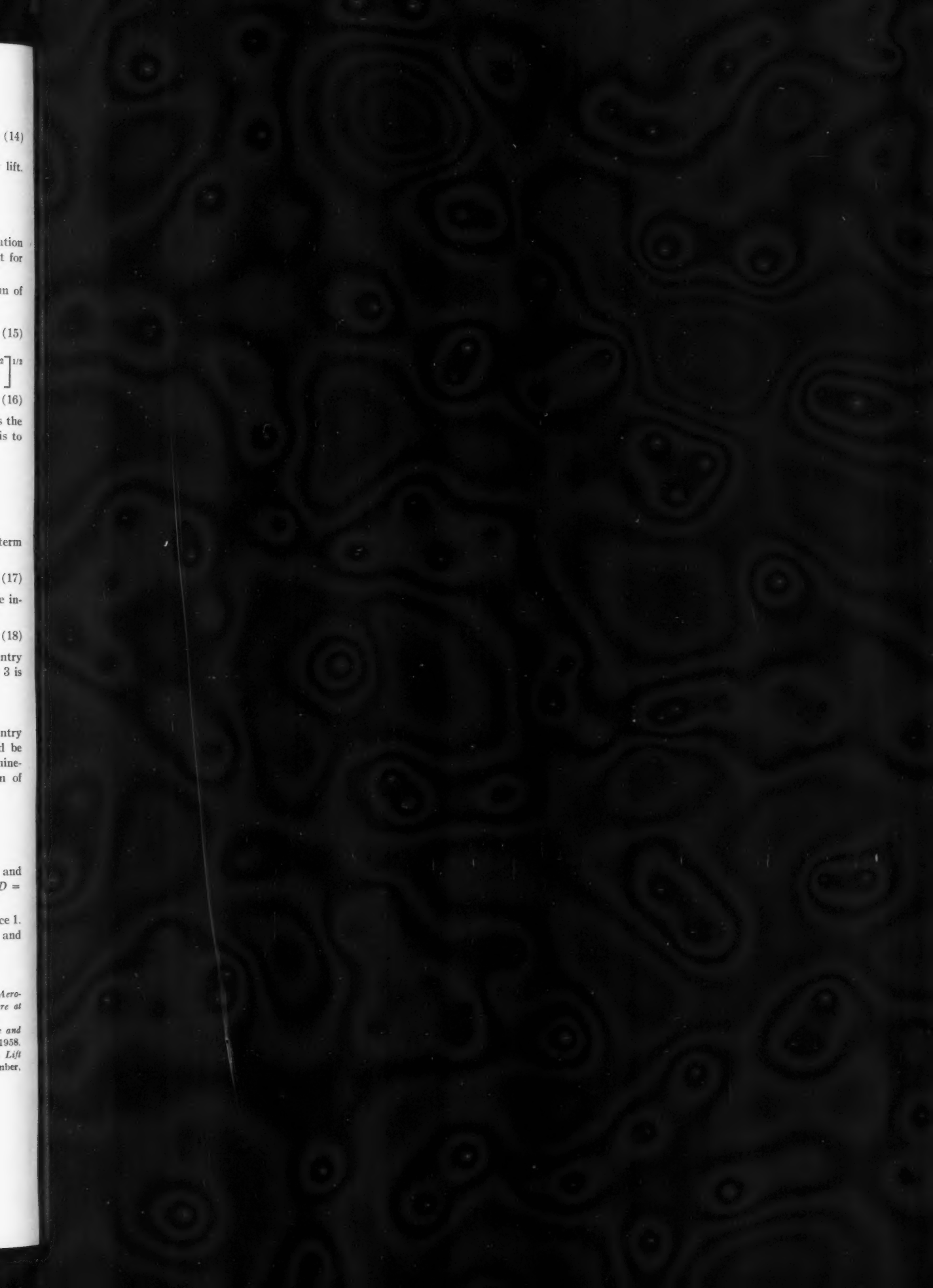

REQUIREMENTS *for* CONTRIBUTIONS
to the publications of the
INSTITUTE *of the* AEROSPACE SCIENCES

The Institute of the Aerospace Sciences invites both members and nonmembers from any country to submit papers for publication in the JOURNAL OF THE AEROSPACE SCIENCES and AEROSPACE ENGINEERING. The Institute, following the practice of other societies, does not pay for contributions.

The following directions for the preparation of papers, if followed by authors, will save correspondence, avoid the return of papers for changes, minimize the work of preparation for the printer, and save the expense due to the charges made for "author's corrections."

MANUSCRIPTS: The original typewritten copy of the paper is desired. **To expedite review, an additional copy of both the manuscript and figures should be submitted.** The manuscript must be double or triple spaced on one side of white paper sheets, consecutively numbered. There should be wide margins to allow for the marking of directions to the printer. Correcting, changing, or adding to papers after they are in type is costly. It is, therefore, imperative that papers submitted be in final form. Typographical errors may be corrected on proofs, but if authors wish to add material, they may do so at their own expense. In mailing, drawings may be rolled, but manuscripts should be sent flat. Send by first-class mail (register if you wish for your own protection) to the Editorial Office, Institute of the Aerospace Sciences, 2 East 64th Street, New York 21, N.Y. All manuscripts will be examined by the Editorial Committee and by the Editor. Authors will be advised as promptly as possible whether the paper is acceptable for publication.

TITLES: The title of the paper should be brief. The name and initials of the author should be written as he prefers. The use of the full name of an author is advocated because of the frequent duplication of initials and surnames which sometimes makes it difficult to establish the identity of the author. This is particularly important for large annual indexing and abstracting services. All titles and degrees or honors are omitted. The name of the organization with which the author is associated should be placed after his name on a separate line. The date on which the paper is received will be inserted by the Editor. The author's title or position should be indicated in a footnote.

SUMMARIES OR ABSTRACTS: An abstract to be printed at the beginning should accompany each article. It should be adequate as an *index* and as a *summary*. It should contain a statement of major conclusions reached, since summaries in many cases constitute the only source of information used in compiling scientific reference indexes. Abstracts printed in other journals, especially foreign, in most cases consist of summaries from printed papers. The summary should explain as adequately as possible the major conclusions to a nonspecialist in the subject and should contain from 100 to 300 words, depending on the length of the paper.

SUBHEADINGS: Subheadings should be inserted by the author at frequent intervals. The work of editorial preparation will be simplified by the author's provision of many subheadings.

MATTER USUALLY DELETED: Photographs or illustrations of little technical interest and not showing advances in general practice. Too detailed tabular matter (general results of such tables may be included in the text). Lengthy descriptions of materials or processes or of preliminary experiments or theories that preceded final results; salient features only are of interest.

REFERENCES: References should be numbered consecutively and grouped together at the end of the manuscript, with only the corresponding number being mentioned in the text. The arrangement should be as follows. For books: [1]Durand, W. F., *Aerodynamic Theory*, 1st Ed., Vol. 1, p. 23; Julius Springer, Berlin, 1934. For magazines: [1]England, C. R., Crawford, A. B., and Mumford, W. W., *Some Results of a Study of Ultra-Short-Wave Transmission Phenomenon*, Proc. IRE, Vol. 20, No. 12, pp. 481–482, March, 1933. Please give author, title, edition, volume, number, page, publisher, and place and date of publication as indicated. Omission of one required fact causes much extra editorial work and possible inaccuracies.

ILLUSTRATIONS: Illustrations should accompany manuscripts, and each should always be referred to in the text by number. Drawings or graphs should not be larger than 12 × 16 inches, and must be made with jet black India ink on white paper or tracing cloth, the latter being preferred. *Do not use typewriter for lettering.* The smallest lettering on 8 × 10 inch figures should be no less than $^1/_4$ inch high. Cross-section paper (white with black lines) may be used, but it should not have more than 4 lines per inch. If finer ruled paper is used, the major division lines should be drawn in with black ink, omitting the finer divisions. In the case of finely ruled paper, only blue-lined paper can be accepted. *Tracing paper and blueprints* are not acceptable. Lettering and all markings must be large enough to be readable after reduction to single-column width ($3^3/_{16}$ in.). Mail rolled or flat; never fold. Drawings that cannot be reproduced (including pencil drawings) will be returned to the author for redrawing, thus delaying publication of the paper. Photographs should be distinct and show clear black and white contrasts. They must be on glossy white paper. Avoid round or oval photographs.

CAPTIONS AND LEGENDS: Legends or captions must accompany each drawing or photograph submitted. If written on the drawing or photograph they should be placed below and well outside the part to be reproduced. Each table should have a caption such as Table 1, Table 2, Table 3, etc. Captions should be complete in themselves so as to make the data intelligible to the reader without reference to the text. A duplicate list of captions for figures should be included as the last page of the manuscript. Use "Fig. 1" (not Figure 1), "Figs. 3 and 4," etc., in both the text and the numbering of illustrations. In the text, "Eq. (1)" or "Eqs. (1) and (2)" is used, not "Equation (1)." In captions, legends, and in table headings, write all words in full; do not abbreviate, except for "Fig." and "Eq."

MATHEMATICAL WORK: Formulas may be typewritten or carefully written in pen and ink, the writing to be large enough so that it can be marked for the printer. Considerable space for marking should be allowed above and below all equations. All complicated equations should be repeated on separate sheets with adequate space left for marking. The solidus should be used for simple fractions appearing within the text. Make all expressions clear to the typesetter. Greek letters used in formulas should be clearly designated by name in the margin of the manuscript. The difference between capital and lower-case letters should be clearly distinguished and care taken to avoid confusion between zero (0) and the letter (o), between the numerical (one) and the letter (ell) and the prime (′), between alpha and a, kappa and k, u and mu, v and nu, n and eta. All subscripts and exponents should be clearly distinguished. Avoid complicated exponents and subscripts. Dots and bars over letters or mathematical expressions should also be avoided. When it is necessary to repeat a complicated expression, it should be represented by some convenient symbol.

SYMBOLS AND ABBREVIATIONS: The symbols recommended in the American Standard Association "Letter Symbols for Aeronautical Sciences," ASA Y10.7—1954, should be used wherever practicable. All symbols should be clearly written and carefully checked. Standard abbreviations should be used, and it should be noted that most abbreviations are lower case.

Corporate Members

OF THE

Institute of the Aerospace Sciences

AC SPARK PLUG DIVISION, GENERAL MOTORS CORPORATION

ACADEMY OF AERONAUTICS

AEROJET-GENERAL CORPORATION

AERONCA MANUFACTURING CORPORATION

AERONUTRONIC, DIVISION OF FORD MOTOR COMPANY

AEROSPACE CORPORATION

AGAWAM AIRCRAFT PRODUCTS, INC.

ALLIED RESEARCH ASSOCIATES, INC.

ALLISON DIVISION, GENERAL MOTORS CORPORATION

AMERICAN AIRLINES, INC.

AMERICAN BOSCH ARMA CORPORATION

AMERICAN OIL COMPANY

AMOCO CHEMICALS CORPORATION

ARDE ASSOCIATES

ASTRO-ELECTRONIC PRODUCTS DIVISION, RADIO CORPORATION OF AMERICA

AVCO-EVERETT RESEARCH LABORATORY

AVIEN, INC.

BEECH AIRCRAFT CORPORATION

BELL AEROSPACE CORPORATION

THE BENDIX CORPORATION

BOEING AIRPLANE COMPANY

BOOZ, ALLEN APPLIED RESEARCH, INC.

BULOVA RESEARCH AND DEVELOPMENT LABORATORIES, INC.

CANADAIR, LTD.

CHANCE VOUGHT CORPORATION

THE CHASE MANHATTAN BANK

CHICAGO AERIAL INDUSTRIES, INC.

CONTINENTAL MOTORS CORPORATION

CORNELL AERONAUTICAL LABORATORY, INC.

COX & COMPANY, INC.

CURTISS-WRIGHT CORPORATION

DANIEL, MANN, JOHNSON, & MENDENHALL

THE DECKER CORPORATION

DEFENSE ELECTRONIC PRODUCTS DIVISION, RADIO CORPORATION OF AMERICA

DEFENSE SYSTEMS DIVISION, GENERAL MOTORS CORPORATION

DEL MAR ENGINEERING LABORATORIES

DELCO-RADIO DIVISION, GENERAL MOTORS CORPORATION

DELCO-REMY DIVISION, GENERAL MOTORS CORPORATION

DOAK AIRCRAFT COMPANY, INC.

DOUGLAS AIRCRAFT COMPANY, INC.

DZUS FASTENER COMPANY, INC.

EASTERN AIR LINES, INC.

EATON MANUFACTURING COMPANY

EDO CORPORATION

ELASTIC STOP NUT CORPORATION OF AMERICA

ENGINEERING SUPERVISION COMPANY

FAIRCHILD CAMERA AND INSTRUMENT CORPORATION

FAIRCHILD ENGINE AND AIRPLANE CORPORATION

THE GARRETT CORPORATION

GENERAL APPLIED SCIENCE LABORATORIES, INC.

GENERAL DYNAMICS CORPORATION

GENERAL ELECTRIC COMPANY

GENERAL PRECISION, INC.

THE B. F. GOODRICH COMPANY

GOODYEAR AIRCRAFT CORPORATION

GRUMMAN AIRCRAFT ENGINEERING CORPORATION

HOFFMANN AIRCRAFT COMPANY

HUGHES AIRCRAFT COMPANY

INSURANCE COMPANY OF NORTH AMERICA COMPANIES

INTERNATIONAL BUSINESS MACHINES CORPORATION FEDERAL SYSTEMS DIVISION

THE INTERNATIONAL NICKEL COMPANY, INC.

ITT FEDERAL LABORATORIES, A DIVISION OF INTERNATIONAL TELEPHONE AND TELEGRAPH CORPORATION

JANITROL AIRCRAFT DIVISION, MIDLAND-ROSS CORPORATION

JOHNS-MANVILLE SALES CORPORATION

KOLLSMAN INSTRUMENT CORPORATION

LAVELLE AIRCRAFT CORPORATION

LEAR, INCORPORATED

C. W. LEMMERMAN, INC.

THE LIQUIDOMETER CORPORATION

ARTHUR D. LITTLE, INC.

LOCKHEED AIRCRAFT CORPORATION

THE MARQUARDT CORPORATION

THE MARTIN COMPANY

McDONNELL AIRCRAFT CORPORATION

MELETRON CORPORATION

MINNEAPOLIS-HONEYWELL REGULATOR COMPANY

MOBIL OIL COMPANY

NATIONAL CREDIT OFFICE, INC.

NORTH AMERICAN AVIATION, INC.

NORTHROP CORPORATION

NUCLEAR DEVELOPMENT CORPORATION OF AMERICA

PAN AMERICAN WORLD AIRWAYS, INC.

THE RALPH M. PARSONS COMPANY

PIASECKI AIRCRAFT CORPORATION

POLY INDUSTRIES, INC.

REPUBLIC AVIATION CORPORATION

ROHR AIRCRAFT CORPORATION

RYAN AERONAUTICAL COMPANY

SHELL OIL COMPANY

SIMMONDS PRECISION PRODUCTS, INC.

SOLAR AIRCRAFT COMPANY

SOUTHWEST PRODUCTS COMPANY

SPACE TECHNOLOGY LABORATORIES, INC.

R. DIXON SPEAS ASSOCIATES

SPERRY GYROSCOPE COMPANY, DIVISION OF SPERRY RAND CORPORATION

STANDARD-THOMSON CORPORATION

STANLEY AVIATION CORPORATION

THERM, INCORPORATED

THIOKOL CHEMICAL CORPORATION

THOMPSON RAMO WOOLDRIDGE INC.

TRANS WORLD AIRLINES, INC.

UNION CARBIDE METALS COMPANY, DIVISION OF UNION CARBIDE CORPORATION

UNITED AIR LINES, INC.

UNITED AIRCRAFT CORPORATION

UNITED STATES AVIATION UNDERWRITERS, INC.

VEHICLE RESEARCH CORPORATION

WESTERN GEAR CORPORATION

WESTINGHOUSE ELECTRIC CORPORATION